

<sup>1</sup> A Search in the Two-Photon Final State for  
<sup>2</sup> Evidence of New Particle Production in pp  
<sup>3</sup> Collisions at  $\sqrt{s} = 7$  TeV

<sup>4</sup> Rachel P. Yohay  
University of Virginia  
`rpy3y@virginia.edu`

<sup>5</sup> June 12, 2012

# **6** Contents

<b>7</b>	<b>1</b>	<b>Introduction</b>	<b>4</b>
<b>8</b>	<b>2</b>	<b>Motivation for Physics Beyond the Standard Model</b>	<b>7</b>
9	2.1	The Standard Model and Electroweak Symmetry Breaking . . . . .	8
10	2.2	Implications of the Higgs Mechanism . . . . .	12
11	2.3	Addressing Problems of the Standard Model with Supersymmetry . .	14
<b>12</b>	<b>3</b>	<b>The Supersymmetric Extension to the Standard Model</b>	<b>18</b>
13	3.1	Supermultiplet Representation . . . . .	18
14	3.2	The Unbroken SUSY Lagrangian . . . . .	19
15	3.3	Soft SUSY Breaking . . . . .	25
16	3.4	Gauge-Mediated SUSY Breaking . . . . .	28
17	3.5	Phenomenology of General Gauge Mediation . . . . .	31
18	3.6	Experimental Status of SUSY . . . . .	34
<b>19</b>	<b>4</b>	<b>The Large Hadron Collider</b>	<b>40</b>
20	4.1	Design Considerations and Performance Limitations . . . . .	41
21	4.2	Beam Injection . . . . .	44
22	4.3	Magnets and Cryogenics . . . . .	46
23	4.4	Radiofrequency Cavities . . . . .	49

24	<b>5 The Compact Muon Solenoid Experiment</b>	<b>51</b>
25	5.1 The Detectors and Their Operating Principles . . . . .	55
26	5.1.1 Tracking System . . . . .	55
27	5.1.2 Electromagnetic Calorimeter . . . . .	64
28	5.1.3 Hadronic Calorimeter . . . . .	69
29	5.1.4 Muon System . . . . .	73
30	5.2 Triggering, Data Acquisition, and Data Transfer . . . . .	78
31	5.2.1 Level 1 and High Level Trigger Systems . . . . .	78
32	5.2.2 Data Acquisition System . . . . .	82
33	5.2.3 Data Processing and Transfer to Computing Centers . . . . .	85
34	<b>6 Event Selection</b>	<b>88</b>
35	6.1 Object Reconstruction . . . . .	89
36	6.1.1 Photons . . . . .	89
37	6.1.2 Electrons . . . . .	100
38	6.1.3 Jets and Missing Transverse Energy . . . . .	100
39	6.2 HLT . . . . .	106
40	6.3 Event Quality . . . . .	109
41	6.4 Photon Identification Efficiency . . . . .	112
42	6.4.1 Tag and Probe Method . . . . .	113
43	6.4.2 Photon Efficiency Scale Factor $\epsilon_e^{\text{data}}/\epsilon_e^{\text{MC}}$ . . . . .	116
44	<b>7 Data Analysis</b>	<b>121</b>
45	7.1 Modeling the QCD Background . . . . .	125
46	7.1.1 Outline of the Procedure . . . . .	125
47	7.1.2 Reweighting . . . . .	126
48	7.1.3 Normalization . . . . .	137
49	7.2 Modeling the Electroweak Background . . . . .	137

50	7.3 Errors on the Background Prediction . . . . .	143
51	7.4 Results . . . . .	149
52	<b>8 Interpretation of Results in Terms of GMSB Models</b>	<b>155</b>
53	8.1 Simplified Models . . . . .	155
54	8.2 Upper Limit Calculation and Model Exclusion . . . . .	157
55	8.2.1 Signal Acceptance $\times$ Efficiency . . . . .	157
56	8.2.2 $CL_s$ and the Profile Likelihood Test Statistic . . . . .	161
57	8.3 Cross Section Upper Limits . . . . .	168
58	8.4 Exclusion Contours . . . . .	169
59	<b>9 Conclusion</b>	<b>174</b>
60	<b>A Monte Carlo Samples</b>	<b>176</b>
61	A.1 List of Samples . . . . .	176
62	A.2 Explanation of Naming Conventions . . . . .	177

# <sup>63</sup> Chapter 1

## <sup>64</sup> Introduction

<sup>65</sup> Although the Standard Model of particle physics has passed every experimental test  
<sup>66</sup> to date, it leaves some very fundamental questions unanswered. Why do particles have  
<sup>67</sup> mass? Why are their masses so different? Up to what energy scale is the Standard  
<sup>68</sup> Model a valid description of nature? Many competing theories have been proposed to  
<sup>69</sup> answer these questions. Establishing the existence of any one of them requires careful  
<sup>70</sup> searches for deviations from Standard Model predictions of particle production or  
<sup>71</sup> decay rates. The stellar performance of the Large Hadron Collider, the 7 TeV center-  
<sup>72</sup> of-mass energy proton collider located at the European Organization for Nuclear  
<sup>73</sup> Research (CERN) in Geneva, Switzerland, presents a golden opportunity to do such  
<sup>74</sup> a search for evidence of new physical phenomena.

<sup>75</sup> One nearly universal prediction of theories of physics beyond the Standard Model  
<sup>76</sup> is that at a high enough collision energy, heavy particles introduced by the new theory  
<sup>77</sup> will be produced. The heavy particles will then decay, leading to distinctive signatures  
<sup>78</sup> in the hermetic detectors that completely surround the collision points. By comparing  
<sup>79</sup> the observed rate of processes with a particular signature to the expected rate from  
<sup>80</sup> the Standard Model alone, the existence of a particular theory of new physics can be  
<sup>81</sup> confirmed or ruled out.

This thesis presents a search for evidence of new heavy particles decaying to a final state with two photons, jets, and a striking momentum imbalance that implies the existence of a new kind of particle that can easily pass through matter without leaving a trace. The signature is motivated by theories that incorporate supersymmetry, a new symmetry of nature that predicts supersymmetric antiparticles to the known particles, just as charge symmetry predicts a positively charged antiparticle for every negatively charged particle and vice versa. Supersymmetry can provide answers to all of the questions posed in the first paragraph. Besides its theoretical motivation, the choice of signature is also driven by the low rate of expected Standard Model background.

The search is performed at the Compact Muon Solenoid experiment, a detector capable of identifying photons, electrons, muons, quark jets,  $\tau$  leptons, and momentum imbalances with high efficiency. The central feature of the experiment is a superconducting solenoid, which, at a length of 13 m and a diameter of 7 m [1], is one of the largest superconducting magnets ever built. By bending the paths of charged particles in the final state under the Lorentz force, the magnetic field produced by the solenoid allows charged particle momenta to be accurately measured. Highly granular calorimeters sit inside the solenoid for the purpose of measuring the energy of neutral final state particles.

This thesis is organized as follows. Chapters 2 and 3 motivate the search for physics beyond the Standard Model and the specific signature of two photons, as well as give an overview of the Standard Model and supersymmetric theoretical frameworks. A description is given of the Large Hadron Collider in Chapter 4 and the Compact Muon Solenoid detector in Chapter 5. Chapters 6 and 7 explain in detail the experimental techniques used in the search. Chapter 6 shows how collisions that are likely to have produced a new particle are selected from the enormous amount of data collected, then Chapter 7 shows the data analysis in detail and presents the results. An interpretation

<sup>109</sup> of the results in terms of new physics models is given in Chapter 8. Finally, the thesis  
<sup>110</sup> is concluded in Chapter 9.

# <sup>111</sup> Chapter 2

## <sup>112</sup> Motivation for Physics Beyond the <sup>113</sup> Standard Model

<sup>114</sup> In the 1960s, Sheldon Glashow, Steven Weinberg, and Abdus Salam proposed a math-  
<sup>115</sup> ematical framework that unified the electromagnetic and weak forces at an energy  
<sup>116</sup> scale in the hundreds of GeV/c, as well as a mechanism for breaking the electroweak  
<sup>117</sup> symmetry at low energies [2]. At the same time, Murray Gell-Mann introduced the  
<sup>118</sup> concept of quarks to describe hadron spectroscopy, a concept that would later grow  
<sup>119</sup> into quantum chromodynamics (QCD), the full theory of the strong force [3]. These  
<sup>120</sup> two key developments motivated the unified representation of particle physics as a set  
<sup>121</sup> of fields whose dynamics are invariant under the Standard Model (SM) gauge group

$$SU(3)_C \otimes SU(2)_L \otimes U(1)_Y \quad (2.1)$$

<sup>122</sup> where  $SU(3)_C$  describes the quark QCD interactions,  $SU(2)_L$  describes the weak  
<sup>123</sup> interactions among quarks and leptons, and  $U(1)_Y$  describes the electromagnetic in-  
<sup>124</sup> teraction.

<sup>125</sup> The Standard Model has been an extremely successful predictor of particle pro-  
<sup>126</sup> duction and interaction cross-sections and decay rates, as well as of the exact masses

<sup>127</sup> of the electroweak force carriers. The case for the validity of the Standard Model was  
<sup>128</sup> bolstered by the many precision QCD and electroweak measurements carried out at  
<sup>129</sup> the Large Electron-Positron (LEP) collider, which ran from 1989-2000 at center-of-  
<sup>130</sup> mass energies between 65 and 104 GeV/ $c$  [4]. Figure 2.1 shows some of the highlights  
<sup>131</sup> of the LEP program.

<sup>132</sup> However, there are still deep theoretical problems with the Standard Model,  
<sup>133</sup> stemming from the introduction of the Higgs scalar into the theory to break elec-  
<sup>134</sup> troweak symmetry [5]. Since the Higgs self-energy diagram is quadratically sensitive  
<sup>135</sup> to the ultraviolet cutoff scale, and assuming that there are no new important en-  
<sup>136</sup> ergy scales of physics between the weak scale ( $\mathcal{O}(10^2 \text{ GeV}/c)$ ) and the Planck scale  
<sup>137</sup> ( $\mathcal{O}(10^{19} \text{ GeV}/c)$ ), in order to be consistent with experimental measurements, this dia-  
<sup>138</sup> gram must include a remarkable 17-orders-of-magnitude cancellation that is otherwise  
<sup>139</sup> poorly motivated [6]. The quest to find new physics at an intermediate energy scale  
<sup>140</sup> between the weak and Planck scales, and thus extend the Standard Model, was the  
<sup>141</sup> driving force behind the construction of the Large Hadron Collider (LHC) in 2009,  
<sup>142</sup> the world's highest energy particle accelerator to date.

<sup>143</sup> Section 2.1 of this chapter gives a brief overview of the Standard Model and  
<sup>144</sup> electroweak symmetry breaking. Sections 2.2 and 2.3 examine the issues raised by  
<sup>145</sup> electroweak symmetry breaking that the Standard Model is as yet ill-prepared to  
<sup>146</sup> address.

## <sup>147</sup> **2.1 The Standard Model and Electroweak Symme- <sup>148</sup> try Breaking**

<sup>149</sup> All of the elementary matter particles (fermions)—quarks, charged leptons, and neutrinos—  
<sup>150</sup> can be put in fundamental representations of the SM gauge groups. The fermion con-  
<sup>151</sup> tent of the Standard Model is summarized in Table 2.1. The left-handed doublets are

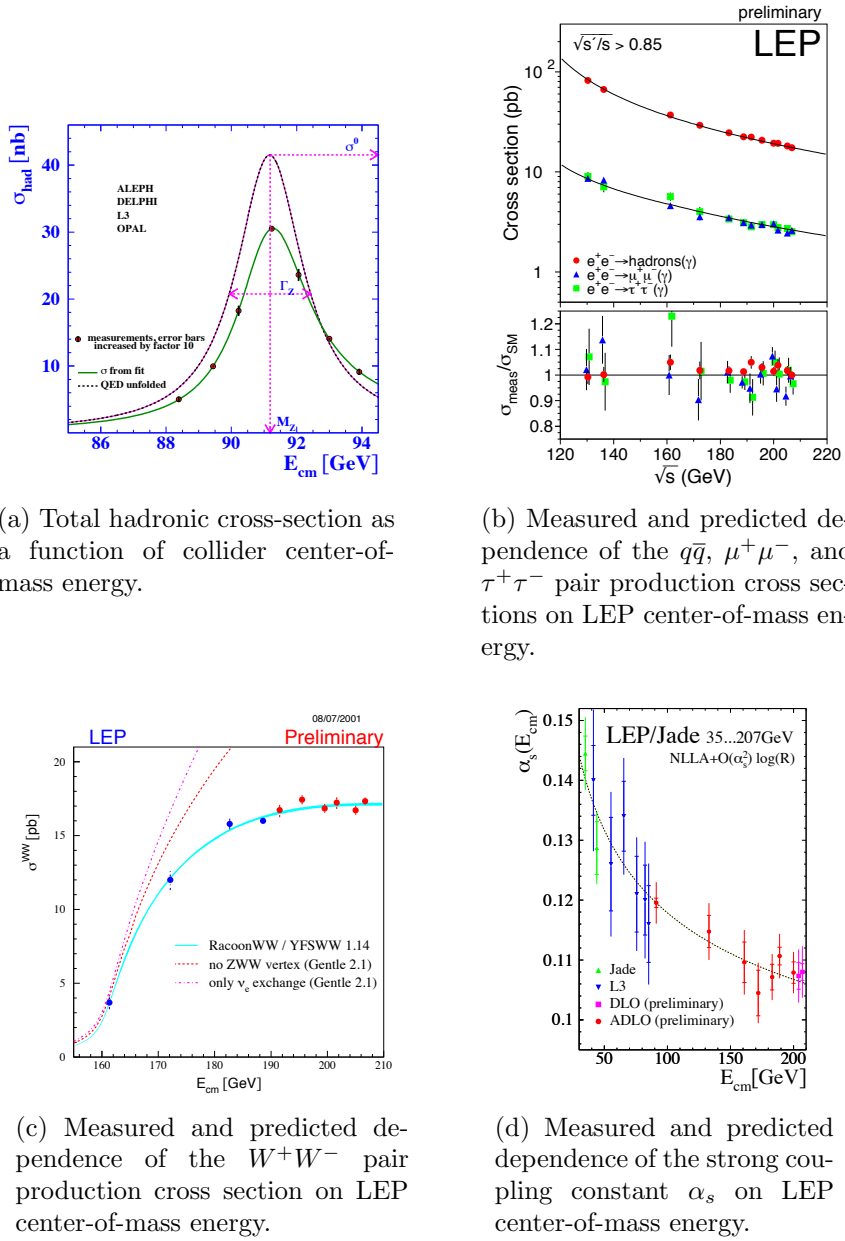


Figure 2.1: Selected LEP measurements demonstrating its contribution to the precise understanding of the Standard Model. Reprinted from ref. [4].

<sub>152</sub> analogous to the spinors of non-relativistic quantum mechanics, with the  $z$  component of “weak isospin”  $I_3$  equal to  $+1/2(-1/2)$  for the upper(lower) component of the <sub>153</sub> doublet.  
<sub>154</sub>

Table 2.1: Fermion content of the Standard Model.

Type	Notation	Representation under $SU(3)_C \otimes SU(2)_L \otimes U(1)_Y$	Couples to
Left-handed quark doublet	$\begin{pmatrix} u_L \\ d_L \\ c_L \\ s_L \\ b_L \\ t_L \end{pmatrix}$	(3, 2, $\frac{1}{6}$ )	$g, W, Z, \gamma$
Right-handed up-type quark singlet	$\begin{pmatrix} u_R^\dagger \\ c_R^\dagger \\ b_R^\dagger \end{pmatrix}$	( $\bar{3}$ , 1, $-\frac{2}{3}$ )	$g, \gamma$
Right-handed down-type quark singlet	$\begin{pmatrix} d_R^\dagger \\ s_R^\dagger \\ t_R^\dagger \end{pmatrix}$	( $\bar{3}$ , 1, $\frac{1}{3}$ )	$g, \gamma$
Left-handed lepton doublet	$\begin{pmatrix} \bar{\nu}_{eL} \\ e_L \\ \bar{\nu}_{\mu L} \\ \mu_L \\ \bar{\nu}_{\tau L} \\ \tau_L \end{pmatrix}$	(1, 2, $-\frac{1}{2}$ )	$W, Z, \gamma^a$
Right-handed charged lepton singlet	$\begin{pmatrix} e_R^\dagger \\ \mu_R^\dagger \\ \tau_R^\dagger \end{pmatrix}$	( $\bar{1}$ , 1, 1)	$\gamma$

<sup>a</sup>Except for neutrinos, which have zero electric charge.

<sub>155</sub> There are two types of weak interactions: flavor-changing charged currents, in  
<sub>156</sub> which an up-type and down-type quark or charged lepton and neutrino couple to  
<sub>157</sub> a charged  $W$ , and neutral currents, in which a fermion couples to another of the  
<sub>158</sub> same flavor and to a neutral  $Z$ . The charged current interaction is maximally parity  
<sub>159</sub> violating—it only couples left-handed fermion doublets. The neutral current inter-  
<sub>160</sub> action has a term coupling left-handed doublets and a term coupling right-handed  
<sub>161</sub> singlets. There are no mass terms of the form  $m_f^2(f_L \bar{f}_R + f_R \bar{f}_L)$  in the electroweak

<sub>162</sub> part of the Lagrangian, as these would violate gauge invariance [7]. The simplest  
<sub>163</sub> way to link the left-handed and right-handed fermions is via a Yukawa interaction  
<sub>164</sub>  $-\xi [\bar{f}_R(\phi^\dagger f_L) + (\bar{f}_L \phi) f_R]$  where  $\phi$  is a doublet of complex scalar fields [7].

<sub>165</sub> The fermion interaction part of the Lagrangian is [7]

$$\begin{aligned}\mathcal{L}_{\text{int}} = & \bar{f}_R i\gamma^\mu (\partial_\mu + i\frac{g_Y}{2} A_\mu Y) f_R \\ & + \bar{f}_L i\gamma^\mu (\partial_\mu + i\frac{g_Y}{2} A_\mu Y + i\frac{g_L}{2} \vec{\tau} \cdot \vec{b}_\mu) f_L\end{aligned}\quad (2.2)$$

<sub>166</sub> where  $g_Y$  and  $g_L$  are the electromagnetic and weak coupling constants, respectively;  
<sub>167</sub>  $Y$  is the weak hypercharge;  $A_\mu$  is the EM gauge field;  $\vec{b}_\mu$  is a three-component  
<sub>168</sub> vector of weak gauge fields; and  $\vec{\tau}$  is a three-component vector of the three Pauli  
<sub>169</sub> matrices. Before electroweak symmetry breaking, the three weak gauge fields and the  
<sub>170</sub> one EM gauge field are massless. The three weak gauge fields correspond to the three  
<sub>171</sub> generators (the Pauli matrices) of  $SU(2)_L$ . The one EM gauge field corresponds to the  
<sub>172</sub> one generator (the real scalar  $Y$ ) of  $U(1)_Y$ , where  $Y = 2(Q - I_3)$  ( $Q$  is electric charge).  
<sub>173</sub> For the  $SU(3)_C$  part of the Lagrangian, there are eight massless gauge fields (the  
<sub>174</sub> gluons) corresponding to the eight generators of  $SU(3)_C$  (the Gell-Mann matrices).

<sub>175</sub> To break the electroweak symmetry implicit in the massless gauge bosons, a dou-  
<sub>176</sub> blet of complex scalar fields (the Higgs) is introduced. It has a potential [7]

$$V(\phi^\dagger \phi) = \mu^2 \phi^\dagger \phi + |\lambda| (\phi^\dagger \phi)^2. \quad (2.3)$$

<sub>177</sub> Since  $\mu^2 < 0$ , the potential has the shape of a sombrero, as shown in Figure 2.2.  
<sub>178</sub> At the minimum of the potential, the scalar fields are not zero, but have some positive  
<sub>179</sub> vacuum expectation value (VEV) (it can be chosen such that one component is zero  
<sub>180</sub> and the other is  $\sqrt{-\mu^2/2|\lambda|}$ ). Nature spontaneously chooses one of the infinitely many

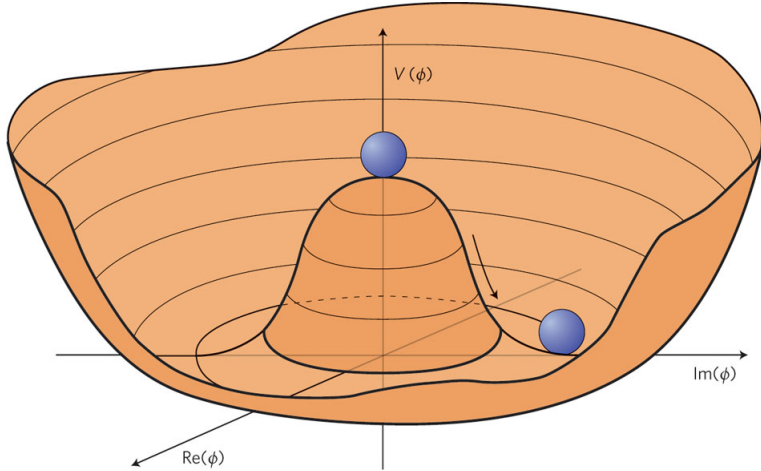


Figure 2.2: Higgs potential (the sombrero) as a function of the real and imaginary parts of the complex scalar field. The movement of the balls shows that the symmetry  $\phi = 0$  is spontaneously broken, the stable vacuum state of nature being somewhere along the circle of minimum potential. Reprinted from Fig. 1 of ref. [8].

181 vacua along the circle of minimum  $V$  in  $(\Re[\phi], \Im[\phi])$  space.

182 Expanding  $\phi$  about its VEV  $v$  in the Lagrangian introduces one massive scalar, the  
183 Higgs, and new mass terms for the gauge bosons. However, the terms with positive  
184 mass are not the original  $b_1$ ,  $b_2$ ,  $b_3$ , and  $A$  (spacetime indices dropped), but the  
185 observable  $W^\pm$  and  $Z^0$ . The  $W^\pm$  are linear combinations of  $b_1$  and  $b_2$ . The  $Z^0$  is  
186 one of the linear combinations of  $b_3$  and  $A$ , the other being the massless photon  $\gamma$ .  
187 After electroweak symmetry breaking (EWSB), the only remaining symmetry of the  
188 vacuum is electric charge, because the value of the electric charge operator acting on  
189 the Higgs VEV is zero. As expected, there is one massless photon in the SM to reflect  
190 this symmetry. The SM fermions can also acquire masses as a by-product of the Higgs  
191 mechanism via Yukawa terms.

## 192 2.2 Implications of the Higgs Mechanism

193 Before the formulation of the Higgs mechanism, physicists suspected that a heavy  
194 boson mediated the weak force from observations of  $\beta$  decay, but had no way of

195 putting a mass term into the Lagrangian without breaking gauge symmetry. The  
 196 Higgs mechanism of EWSB provided a way to generate masses for the  $SU(2)_L$  gauge  
 197 bosons. Furthermore, it predicted the  $W$  and  $Z$  masses in terms of  $g_L$ ,  $g_Y$ , and  $v$ .  $g_L$   
 198 and  $g_Y$  could be measured in scattering experiments, and in 1983 the  $W$  and  $Z$  were  
 199 first observed at the Super Proton-Antiproton Synchrotron (Sp $\bar{p}$ S) at the European  
 200 Organization for Nuclear Research (CERN) in Geneva, Switzerland [9, 10]. Crucially,  
 201 the values of the coupling constants and the gauge boson masses predict that the  
 202 Higgs VEV should be 246 GeV, so the Higgs mass should not be too much different  
 203 than that if  $\lambda$  is to remain small enough to do perturbation theory [11].

204 The Higgs mechanism raises some interesting questions that cannot be immedi-  
 205 ately answered by SM physics. First of all, why should  $\mu^2$  be negative? The form of  
 206 the Higgs potential given in Eq. 2.3 is about the simplest renormalizable form that  
 207 can be written for a scalar field, but the choice of  $\mu^2 < 0$  is completely arbitrary.  
 208 Second, how can the hierarchy problem be avoided?

209 The Higgs mass squared receives one-loop corrections from all the particles it  
 210 couples to; namely, all particles with mass. Because the Higgs is a scalar particle, one-  
 211 loop corrections are proportional to  $\Lambda_{\text{UV}}^2$ , where  $\Lambda_{\text{UV}}$  is the ultraviolet cutoff energy of  
 212 the loop integral.  $\Lambda_{\text{UV}}$  can be interpreted as the energy at which the SM can no longer  
 213 describe particle physics and non-SM physics takes over. Ideally,  $\Lambda_{\text{UV}}$  is something  
 214 like the Planck scale. However, taking  $\Lambda_{\text{UV}} = M_{\text{Planck}}$  implies that in order to keep the  
 215 Higgs mass of order a few hundred GeV, as required by experimental tests of EWSB, a  
 216 very large and precise counterterm must be applied at all orders in perturbation theory  
 217 to the bare  $m_H^2$ . The quadratic sensitivity of the Higgs mass to the cutoff scale and the  
 218 extremely fine-tuned counterterms it necessitates is called the hierarchy problem. SM  
 219 fermions do not experience this problem because chiral symmetry prevents explicit  
 220 fermion mass terms at any order, so by dimensional analysis, fermion masses can only  
 221 be sensitive to  $\ln \frac{\Lambda_{\text{UV}}}{\Lambda_{\text{other}}}$ .

<sup>222</sup> One of the most elegant ways to address these problems is to incorporate *super-*  
<sup>223</sup> *symmetry* (SUSY) into the SM. Supersymmetry is new fundamental symmetry of  
<sup>224</sup> nature between bosons and fermions, and will be discussed more thoroughly in Chap-  
<sup>225</sup> ter 3. The next section just briefly describes how supersymmetry can mitigate some  
<sup>226</sup> of the problems of the Higgs mechanism.

## <sup>227</sup> 2.3 Addressing Problems of the Standard Model <sup>228</sup> with Supersymmetry

<sup>229</sup> As in the ordinary Standard Model, the couplings and masses in supersymmetric  
<sup>230</sup> theory can be imposed at the supersymmetric scale and evolved down to the weak  
<sup>231</sup> scale by use of renormalization group equations. For many typical supersymmetric  
<sup>232</sup> scenarios (like the one shown in Figure 2.3),  $\mu^2$  is positive at the supersymmetric  
<sup>233</sup> scale but runs negative at the weak scale, leading to precisely the conditions needed  
<sup>234</sup> for EWSB. This is a consequence of the fact that the evolution of  $m_H^2$  depends on the  
<sup>235</sup> top quark Yukawa coupling, which, since the top is very heavy compared to the other  
<sup>236</sup> quarks ( $m_t \sim 42m_b$ ,  $m_t \sim 136m_c$  [13]), is large. In some sense, then, supersymmetry  
<sup>237</sup> not only provides the conditions for EWSB, but also explains why the top quark must  
<sup>238</sup> be so much heavier than the other quarks.

<sup>239</sup> SUSY's greatest strength, however, comes from the way it elegantly solves the  
<sup>240</sup> hierarchy problem. The Higgs squared mass corrections from fermion loops take the  
<sup>241</sup> form [12]

$$\Delta m_H^2 = -\frac{|\lambda_F|^2}{8\pi^2} \Lambda_{\text{UV}}^2 + \dots \quad (2.4)$$

<sup>242</sup> while the corrections from scalar loops would take the form [12]

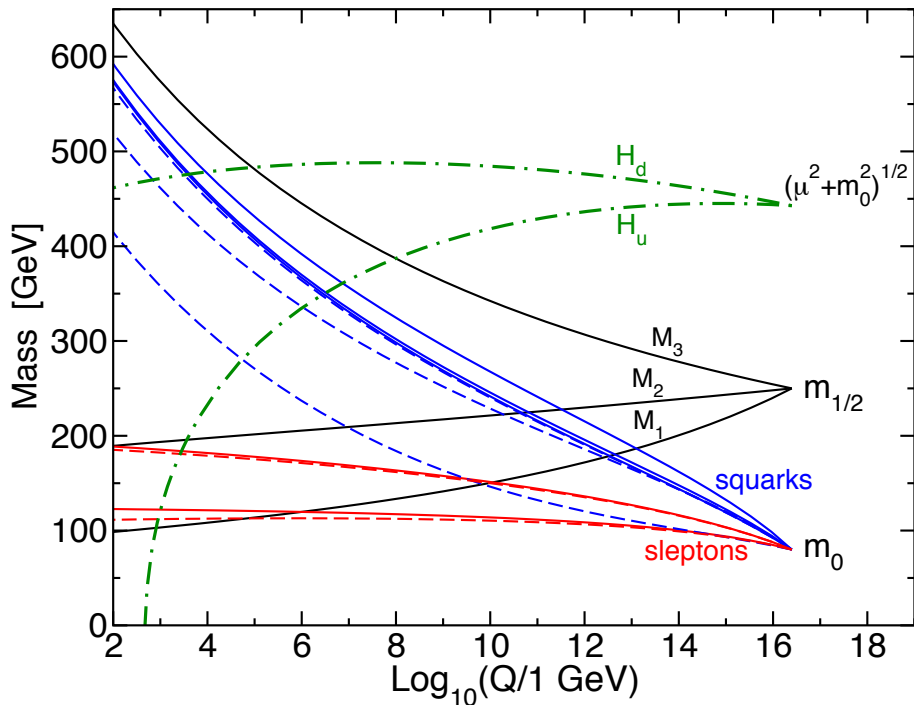


Figure 2.3: Predicted evolution of the free parameters of supersymmetry as a function of renormalization scale for a representative set of SUSY parameters. Note the dash-dotted line marked “ $H_u$ ” that goes negative at  $\sim 1$  TeV; this indicates  $\mu^2$  running negative. Reprinted from Fig. 7.4 of ref. [12].

$$\Delta m_H^2 = \frac{|\lambda_S|^2}{16\pi^2} \Lambda_{\text{UV}}^2 + \dots \quad (2.5)$$

where the ellipsis indicates terms proportional to  $\ln \Lambda_{\text{UV}}$  that do not pose a problem for the validity of the SM up to the Planck scale. Since the fermion and scalar contributions have opposite signs, if each SM fermion were accompanied by two as-yet undiscovered scalar particles with  $\lambda_S = |\lambda_F|^2$ , then the problematic quadratic terms in Eqs. 2.4 and 2.5 would exactly cancel. This is precisely the foundation of supersymmetry: for each fermion, there is a supersymmetric partner boson. This would remove the hierarchy problem altogether, and is the main reason physicists are eager to find evidence for the existence of supersymmetry at the LHC.

In addition to providing some rationale for the Higgs mechanism, SUSY makes two other very desirable predictions. The first is that the strong, weak, and electromagnetic coupling constants will exactly unify at an energy scale of  $10^{16}$  GeV/ $c$ , as shown in Figure 2.4. Unification of forces is not required by any experimental consideration, but is an elegant result nonetheless. The second prediction of SUSY, explained in more detail in Sec. 3.5, is the existence of a new stable particle, undiscovered as of yet because of its extremely feeble interactions with ordinary matter. This particle might be what astronomers have observed as dark matter. In fact, regardless of any theory, searches for evidence of dark matter at colliders are well motivated by suggestions from astronomy that some or all of the dark matter should have a mass at the weak scale [14].

Everything discussed in this chapter assumes that the Higgs mechanism is indeed the origin of EWSB. It is important to remember that no experimental observation to date unequivocally establishes the existence of the Higgs scalar, although small excesses recently unearthed in the LHC data [15, 16] tentatively suggest a Higgs mass

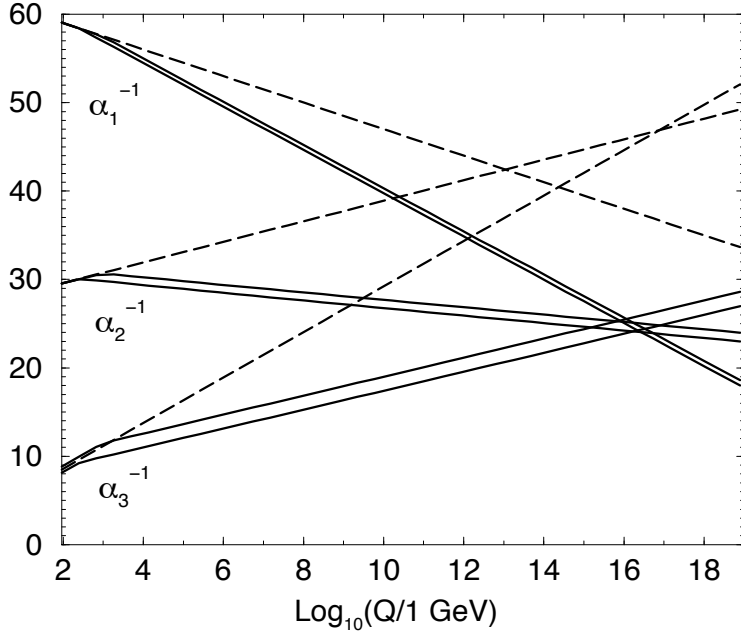


Figure 2.4: Inverse gauge couplings as a function of renormalization scale for the Standard Model assumption (dotted lines) and the SUSY assumption (solid lines; the double lines represent variations in SUSY parameters and in  $\alpha_S(m_Z)$ ). Reprinted from Fig. 5.8 of ref. [12].

of  $\sim 125$  GeV. The discovery of the Higgs scalar would place an important restriction on the types of SUSY theories that might be consistent with experiment. Operating at a 7 TeV center-of-mass energy, the LHC can thoroughly probe the scale of EWSB and the expected mass range of the Higgs, as well as the mass range of supersymmetric particles if SUSY is the solution to the hierarchy problem. Therefore, discovering or excluding SUSY is a key goal of the LHC physics program. The next chapter discusses SUSY more formally and shows what phenomenological consequences it entails.

# <sup>273</sup> Chapter 3

## <sup>274</sup> <sup>275</sup> The Supersymmetric Extension to the Standard Model

<sup>276</sup> The following introduction to SUSY focuses primarily on the aspects of the formalism that are relevant to phenomenology. In particular, most of the details of SUSY breaking (about which there is little theoretical consensus) are omitted, except where they are relevant to experiment. The notation is similar to that used in refs. [6] and [12], and much of the information presented is culled from those references.

### <sup>281</sup> 3.1 Supermultiplet Representation

<sup>282</sup> The Standard Model is extended to include supersymmetry by the introduction of a supersymmetry transformation that takes fermionic states to bosonic states and vice versa. The resulting model is called the *supersymmetric Standard Model*. In analogy with the known symmetries of the Standard Model, the SUSY transformation has associated generators that obey defining commutation and anticommutation relations, and a fundamental representation. All SM particles and their *superpartners* fall into one of two *supermultiplet* representations. Using the property of SUSY that

$$n_F = n_B, \quad (3.1)$$

289 where  $n_F$  is the number of fermionic degrees of freedom per supermultiplet and  $n_B$  is  
 290 the number of bosonic degrees of freedom, the two types of supermultiplets are

- 291     1. *Chiral supermultiplets*: Weyl fermions (two helicity states  $\Rightarrow n_F = 2$ ) associated  
 292       with complex scalar fields (with two real components  $\Rightarrow n_B = 2$ )
- 293     2. *Gauge supermultiplets*: Spin-1 vector bosons (two helicity states  $\Rightarrow n_B = 2$ )  
 294       associated with Weyl fermions (two helicity states  $\Rightarrow n_F = 2$ )

295     In the gauge supermultiplet, the vector boson is assumed massless (i.e. before  
 296 EWSB generates a mass for it). Since the superpartners to the SM particles have not  
 297 yet been discovered, they must be significantly heavier than their SM counterparts.  
 298 Unbroken SUSY predicts that the SM particles and their superpartners must have  
 299 exactly the same mass, so ultimately a mechanism for SUSY breaking, in addition to  
 300 EWSB, must be introduced to generate masses for the superpartners (see Sec. 3.3).  
 301 Tables 3.1 and 3.2 show the chiral and gauge supermultiplets of the supersymmetric  
 302 Standard Model, respectively. Note that the scalar partners to the SM fermions are  
 303 denoted by placing an “s” in front of their names, while the chiral fermion partners  
 304 to the SM gauge bosons are denoted by appending “ino” to their names.

### 305 3.2 The Unbroken SUSY Lagrangian

306 The first piece of the full unbroken SUSY Lagrangian density consists of the kinetic  
 307 and interacting terms related to the chiral supermultiplets. As explained in Sec. 3.1, a  
 308 chiral supermultiplet consists of Weyl fermions  $\psi$  (the ordinary fermion) and complex  
 309 scalars  $\phi$  (the sfermion). For a collection of such chiral supermultiplets, the Lagrangian  
 310 is

Table 3.1: Chiral supermultiplets of the supersymmetric Standard Model. In the last column, the first number refers to the supermultiplet representation under  $SU(3)_C$  (e.g. **3** means it has color charge and feels QCD), the second number refers to the representation under  $SU(2)_L$  (e.g. **2** means it has weak isospin and feels the weak interaction), and the third number is the value of the hypercharge. A bar over a number refers to the adjoint representation. **1** means that the supermultiplet is not charged under that group, and thus does not feel the associated force (for example, the right-handed fermion singlets do not feel the weak interaction). Adapted from Table 1.1 of ref. [12].

Type of supermultiplet	Notation	Spin-0 component	Spin-1/2 component	Representation under $SU(3)_C \otimes SU(2)_L \otimes U(1)_Y$
Left-handed quark/squark doublet ( $\times 3$ families)	$Q$	$(\tilde{u}_L \tilde{d}_L)$	$(u_L d_L)$	$(\mathbf{3}, \mathbf{2}, \frac{1}{6})$
Right-handed up-type quark/squark singlet ( $\times 3$ families)	$\bar{u}$	$\tilde{u}_R^*$	$u_R^\dagger$	$(\overline{\mathbf{3}}, \mathbf{1}, -\frac{2}{3})$
Right-handed down-type quark/squark singlet ( $\times 3$ families)	$\bar{d}$	$\tilde{d}_R^*$	$d_R^\dagger$	$(\overline{\mathbf{3}}, \mathbf{1}, \frac{1}{3})$
Left-handed lepton/slepton doublet ( $\times 3$ families)	$L$	$(\tilde{\nu}_{eL} \tilde{e}_L)$	$(\bar{\nu}_{eL} e_L)$	$(\mathbf{1}, \mathbf{2}, -\frac{1}{2})$
Right-handed lepton/slepton singlet ( $\times 3$ families)	$\bar{e}$	$\tilde{e}_R^*$	$e_R^\dagger$	$(\overline{\mathbf{1}}, \mathbf{1}, 1)$
Up-type Higgs/Higgsino doublet	$H_u$	$(H_u^+ H_u^0)$	$(\tilde{H}_u^+ \tilde{H}_u^0)$	$(\mathbf{1}, \mathbf{2}, \frac{1}{2})$
Down-type Higgs/Higgsino doublet	$H_d$	$(H_d^0 H_d^-)$	$(\tilde{H}_d^0 \tilde{H}_d^-)$	$(\mathbf{1}, \mathbf{2}, -\frac{1}{2})$

Table 3.2: Gauge supermultiplets of the supersymmetric Standard Model. Adapted from Table 1.2 of ref. [12].

Type of supermultiplet	Spin-1/2 component	Spin-1 component	Representation under $SU(3)_C \otimes SU(2)_L \otimes U(1)_Y$
Gluon/gluino	$\tilde{g}$	$g$	(8, 1, 0)
W/wino	$\widetilde{W}^\pm \widetilde{W}^0$	$W^\pm W^0$	(1, 3, 0)
B/bino	$\tilde{B}^0$	$B^0$	(1, 1, 0)

$$\begin{aligned} \mathcal{L}_{\text{chiral}} = & -\partial^\mu \phi^{*i} \partial_\mu \phi_i - V_{\text{chiral}}(\phi, \phi^*) - i\psi^{\dagger i} \bar{\sigma}^\mu \partial_\mu \psi_i - \frac{1}{2} M^{ij} \psi_i \psi_j \\ & - \frac{1}{2} M_{ij}^* \psi^{\dagger i} \psi^{\dagger j} - \frac{1}{2} y^{ijk} \phi_i \psi_j \psi_k - \frac{1}{2} y_{ijk}^* \phi^{*i} \psi^{\dagger j} \psi^{\dagger k} \end{aligned} \quad (3.2)$$

where  $i$  runs over all supermultiplets in Table 3.1,  $\bar{\sigma}^\mu$  are the negative of the Pauli matrices (except for  $\sigma^0 = \bar{\sigma}^0$ ),  $M^{ij}$  is a mass matrix for the fermions,  $y^{ijk}$  are the Yukawa couplings between one scalar and two spinor fields, and  $V_{\text{chiral}}(\phi, \phi^*)$  is the scalar potential

$$\begin{aligned} V_{\text{chiral}}(\phi, \phi^*) = & M_{ik}^* M^{kj} \phi^{*i} \phi_j + \frac{1}{2} M^{in} y_{jkn}^* \phi_i \phi^{*j} \phi^{*k} \\ & + \frac{1}{2} M_{in}^* y^{jkn} \phi^{*i} \phi_j \phi_k + \frac{1}{4} y^{ijn} y_{klm}^* \phi_i \phi_j \phi^{*k} \phi^{*l}. \end{aligned} \quad (3.3)$$

The Lagrangian can also be written as the kinetic terms plus derivatives of the *superpotential*  $W$ :

$$\begin{aligned} \mathcal{L}_{\text{chiral}} = & -\partial^\mu \phi^{*i} \partial_\mu \phi_i - i\psi^{\dagger i} \bar{\sigma}^\mu \partial_\mu \psi_i \\ & - \frac{1}{2} \left( \frac{\delta^2 W}{\delta \phi^i \delta \phi^j} \psi_i \psi_j + \frac{\delta^2 W^*}{\delta \phi_i \delta \phi_j} \psi^{\dagger i} \psi^{\dagger j} \right) - \frac{\delta W}{\delta \phi^i} \frac{\delta W^*}{\delta \phi_i} \end{aligned} \quad (3.4)$$

<sup>317</sup> where

$$W = M^{ij} \phi_i \phi_j + \frac{1}{6} y^{ijk} \phi_i \phi_j \phi_k. \quad (3.5)$$

<sup>318</sup> The second part of the Lagrangian involves the gauge supermultiplets. In terms  
<sup>319</sup> of the spin-1 ordinary gauge boson  $A_\mu^a$  and the spin-1/2 Weyl spinor gaugino  $\lambda^a$  of  
<sup>320</sup> the gauge supermultiplet, where  $a$  runs over the number of generators for the SM  
<sup>321</sup> subgroup (i.e. 1-8 for  $SU(3)_C$ , 1-3 for  $SU(2)_L$ , and 1 for  $U(1)_Y$ ), this part of the  
<sup>322</sup> Lagrangian is

$$\mathcal{L}_{\text{gauge}} = -\frac{1}{4} F_{\mu\nu}^a F^{\mu\nu a} - i \lambda^a \bar{\sigma}^\mu D_\mu \lambda^a + \frac{1}{2} D^a D^a \quad (3.6)$$

<sup>323</sup> where

$$F_{\mu\nu}^a = \partial_\mu A_\nu^a - \partial_\nu A_\mu^a + g f^{abc} A_\mu^b A_\nu^c \quad (3.7)$$

<sup>324</sup> ( $g$  is the coupling constant and  $f^{abc}$  are the structure constants for the particular SM  
<sup>325</sup> gauge group),

$$D_\mu \lambda^a = \partial_\mu \lambda^a + g f^{abc} A_\mu^b \lambda^c, \quad (3.8)$$

<sup>326</sup> and  $D^a$  is an auxiliary field that is introduced as a bookkeeping tool to keep the  
<sup>327</sup> fermionic and bosonic degrees of freedom equal both on- and off-shell. There is no  
<sup>328</sup> kinetic term for  $D^a$  in the Lagrangian, so therefore it does not propagate or represent

<sup>329</sup> any real particle. Its equation of motion, from  $\delta\mathcal{L}/\delta D^a = 0$ , yields a simple algebraic  
<sup>330</sup> expression for  $D^a$  that can be used to eliminate it from the Lagrangian if desired.

<sup>331</sup> To build a fully supersymmetric and gauge-invariant Lagrangian, the ordinary  
<sup>332</sup> derivatives in  $\mathcal{L}_{\text{chiral}}$  (Eq. 3.2) must be replaced by covariant derivatives

$$D_\mu \phi_i = \partial_\mu \phi_i - ig A_\mu^a (T^a \phi)_i \quad (3.9)$$

$$D_\mu \phi^{*i} = \partial_\mu \phi^{*i} + ig A_\mu^a (\phi^* T^a)^i \quad (3.10)$$

$$D_\mu \psi_i = \partial_\mu \psi_i - ig A_\mu^a (T^a \psi)_i. \quad (3.11)$$

<sup>333</sup> This leads to the full Lagrangian

$$\begin{aligned} \mathcal{L} &= \mathcal{L}_{\text{chiral}} + \mathcal{L}_{\text{gauge}} \\ &\quad - \sqrt{2} g (\phi^{*i} T^a \psi_i) \lambda^a - \sqrt{2} g \lambda^{\dagger a} (\psi^{\dagger i} T^a \phi_i) + g (\phi^{*i} T^a \phi_i) D^a \\ &= -\partial^\mu \phi^{*i} \partial_\mu \phi_i - i \psi^{\dagger i} \bar{\sigma}^\mu \partial_\mu \psi_i + ig \partial^\mu \phi^{*i} A_\mu^a (T^a \phi)_i - ig \partial_\mu \phi_i A^{\mu a} (\phi^* T^a)^i \\ &\quad - g^2 A^{\mu a} (\phi^* T^a)^i A_\mu^a (T^a \phi)_i - g \psi^{\dagger i} \bar{\sigma}^\mu A_\mu^a (T^a \psi)_i - V_{\text{chiral}}(\phi, \phi^*) \\ &\quad - \frac{1}{2} M^{ij} \psi_i \psi_j - \frac{1}{2} M_{ij}^* \psi^{\dagger i} \psi^{\dagger j} - \frac{1}{2} y^{ijk} \phi_i \psi_j \psi_k - \frac{1}{2} y_{ijk}^* \phi^{*i} \psi^{\dagger j} \psi^{\dagger k} \\ &\quad - \frac{1}{4} F_{\mu\nu}^a F^{\mu\nu a} - i \lambda^{\dagger a} \bar{\sigma}^\mu \partial_\mu \lambda^a - ig \lambda^{\dagger a} \bar{\sigma}^\mu f^{abc} A_\mu^b \lambda^c + \frac{1}{2} D^a D^a \\ &\quad - \sqrt{2} g (\phi^{*i} T^a \psi_i) \lambda^a - \sqrt{2} g \lambda^{\dagger a} (\psi^{\dagger i} T^a \phi_i) + g (\phi^{*i} T^a \phi_i) D^a. \end{aligned} \quad (3.12)$$

<sup>334</sup> Writing out  $F_{\mu\nu}^a$  and  $V_{\text{chiral}}(\phi, \phi^*)$  explicitly combining the  $D^a$  terms using the equation  
<sup>335</sup> of motion  $D^a = -g \phi^{*i} T^a \phi_i$ , and rearranging some terms, the final unbroken SUSY  
<sup>336</sup> Lagrangian is

$$\begin{aligned}
\mathcal{L} = & -\partial^\mu \phi^{*i} \partial_\mu \phi_i - i\psi^{\dagger i} \bar{\sigma}^\mu \partial_\mu \psi_i \\
& - \frac{1}{4} (\partial_\mu A_\nu^a - \partial_\nu A_\mu^a) (\partial^\mu A^{\nu a} - \partial^\nu A^{\mu a}) - i\lambda^{\dagger a} \bar{\sigma}^\mu \partial_\mu \lambda^a \\
& - M_{ik}^* M^{kj} \phi^{*i} \phi_j - \frac{1}{2} M^{ij} \psi_i \psi_j - \frac{1}{2} M_{ij}^* \psi^{\dagger i} \psi^{\dagger j} \\
& + ig \partial^\mu \phi^{*i} A_\mu^a (T^a \phi)_i - ig \partial_\mu \phi_i A^{\mu a} (\phi^* T^a)^i - g \psi^{\dagger i} \bar{\sigma}^\mu A_\mu^a (T^a \psi)_i \\
& - ig \lambda^{\dagger a} \bar{\sigma}^\mu f^{abc} A_\mu^b \lambda^c \\
& - \frac{1}{4} g f^{abc} [(\partial_\mu A_\nu^a - \partial_\nu A_\mu^a) A^{\mu b} A^{\nu c} + A_\mu^b A_\nu^c (\partial^\mu A^{\nu a} - \partial^\nu A^{\mu a})] \\
& - \frac{1}{2} M_{in}^* y^{jkn} \phi^{*i} \phi_j \phi_k - \frac{1}{2} M^{in} y_{jkn}^* \phi_i \phi^{*j} \phi^{*k} \\
& - \frac{1}{2} y^{ijk} \phi_i \psi_j \psi_k - \frac{1}{2} y_{ijk}^* \phi^{*i} \psi^{\dagger j} \psi^{\dagger k} \\
& - \sqrt{2} g (\phi^{*i} T^a \psi_i) \lambda^a - \sqrt{2} g \lambda^{\dagger a} (\psi^{\dagger i} T^a \phi_i) \\
& - g^2 A^{\mu a} (\phi^* T^a)^i A_\mu^a (T^a \phi)_i - \frac{1}{4} g^2 f^{abc} A_\mu^b A_\nu^c f^{abc} A^{\mu b} A^{\nu c} \\
& - \frac{1}{4} y^{ijn} y_{kln}^* \phi_i \phi_j \phi^{*k} \phi^{*l} - \frac{1}{2} g^2 (\phi^{*i} T^a \phi_i)^2.
\end{aligned} \tag{3.13}$$

<sup>337</sup> The above Lagrangian applies to chiral supermultiplets interacting with one kind  
<sup>338</sup> of gauge supermultiplet (i.e. one SM gauge group). In the general case, there are  
<sup>339</sup> additional terms corresponding to interactions with all three SM gauge groups.

<sup>340</sup> The following list gives a description of the terms in Eq. 3.13:

- <sup>341</sup> • First two lines: kinetic terms for the four types of fields  $\phi_i$ ,  $\psi_i$ ,  $A_\mu^a$ , and  $\lambda^a$
- <sup>342</sup> • Third line: mass terms for the  $\phi_i$  and  $\psi_i$  (see Figs. 3.1(a) and 3.1(b))
- <sup>343</sup> • Fourth and fifth lines: cubic couplings in which  $\phi_i$ ,  $\psi_i$ , or  $\lambda^a$  radiates an  $A_\mu^a$  (see  
<sup>344</sup> Figs. 3.1(c), 3.1(d), and 3.1(e))
- <sup>345</sup> • Sixth line: triple gauge boson couplings (see Fig. 3.1(f))
- <sup>346</sup> • Seventh line: triple sfermion couplings (see Fig. 3.1(g))

- 347     • Eighth line: cubic couplings in which  $\psi_i$  radiates a  $\phi_i$  (see Fig. 3.1(h))
- 348     • Ninth line:  $\phi_i$ - $\psi_i$ - $\lambda^a$  vertices (see Fig. 3.1(i))
- 349     • 10<sup>th</sup> line:  $A_\mu^a$ - $A_\mu^a$ - $\phi_i$ - $\phi_i$  and quadruple gauge boson couplings (see Figs. 3.1(j)  
350               and 3.1(k))
- 351     • 11<sup>th</sup> line:  $\phi_i^4$  vertices (see Figs. 3.1(l) and 3.1(m))

### 352   3.3 Soft SUSY Breaking

353   Since quadratic divergences in sfermion masses vanish to all orders in perturbation  
354   theory in plain unbroken SUSY [12] due to the presence of gauge and Yukawa in-  
355   teractions with the necessary relationships between coupling constants (i.e. chiral  
356   symmetry inherited from the partner fermion protects the sfermion masses, as ex-  
357   plained in Sec. 2.2), it is desirable that the terms that break SUSY not disturb this  
358   property. In addition, SUSY should be broken spontaneously, as electroweak symme-  
359   try is broken in the Standard Model, so that it is only made manifest at high energies.  
360   To satisfy these constraints, SUSY-breaking terms are simply added to the unbroken  
361   SUSY Lagrangian in Eq. 3.13 such that  $\mathcal{L}_{\text{total}} = \mathcal{L}_{\text{unbroken}} + \mathcal{L}_{\text{breaking}}$ . The coefficients  
362   of terms in  $\mathcal{L}_{\text{breaking}}$  must have positive mass dimension in order not to contribute  
363   quadratically divergent loop corrections to the scalar masses (like the Higgs mass);  
364   i.e. to not create a hierarchy problem (Sec. 2.2) for the scalars.<sup>1</sup> This form of SUSY

---

<sup>1</sup>This point can be argued via dimensional analysis. Radiative corrections take the form  $\Delta m_S^2$ , where  $m_S$  is the mass of the scalar particle in question. The dimensions of  $\Delta m_S^2$  are mass<sup>2</sup>.  $\Delta m_S^2$  is proportional to some coupling constant or mass coefficient  $k$  multiplied by a function of  $\Lambda_{\text{UV}}$ , the high energy cutoff scale. The function of  $\Lambda_{\text{UV}}$  is determined by a loop integral, and thus typically takes the form  $\Lambda_{\text{UV}}^2$  (quadratically divergent) or  $\ln \frac{\Lambda_{\text{UV}}}{m_{\text{low}}}$  (logarithmically divergent, where  $m_{\text{low}}$  is some other lower-mass scale in the problem). Now, if  $k$  already contributes at least one power of mass to  $\Delta m_S^2$ , then the high-energy behavior—the function of  $\Lambda_{\text{UV}}$ —can only contribute at most one power of the dimensionful parameter  $\Lambda_{\text{UV}}$ . However, there are typically no loop integrals that diverge linearly in  $\Lambda_{\text{UV}}$ , so by forcing  $k$  to have positive mass dimension, the form of the radiative corrections contributed by SUSY-breaking terms is limited to  $\Delta m_S^2 \sim m_{\text{low}}^2 \ln \frac{\Lambda_{\text{UV}}}{m_{\text{low}}}$ . In effect, the possibility of dangerous corrections proportional to  $\Lambda_{\text{UV}}^2$  is excluded by dimensional analysis if the requirement that  $k$  contribute at least one power of mass is enforced.

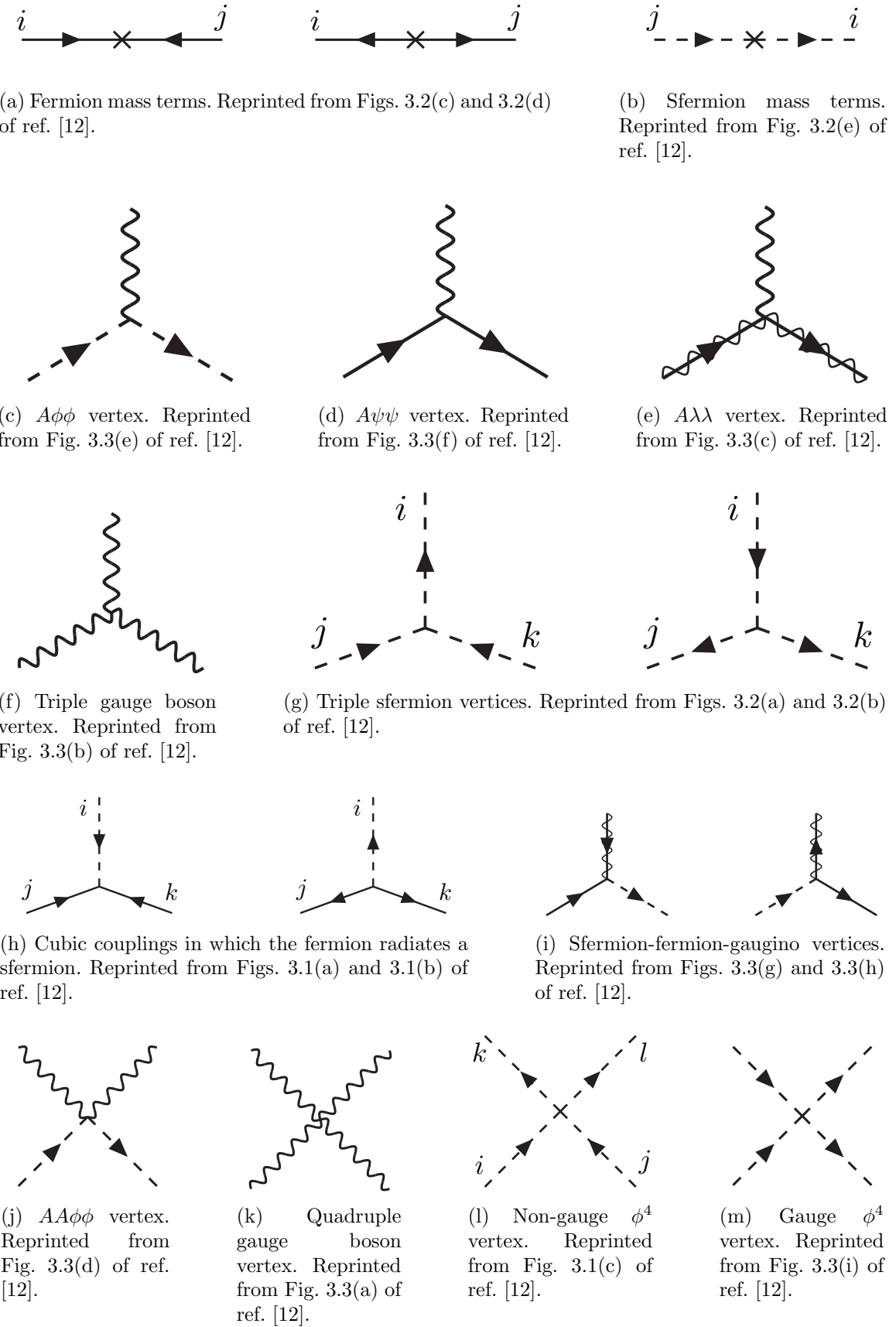


Figure 3.1: Interactions in the unbroken SUSY Lagrangian.

<sup>365</sup> breaking is called *soft*, and all coefficients of soft SUSY breaking terms are expected  
<sup>366</sup> to be of order  $m_{\text{soft}}$  or  $m_{\text{soft}}^2$ .

<sup>367</sup> Soft SUSY breaking terms give masses to the sfermions and gauginos and introduce  
<sup>368</sup> a cubic sfermion vertex. The soft terms are given by

$$\begin{aligned} \mathcal{L}_{\text{soft}} = & -\frac{1}{2}(M_3\tilde{g}^a\tilde{g}^a + M_2\tilde{W}^a\tilde{W}^a + M_1\tilde{B}\tilde{B} + \text{h.c.}) \\ & - (a_u^{ij}\tilde{u}_{Ri}^*\tilde{Q}_jH_u - a_d^{ij}\tilde{d}_{Ri}^*\tilde{Q}_jH_d - a_e^{ij}\tilde{e}_{Ri}^*\tilde{L}_jH_d + \text{h.c.}) \\ & - m_{\tilde{Q}_{ij}}^2\tilde{Q}_i^\dagger\tilde{Q}_j - m_{\tilde{L}_{ij}}^2\tilde{L}_i^\dagger\tilde{L}_j \\ & - m_{\tilde{u}_{ij}}^2\tilde{u}_{Ri}\tilde{u}_{Rj}^* - m_{\tilde{d}_{ij}}^2\tilde{d}_{Ri}\tilde{d}_{Rj}^* - m_{\tilde{e}_{ij}}^2\tilde{e}_{Ri}\tilde{e}_{Rj}^* \\ & - m_{H_u}^2H_u^*H_u - m_{H_d}^2H_d^*H_d - (bH_uH_d + \text{h.c.}) \end{aligned} \quad (3.14)$$

<sup>369</sup> where  $a$  runs from 1-8 for  $\tilde{g}^a$  and from 1-3 for  $\tilde{W}^a$ , and  $i, j$  run over the three families.  
<sup>370</sup> The color indices are not shown. The first line of Eq. 3.14 contains the gaugino mass  
<sup>371</sup> terms. The second line contains cubic scalar couplings that contribute to mixing  
<sup>372</sup> between the left- and right-handed third generation sfermions (it is assumed in the  
<sup>373</sup> supersymmetric Standard Model that the  $a_u^{ij}$ ,  $a_d^{ij}$ , and  $a_e^{ij}$  are negligible unless  $i =$   
<sup>374</sup>  $j = 3$ ). The third and fourth lines of Eq. 3.14 contain squark and slepton mass terms,  
<sup>375</sup> and finally the last line contains the Higgs mass terms.

<sup>376</sup> Many viable models of achieving soft SUSY breaking have been studied over the  
<sup>377</sup> last 30 years. For an overview, see Sec. 6 of ref. [12]. However, this thesis will only cover  
<sup>378</sup> *gauge-mediated SUSY breaking* (GMSB), because the two-photon search performed  
<sup>379</sup> is far more sensitive to this model than to other models of SUSY breaking.

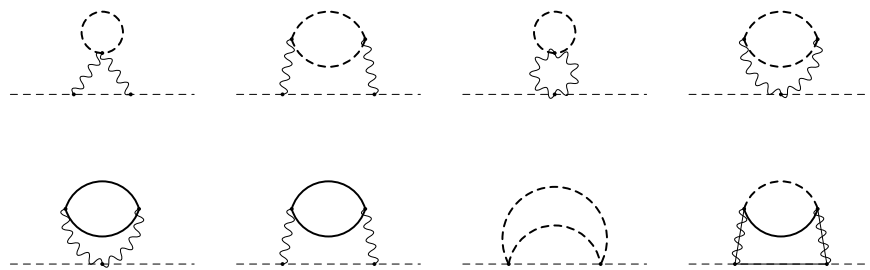
### 380 3.4 Gauge-Mediated SUSY Breaking

381 In gauge-mediated models [17], “hidden” fields spontaneously break the supersymme-  
 382 try of very heavy chiral *messenger* supermultiplets. There are a number of competing  
 383 models (see ref. [17]) that attempt to explain the precise mechanism of spontaneous  
 384 SUSY breaking, but fortunately the details of those models mostly decouple from the  
 385 phenomenology of GMSB. The messengers then communicate the SUSY breaking  
 386 to the sparticles via self-energy loop diagrams of gauge interaction strength (i.e. via  
 387 vertices like those shown in Figs. 3.1(c), 3.1(d), 3.1(i), 3.1(j), and 3.1(m), which are  
 388 proportional to the SM gauge couplings constants). The messengers are very heavy,  
 389 so they cannot be detected in current collider experiments. Feynman diagrams corre-  
 390 sponding to gaugino and sfermion mass terms are shown in Figure 3.2.

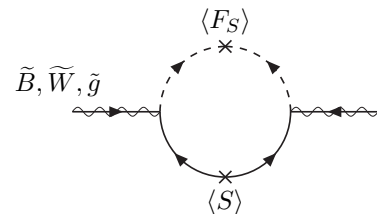
391 Historically, GMSB and gravity-mediated SUSY breaking, or mSUGRA [18], have  
 392 been the two most thoroughly experimentally studied scenarios of SUSY breaking.  
 393 One advantage of GMSB over mSUGRA is that it naturally suppresses flavor vio-  
 394 lation, a generic prediction of supersymmetry. Flavor violation is introduced in the  
 395 scalar<sup>3</sup> couplings and sfermion mass terms of  $\mathcal{L}_{\text{soft}}$  (second, third, and fourth lines of  
 396 Eq. 3.14). Since  $a_u^{ij}$ ,  $a_d^{ij}$ ,  $a_e^{ij}$ ,  $m_{\tilde{Q}ij}$ ,  $m_{\tilde{L}ij}$ ,  $m_{\tilde{u}ij}$ ,  $m_{\tilde{d}ij}$ , and  $m_{\tilde{e}ij}$  are matrices in family  
 397 space, any nonzero off-diagonal elements will lead to mixing between sfermions of  
 398 different families. This can lead, for example, to contributions to the diagram  $\mu \rightarrow e\gamma$   
 399 (Figure 3.3) exceeding the experimental bounds. To avoid this disaster, *universality*  
 400 conditions are assumed:

$$\mathbf{m}_{\tilde{\mathbf{Q}}}^2 = m_{\tilde{Q}}^2 \mathbf{1}, \mathbf{m}_{\tilde{\mathbf{L}}}^2 = m_{\tilde{L}}^2 \mathbf{1}, \mathbf{m}_{\tilde{\mathbf{u}}}^2 = m_{\tilde{u}}^2 \mathbf{1}, \mathbf{m}_{\tilde{\mathbf{d}}}^2 = m_{\tilde{d}}^2 \mathbf{1}, \mathbf{m}_{\tilde{\mathbf{e}}}^2 = m_{\tilde{e}}^2 \mathbf{1} \quad (3.15)$$

401 i.e. all sfermion mass matrices arising from the soft terms are assumed to be propor-  
 402 tional to the unit matrix  $\mathbf{1}$ , such that there can be no flavor mixing from these terms



(a) Sfermion mass terms. Heavy dashed lines denote messenger sfermions; solid lines denote messenger fermions. Reprinted from Fig. 6.4 of ref. [12].



(b) Gaugino mass term. The  $\langle S \rangle$  part of the loop is a messenger fermion contribution; the  $\langle F_S \rangle$  part is a messenger sfermion contribution. Reprinted from Fig. 6.3 of ref. [12].

Figure 3.2: Contributions to sfermion and gaugino masses from loop interactions with messenger particles in the GMSB framework.

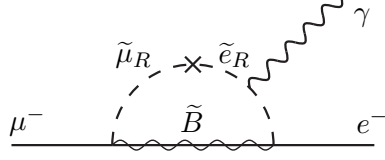


Figure 3.3: Possible contribution to  $\mu \rightarrow e\gamma$  from  $m_{\tilde{e}ij}$  soft term. Reprinted from Fig. 5.6(a) of ref. [12].

and contributions to flavor-changing processes are drastically reduced.<sup>2</sup> In mSUGRA models, universality is assumed from the beginning, while in GMSB it is a natural consequence of the fact that the sparticle-messenger vertices are the ordinary flavor-blind gauge couplings that prevent things like flavor-changing neutral currents.

In minimal GMSB (mGMSB), there are four messenger supermultiplets  $q, \bar{q}, l, \bar{l}$  providing the messenger (s)quarks and (s)leptons. There is one breaking scale  $\Lambda$ . The gaugino masses computed from diagrams like Fig. 3.2(b) are given by

$$M_a = \frac{\alpha_a}{4\pi} \Lambda \quad (3.16)$$

where  $a$  runs from 1-3 and the  $\alpha_a$  are the SM gauge coupling constants. The sfermion masses computed from diagrams like Fig. 3.2(a) are given by

$$m_{\phi_i}^2 = 2\Lambda^2 \sum_{a=1}^3 \left(\frac{\alpha_a}{4\pi}\right)^2 C_a(i) \quad (3.17)$$

where  $C_a(i)$  are group theory factors that are identical for all particles residing in the same type of supermultiplet (e.g. for all left-handed (s)quarks or left-handed (s)leptons). As explained in the previous paragraph, the gaugino and sfermion masses do not depend on fermion family.

---

<sup>2</sup>Universality also includes some assumptions about the form of  $a_{uij}$ ,  $a_{dij}$ , and  $a_{eij}$  and the stipulation that the soft terms not introduce any CP-violating phases.

416 In recent years, much theoretical progress has been made in unifying models of  
 417 gauge mediation and developing less restrictive models than mGMSB. *General gauge*  
 418 *mediation* (GGM) [19] retains the essential features of mGMSB, such as flavor de-  
 419 generacy and communication of SUSY breaking via messengers, but does not make  
 420 assumptions about the specific messenger sector or SUSY breaking scale. Many dif-  
 421 ferent collider final states can be interpreted in terms of GGM, and conversely, GGM  
 422 implies a wealth of signatures, only a small fraction of which have been searched for  
 423 at colliders [20, 21, 22]. The following section discusses the aspects of GGM collider  
 424 phenomenology relevant to this thesis.

### 425 3.5 Phenomenology of General Gauge Mediation

426 The main distinguishing feature of all GMSB phenomenology is that the gravitino  $\tilde{G}$  is  
 427 very light (eV-keV). In general, the gravitino mass is proportional to  $\langle F \rangle / M_P$ , where  
 428  $\langle F \rangle$  is the vacuum expectation value (VEV) of a field  $F$  that spontaneously breaks  
 429 SUSY in the vacuum state and  $M_P$  is the Planck mass. In GGM models,  $\langle F \rangle \sim 10^8$   
 430 GeV, leading to a very light gravitino. In contrast, mSUGRA predicts  $\langle F \rangle \sim 10^{20}$   
 431 GeV. The fact that the gravitino is so much lighter than any other particles in the  
 432 supersymmetric Standard Model, and that it interacts only gravitationally (and thus  
 433 extremely feebly), leads to two important phenomenological consequences:

- 434 1. All sparticle decay chains in GMSB end with the production of a gravitino.  
 435 2. The gravitino escapes  $4\pi$ , hermetic collider detectors without interacting, leav-  
 436 ing a signature of “missing” momentum transverse to the beam direction.

437 Even if the gravitino were lighter than any other sparticle, but heavier than an  
 438 ordinary SM particle, it still could not decay to the SM particle due to *R-parity*. R-  
 439 parity is a conserved quantity of the supersymmetric Standard Model introduced to

440 enforce baryon and lepton number conservation, which would otherwise be generically  
 441 allowed at levels in conflict with experiment (e.g. the non-observation of baryon-  
 442 and lepton-number-violating proton decay). All sparticles have R-parity -1, while all  
 443 ordinary SM particles have R-parity +1, and R-parity conservation dictates that at  
 444 any vertex, the product of the R-parities of each leg must be +1. This leads to two  
 445 more important consequences:

- 446 1. Since conservation of energy only allows it to decay to ordinary SM particles,  
 447 but R-parity prevents a sparticle-particle-particle vertex, the *lightest supersym-  
 448 metric particle* (LSP) must be absolutely stable. All sparticle decays proceed  
 449 through the *next-to-lightest supersymmetric particle* (NLSP), which in turn de-  
 450 cays to the LSP. The fact that it is stable and only gravitationally interacting  
 451 makes the gravitino a candidate dark matter particle (see Sec. 3.6).
- 452 2. In colliders, sparticles are produced in pairs (particle + particle  $\rightarrow$  sparticle +  
 453 sparticle).

454 In GMSB, then, the gravitino is the LSP. If the NLSP is a gaugino,<sup>3</sup> then the  
 455 possible decays depend on mixing among the gauginos. The four neutral gauginos  
 456  $\tilde{H}_u^0, \tilde{H}_d^0, \tilde{B}, \tilde{W}^0$  mix into four *neutralino* mass eigenstates  $\tilde{\chi}_1^0, \tilde{\chi}_2^0, \tilde{\chi}_3^0, \tilde{\chi}_4^0$ , and the four  
 457 charged gauginos  $\tilde{H}_u^+, \tilde{H}_d^-, \tilde{W}^+, \tilde{W}^-$  mix into two *chargino* mass eigenstates  $\tilde{\chi}_1^\pm, \tilde{\chi}_2^\pm$   
 458 (two mass eigenstates each with two possible charges = four particles). In the limit  
 459 that EWSB effects are small, the neutralino and chargino masses can be written as  
 460 the gauge eigenstate masses plus a small perturbation:

---

<sup>3</sup>In principle, the NLSP could be anything, but in most popular GGM models, it is either a gaugino or a stau. The stau NLSP search is not the subject of this thesis, so it will not be considered in this section.

$$m_{\tilde{\chi}_1^0} = M_1 - \frac{m_Z^2 \sin^2 \theta_W (M_1 + \mu \sin 2\beta)}{\mu^2 - M_1^2} + \dots \quad (3.18)$$

$$m_{\tilde{\chi}_2^0} = M_2 - \frac{m_W^2 (M_2 + \mu \sin 2\beta)}{\mu^2 - M_2^2} + \dots \quad (3.19)$$

$$m_{\tilde{\chi}_3^0} = |\mu| + \frac{m_Z^2 (\text{sgn}(\mu) - \sin 2\beta)(\mu + M_1 \cos^2 \theta_W + M_2 \sin^2 \theta_W)}{2(\mu + M_1)(\mu + M_2)} + \dots \quad (3.20)$$

$$m_{\tilde{\chi}_4^0} = |\mu| + \frac{m_Z^2 (\text{sgn}(\mu) + \sin 2\beta)(\mu - M_1 \cos^2 \theta_W - M_2 \sin^2 \theta_W)}{2(\mu - M_1)(\mu - M_2)} + \dots \quad (3.21)$$

$$m_{\tilde{\chi}_1^\pm} = M_2 - \frac{m_W^2 (M_2 + \mu \sin 2\beta)}{\mu^2 - M_2^2} + \dots \quad (3.22)$$

$$m_{\tilde{\chi}_2^\pm} = |\mu| + \frac{m_W^2 \text{sgn}(\mu)(\mu + M_2 \sin 2\beta)}{\mu^2 - M_2^2} + \dots \quad (3.23)$$

461 where  $\tan \beta = \langle H_u^0 \rangle / \langle H_d^0 \rangle$ .

462 The two scenarios studied in ref. [22] are the following:

463 • **Bino NLSP:**  $M_1 \sim$  few hundred GeV,  $M_2, |\mu| \gg M_1$ . All but the lightest  
464 neutralino (Eq. 3.18) are effectively inaccessible at the LHC due to their large  
465 masses. The NLSP can always decay to  $\gamma + \tilde{G}$ , and if it is heavy enough, to  
466  $Z + \tilde{G}$  or  $H + \tilde{G}$ .

467 • **Wino NLSP:**  $M_2 \sim$  few hundred GeV,  $M_1, |\mu| \gg M_2$ . The lightest neutralino  
468 (Eq. 3.18) and the lightest chargino (Eq. 3.22) are nearly degenerate in mass,  
469 and are the only two particles to play a role at the LHC. The decays described  
470 in the previous bullet point can happen, as well as chargino decays to  $W + \tilde{G}$ .

471 The search described in this thesis is optimized for the classic bino NLSP decay  $\gamma + \tilde{G}$ ,  
472 but sensitivity to the wino co-NLSP scenario is also studied (see Chapter 8).

473 Since strong production of SUSY particles, for instance via  $gg \rightarrow \tilde{g}\tilde{g}$ , dominates  
474 over electroweak production, for instance via  $q\bar{q} \rightarrow \tilde{\chi}_1^\pm \tilde{\chi}_1^\mp$ , at the LHC due to the  
475 enhanced  $gg$  parton luminosity over the  $q\bar{q}$  parton luminosity, early LHC searches are  
476 particularly sensitive to light squarks and gluinos. General gauge mediation makes no

<sup>477</sup> a priori restrictions on the mass splitting between the strongly interacting sparticles  
<sup>478</sup> and the weakly interacting sparticles, so models with light squarks and gluinos are  
<sup>479</sup> viable. In fact, such models could not be probed as well at the Tevatron<sup>4</sup> as they are  
<sup>480</sup> at the LHC due to the aforementioned parton luminosities.

<sup>481</sup> Typical LHC signatures of the bino and wino NLSP scenarios are shown in Fig-  
<sup>482</sup> ure 3.4.

### <sup>483</sup> 3.6 Experimental Status of SUSY

<sup>484</sup> Collider searches for evidence of supersymmetry began in earnest in the 1980s [24]  
<sup>485</sup> and continue to this day. Most recently, the LHC and Tevatron experiments have set  
<sup>486</sup> the strictest limits on a variety of SUSY breaking scenarios, including GMSB and  
<sup>487</sup> mSUGRA.

<sup>488</sup> Figure 3.5 shows the current limits set by the CMS experiment on the mSUGRA  
<sup>489</sup> model (with  $\tan \beta = 10$ ) in the  $m_0$ - $m_{1/2}$  plane. (Note that although the plot is trun-  
<sup>490</sup> cated at  $m_0 = 1000 \text{ GeV}/c^2$ , some searches are sensitive out to  $m_0 \sim 2000 \text{ GeV}/c^2$ .)  
<sup>491</sup> Although the LHC has pushed  $m_0$  above  $\sim 1 \text{ TeV}/c^2$  for  $m_{1/2}$  up to  $\sim 400 \text{ GeV}/c^2$ ,  
<sup>492</sup> casting some doubt onto the theory's prospects for solving the hierarchy problem,  
<sup>493</sup> there is still a sizable chunk of mSUGRA parameter space that is not ruled out by  
<sup>494</sup> collider experiments. Furthermore, parts of the CMS unexplored regions overlap with  
<sup>495</sup> areas allowed by astrophysics experiments [25].

Removed

<sup>496</sup> Figure 3.6 shows the most up-to-date limit (using  $1 \text{ fb}^{-1}$  of integrated luminosity CMS  
<sup>497</sup> collected by the ATLAS experiment [27] at the LHC) on the Snowmass Points and Moriond  
<sup>498</sup> Slopes (SPS) model of mGMSB, dubbed SPS8 [28]. In general, the lifetime of the result  
<sup>499</sup> lightest neutralino in GMSB models can take on any value between hundreds of  
<sup>500</sup> nanometers to a few kilometers depending on the mass of the lightest neutralino and

---

<sup>4</sup>Located on the Fermilab site in Batavia, Illinois, the Tevatron was a proton-antiproton collider operating at 1.96 TeV center-of-mass energy. The Tevatron ran from 1987 to 2011 [23].

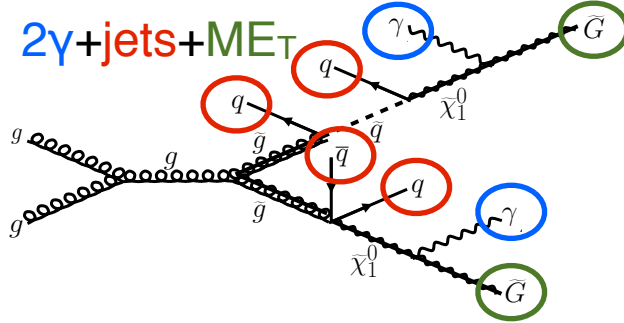
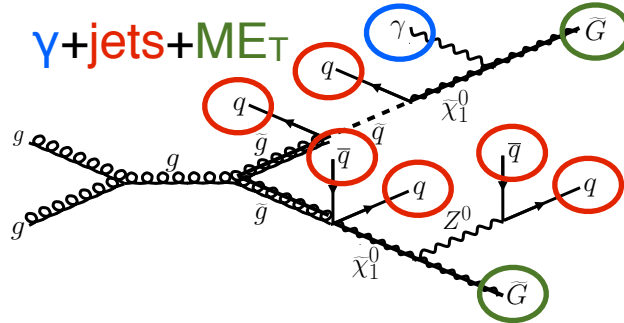
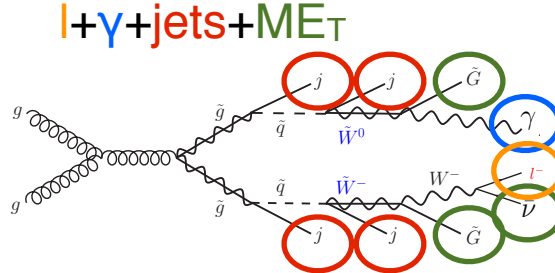
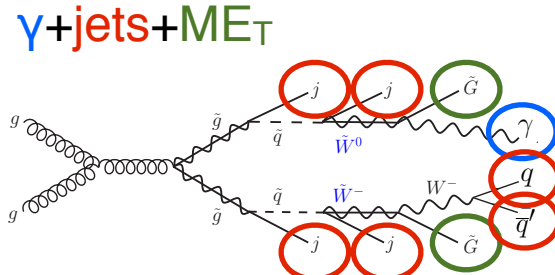
(a) Two gluinos each decay via  $\tilde{\chi}_1^0 \rightarrow \gamma \tilde{G}$ .(b) One gluino decays via  $\tilde{\chi}_1^0 \rightarrow \gamma \tilde{G}$ , the other via  $\tilde{\chi}_1^0 \rightarrow Z(\rightarrow q\bar{q})\tilde{G}$ .(c) One gluino decays via  $\tilde{\chi}_1^0 \rightarrow \gamma \tilde{G}$ , the other via  $\chi_1^\pm \rightarrow W^\pm(\rightarrow l^\pm \nu_l)\tilde{G}$ .(d) One gluino decays via  $\tilde{\chi}_1^0 \rightarrow \gamma \tilde{G}$ , the other via  $\chi_1^\pm \rightarrow W^\pm(\rightarrow q\bar{q}')\tilde{G}$ .

Figure 3.4: Typical LHC signatures of the bino and wino NLSP scenarios.

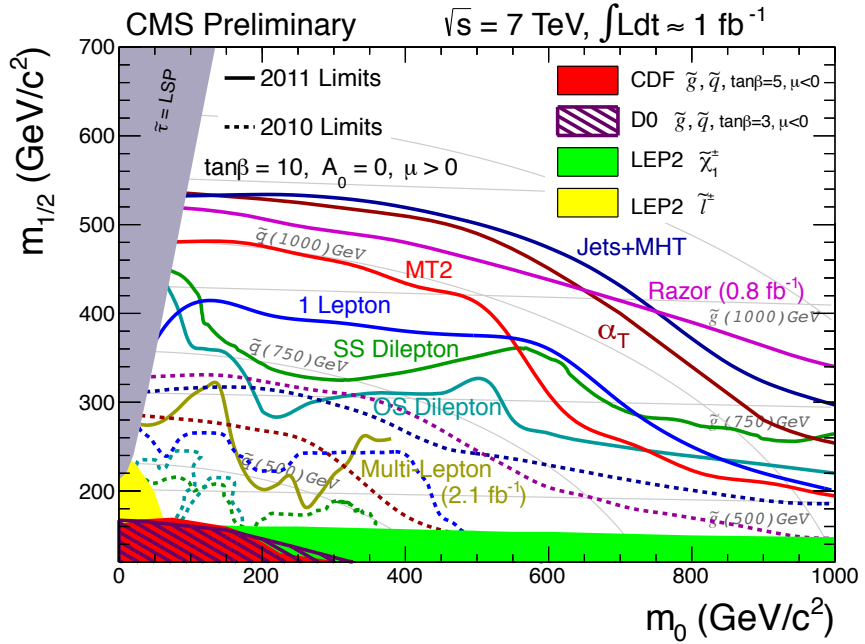


Figure 3.5: CMS limits on mSUGRA with  $\tan\beta = 10$ , corresponding to a model with third-generation squarks and sfermions somewhat lighter than their first- and second-generation counterparts. The limits set by individual searches are shown as separate colored lines. Solid lines refer to 2011 searches (i.e. using an integrated luminosity of  $\sim 1 \text{ fb}^{-1}$ ), while dashed lines refer to 2010 searches ( $\sim 36 \text{ pb}^{-1}$ ). Reprinted from ref. [26].

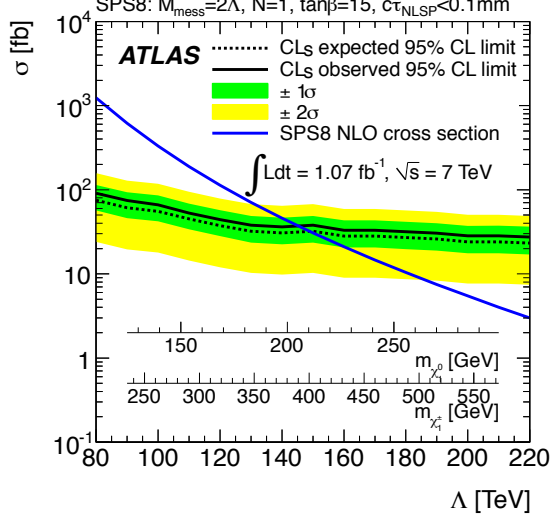


Figure 3.6: ATLAS cross section upper limit on the SPS8 [28] model of mGMSB as a function of SUSY breaking scale  $\Lambda$ , lightest neutralino mass  $m_{\tilde{\chi}_1^0}$ , or lightest chargino mass  $m_{\tilde{\chi}_1^\pm}$ . Values of  $\Lambda$ ,  $m_{\tilde{\chi}_1^0}$ , or  $m_{\tilde{\chi}_1^\pm}$  below the intersection point between the blue (predicted SPS8 cross section) and black (observed cross section upper limit) curves are excluded. The model parameters listed above the plot are defined in Secs. 3.4 and 3.5, except for  $\tau_{\text{NLSP}}$ , which is the neutralino lifetime. Reprinted from ref. [20].

501 the SUSY breaking scale [12]. The search published in ref. [20] (from which Fig. 3.6 is  
 502 culled) considers only *prompt* neutralino variants, i.e. with neutralino lifetime short  
 503 enough that the distance traveled by the neutralino before decay cannot be resolved  
 504 by the detector. The most recent limits on non-prompt SPS8-style neutralino models  
 505 were set by the Collider Detector at Fermilab (CDF) collaboration with  $570 \text{ pb}^{-1}$ ,  
 506 and are shown in Figure 3.7 [21].

507 Finally, if the gravitino is to make up some or all of the dark matter, constraints  
 508 on the form of gauge mediation must come from cosmological considerations and  
 509 astronomical observations. The gravitino in gauge mediation models is usually very  
 510 light ( $\mathcal{O}(\text{eV-MeV})$ ) because it is proportional to the SUSY breaking scale divided  
 511 by the Planck mass, and in GMSB the breaking scale is typically only of order a  
 512 few hundred TeV ([12] and Sec. 3.5). A light, highly relativistic dark matter particle  
 513 might have been produced, for instance, in the early, radiation-dominated period  
 514 of the universe [30]. This *warm dark matter* (WDM) may be responsible for all of

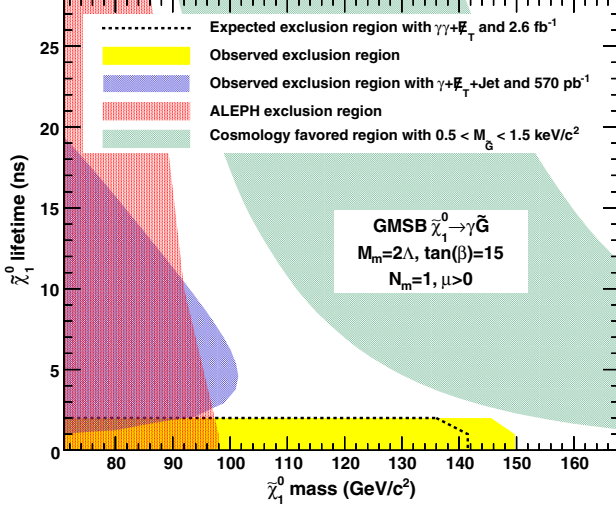


Figure 3.7: CDF exclusion contour in the  $\tau_{\tilde{\chi}_1^0}$ - $m_{\tilde{\chi}_1^0}$  plane, where  $\tau_{\tilde{\chi}_1^0}$  is the lifetime of the neutralino. Reprinted from ref. [21].

the dark matter needed to account for galactic structure, or it may share the duties with *cold dark matter* (CDM, weakly interacting particles with masses in the GeV range). In any viable model, the predicted relic density of the dark matter species must match the observed value of  $\Omega h^2 \sim 0.1$  [31]. For many GMSB models, this measurement constrains the gravitino mass to the keV range [32]. This constraint, however, does not translate into a very strong bound on the lifetime of the lightest neutralino. Using the following equation (taken from [32]):

$$\tau_{\tilde{\chi}_1^0} \sim 130 \left( \frac{100 \text{ GeV}}{m_{\tilde{\chi}_1^0}} \right)^5 \left( \frac{\sqrt{\langle F \rangle}}{100 \text{ TeV}} \right)^4 \mu \text{m} \quad (3.24)$$

and applying the gravitino mass constraint  $\sqrt{\langle F \rangle} \lesssim 3000 \text{ TeV}$  (cf. the first paragraph of Sec. 3.5 with  $m_{\tilde{G}} \sim \text{keV}$ ) and  $m_{\tilde{\chi}_1^0} = 100 \text{ GeV}$ , the upper bound on the neutralino lifetime is 100 meters. For  $\sqrt{\langle F \rangle} \sim 100 \text{ TeV}$ , the neutralino lifetime is detectable on collider time scales.

Recently, a lower bound on the WDM particle mass in either pure warm or mixed warm and cold dark matter scenarios was set using observations of the Lyman- $\alpha$  forest. For pure WDM,  $m_{\text{WDM}} > 8 \text{ keV}$ , while for some mixed WDM-CDM scenarios,

529  $m_{\text{WDM}} > 1.1\text{-}1.5 \text{ keV}$  [30, 33]. These bounds and others have motivated the develop-  
530 ment of more complicated gauge mediation models [33].

531 However, rather than focus on a specific GMSB model, of which there are many,  
532 the search detailed in the following chapters is interpreted in a minimally model  
533 dependent way. With this approach, the results can be applied to many competing  
534 models. The remainder of this thesis is devoted to the experimental details of the  
535 search, analysis strategy, and presentation of the results. The work described in this  
536 thesis forms the basis for the CMS public result “Search for Supersymmetry in Events  
537 with Photons and Missing Energy” [29], published in April 2012 (see Chapters 7 and 8  
538 for results). Ref. [29] contains the best limits on bino-like NLSP and wino-like NLSP  
539 GGM models to date.

540 **Chapter 4**

541 **The Large Hadron Collider**

542 At a 2010-2011 energy of 3.5 TeV/beam (7 TeV/beam design [34]) and maximum  
543 instantaneous luminosity of  $3.55 \times 10^{33} \text{ cm}^{-2} \text{ s}^{-1}$  [35] ( $10^{34} \text{ cm}^{-2} \text{ s}^{-1}$  design [34]),  
544 the CERN Large Hadron Collider (LHC) is the highest energy and highest intensity  
545 proton-proton collider ever built. Its purpose is to allow the four LHC experiments to  
546 explore TeV scale physics. For CMS and ATLAS, this implies examining the origins of  
547 EWSB via searches for the SM Higgs boson and physical phenomena not predicted by  
548 the SM that may explain the mass hierarchy in the SM. It also includes searches for  
549 possible dark matter candidates that are often proposed to have masses at the weak  
550 scale. The LHC needs to provide high energy proton collisions because the masses  
551 of the sought-after particles are higher than those already incorporated into the SM.  
552 It must also provide an unprecedented collision rate because signatures of the Higgs  
553 boson and physics beyond the SM are very rare compared to SM processes.

554 The rest of this chapter is devoted to an overview of the LHC machine. Section  
555 4.1 gives the overall layout of the machine and design choices made in light of  
556 energy and luminosity demands. Section 4.2 describes the LHC injection scheme. The  
557 different types of magnets and their functions is illustrated in Section 4.3, and finally  
558 the radiofrequency cavities are covered in Section 4.4. Unless otherwise noted, all

559 information in this chapter comes from ref. [34].

## 560 4.1 Design Considerations and Performance Lim- 561 itations

562 The layout of the 26.7-km long [36] LHC ring, located  $\sim$  100 m underground on the  
563 border between France and Switzerland northwest of Geneva, is shown in Figure 4.1.  
564 The two circulating beams of protons travel in opposite directions, colliding only at  
565 the experimental points. There are eight straight sections, each  $\sim$  528 m long, and  
566 eight arcs, each made of 23 106.9-m long arc cells. Beam crossings occur in four of  
567 the straight sections. The arcs contain six 14.3-m long dipole magnets, the cryogenics  
568 to cool the magnets, and short straight sections (SSS) with focusing and corrector  
569 magnets. The high luminosity experiments CMS and ATLAS are located diametrically  
570 opposite each other on the ring, ensuring that in principle each should receive the  
571 same integrated luminosity from the LHC.

572 To achieve a maximum energy per beam of 7 TeV, the peak magnetic field pro-  
573 duced by the dipole magnets must be 8.33 T, demanding the use of superconducting  
574 technology. Due to the like charges of the two beams, two separate magnet systems  
575 and evacuated beam pipes must be used to accelerate the protons in opposite direc-  
576 tions. Space limitations in the LHC tunnel, which was previously used for the LEP  
577 collider, prevent the installation of two separate rings of magnets, so each dipole in-  
578 stead contains two beam pipe bores and two sets of superconducting coils to produce  
579 two fields in opposite directions. In order to safely operate the magnets at 8.33 T,  
580 the cryogenic bath temperature is chosen to be 1.9 K, colder than any other acceler-  
581 ator cryogen and well below the critical temperature of the niobium-titanium (NbTi)  
582 superconducting wires of 9.2 K [39]. The extremely low bath temperature leads to  
583 a lessened heat capacity in the wires and consequently a lower energy threshold for

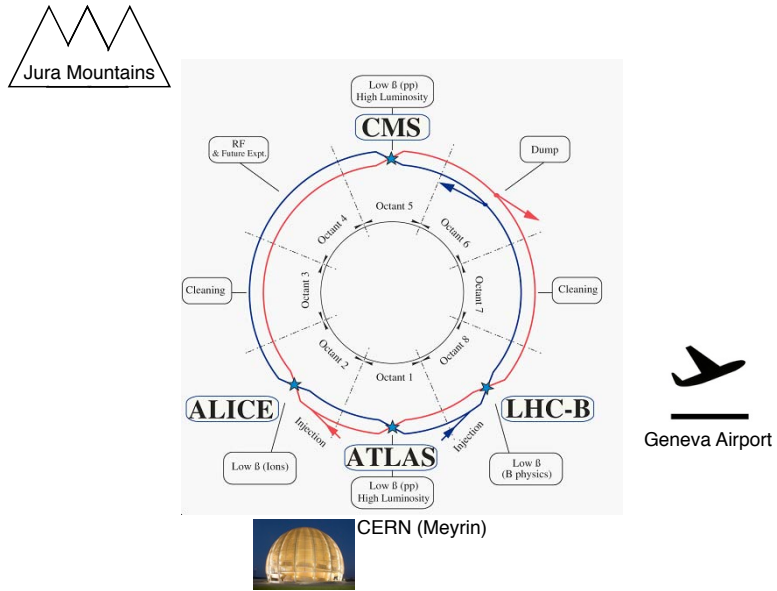


Figure 4.1: Bird's-eye view of the LHC ring, showing the locations of the experiments and local landmarks. Arrows show the beam direction. The ring figure is reprinted from Fig. 2.1 of ref. [34]. The CERN Globe of Innovation photo comes from ref. [37] and the airplane cartoon comes from ref. [38].

584 triggering a quench, so movements and heat dissipation within the cables must be  
 585 controlled more tightly than in previous accelerators.

586 The LHC beams are arranged in bunches of protons, with each bunch separated  
 587 by an integer multiple of the 25 ns minimum bunch spacing. The machine luminosity  
 588  $L$  is given by

$$L = \frac{N_b^2 n_b f_{\text{rev}} \gamma_r}{4\pi \epsilon_n \beta^*} F \quad (4.1)$$

589 where  $N_b$  is the number of protons per bunch (squared for the two beams),  $n_b$  is  
 590 the number of bunches per beam,  $f_{\text{rev}}$  is the bunch revolution frequency,  $\gamma_r$  is the  
 591 relativistic  $\gamma$  of the protons,  $\epsilon_n$  is the normalized transverse beam emittance,  $\beta^*$  is  
 592 the value of the  $\beta$  function at the collision point, and  $F$  is a geometrical factor less  
 593 than one related to the *crossing angle* of the bunches with respect to the horizontal

594 (ATLAS) or vertical (CMS) planes and the beam size. The normalized transverse  
 595 beam emittance is a measure of the RMS spread of the beam in the plane transverse  
 596 to its direction of motion, irrespective of its energy. A smaller emittance implies that  
 597 particles are squeezed into a smaller area in phase space, leading to larger luminosity.  
 598 The  $\beta$  function is defined as the square of the transverse beam size divided by the  
 599 emittance. It describes the oscillations of the transverse beam size as a function of  
 600 position in the ring. To achieve high luminosity,  $\beta^*$  is the minimum of the  $\beta$  function,  
 601 and it is related to the focusing strength of the triplet magnets near the interaction  
 602 points. In accelerating sections of the ring, the  $\beta$  function gets large so that the proton  
 603 momenta may be more uniform. Each piece of the luminosity is limited by safety or  
 604 design considerations.

605 Above some saturated bunch intensity, nonlinear beam-beam interactions experi-  
 606 enced by the protons during collisions cause the luminosity to scale as  $N_b$ , not  $N_b^2$   
 607 [40]. The scale of these interactions is set by  $N_b/\epsilon_n$ , and the size of the beam pipe and  
 608 maximum  $\beta$  function limit  $\epsilon_n$  to  $3.75 \mu\text{m}$ . Instabilities are also introduced through  
 609 interactions between the protons and the wall of the beam pipe that scale with the  
 610 beam current. Last but not least, the beam dump and magnet safety systems limit the  
 611 total stored energy in the ring. For these reasons, the maximum number of bunches  
 612 is limited to  $1.15 \times 10^{11}$ . In bunches of this proton multiplicity, the average num-  
 613 ber of proton-proton collisions per bunch crossing, or *pileup*, in CMS and ATLAS is  
 614 approximately 20. This unprecedented level of pileup poses unique triggering, event  
 615 reconstruction, and analysis challenges for the experiments.

616  $n_b$  can range from zero to 2808 and had a maximum of  $\sim 1400$  in 2011, corre-  
 617 sponding to 50 ns bunch spacing.  $f_{\text{rev}}$  is set by the circumference of the ring to 11.2  
 618 kHz [41].  $\gamma_r$  is set by the beam energy, which was 3.5 TeV in 2011.

619 The mechanical aperture of the triplet assemblies of quadrupole magnets limit  
 620 the minimum  $\beta^*$  to 0.55 [41] and maximum crossing angle to  $285 \mu\text{rad}$  [41] at the

## The LHC injection complex

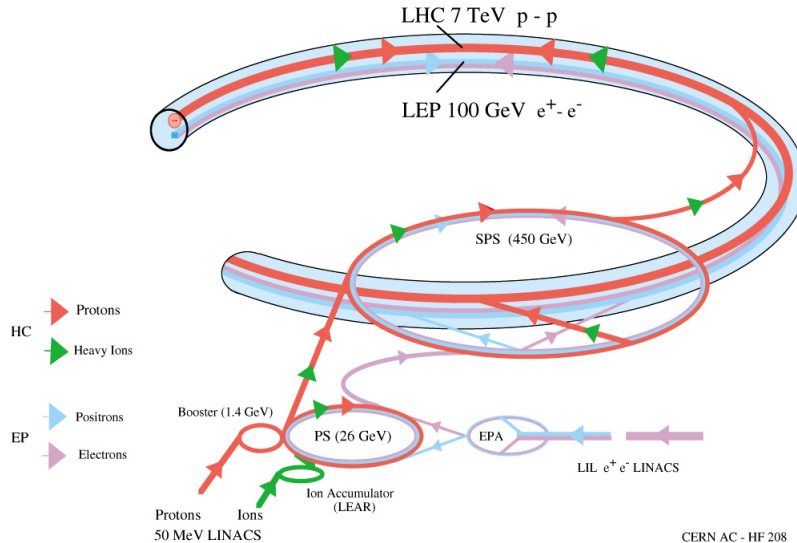


Figure 4.2: Overview of the LHC injector complex at CERN [42].

621 interaction points. The purpose of the crossing angle is to prevent parasitic collisions  
 622 in the 23-m length of shared beam pipe upstream and downstream of the interaction  
 623 points.

## 624 4.2 Beam Injection

625 The ultimate source of protons for the LHC is a bottle of hydrogen connected to the  
 626 CERN Linac2 linear accelerator, which accelerates the protons up to 50 MeV. From  
 627 there they enter the Proton Synchrotron Booster (PSB), which accelerates them to  
 628 1.4 GeV, and then the Proton Synchrotron (PS) itself, which brings them to 25 GeV.  
 629 The Super Proton Synchrotron (SPS) is the next stage, accelerating the protons to  
 630 an energy of 450 GeV. Finally, they leave the SPS and enter the LHC, where they are  
 631 accelerated to the desired beam energy (3.5 TeV in 2011). An overview of the LHC  
 632 injector complex is shown in Figure 4.2.

633 The 25-ns spaced bunches (or 50 ns for 2011 operation) are produced in trains  
 634 of 72 in the PS via a process of splitting six initial bunches into 12 smaller bunches

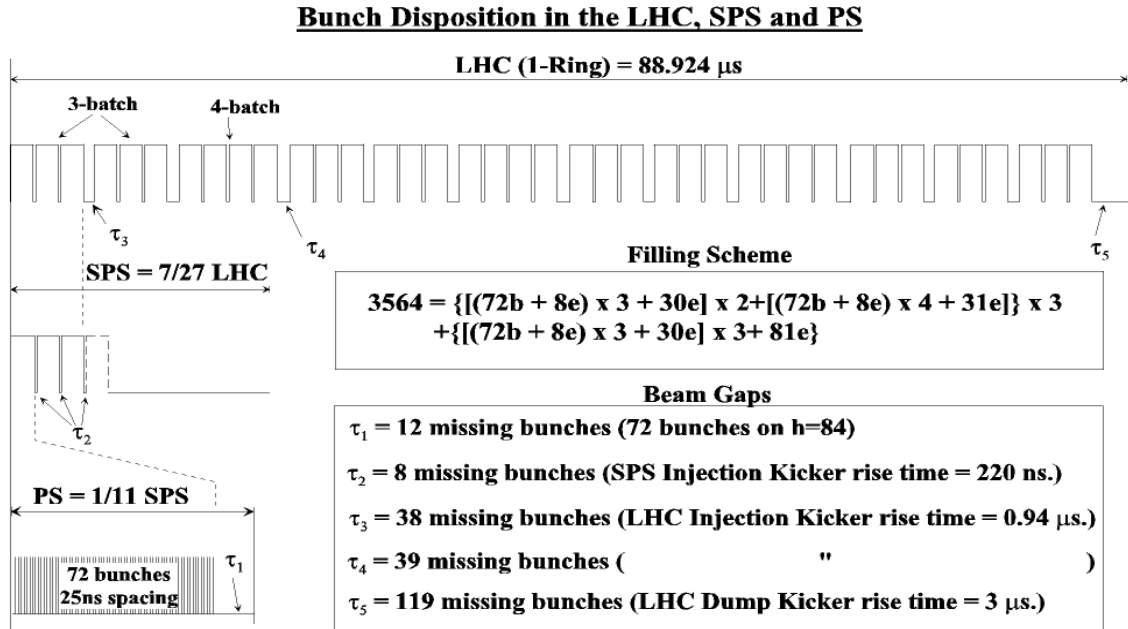


Figure 4.3: LHC injection scheme. Reprinted from Fig. 12.2 of ref. [34].

635 at specified points along the ring. At the end of each train is a 300 ns (12 bunch)  
 636 gap, which is an artifact of the splitting process. The SPS is limited by its maximum  
 637 allowed bunch intensity to storing three or four PS trains at a time. There is an 220  
 638 ns (8 bunch) gap at the end of each train due to the SPS injection kicker rise time.  
 639 The LHC is filled three or four trains at a time from the SPS. At the end of each  
 640 three-train and four-train group is a gap of 0.94  $\mu$ s (38 or 39 bunches) due to the  
 641 LHC injection kicker rise time. Finally, at the end of an entire 88.924- $\mu$ s long LHC  
 642 orbit is a gap of 3  $\mu$ s (119 bunches), known as the *abort gap*, to allow for the LHC  
 643 dump kicker rise time. The injection scheme is shown in Figure 4.3.

644 LHC injection occurs at points 2 and 8. At the intersection of the SPS-LHC  
 645 transfer line and the LHC beam pipe are five septum magnets that deflect the bunches  
 646 12 mrad horizontally into orbit. The septum magnets have a gap into which the  
 647 beam is injected as well as two separate holes for the circulating beams, as shown in  
 648 Figure 4.4. Four kicker magnets then deflect the bunches 0.85 mrad vertically into  
 649 orbit. The kicker magnets supply a pulsed magnetic field with a 0.94  $\mu$ s rise time

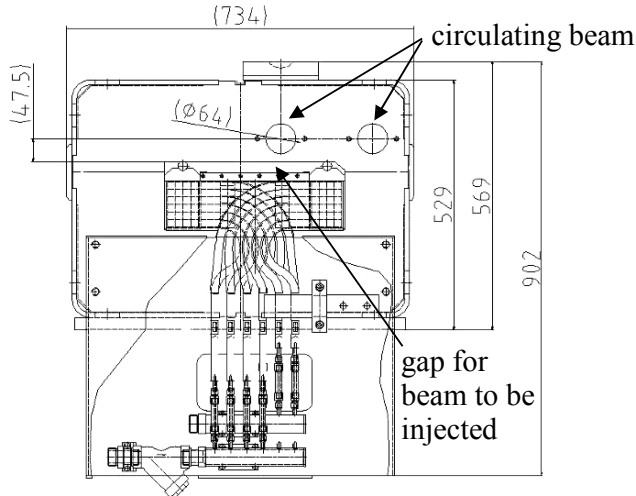


Figure 4.4: Cross-sectional view of septum magnet (beam direction is into or out of the page) showing the holes for the circulating beams and the separate gap for injected particles. Reprinted from Fig. 11.2 of ref. [34].

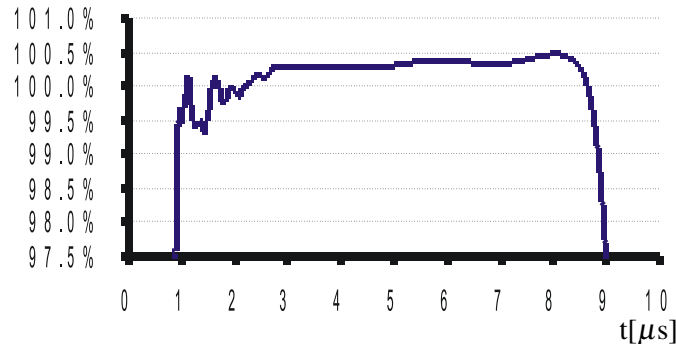


Figure 4.5: LHC injection kicker pulse shape. The  $y$ -axis measures percentage of maximum current. Reprinted from Fig. 11.7 of ref. [34].

650 (see Fig. 4.3) and a 5.84(7.86)  $\mu s$  flat top for three-train(four-train) injection (see  
 651 Figure 4.5). To limit emittance growth at injection due to over- or under-kicking the  
 652 injected bunches such that they miss the core of the LHC orbit, the kicker current is  
 653 limited to  $< 0.5\%$  flat top ripple in any direction.

### 654 4.3 Magnets and Cryogenics

655 There are 1232 twin-bore dipole magnets along the LHC ring used for establishing  
 656 the circular orbit of the protons. They consist of two evacuated beam pipes, each

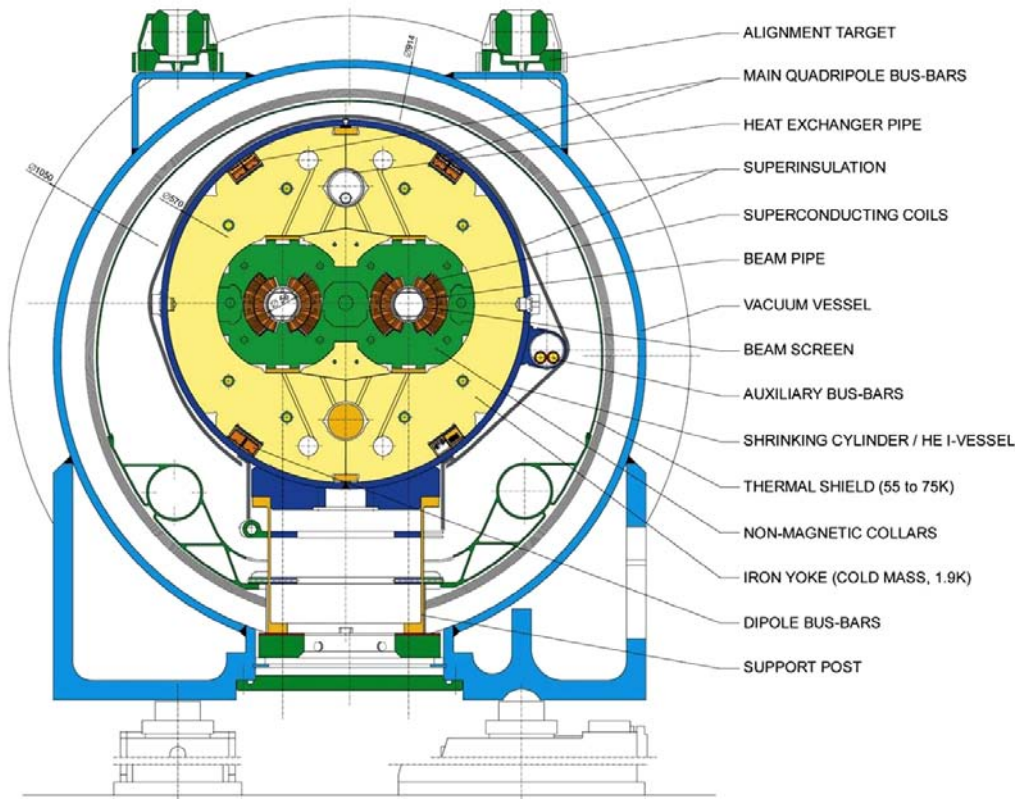


Figure 4.6: Cross-sectional view of LHC dipole + cryostat. Reprinted from Fig. 3.3 of ref. [34].

657 flanked by its own set of superconducting coils, inside an iron yoke which serves as  
 658 the 1.9 K cold mass. The entire assembly sits inside a helium vessel, which is itself  
 659 surrounded by a vacuum chamber thermally insulating the cold mass from the room  
 660 temperature LHC cavern. The entire dipole + cryostat device is  $\sim 16.5$  m long and  
 661 weighs about 27.5 t. A cross-sectional view of the dipole is given in Figure 4.6.

662 To provide a centripetal Lorentz force on the protons, the dipole field points  
 663 vertically up or down, depending on the sense of the beam. The magnetic field lines for  
 664 a single beam pipe are shown in Figure 4.7. Figure 4.8 shows the coil windings in two  
 665 bores. To provide the correct field direction, the coils are wound around blocks that  
 666 are  $\sim 14$  m long (the length of the dipole), so that each winding has a circumference  
 667 of  $\sim 28$  m.

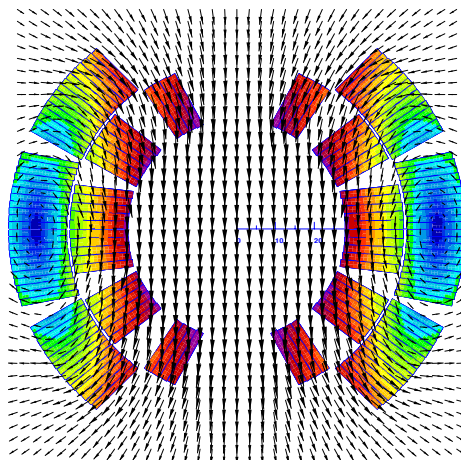


Figure 4.7: Magnetic field lines of the dipole field. The beam direction is into the page. Reprinted from Fig. 4 of ref. [43].

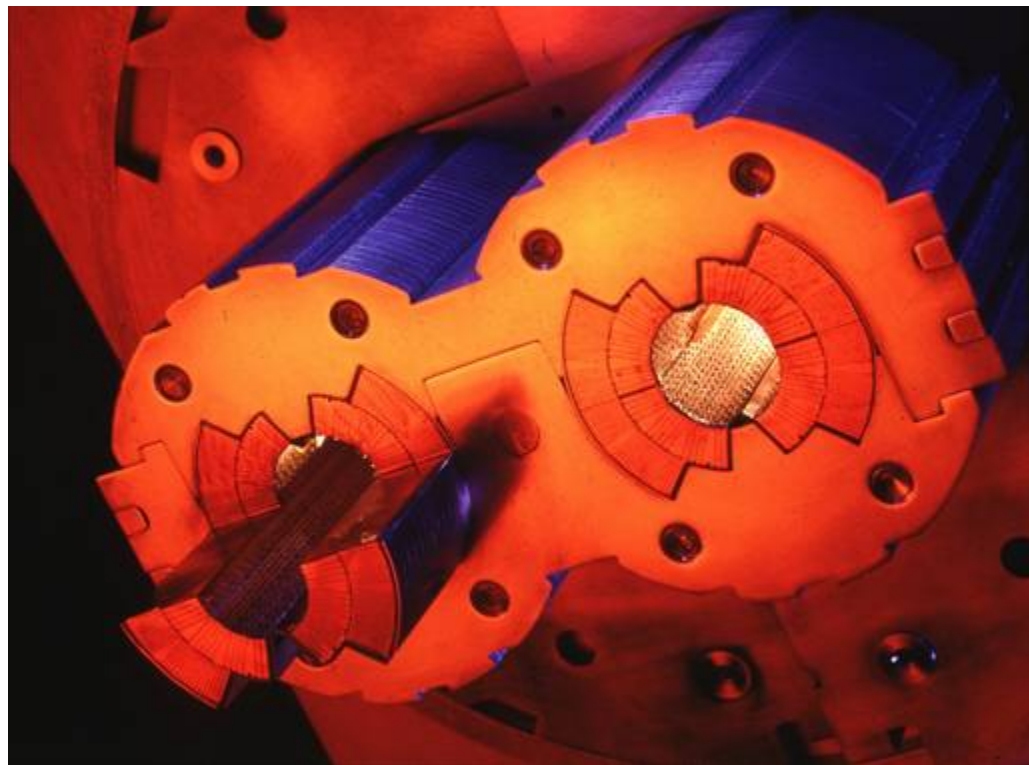


Figure 4.8: Superconducting coils in a twin-bore dipole [44].

668 In addition to the dipoles, a number of different types of orbit corrector magnets  
 669 are installed throughout the ring. The main quadrupole magnets, as well as higher  
 670 order field corrector magnets, are located in the arcs and short straight sections. The  
 671 function of these magnets is to provide fine grained control over the magnetic field  
 672 in order to keep the bunches in the proper orbit and control the emittance and  $\beta$   
 673 functions.

674 In the straight sections, there are four specialized types of magnets related to SPS  
 675 extraction and bringing the beams into collision. Matching section quadrupoles near  
 676 the transfer lines help to match the injected bunch orbit to the circulating bunch orbit.  
 677 Dispersion suppressors, consisting of dipoles and quadrupoles, help to reduce beam  
 678 dispersion near the collision points due to off-momentum protons. Matching section  
 679 separation dipoles control the separation between the two beams near the collision  
 680 points. The magnets that perform the final squeeze of the beams before collision,  
 681 called the low- $\beta$  inner triplets, must provide a very high field gradient of 215 T/m,  
 682 withstand a high radiation dose, and sustain high heat loads in the superconducting  
 683 coils.

684 The superfluid helium cryogen is delivered to the magnets via a distribution line  
 685 from the main refrigerator. A cross section of the LHC tunnel, showing the cryogen  
 686 delivery apparatus for a dipole, is shown in Figure 4.9.

## 687 4.4 Radiofrequency Cavities

688 LHC bunches are captured and accelerated in 400 MHz superconducting radiofre-  
 689 quency (RF) cavities. 400 MHz defines the bunch length of  $\lesssim 2$  ns. As bunches pass  
 690 through the cavities, the oscillating electric field is at its peak and accelerates the  
 691 protons through a potential difference of 2 MV per cavity (16 MV per turn). The  
 692 finite bunch length is due to particles that arrive out of phase with the electric field

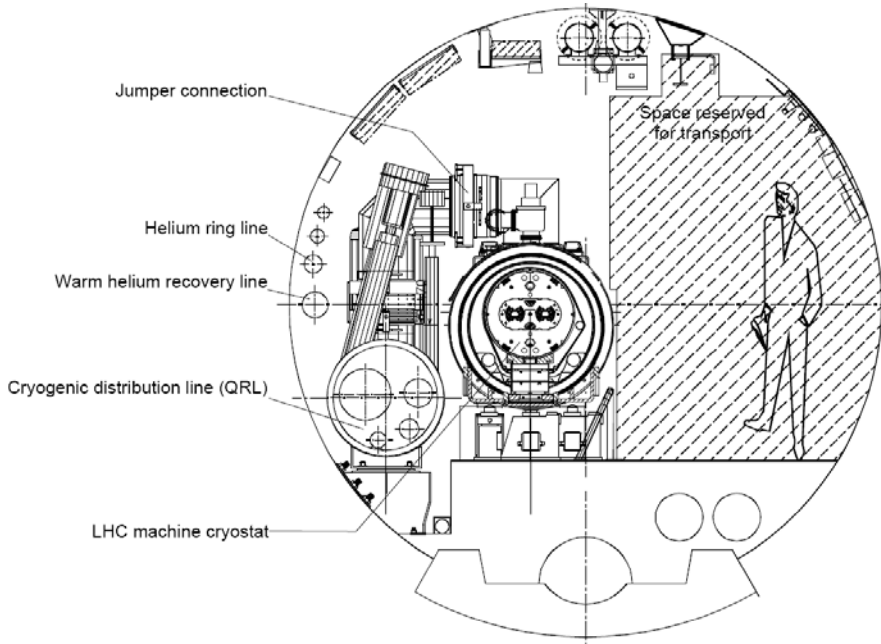


Figure 4.9: Cross section of the LHC tunnel, showing the cryogen delivery apparatus for a dipole. Reprinted from Fig. 7.1 of ref. [34].

693 due to deviations in their momenta from the nominal. During a ramp of the beam  
 694 energy from 450 GeV to 3.5 or 7 TeV, bunches repeatedly travel around the ring, re-  
 695 ceiving an energy kick each time, until the desired energy is reached. Feedback from  
 696 the RF accelerating system causes an increase in magnet current to keep the bunches  
 697 in a fixed orbit.

698 Superconducting material (niobium) coats the cylindrical walls of the cavity. RF  
 699 power is coupled to the cavity via a klystron. The RF electric field standing wave is set  
 700 up across the cavity in the beam direction. The transverse magnetic field dissipates  
 701 some energy into the walls, but much less than in a normal conducting cavity.

702 **Chapter 5**

703 **The Compact Muon Solenoid**  
704 **Experiment**

705 The Compact Muon Solenoid (CMS) detector sits at point 5 of the LHC ring, diamet-  
706 rically opposite the ATLAS detector at point 1. It is a  $4\pi$  hermetic general purpose  
707 detector, meaning that it has the capability to detect charged and neutral hadrons,  
708 photons, electrons, muons, taus, neutrinos, and non-Standard-Model particles pre-  
709 dicted to escape the detector with good efficiency over a large range of rapidity.  
710 Its main distinguishing feature is a superconducting solenoid that provides a 3.8T  
711 magnetic field parallel to the beam line. This strong magnetic field allows precise de-  
712 termination of the momentum and charge of muons and electrons up to a momentum  
713 of  $\sim 1$  TeV.

714 The origin of the CMS coordinate system is at the nominal interaction point. The  
715  $y$ -axis points skyward, the  $x$ -axis points towards the center of the LHC ring, and  
716 the  $z$ -axis points counterclockwise along the LHC ring.  $r$  denotes radial distances  
717 from the beam line,  $\phi$  is the azimuthal angle measured with respect to the positive  
718  $x$ -axis, and  $\theta$  is the polar angle measured with respect to the positive  $z$ -axis. The  
719 *pseudorapidity*  $\eta$  is defined as  $\eta = -\ln \tan(\theta/2)$ , and is a good approximation to

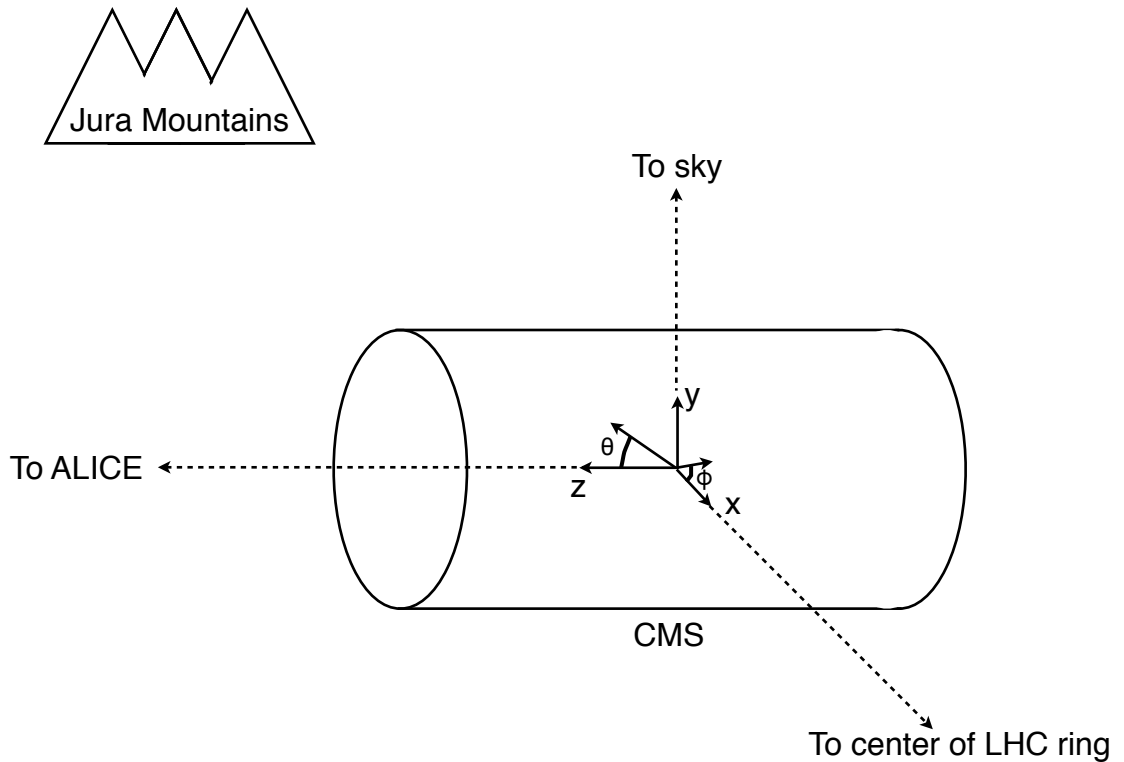


Figure 5.1: CMS coordinate system.

720 rapidity  $y = (1/2) \ln((E + p_z c)/(E - p_z c))$  for relativistic particles. The transverse  
 721 momentum and energy ( $p_T$  and  $E_T$ ) of a particle are defined as  $p_T = p \cos \phi$  and  
 722  $E_T = E \cos \phi$ , where  $p$  and  $E$  are the magnitude of the particle's momentum vector  
 723 and the particle's total energy, respectively. A depiction of the CMS coordinate system  
 724 is shown in Figure 5.1.

725 The CMS sub-detectors are arranged in concentric cylindrical layers, plus “end-  
 726 caps,” around the beam line, as shown in Figure 5.2. Closest to the beam line are  
 727 three layers of silicon pixel detectors, with the innermost at radius 4.4 cm and out-  
 728 ermost at radius 10.2 cm [45]. Including the pixel endcaps, the total pixel coverage

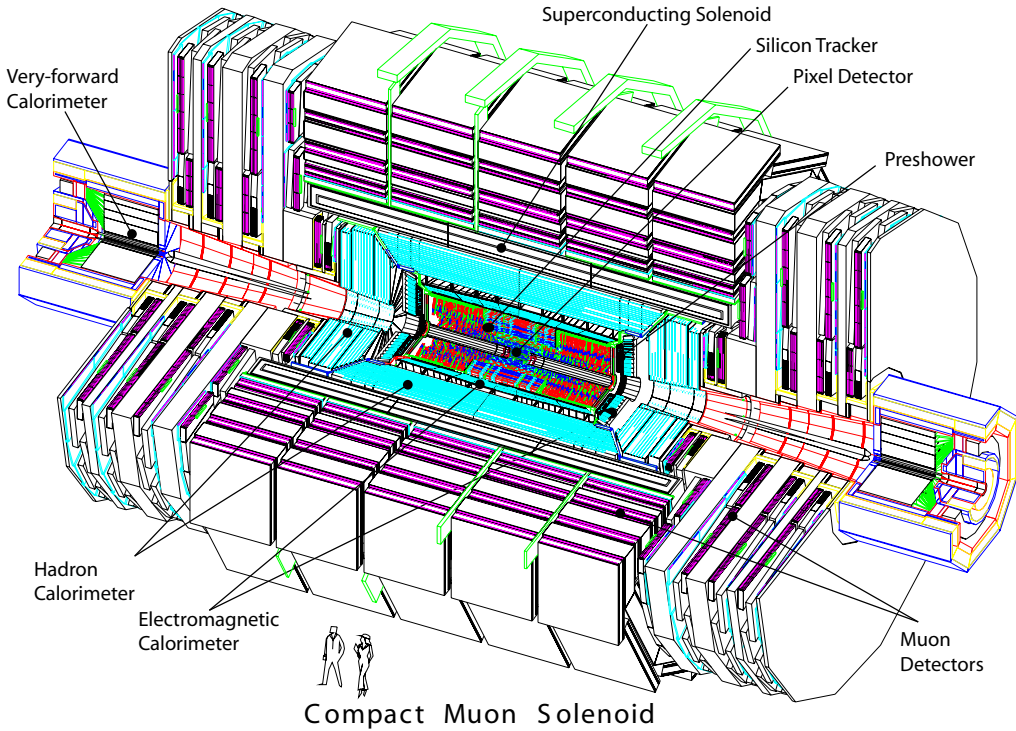


Figure 5.2: Cutaway view of CMS. Reprinted from Fig. 1.1 of ref. [45].

729 extends to  $\eta = 2.5$  [45]. The pixel detector plays an important role in determining the  
 730 proton-proton interaction position (*beam spot*) and the impact parameters of charged  
 731 particle trajectories, and is critical for the measurement of decay positions some dis-  
 732 tance from the beam spot (*displaced vertices*), such as those due to the showering and  
 733 hadronization of a  $b$  quark.

734 The 10 next layers of CMS are comprised of silicon microstrip detectors, with the  
 735 outermost layer at a radius of 1.3 m from the beam line [45]. As for the pixel detectors,  
 736 the silicon strip endcaps extend tracking coverage to  $\eta = 2.5$ . The silicon microstrip  
 737 layers are the workhorse of the CMS tracking system, and provide excellent charged  
 738 particle momentum resolution and track finding efficiency.

739 Outside the tracking detectors are the calorimeters, starting with the single-layer  
 740 lead tungstate crystal electromagnetic calorimeter at a radius of 1.3 m from the beam  
 741 line (location of crystal front faces) [45]. Each crystal is 23 cm long, corresponding

742 to 25.8 radiation lengths ( $X_0$ ) [45]. The crystal dimensions are such that most of one  
 743 electromagnetic shower, and no more, can be contained in a single crystal, leading to  
 744 excellent energy resolution for photons and electrons. The electromagnetic calorime-  
 745 ter radial and endcap layers cover a pseudorapidity range up to 3.0. A lead/silicon  
 746 sampling calorimeter sits in front of the crystal endcaps to provide better rejection  
 747 of neutral pions.

748 The last layer of calorimetry inside the solenoid is the brass/scintillator sampling  
 749 hadronic calorimeter, which has a radial extent from 1.77-2.95 m [45]. The hadronic  
 750 barrel and endcap calorimeters cover up to  $|\eta| = 3.0$ , while the iron/quartz-fiber for-  
 751 ward hadronic calorimeter covers the region  $3.0 \leq |\eta| \leq 5.2$ .<sup>1</sup> There is one more  
 752 layer of hadronic calorimetry outside the solenoid in  $|\eta| < 1.3$  which, together with  
 753 the layers inside the solenoid, provides approximately 12 hadronic interaction lengths  
 754 of instrumented absorber. Because of its large  $|\eta|$  coverage and depth, the hadronic  
 755 calorimeter provides good missing transverse energy resolution and accurate measure-  
 756 ments of high energy jets.

757 The iron return yoke of the solenoidal magnetic field is interleaved with muon  
 758 detectors from 4.1-7.4 m in  $r$  and 6.6-10.6 m in  $z$ , providing muon detection up to  
 759  $|\eta| = 2.4$  [45]. In the barrel region of  $|\eta| < 1.2$ , drift tubes are used to read out the  
 760 muon tracks, while in the endcaps cathode strip chambers are used. Due to their  
 761 speed, resistive plate chambers are used throughout the muon system to provide  
 762 an independent trigger and timing measurement. Combining the tracker and muon  
 763 system hits, the momenta and charge of muons up to  $p_T = 1$  TeV can be precisely  
 764 reconstructed.

765 A longitudinal quarter cross-sectional view of CMS is shown in Figure 5.3. The  
 766 remainder of this chapter is devoted to explaining the CMS subdetectors and readout

---

<sup>1</sup>The Centauro and Strange Object Research (CASTOR) and Zero Degree Calorimeter (ZDC) detectors provide additional calorimetry beyond  $|\eta| = 5.2$ . However, they are mainly used in the heavy ion and diffractive physics programs of CMS, and play no role in the detection of heavy SUSY particles. Therefore, they will not be discussed here.

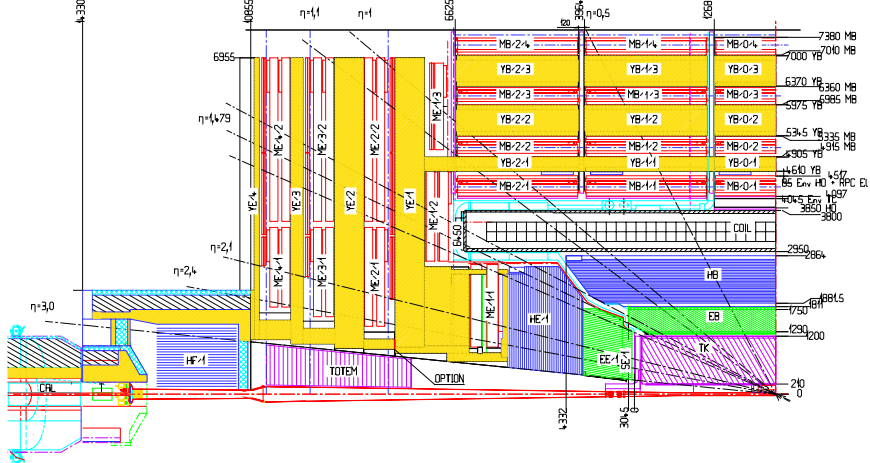


Figure 5.3: Longitudinal quarter cross-sectional view of CMS. The nominal interaction point is at the lower right-hand corner of the drawing. The tracker is shown in purple diagonal hashing, the electromagnetic calorimeter in green, the hadronic calorimeter in blue, and the muon stations in red. The solenoid is shown in black and white and labeled COIL, and the magnet return yoke is shown in yellow. Radial and longitudinal distances are measured in millimeters. Reprinted from Fig. CP 1 of ref. [46].

systems. Section 5.1 describes the subdetector technologies and performance benchmarks, while Section 5.2 details the CMS trigger and data acquisition systems and framework for promptly reconstructing and transferring data worldwide. For a thorough description of CMS, see ref. [45]. Unless otherwise noted, all information in this chapter comes from ref. [45].

## 5.1 The Detectors and Their Operating Principles

### 5.1.1 Tracking System

Given the LHC design instantaneous luminosity, efficient reconstruction of charged particle tracks from transverse momenta of 1 GeV up to 1 TeV can only be achieved with a low occupancy tracker. For  $r < 10$  cm, the hit rate density is highest, leading to the choice of  $100 \mu\text{m} \times 150 \mu\text{m}$  silicon pixel sensors for hit detection. For  $20 \text{ cm} < r < 110 \text{ cm}$ , the lower hit rate allows the use of silicon strips, with length along  $z$  of

779 order centimeters and length along the  $r \cdot \phi$  curve of order hundreds of microns. This  
 780 design leads to a pixel hit occupancy of  $\sim 10^{-4}$ /pixel/BX and a strip hit occupancy  
 781 of  $\sim 10^{-2}$ /pixel/BX, where BX refers to 1 LHC bunch crossing.

782 As radiation dose from hadrons accumulates over the lifetime of the tracker, silicon  
 783 leakage current through the semiconductor junctions increases, heating up the sensors.  
 784 Since the leakage current itself depends on temperature, this can lead to *thermal*  
 785 *runaway* that damages the detector. To avoid this, the tracker must be cooled to  
 786 approximately  $-10^{\circ}\text{C}$ . Operating at this temperature, the signal:noise ratio in the  
 787 silicon sensors is 10:1, and should remain at that level over the 10-year lifetime of the  
 788 tracker.

789 At its thickest ( $|\eta| \sim 1.5$ ), the tracker depth (including services) is  $\sim 1.8X_0$ ,  
 790 and the depth falls off to  $\sim 1X_0$  in thinner areas. Unfortunately, the large mass of  
 791 the tracker degrades somewhat the performance of the electromagnetic calorimeter  
 792 behind it, as  $\sim 50\%$  of photons will convert to  $e^+e^-$  pairs in the tracker.

### 793 Pixel Detector

794 A longitudinal quarter view of the three barrel pixel (BPix) layers and two forward  
 795 pixel (FPix) disks is shown in Figure 5.4. There are 768 BPix modules in total.  
 796 Each BPix layer is divided into 32  $\phi$ -wedges, with eight modules per wedge arranged  
 797 end-to-end in  $z$ . The  $\phi$ -wedges operate nearly independently in terms of clock and  
 798 readout. Each FPix disk consists of 24  $\phi$ -wedges, with pie-shaped modules attached  
 799 to the front and back of the disk, for a total of 192 modules. The front- and back-side  
 800 modules of the FPix disks are constructed of different sized *plaquettes*, or multi-pixel  
 801 sensor chips, such that the gaps in the front-side module are covered by plaquette  
 802 area in the back-side module and vice versa. An illustration of the BPix and FPix  
 803 mechanical layouts is given in Figure 5.5.

804 Since the electric field in the depletion region of the BPix sensors is perpendicular

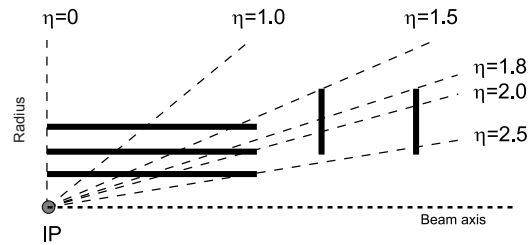
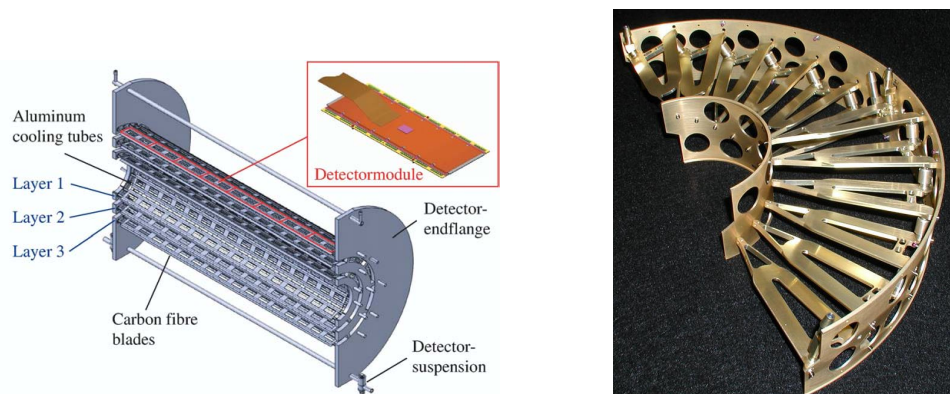


Figure 5.4: Longitudinal quarter view of the pixel detector. Reprinted from Fig. 3.6 of ref. [45].



(a) Cutaway view of the barrel pixel layers, showing the three layers and the eight end-to-end modules along  $z$ . Reprinted from Fig. 3.11 of ref. [45].

(b) Half-disk of the forward pixel detector, showing the 12 pie-shaped module mounts. Reprinted from Fig. 3.15 of ref. [45].

Figure 5.5: BPix and FPix mechanical structures.

805 (i.e. pointing along  $r$ ) to the magnetic field of CMS (i.e. pointing along  $z$ ), the charge  
 806 carriers in the silicon experience a Lorentz drift along  $\phi$ . The multi-pixel sensor pitch  
 807 is such that this causes the charge from one particle hit to be shared among multiple  
 808 pixels. Particle hits are reconstructed reading out the analog pixel signal and inter-  
 809 polating between signals in multiple pixels. This method achieves a  $15\text{-}20 \mu\text{m}$  spatial  
 810 resolution, which is comparable to the sensor pitch. To induce this effect in FPix,  
 811 the sensor wedges are tilted by the approximate BPix Lorentz angle of  $20^\circ$  [47] with  
 812 respect to the  $y$ -axis.

813 Each multi-pixel sensor consists of an array of  $52 \times 80$  n-type pixels implanted onto  
 814 an n-type substrate with  $320 \mu\text{m}$  thickness. The other face of the substrate is covered  
 815 with a thin layer of p-type semiconductor. Except for the outer edges, which are held  
 816 at ground potential to prevent sparking between the sensor edges and the connected  
 817 readout chip [48], the p-side is reverse biased at  $150 \text{ V}$  (BPix) or  $300 \text{ V}$  (FPix). The  
 818 pixels are held at ground potential. A particle entering through the p-side will cause  
 819 a burst of current to flow across the p-n junction. The charge will be collected by the  
 820 pixels, which are bump-bonded to the readout. The BPix and FPix sensors employ  
 821 slightly different technologies for electrically isolating the individual pixels, but both  
 822 rely on the idea of surrounding the pixels with a p-type material to provide a p-n  
 823 junction that acts as a barrier to current flow.

824 Each  $52 \times 80$  pixel sensor is bump bonded to a readout chip (ROC). The ROCs  
 825 provide zero suppression and amplify, buffer, and communicate the signals from the  
 826 sensors. A single token bit manager (TBM) controls  $\sim 16$  ROCs in the barrel or  $\sim 24$   
 827 ROCs in the endcaps. Its purpose is to distribute the clock and trigger to the ROCs  
 828 (the latter initiates a transmission of the signal further upstream to be assembled  
 829 into the full event readout of CMS). The clock and trigger are supplied by the pixel  
 830 front end controller (pFEC), which interfaces to the central clock and data acquisition  
 831 systems. Analog signals that are collected from the pixel front ends are digitized by

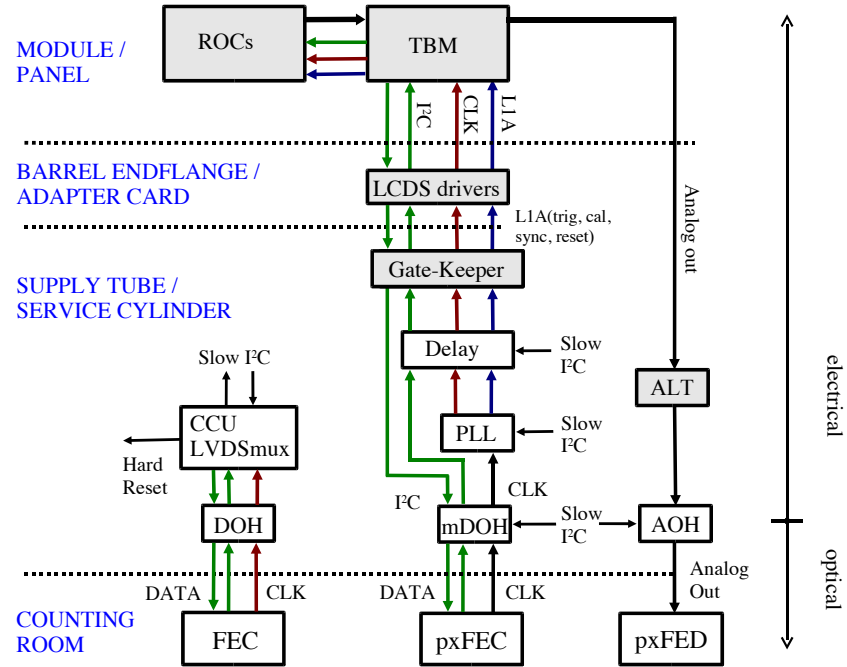


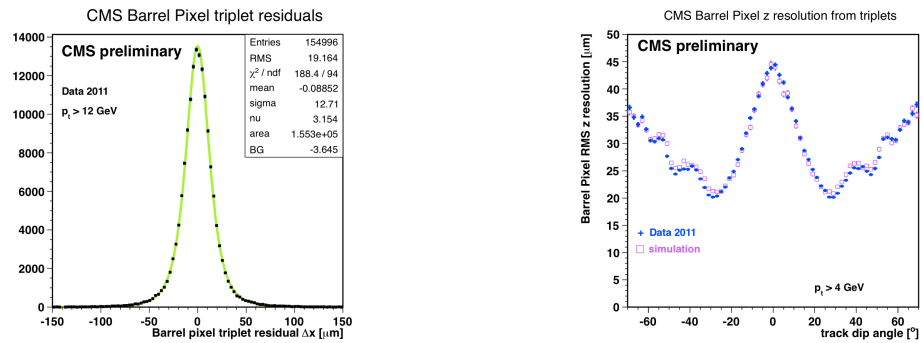
Figure 5.6: Pixel control and readout system. Reprinted from Fig. 3.9 of ref. [45].

832 the pixel front end digitizer (pxFED). A diagram of the readout system is shown in  
 833 Figure 5.6.

834 Figure 5.7 shows some results highlighting the performance of the pixel detector.

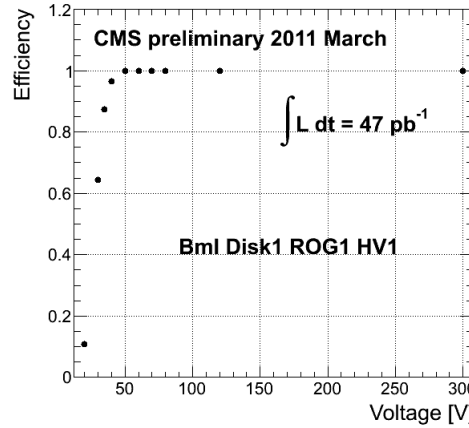
### 835 Silicon Strip Tracker

836 The silicon strip tracker is divided into four parts: the inner barrel (TIB) and inner  
 837 disks (TID), covering the radial extent  $20 \text{ cm} < r < 55 \text{ cm}$  and  $z$  extent  $80 \text{ cm} <$   
 838  $|z| < 90 \text{ cm}$ ; and the outer barrel (TOB) and endcap (TEC), covering the radial  
 839 extent  $61 \text{ cm} < r < 108 \text{ cm}$  and  $z$  extent  $124 \text{ cm} < |z| < 282 \text{ cm}$ . A number of the  
 840 tracker layers and endcaps hold double-sided strip modules (shown as double lines  
 841 in Figure 5.8), with the rear module tilted at an angle of 100 mrad with respect to  
 842 the front module, to provide a measurement in two coordinates. There are a total of  
 843 15,148 modules in the tracker, arranged as shown in the longitudinal cross-sectional  
 844 view of Fig. 5.8. For the TIB and TOB, the modules are arranged in straight rows



(a) BPix hit resolution in the  $r \cdot \phi$  coordinate [49].

(b) BPix hit resolution in the  $z$  coordinate vs. track dip angle, showing the effect of charge sharing on resolution [50].



(c) Pixel reconstruction efficiency vs. bias voltage for a group of three wedges in FPix [51].

Figure 5.7: Pixel detector performance highlights.

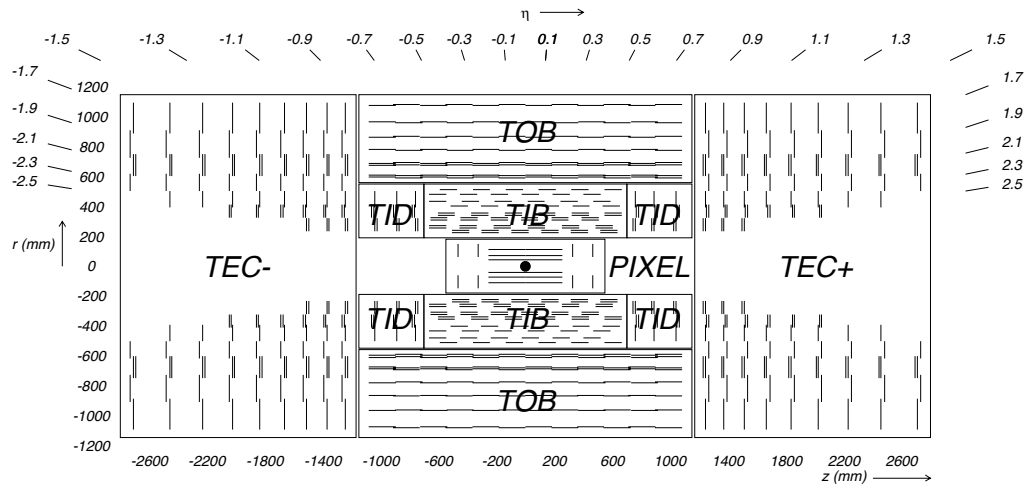


Figure 5.8: Longitudinal cross section of the silicon strip detector. Reprinted from Fig. 3.1 of ref. [45].

end-to-end along  $z$ , with repeating rows covering the full  $2\pi$  extent in  $\phi$ . In each of the TID disks, the modules are arranged into three concentric circular rings of increasing  $r$ . In the TEC, the modules are affixed to  $\phi$ -wedges called *petals*. One side of the TEC and its petal structure is shown in Figure 5.9.

Like the pixels, the strip sensors generate a signal when current flows across a p-n junction in response to interaction with a charged particle. Whereas the pixels are n-type implants on an n-type substrate, with a solid p-type rear layer to which the high voltage is connected, the strips are p-type implants on an n-type substrate, with a solid n-type rear layer connecting to the high voltage. The p-n junction in the strip sensors is at the strip-substrate boundary, whereas in the pixel sensors it is at the boundary between the rear layer and the substrate. Each sensor has either 512 or 768 electrically isolated strips, with pitch varying from 80-205  $\mu\text{m}$  depending on location. Strip lengths in  $z$  range from  $\sim 10$  to  $\sim 25$  cm. Thin ( $320 \mu\text{m}$ ) sensors are used in the TIB, TID, and inner four rings of the TEC, while thick ( $500 \mu\text{m}$ ) sensors are used in the TOB and the outer rings of the TEC. The thicker sensors compensate for the increased strip capacitance (and hence electronics noise) of the longer strips in the outer layers/disk of the tracker such that strip signal:noise is maintained above

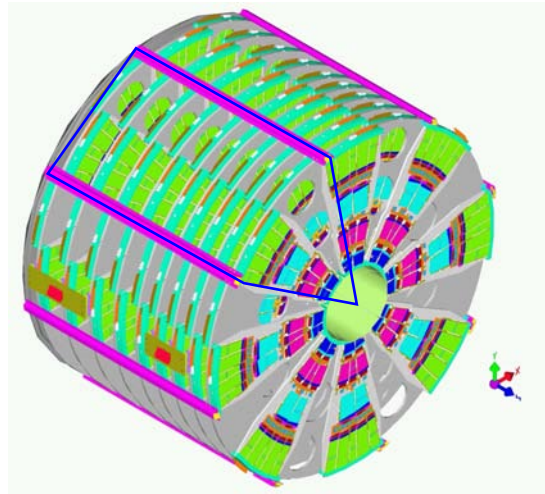


Figure 5.9: View of one tracker endcap, with the outline of a petal shown in blue. There are nine petals per wedge-shaped sector (one per TEC disk). Reprinted from Fig. 3.30 of ref. [45].

862 10 everywhere.

863     The strips are wire bonded to a front end readout chip called the APV25. The  
 864     APV25 amplifies and shapes the strip signals before sending the full analog pulse  
 865     information to an APVMUX, which multiplexes the output of two APV25s. Then,  
 866     the electrical signal from the APVMUX is sent differentially a few centimeters to an  
 867     optical driver, where it is converted to an optical signal and sent to one of the 450  
 868     front end drivers (FEDs). The FEDs convert the signal back to an electrical pulse  
 869     and digitize it for use in the global event assembly. As for the pixels, analog readout  
 870     is used on detector so that hit reconstruction may benefit from charge sharing.

871     Clock, trigger, and control signals are sent from the front end controllers (FECs)  
 872     to phase locked loop (PLL) chips on the front ends. The FECs interface to the global  
 873     clock and trigger system. Four or six APV25s, an APVMUX, and a PLL chip all sit on  
 874     a *hybrid*, two which one thin or two thick sensors are also affixed. The sensor-hybrid  
 875     combination and its frame form a module. Figure 5.10 shows a diagram of a module,  
 876     while Figure 5.11 shows a block diagram of the strip readout architecture.

877     As an example of the strip capabilities, strip hit resolution and signal:noise mea-

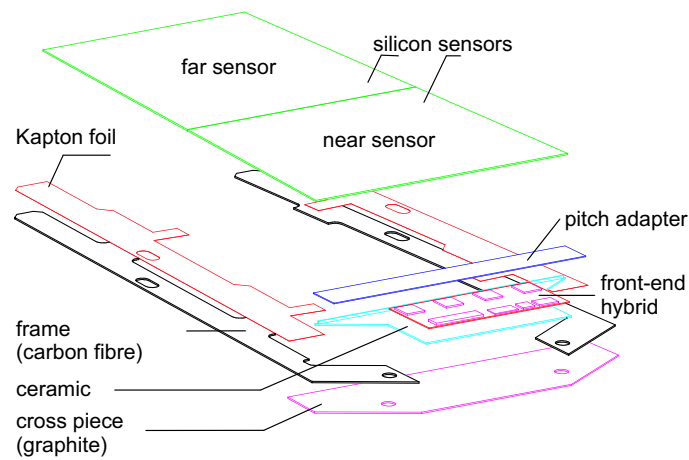


Figure 5.10: Exploded view of a strip module with two sensors. Reprinted from Fig. 3.22 of ref. [45].

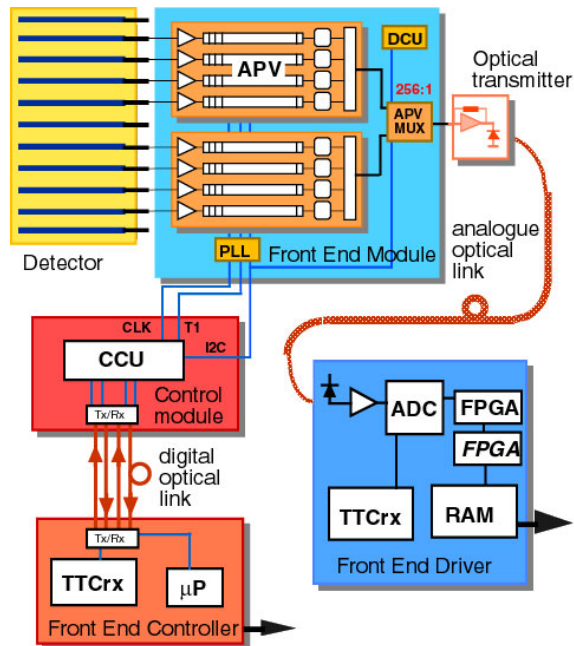


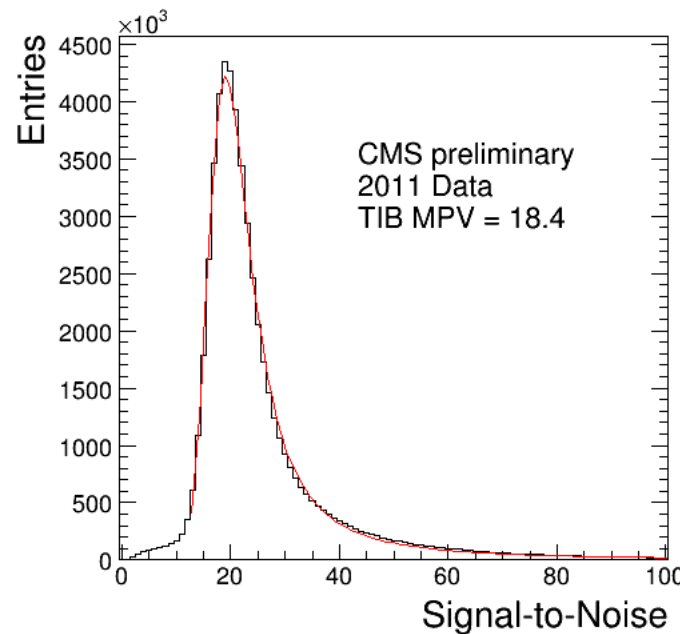
Figure 5.11: Block diagram of the strip readout architecture. Reprinted from Fig. 3.20 of ref. [45].

surements are shown in Figure 5.12. The entire pixel + strip tracker has been used successfully in the reconstruction of primary and secondary vertices, electrons, muons, tau decays, and charm and bottom hadron decays. In addition, the superior performance of the tracker over the hadronic calorimeter for low energy charged hadrons has been exploited in the the particle flow jet and  $\cancel{E}_T$  reconstruction technique (see Sec. 6.1.3). The CMS silicon strips, as well as the pixels, are well aligned and operating at close to design performance.

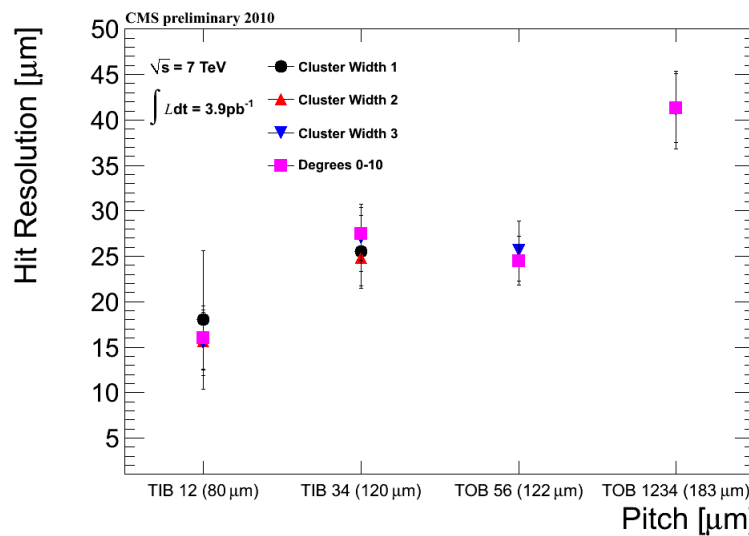
### 5.1.2 Electromagnetic Calorimeter

The electromagnetic calorimeter (ECAL) is composed of 68,524 lead tungstate ( $\text{PbWO}_4$ ) crystals, divided into one barrel (EB) layer and two endcap (EE) disks. In EB, there are 1700 crystals per *supermodule* (SM), arranged in a  $20 \times 85$  grid in  $\phi \times \eta$ . Two SMs are laid out end-to-end to form one row at fixed  $\phi$ , with a total of 18 rows needed to cover the entire  $2\pi$  extent in  $\phi$ . The SMs may be operated independently. In EE, the independent unit is a wedge-shaped sector, with nine sectors covering each endcap side. The 7,324 EE crystals are divided approximately evenly between the 18 EE sectors. A two-layer preshower detector is placed in front of the EE disks, each layer consisting of a lead absorber followed by 1.9 mm pitch silicon strip detectors (the strips in the first layer are rotated  $90^\circ$  with respect to the second layer). The ECAL layout is shown in Figure 5.13.

The electromagnetic energy resolution can be parametrized as  $(\sigma/E)^2 = (S/\sqrt{E})^2 + (N/E)^2 + (C)^2$ , where  $S$  characterizes the size of photostatistical fluctuations,  $N$  characterizes the contribution from electronics noise, and  $C$  is a constant accounting for imperfect intercalibration between crystals, non-uniformity of crystal performance, and incomplete shower containment within one crystal. The design goal of the ECAL is to achieve  $C = 0.5\%$ . Therefore, fast, dense, and relatively radiation hard  $\text{PbWO}_4$  was chosen as the crystal material. When a photon or electron strikes the crystal, it



(a) TIB signal:noise [52].



(b) TIB and TOB hit resolution as a function of strip pitch [53].

Figure 5.12: Strip detector performance highlights.

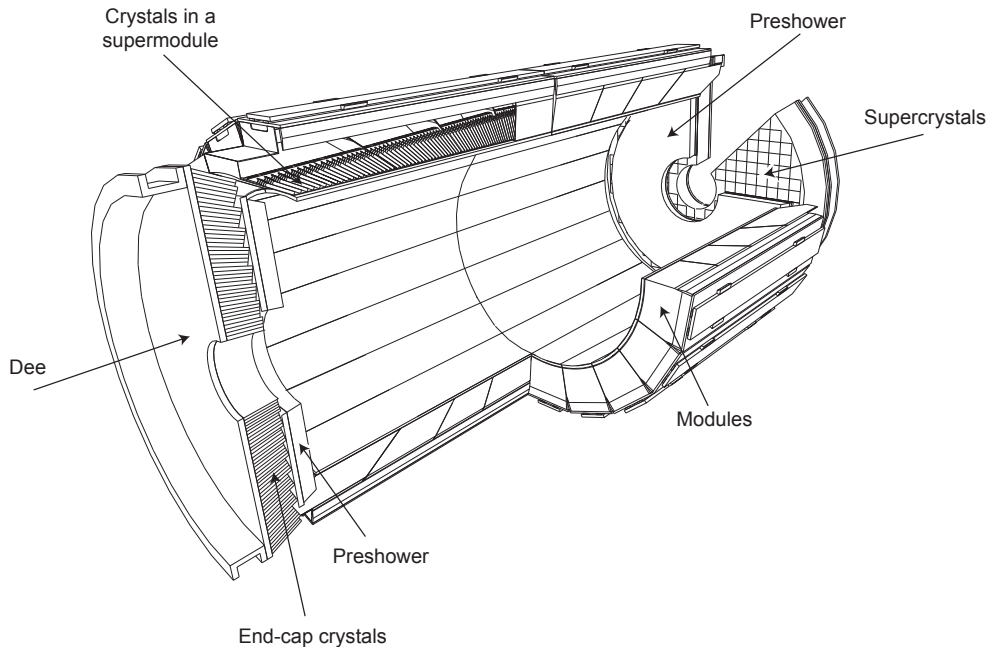


Figure 5.13: Layout of the ECAL detector. Reprinted from Fig. 4.5 of ref. [45].

904 initiates an electromagnetic (EM) shower. Due to the density, short radiation length,  
 905 and small Molière radius of  $\text{PbWO}_4$ , nearly the entirety of an EM shower can be  
 906 contained in a single 23-cm long crystal with front face dimensions  $2.2 \text{ cm} \times 2.2 \text{ cm}$ .  
 907 The crystals scintillate in the blue-green part of the spectrum, emitting  $\sim 80\%$  of the  
 908 scintillation light within 25 ns. Light is transmitted along the length of the crystals  
 909 and collected at the rear with avalanche photodiodes (semiconductor diodes) in EB or  
 910 vacuum phototriodes (conventional photomultipliers) in EE. Since the light output is  
 911 low and varies with temperature, the crystals must be kept precisely at  $18^\circ\text{C}$ . The EB  
 912 and EE crystals, which are slightly tapered to match the lateral shower development,  
 913 are shown in Figure 5.14.

914 For each trigger, 10 samples, each separated by 25 ns, are read out. The 10-sample  
 915 pulse is amplified and shaped by a multi-gain preamplifier (MGPA) residing on a very  
 916 front end (VFE) card serving five crystals. The MGPA can switch between gains 1,  
 917 6, and 12 to avoid saturation of the electronics, and affords a dynamic range up to

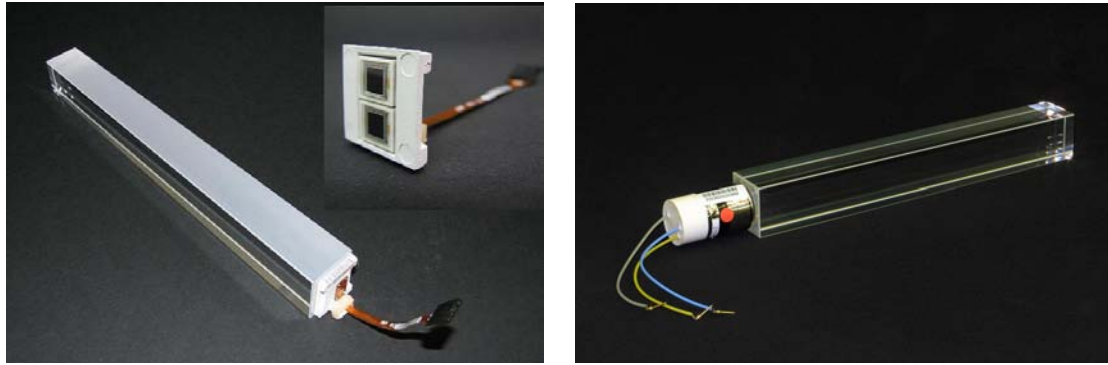


Figure 5.14: Left: EB crystal with attached APD. Right: EE crystal with attached VPT. Reprinted from Fig. 4.2 of ref. [45].

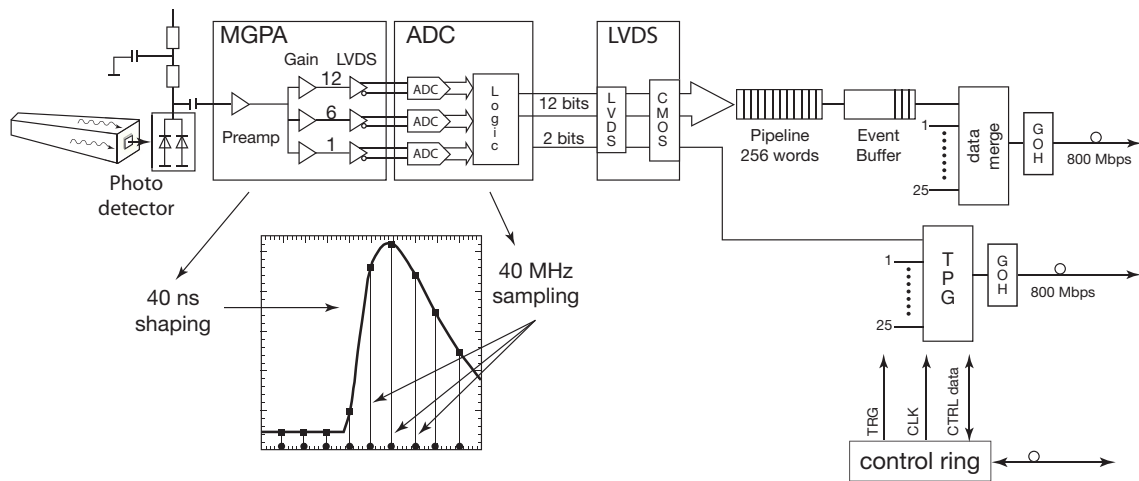


Figure 5.15: Flow chart of the crystal readout, showing the 10-sample pulse shape. Reprinted from Fig. 4.9 of ref. [45].

918 3 TeV. The samples are digitized on the VFE card, then sent to the front end (FE)  
 919 card serving five VFEs. Digitized samples are buffered in the FE card until receipt  
 920 of a trigger, when they are sent over an optical link to the data concentrator card  
 921 (DCC) that interfaces to the global DAQ. The DCC interfaces to the *selective readout*  
 922 processor, which decides whether a crystal should be read out with or without zero  
 923 suppression based on its proximity to a high-energy hit. The clock is transmitted to  
 924 the FE cards from the Clock and Control System (CCS) boards. A flow chart of the  
 925 crystal readout is given in Figure 5.15.

At each bunch crossing, the trigger concentrator cards (TCC) of the ECAL compute *trigger primitives* from  $5 \times 5$  non-overlapping transverse energy sums (in the endcaps the geometry is not always  $5 \times 5$ ). This information, along with a special bit in EB only characterizing the transverse shower profile that is used for rejection of anomalous APD hits (see Sec. 6.1.1), is transmitted from the TCCs to the synchronization and link boards (SLBs), and then on to the global trigger system. The trigger decision is communicated to the DCCs, which request the buffered data from the front ends if the decision is affirmative.

Despite the radiation hardness of lead tungstate relative to other types of crystals, it still suffers from transparency loss due to radiation-induced lattice damage, as shown in Figure 5.16. In addition, any unforeseen change in the gains of the MGPAs and VPTs, or in the pedestal levels, will degrade the energy resolution. For this reason, a continuously running calibration system is installed with the ECAL. The system makes use of the LHC abort gaps to read out the pedestal levels, test pulses fired into the MGPAs, and laser (EB and EE) or LED (EE only) pulses fired into the crystals at regular intervals. Laser and LED events are used to compute corrections to the crystal gains for transparency loss, while the other types of calibration events serve to monitor changes in the electronics performance due to magnetic field or high voltage cycling. The mean time between transparency measurements is  $\sim 40$  minutes. Figure 5.17 shows the architecture of the laser monitoring system.

The current ECAL energy resolution is somewhat worse than the design goal of 0.5%. An incomplete understanding of (a) the transparency loss and (b) the photon conversion and electron bremsstrahlung processes in the  $\sim 1X_0$  of tracker material in front of the ECAL are the main limiting factors in improving the resolution. However, as more data accumulate, more refined models of transparency loss and EM interactions in the tracker can be built, leading to better resolution. Energy resolution vs.  $|\eta|$  can be seen in Figure 5.18.

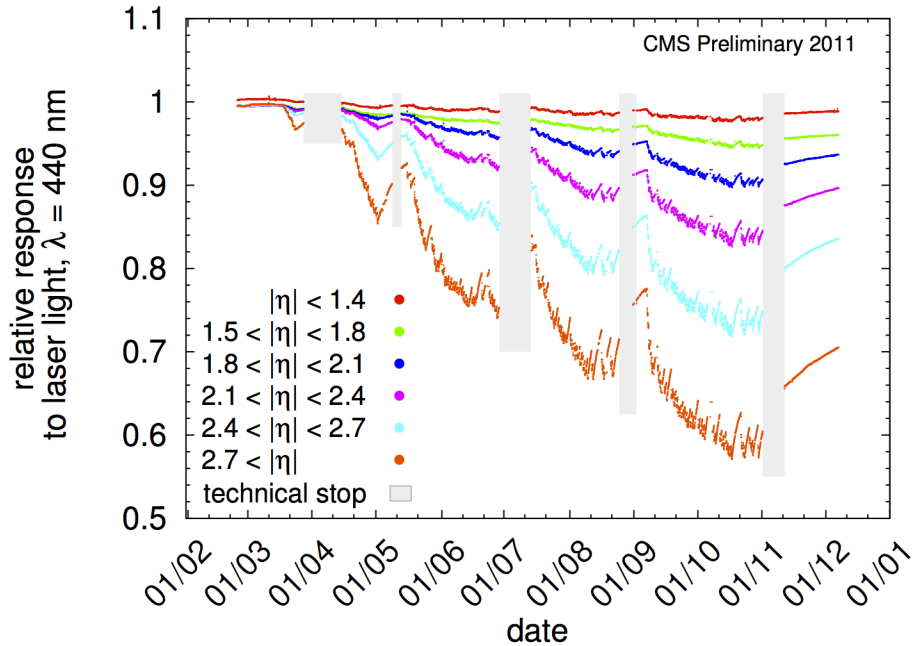


Figure 5.16: Relative response of the crystals to blue laser pulses from February 1, 2011 to January 1, 2012 [54]. Technical stops, during which the LHC is turned off for maintenance and development, are shown in gray. These periods of inactivity correspond to growth in the crystal response, as radiation damage recovery occurs.

953        The 10-sample readout coupled with the fast scintillation time of lead tungstate  
 954        allows for a very precise reconstruction of the time of ECAL hits. ECAL timing is used  
 955        for searches for long-lived particles that decay to photons or jets, such as long-lived  
 956        neutralinos in GMSB [?]. Figure 5.19 shows the timing resolution in EE.

### 957        5.1.3 Hadronic Calorimeter

958        The CMS hadronic calorimeter (HCAL) has four parts: HCAL barrel (HB), HCAL  
 959        endcap (HE), and HCAL outer (HO), which all utilize the same brass absorber /  
 960        plastic scintillator sandwich technology; and HCAL forward (HF), which is a Čerenkov  
 961        detector made of quartz fibers. A quarter longitudinal cross-sectional view of HCAL  
 962        is shown in Figure 5.20. Like EB, HB is formed of 36  $\phi$ -wedges (18 cover  $2\pi$  in positive  
 963         $\eta$ , 18 cover  $2\pi$  in negative  $\eta$ ). Each wedge is divided into 16 along  $\eta$  and four along  
 964         $\phi$ , for a total of 64 readout towers per wedge (compare 1700 individually read out

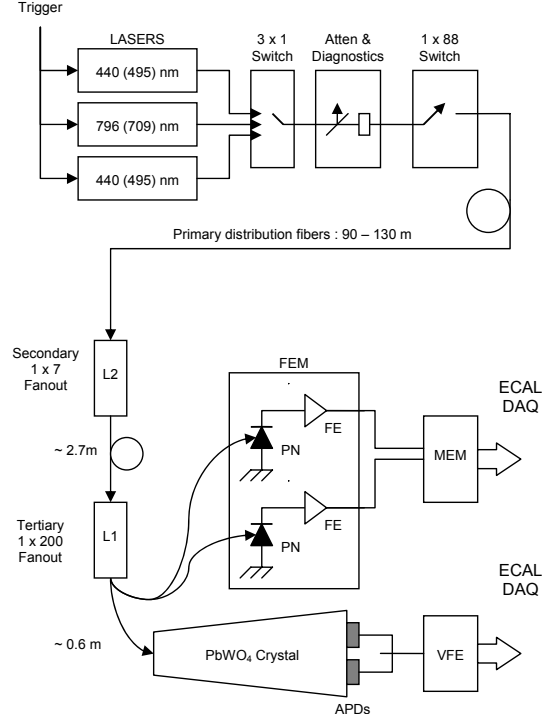


Figure 5.17: Architecture of the laser monitoring system. Reprinted from Fig. 4.16 of ref. [45].

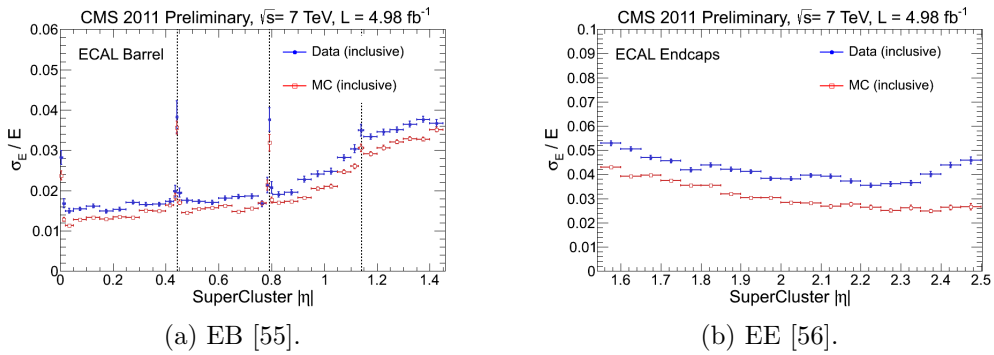


Figure 5.18: Energy resolution vs.  $|\eta|$  for  $Z$  decay electrons for data (filled blue circles) and MC (empty red squares). The dotted lines show the locations of module gaps (three per SM).

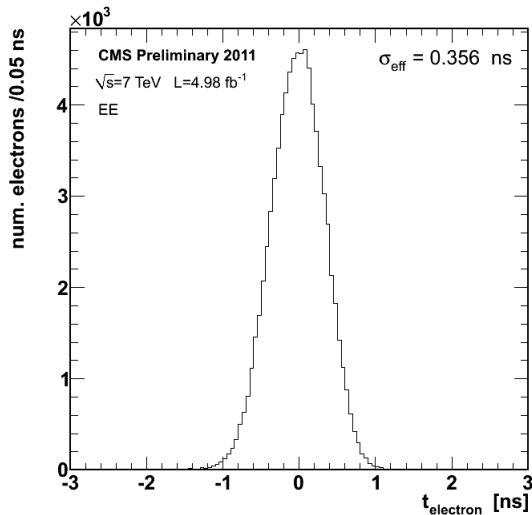


Figure 5.19: Distribution of reconstructed times of  $Z$  decay electrons in EE [57].

965 crystals per EB wedge). HE is divided into 36  $\phi$ -wedges containing 38 readout towers  
 966 each. HO consists of five rings around HB and HE distributed symmetrically along  $z$ .  
 967 There are 72  $\phi$ -slices per ring, with each  $\phi$ -slice further divided into 5, 6, or 8 along  
 968  $z$  depending on ring. The HF fibers are distributed within the steel absorber. HF is  
 969 divided into 18  $\phi$ -wedges per endcap side, each containing 24 readout towers. All HB  
 970 towers have a single readout channel except for the two in each wedge at highest  $|\eta|$ ,  
 971 which are segmented into two longitudinal layers for readout. In HE, all towers have  
 972 two longitudinal readout layers, except for the three rings of towers closest to the  
 973 beam line, which have three. There are also two longitudinal depths of HF fibers.

974 HB, HE, and HO are all sampling calorimeters consisting of alternating layers of  
 975 brass absorber and plastic scintillator. The absorber initiates the hadronic shower,  
 976 and as shower particles travel through the scintillator the scintillation light is read  
 977 out by wavelength-shifting (WLS) fibers connected to the scintillator tiles.<sup>2</sup> The full  
 978 development of the shower is sampled by the layers of instrumented scintillator. The  
 979 scintillator tiles are staggered so that there are no cracks in coverage along the direc-

<sup>2</sup>By contrast, in the ECAL, the crystal material acts as both absorber and scintillator, greatly reducing the contribution to energy resolution from sampling fluctuations.

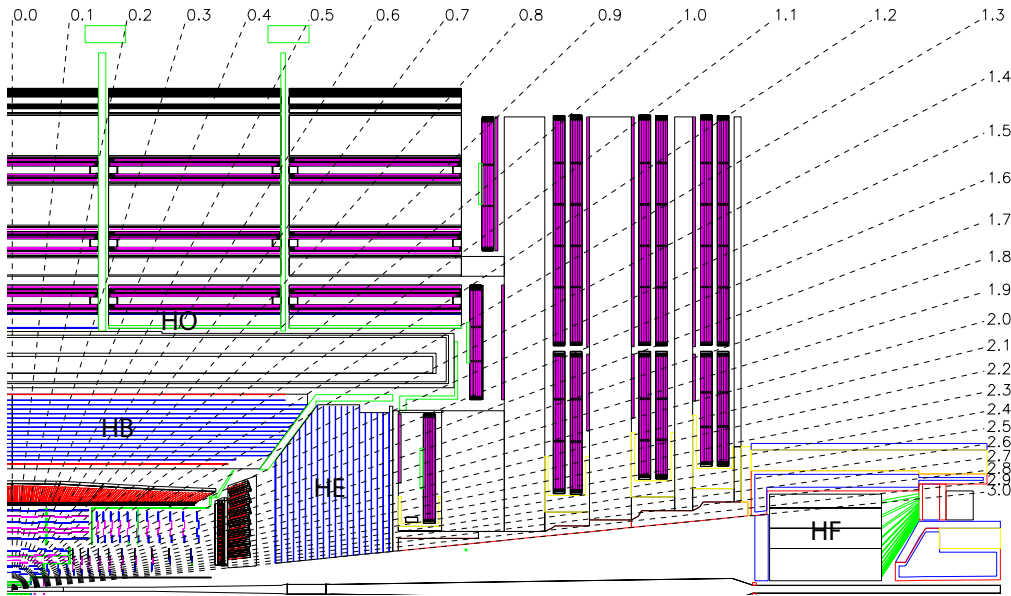


Figure 5.20: Quarter longitudinal cross-sectional view of HCAL (and muon stations in purple). Reprinted from Fig. 5.1 of ref. [45].

tion projected back to the beam spot. Light output from all tiles in a single readout tower is collected via the WLS fibers and merged into a single signal that is amplified by a hybrid photodiode (HPD). A diagram of the optical readout of HB (similar for HE and HO) is shown in Figure 5.21.

Due to the extremely harsh radiation environment near the beam line, HF is constructed of a 1.2-m thick, 1.7-m long ring of steel absorber with radiation hard quartz fibers distributed within the steel and running parallel to the beam line. Hadronic showers develop in the steel and are sampled in the quartz fibers when charged shower particles hit the the fibers and emit Čerenkov light. The light is transmitted by total internal reflection down the fibers to a photomultiplier tube (PMT), where the signals from all fibers in an HF tower are merged into one. Since only relativistic particles emit Čerenkov light in these fibers, it is mostly the EM component of the hadronic shower, consisting of neutral pions decaying to photons that interact electromagnetically with the absorber, that is sampled [58]. The charged hadrons produced in hadronic showers are typically too slow to generate Čerenkov light. Figure 5.22

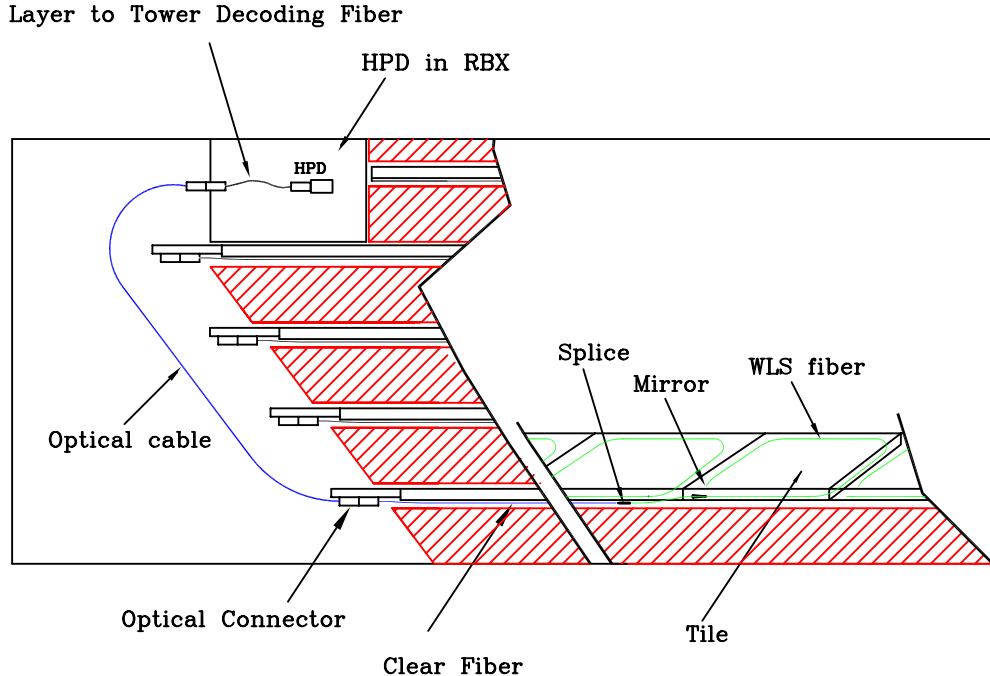


Figure 5.21: Diagram of the optical readout of HB. Reprinted from Fig. 5.7 of ref. [45].

995 shows a cross-sectional view of one side of HF.

996 Electrical signals from either HPDs (HB/HE/HO) or PMTs (HF) are digitized on  
 997 the front ends by means of a fast charge-integrating ADC. The digitized signals are  
 998 sent off-detector to the HCAL Trigger/Read-Out (HTR) boards, where they await a  
 999 trigger decision. If the trigger is accepted, the signals are sent on to the HCAL data  
 1000 concentrator cards (DCCs), which interface to the global DAQ system. HCAL trigger  
 1001 primitives, consisting of transverse energy sums over an entire tower, are calculated  
 1002 in the HTR boards and sent to the global trigger system.

1003 Selected HCAL performance results can be seen in Figure 5.23.

#### 1004 5.1.4 Muon System

1005 Beginning at a radius of  $\sim 10$  interaction lengths from the beam line, where all parti-  
 1006 cles except muons should have been stopped by the HCAL, are the muon chambers,  
 1007 interspersed with the iron return yoke of the CMS magnetic field. Three technologies

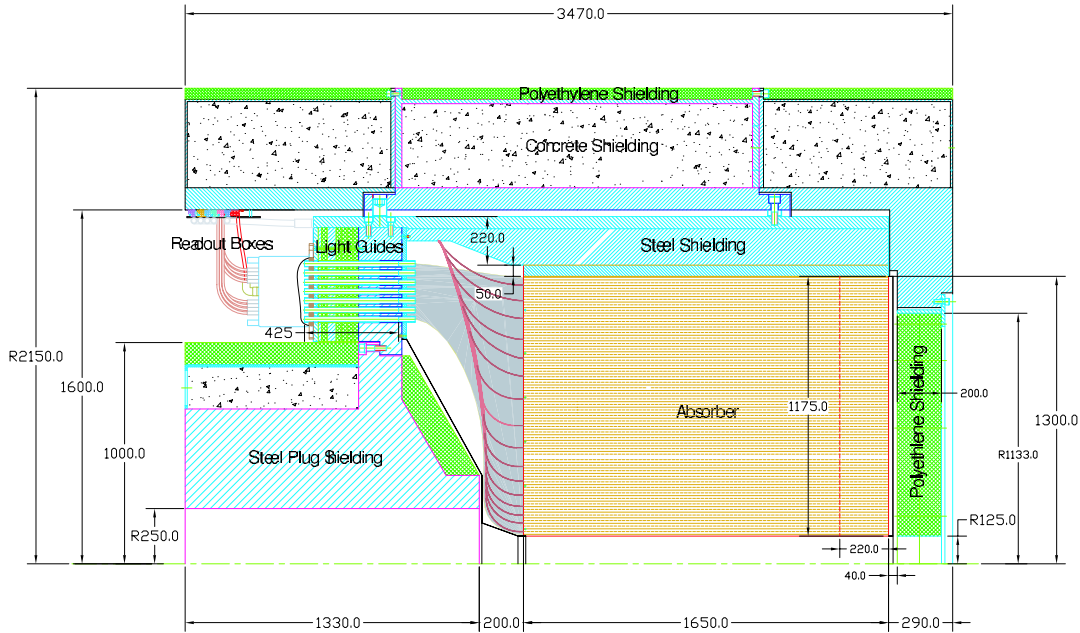
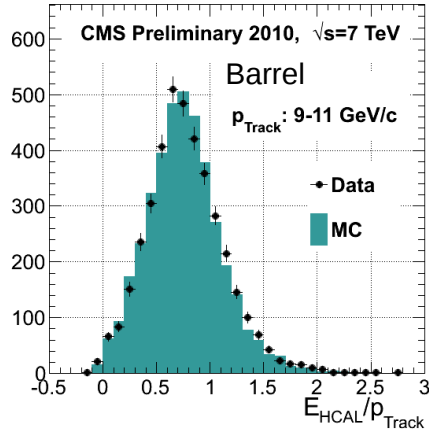


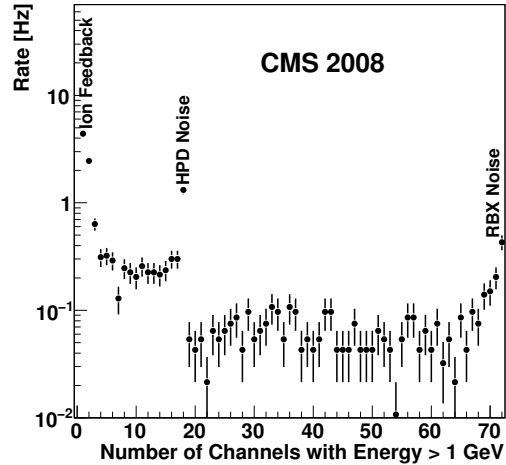
Figure 5.22: Cross-sectional view of one side of HF. The  $z$ -axis is horizontal. Reprinted from Fig. 5.28 of ref. [45].

1008 are employed: drift tubes in the barrel section (MB), cathode strip chambers (CSCs)  
 1009 in the endcap section (ME), and resistive plate chambers (RPCs) in both sections to  
 1010 provide an independent trigger with superior time resolution. There are four barrel  
 1011 layers of stations extending out to  $|\eta| = 1.2$ . Each endcap consists of five disks of  
 1012 stations as shown in Figure 5.24b, covering  $1.4 < |\eta| < 2.4$ . RPCs populate the barrel  
 1013 and endcap muon systems alongside the DT chambers and CSCs. Since they have  
 1014 time resolution much better than a few ns, they are used to assign the bunch crossing  
 1015 of muon tracks and provide a  $p_T$  trigger with sharp turn-on.

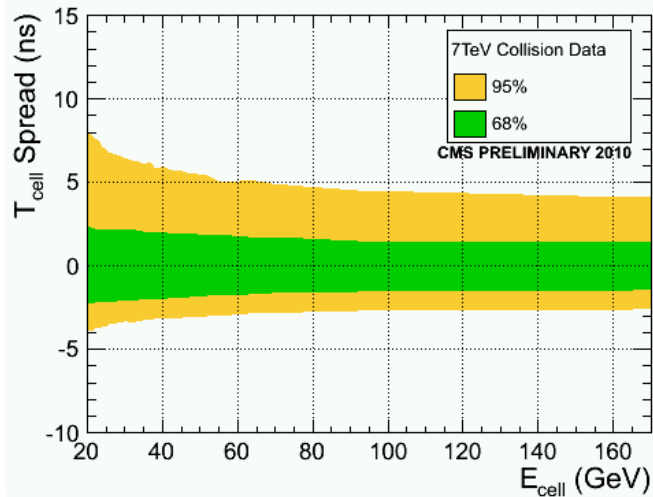
1016 Each DT chamber consists of two  $r \cdot \phi$  superlayers (SLs) and optionally one  $z$   
 1017 SL (in all chambers except those in the fourth layer). The SLs contain four rows of  
 1018 drift tubes, with the rows staggered such that there are no gaps in the coverage. The  
 1019  $r \cdot \phi$  SLs have the tube axis parallel to the beam line, while the  $z$  SL is perpendicular  
 1020 to the beam line. The tubes are  $\sim 2.4$  m in length and  $13 \text{ mm} \times 42 \text{ mm}$  in cross  
 1021 section. Each chamber therefore records eight  $r \cdot \phi$  tracking points and optionally four



(a) Data/MC comparison of HB response to charged tracks of 9-11  $\text{GeV}/c$  momentum [59].

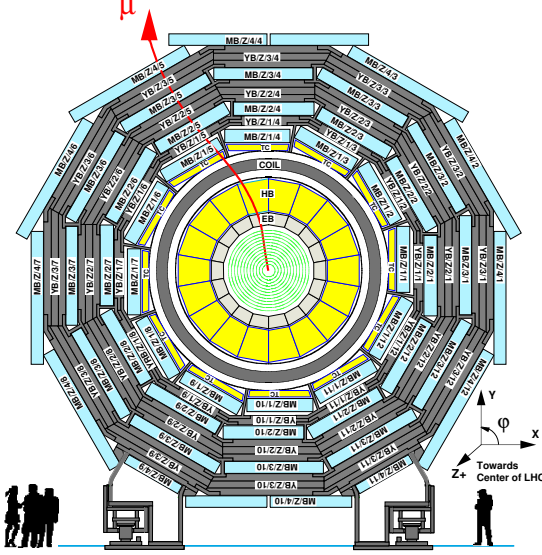


(b) Distribution of tower multiplicity, clearly showing three peaks in rate corresponding to noise sources (see Sec. 6.3) [99].

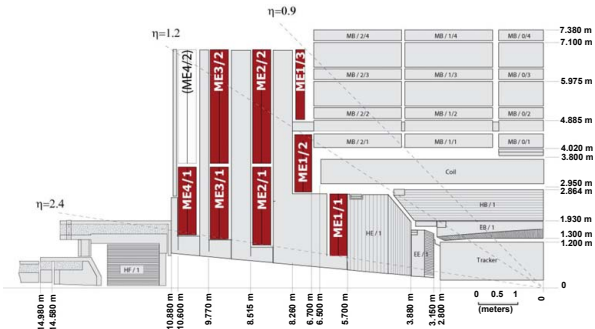


(c) Timing resolution vs. tower energy [59].

Figure 5.23: Selected HCAL performance results.



(a) One of the five wheels of MB, showing the four layers of muon stations. The five wheels are spaced symmetrically in  $z$  about  $z = 0$ . As a muon traverses the muon detectors, its curvature in the transverse plane changes direction and magnitude due to the magnetic field in the return yoke, which is of opposite sign and reduced strength relative to the field within the solenoid volume. Reprinted from Fig. 7.3 of ref. [45].



(b) Quarter longitudinal cross section of CMS highlighting the location of the ME disks. Reprinted from Fig. 7.47 of ref. [45].

Figure 5.24: View of the MB and ME layout in CMS.

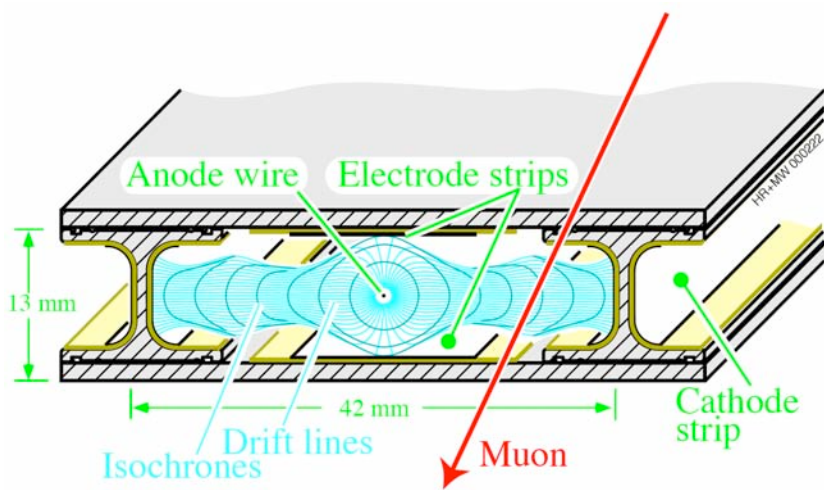


Figure 5.25: Electric field lines within a drift tube as well as the contours of equal drift time. Reprinted from Fig. 7.5 of ref. [45].

1022  $z$  tracking points. The tubes are filled with an 85%Ar + 15% CO<sub>2</sub> gas mixture. An  
 1023 anode wire at 3600 V runs the length of the tube, while the walls are covered with  
 1024 electrodes held at 1800 V or -1200 V depending on wall. When a muon passes through  
 1025 the tube, it ionizes the gas atoms. The liberated electrons drift along the electric field  
 1026 lines created by the electrodes to the anode, which is read out. Figure 5.25 shows  
 1027 the electric field lines within a drift tube as well as the contours of equal drift time.  
 1028 The maximum drift time is 380 ns.

1029 CSCs consist of alternating layers of cathode strips (four planes oriented along  $r$ )  
 1030 and anode wires (three planes oriented along  $\phi$ ). A 40%Ar + 50%CO<sub>2</sub> + 10%CF<sub>4</sub> gas  
 1031 mixture fills the space between two successive planes, forming six gas gaps. When a  
 1032 muon ionizes the gas atoms, the positive ions drift toward the anode and are read  
 1033 out to provide a measurement of  $r$ , just as in the DTs. However, an image charge is  
 1034 induced on the cathode strips, which is also read out to provide a measurement of  $\phi$ .  
 1035 The wires are spaced 3.2 mm apart. The cathode strips have pitch varying from 8.4  
 1036 mm at the end closest to the beam line to 16 mm at the other end, and are spaced  
 1037 0.5 mm apart. A trapezoidal CSC is shown in Figure 5.26.

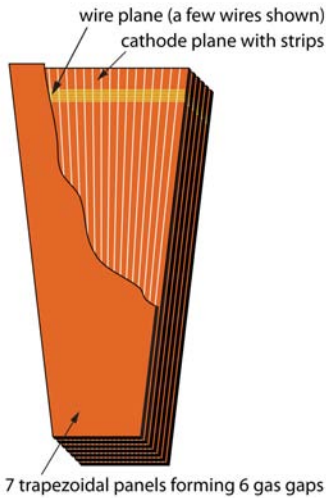


Figure 5.26: CSC wedge, showing the cathode and wire planes. Reprinted from Fig. 7.49 of ref. [45].

1038      Track stubs from the muon system are combined with tracks from the tracking  
 1039      system to form more precise muon tracks than either system could form alone, as  
 1040      shown in Figure 5.27. This leads to extremely good di-muon invariant mass resolution  
 1041      (Figure 5.28) over a large  $p_T$  range.

## 1042      **5.2 Triggering, Data Acquisition, and Data Trans-** 1043      **fer**

### 1044      **5.2.1 Level 1 and High Level Trigger Systems**

1045      The Level-1 (L1) trigger system, which encompasses dedicated hardware processors  
 1046      to construct trigger objects (typically high  $p_T$  jets, electrons, photons, taus, and  
 1047      muons) out of the calorimeter and muon hits, distributes a L1 accept or reject to all  
 1048      subdetectors at the LHC bunch crossing frequency of 40 MHz. Further data filtering  
 1049      is performed by the High Level Trigger (HLT) system, a farm of  $\sim 1000$  commercially  
 1050      available processors running a slimmed down version of the CMS event reconstruction

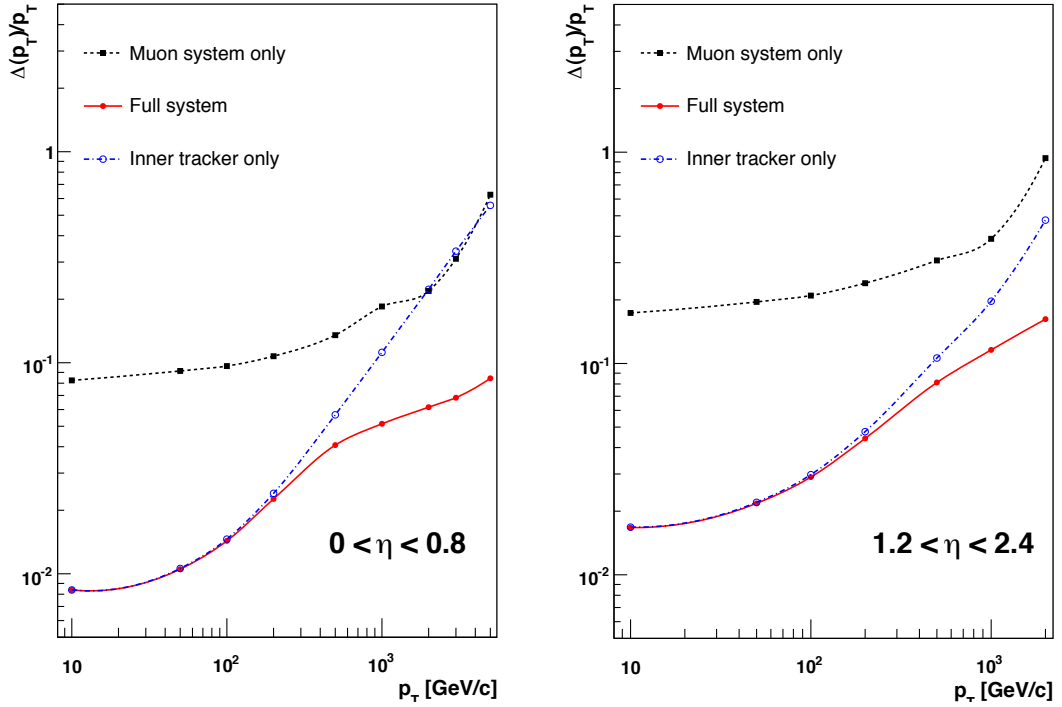


Figure 5.27: Muon  $p_T$  resolution as a function of muon  $p_T$  for tracker information only (blue), muon information only (black), and both tracker and muon information combined (red). Reprinted from Fig. 1.2 of ref. [45].

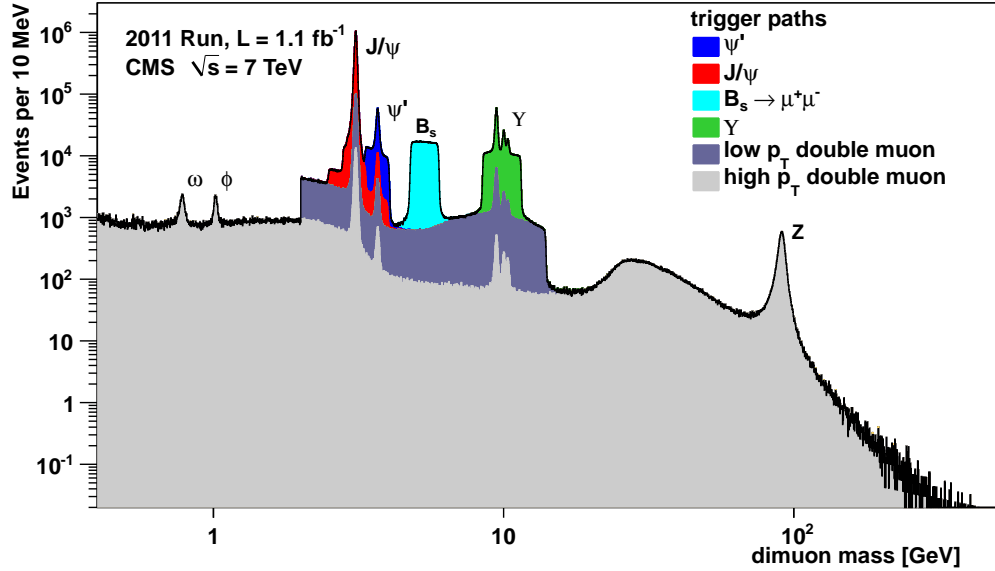


Figure 5.28: Di-muon invariant mass spectrum broken down by trigger path [60]. The light(dark) gray regions show the contribution from high- $p_T$ (low- $p_T$ ) di-muon triggers. Note that no  $B_s \rightarrow \mu^+\mu^-$  decays have been observed [61]; the light blue region just shows the amount of triggers dedicated to the  $B_s \rightarrow \mu^+\mu^-$  search.

1051 software CMSSW. The data rate received by the HLT is  $\sim 100$  kHz; the output rate of  
 1052 events permanently written to disk is  $\sim 100$  Hz. An L1 trigger *latency* (time between  
 1053 the collision and the distribution of the L1 decision to the subdetectors) of  $3.2\ \mu\text{s}$  is  
 1054 achieved via the use of fast electronics and sufficiently deep buffers to pipeline trigger  
 1055 primitives waiting to be analyzed. This latency corresponds to the length of the LHC  
 1056 abort gap, so in principle CMS may be operated with zero *dead time* (during which  
 1057 LHC bunches are missed because the L1 system is blocked while processing other  
 1058 triggers).

1059 At the bottom, the L1 trigger consists of trigger primitive generators (TPGs) in  
 1060 the calorimeter and muon systems that send  $E_T$  sums or muon track stubs to the  
 1061 regional calorimeter trigger (RCT) or muon track finders, respectively. The RCT,  
 1062 DT track finder (DTTF), and CSC track finder (CSCTF) sort and rank the regional  
 1063 trigger primitives based on  $p_T$  and quality. The ranked RCT candidates and muon  
 1064 track stubs are sent to the global calorimeter trigger (GMT) and global muon trigger  
 1065 (GMT), respectively, where high-level objects like isolated and non-isolated muons  
 1066 and EM candidates, jets, taus, and  $\cancel{E}_T$  are constructed from all the regional inputs  
 1067 and ranked. Calorimeter isolation sums for muons are also sent from the RCT to  
 1068 the GMT. The highest ranked global objects are sent to the global trigger (GT),  
 1069 which sits at the top of the L1 trigger. The GT issues the final L1 accept or reject to  
 1070 all subdetectors based on a comparison of the GMT and GCT candidates with the  
 1071 requirements of its programmed trigger menu. A block diagram of the L1 trigger is  
 1072 shown in Figure 5.29.

1073 A region in the RCT consists of a matrix of  $4 \times 4$  trigger towers. A trigger tower  
 1074 in EB/HB is one HCAL tower + the  $5 \times 5$  matrix of ECAL crystals in front of it;  
 1075 in EE/HE the idea is similar but the counting of crystals and HE towers is slightly  
 1076 more complicated. An EM RCT candidate is built around a high  $E_T$  seed tower.  
 1077 The  $E_T$  of the candidate is the sum of the tower  $E_T$  and the  $E_T$  of its highest- $E_T$

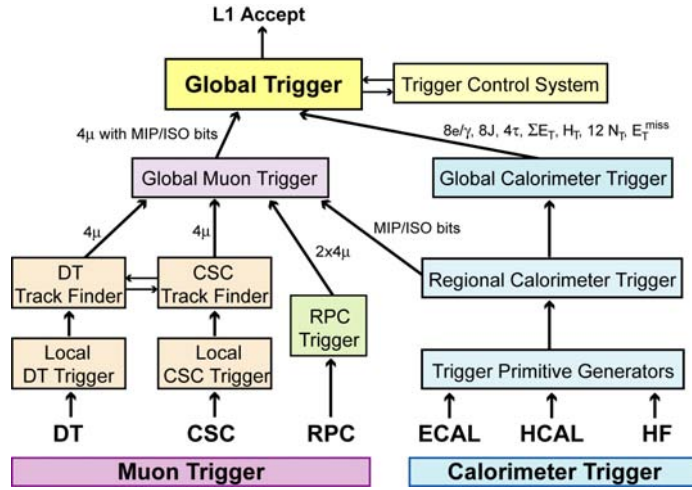


Figure 5.29: Block diagram of the L1 trigger. Reprinted from Fig. 8.1 of ref. [45].

1078 broad side neighbor (see Figure 5.30 for a definition of the broad side neighbors). Two  
 1079 isolation criteria are defined based on (a) the ratio of the EM energy to the HCAL  
 1080 energy in the tower and (b) the shower shape. For a non-isolated EM candidate, the  
 1081 highest- $E_T$  broad side neighboring tower must pass these two isolation criteria; for  
 1082 an isolated EM candidate, all eight neighboring towers must the criteria, and there  
 1083 must also be at least one quiet corner with the  $E_T$  of all five towers in the corner  
 1084 below some threshold (see Fig. 5.30). The process is repeated until four isolated and  
 1085 four non-isolated EM candidates are found, starting with the highest- $E_T$  tower in the  
 1086 region and moving down in tower  $E_T$ . An RCT region is flagged as consistent with  
 1087 tau decay only if the pattern of tower transverse energy sums defines at most a  $2 \times 2$   
 1088 matrix of energetic towers within the  $4 \times 4$  RCT region.

1089 From the tower transverse energy sums, eight EM candidates, and tau flag received  
 1090 from each RCT, the GCT computes the total  $E_T$  in the calorimeter (and the total  $E_T$   
 1091 above some programmable threshold, called  $H_T$ ), and the  $\cancel{E}_T$ . It also classifies the  
 1092 towers into jets and determines the globally highest ranked isolated and non-isolated  
 1093 EM candidates. The jet finding uses a clustering algorithm based on the energy of a  
 1094 sub-cluster with respect to its neighbors [62]. Jets are classified as tau decays if all

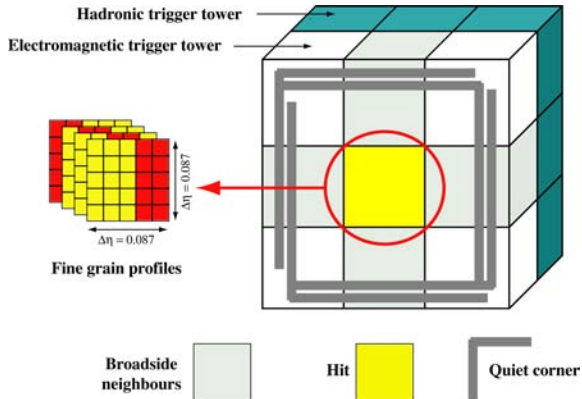


Figure 5.30: Geometry of an EM RCT candidate. Reprinted from Fig. 8.2 of ref. [45].

of the RCT regions participating in the jet clustering had energy patterns consistent with tau decay. Counts of jets above 12 different programmable  $E_T$  thresholds are calculated. The jet counts, energy sums,  $\mathcal{E}_T$ , and highest ranked EM candidates are sent to the GT, where the final L1 decision is taken and transmitted to the subdetectors. The GT can execute a maximum of 128 trigger algorithms in parallel. If any one of these algorithms yields an accept, the event is accepted, and all trigger information is sent on to the HLT for further filtering. The double-photon HLT paths used in this analysis (see Sec. 6.2) require isolated L1 seeds (i.e. EM candidates built by the RCT) with  $E_T > 12$  or 20 GeV, depending on path.

No muon triggers are used in the two-photon analysis. A description of the muon trigger system can be found in ref.[45].

### 5.2.2 Data Acquisition System

The CMS data acquisition (DAQ) system takes event fragments (calorimeter hits, track hits, etc.) from each of the 626 subdetector front end drivers (FEDs), assembles them into a data structure representing the full event, and sends the event on to the HLT for further filtering. The DAQ must operate at an input rate of  $\sim 100$  GB/s, corresponding to an input rate from the L1 trigger of  $\sim 100$  kHz. To facilitate

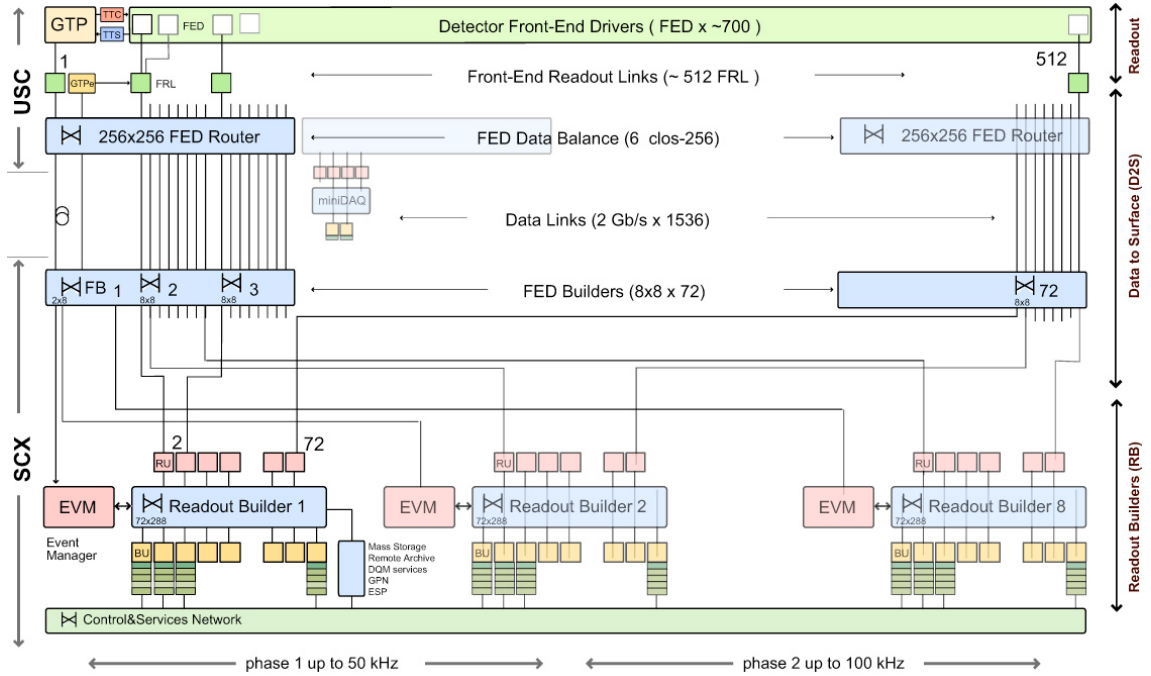


Figure 5.31: Diagram of the DAQ system. The identical event builder systems, shown as inputs and outputs to the boxes labeled “Readout Builder 1”, “Readout Builder 2”, etc., represent the eight slices. Within one slice, data can flow from the detector front ends to the readout systems to the builder network (which assembles the event fragments) to the filter systems (HLT) independently of the other slices. Reprinted from Fig. 9.8 of ref. [45].

expansion of the system as the need arises, the DAQ is composed of eight nearly independent slices. Each slice functions as a smaller version of the whole DAQ that can handle an input event rate up to  $\sim 12.5$  kHz. A diagram of the DAQ system, showing schematically the eight slices, is given in Figure 5.31.

Data from the front ends is collected by the FEDs and pushed to the front end readout links (FRLs), which may take inputs from up to two FEDs simultaneously. The FRLs check for transmission errors, generate event fragments with size  $\sim 2$  kB, buffer the fragments in 64 kB memories, and finally send them to the FED builders. The FEDs, FRLs, and FED builders are located in the underground control room. The 72 FED builders each construct one  $\sim 16$  kB *super-fragment* from the input event fragments, then send the super-fragment on to a readout unit (RU) located in

the surface control room  $\sim 80$  m away. Super-fragments belonging to the same event are sent to RUs in the same DAQ slice. There are 72 RUs per readout builder, one for each super-fragment of an event, with each DAQ slice built around one readout builder (see Fig. 5.31). Each readout builder hosts a number of builder units (BUs) that perform the final integration of super-fragments into complete events.

Resource brokers (RBs) in the HLT filter farm request complete events from the BUs and distribute those events to the filter units (FUs) for HLT selection. If an event passes any one of the HLT paths in the predefined menu, it is sent back to the RB for transfer to the storage manager (SM). The SM nodes transfer accepted events to the CERN Tier-0 prompt reconstruction facility for unpacking of the raw data into ROOT [63] files that can be accessed by physicists wishing analyze the data. The lag time between recording of an event in the DAQ and availability of the fully reconstructed event for analysis is typically 48 hours.

If the buffers of the upstream DAQ elements (the filter farm, readout builders, FED builders, or FRLs) are full, those elements will not request new events from downstream. This can lead to a buildup of events in the downstream element buffers, *back-pressuring* all the way down to the FEDs themselves. The CMS trigger throttling system (TTS) consists of dedicated lines between the FEDs and the GT for the purpose of sending predefined signals to the GT about the state of the FED buffers. If the buffer of a particular FED is getting full, it can alert the GT to reduce the trigger rate so as to prevent FED buffer overflows and loss of time synchronization between event fragments. The TTS latency is  $\sim 1\mu\text{s}$ . Causes of back-pressure (hence dead time) include: problems with the FED electronics (in this case, the upstream elements request events but the FEDs have trouble sending them), increases in the L1 accept rate (perhaps due to a noisy detector channel) beyond what the upstream DAQ elements can handle, increases in the event size due to high pileup or a poor quality beam that scrapes against the beam pipe, failures of the DAQ transmission

1150 lines or DAQ hardware such that events are not requested from the FEDs fast enough,  
 1151 or bottlenecks at the SM nodes or filter farm due to hardware failures or large event  
 1152 sizes.

1153 All components of the DAQ, from the FEDs up to the SMs, are controlled by  
 1154 cross-platform DAQ (XDAQ) [64] processes, or *executives*. The Simple Object Access  
 1155 Protocol (SOAP) [65] protocol is used to transmit control and monitoring data be-  
 1156 tween XDAQ-enabled devices and to the end user, who can view the running of a  
 1157 XDAQ executive via a Web interface called HyperDAQ [66]. The Run Control and  
 1158 Monitoring System (RCMS) handles the configuration and control of all XDAQ exec-  
 1159 utives via a hierarchical structure. At the top of the hierarchy is the Level-0 *function*  
 1160 *manager* (FM), controlling the Level-1 sub-detector FMs, which in turn control their  
 1161 Level-2 system-specific XDAQ executives. The central DAQ and L1 trigger each have  
 1162 their own Level-1 FM. A unit of data acquisition, called a *run*, may be configured,  
 1163 started, and stopped by an end user interacting with the RCMS Web interface.

### 1164 5.2.3 Data Processing and Transfer to Computing Centers

1165 Data leaving the filter farm are grouped into datasets based on HLT path, i.e. there  
 1166 are different datasets for events passing diphoton triggers, jet triggers, muon + elec-  
 1167 tron triggers, etc. At the Tier-0 facility, the datasets are go through three levels of  
 1168 processing to create three *data tiers*. The first layer produces RAW data by unpack-  
 1169 ing the detector byte streams sent from the DAQ and L1 trigger into data structures  
 1170 holding the ADC counts recorded for each channel of the detector, digitized trigger  
 1171 primitives, and the L1 decision. A single event has  $\sim 1.5$  MB of RAW data. The next  
 1172 layer of processing is the reconstruction, which forms channel energies in GeV, ap-  
 1173 plies calibrations, and creates high-level objects like photons, electrons, muons, taus,  
 1174 jets,  $E_T$ , and charged tracks. The RECO data tier occupies  $\sim 0.5$  MB per event.  
 1175 Finally, analysis object data (AOD) is a subset of the RECO data, comprising the

1176 high-level objects but usually excluding the individual channel hit information if it is  
1177 not associated to a physics object. This tier occupies  $\sim 0.1$  MB per event. One copy  
1178 of the RAW data is stored permanently at CERN and another copy is distributed  
1179 amongst the Tier-1 facilities (see below) for permanent storage. Changes in the re-  
1180 construction algorithms periodically require reprocessing of the RAW data to form a  
1181 new RECO tier. In general, only the AOD tier is available to physicists wishing to  
1182 perform analyses due to the smaller size and faster replication and transfer time of  
1183 AOD with respect to RAW or RECO.

1184 There are three tiers of computing and data storage sites within the Worldwide  
1185 LHC Computing Grid (WLCG) [67]. The tier closest to CMS is Tier-0, which is  
1186 located at CERN and performs archiving of the RAW data, prompt reconstruction  
1187 of the data within  $\sim 48$  hours of its being collected, and transferral of copies of the  
1188 RECO datasets to Tier-1 facilities. There are a few Tier-1 centers worldwide, hosted  
1189 by national computing facilities and laboratories. They store parts of the RAW dataset  
1190 and copies of the RECO datasets, participate in subsequent reconstruction passes  
1191 after the prompt reconstruction at Tier-0, and ship AOD datasets upon request to the  
1192 Tier-2 centers. Analysts interact primarily with the Tier-2 centers, which store AOD  
1193 datasets and run batch processing queues for running analysis jobs over the datasets.  
1194 Different layers of WLCG software control data transfer between sites, data storage,  
1195 and batch processing. A diagram of the WLCG tier system is given in Figure 5.32.

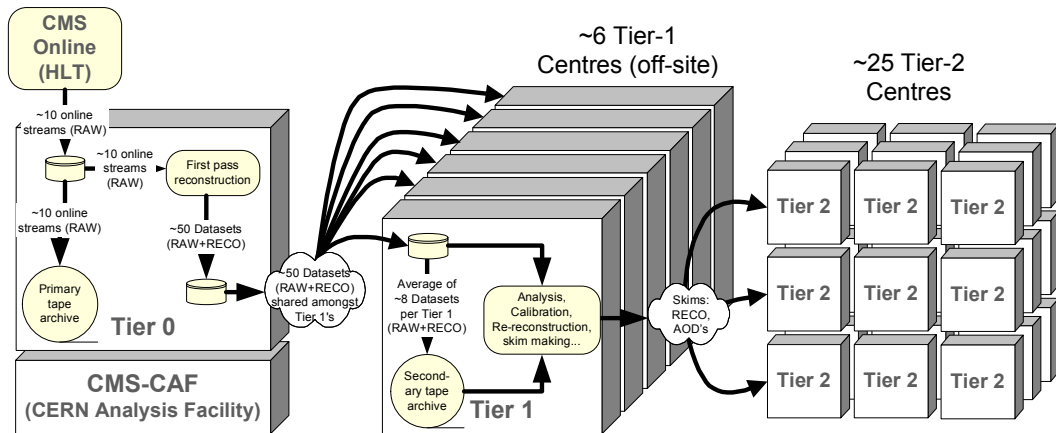


Figure 5.32: Diagram of the WLCG tier system showing data archival and reconstruction at each tier along with data transfer between tiers. Reprinted from Fig. 11.2 of ref. [45].

1196 **Chapter 6**

1197 **Event Selection**

1198 In keeping with the phenomenology described in Sec. 3.5, the candidate GGM events  
1199 selected in this search consist of two high- $E_T$  photons and a significant momentum  
1200 imbalance transverse to the beam, indicating the production of an escaping gravitino.  
1201 This momentum imbalance is usually referred to as *missing transverse energy* and is  
1202 denoted by the symbol  $\cancel{E}_T$ .

1203 However, in order to use real CMS data (as opposed to simulation) to derive pre-  
1204 dictions for the backgrounds to the search, *control samples* distinct from the *candidate*  
1205 two-photon sample must be collected. These samples consist of different numerical  
1206 combinations of photons, electrons, and jets, and are explained in more detail in  
1207 Chapter 7. Since this search is performed in the high- $\cancel{E}_T$  tail of the  $\cancel{E}_T$  distribution,  
1208 where adequate detector simulation is very difficult, it is advantageous to use *data-  
1209 driven* background estimates, which capture the true detector response, over numbers  
1210 derived from simulation.

1211 In the following sections, the reconstruction of photons, electrons, jets, and  $\cancel{E}_T$   
1212 is explained. Sec. 6.1 begins with an explanation of the high level reconstruction.  
1213 It is followed by Sec. 6.2, which describes the triggers used to collect the candidate  
1214 and control samples. Sec. 6.3 describes event cleaning cuts that are applied to the

1215 candidate and control samples. Finally, the chapter concludes with a measurement of  
1216 the photon identification efficiency in Sec. 6.4.

## 1217 6.1 Object Reconstruction

1218 This section describes the *offline* object reconstruction, i.e. the reconstruction of par-  
1219 ticle objects from events that have already been triggered and written to permanent  
1220 storage, as opposed to the building of trigger objects explained in Secs. 5.2.1 and 6.2.

### 1221 6.1.1 Photons

#### 1222 Uncalibrated EB/EE Hits

1223 Photon reconstruction begins with the ADC count value for each of the 10 recorded  
1224 time samples per ECAL crystal per trigger. To construct an *uncalibrated hit*, the  
1225 gain (1, 6, or 12; see Sec. 5.1.2) of each sample is determined and the ADC count  
1226 value scaled appropriately. The pedestal is estimated from the average of the first  
1227 three samples, which, for a properly timed in hit, should contain no signal. This  
1228 pedestal value is subtracted from the rest of the samples. Finally, the amplitude of the  
1229 pulse is reconstructed using a predetermined weight for each sample [68]. The weights  
1230 correspond to the pulse shape expected from the MGPA and shaping circuit response.  
1231 The time of the hit is also reconstructed using the ratios between neighboring time  
1232 samples [69]. A typical ECAL channel pulse shape is shown in Figure 6.1.

#### 1233 Calibrated EB/EE Hits

1234 In the next phase of the photon reconstruction, calibrations are applied to the un-  
1235 calibrated hits to form *calibrated hits* with energy measured in GeV. Channels are  
1236 excluded from seeding calibrated hits if

- 1237 • they are excessively noisy,

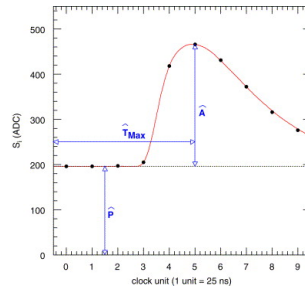


Figure 6.1: Typical ECAL channel pulse shape.  $\hat{P}$  is the pedestal value,  $\hat{A}$  is the pulse amplitude, and  $\hat{T}_{\max}$  is the hit time. The red line is the assumed pulse shape from which the weights are derived. Reprinted from ref. [68].

- 1238     • they are stuck in fixed gain (i.e. the MGPA gain does not change properly to  
1239            avoid saturation),
- 1240     • they are totally dead,
- 1241     • they have one or more neighboring dead channels, or
- 1242     • they do not have good trigger primitives (i.e. trigger primitive is missing, satu-  
1243            rated, or *spike-like*).

Added

1244     *ECAL spikes* are hits in which low energy protons and heavy ions from jets ionize this  
1245     in the sensitive volume of the EB APD, causing the APD to register a fake large- para-  
1246     amplitude hit. Because they are not the result of a real electromagnetic shower, spikes graph  
1247     tend to be isolated. They may also appear to arrive early or late with respect to the and the  
1248     nominal bunch crossing. Most spikes are reconstructed with a hit time  $\sim 10$  ns earlier next  
1249     than real EM hits because unlike real hits, whose pulse shapes include the time about  
1250     constant associated with crystal scintillation, the reconstructed spikes only involve spikes  
1251     the rise time of the electronics. There also is a long tail of late arriving spikes due to  
1252     slow neutrons from jets [70].

1253     Because of their particular timing and topological characteristics, cuts have been  
1254     developed to effectively identify and reject spike-like hits. This analysis utilizes both  
1255     the “Swiss cross” cut  $1 - E_4/E_1 > 0.95$ , where  $E_1$  is the energy of the spike candidate

1256 crystal and  $E_4$  is the sum of the energies in the four crystals whose edges are parallel to  
 1257 the four edges of the spike candidate crystal, and a timing cut  $t \geq 3$  ns, to flag spikes.  
 1258 More information about these cuts can be found in ref. [70]. A simpler algorithm  
 1259 using the fine grain veto bit of the L1 TPG is used to reject spikes at the trigger level  
 1260 **[insert citation]**.

1261 In addition to the trigger primitives, no uncalibrated hits that are spike-like are eli-  
 1262 gible for calibration. The calibrations applied are crystal transparency loss corrections  
 1263 measured continuously by the laser/LED system, energy intercalibrations (relative en-  
 1264 ergy calibration between crystals), absolute scale calibrations between ADC counts  
 1265 and GeV,<sup>1</sup> and time intercalibrations (relative time calibration between crystals).

1266 The ECAL crystals were pre-calibrated before installation in CMS using labora-  
 1267 tory light yield and photodetector gain measurements [72]. In addition, some EB and  
 1268 EE crystals were intercalibrated using test beams [73], and all EB crystals were inter-  
 1269 calibrated with cosmic ray muons [74]. EE precalibrations were validated with LHC  
 1270 *splash events* in 2009 [74, 75], in which the beam was dumped onto a collimator ap-  
 1271 proximately 150 meters upstream of CMS, causing a spray of muons to enter CMS at  
 1272 one endcap and exit at the other. Splash events were also used to derive time intercal-  
 1273 ibration constants. Before colliding beam operations commenced, the intercalibration  
 1274 precision was estimated to be 0.5%-2.2% in EB and 1%-5% in EE [76].

1275 Three calibration methods were employed once colliding beam operations began:

- 1276     •  $\phi$  symmetry relative calibration between crystals, exploiting the azimuthal sym-  
 1277         metry of CMS
- 1278     •  $\pi^0$  and  $\eta$  relative calibration between crystals, using the diphoton decays of  
 1279         these particles

---

<sup>1</sup>The ADC-GeV scale factors (one for EB and one for EE) are defined such that the sum of fully calibrated and scaled hits in a particular  $5 \times 5$  cluster of crystals (plus the associated energy deposited in ES) is 50 GeV for a 50 GeV incident unconverted photon [71].

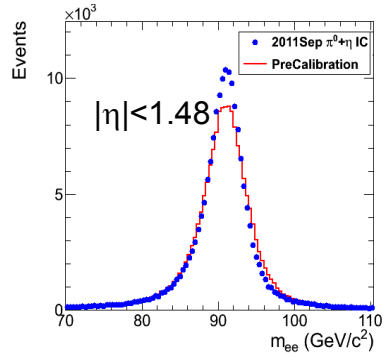


Figure 6.2:  $Z$  peak reconstructed using pre-LHC calibration constants (red) or September 2011  $\pi^0/\eta$ -derived intercalibration constants (blue). Reprinted from ref. [77].

1280     •  $E/p$  absolute calibration, comparing the momentum measured in the tracker  $p$   
1281               to the energy measured in the ECAL  $E$  of a sample of electrons from  $Z$  decay

1282     By September 2011, the intercalibration precision in EB was measured to be be-  
1283     tween 0.3% and 1.1% using the  $\pi^0/\eta$  method [77]. Figure 6.2 shows the improvement  
1284     in  $Z$  reconstruction from pre-LHC calibration constants to the latest  $\pi^0/\eta$ -derived  
1285     constants.

## 1286     Calibrated ES Hits

Added

1287     ES calibrated hits are formed from the three samples read out per sensor. Just as in the paren-  
1288     case of EB/EE crystals, ES uncalibrated hits gain-adjusted, pedestal-subtracted, and thetical  
1289     reconstructed using weights. To make a calibrated ES hit, intercalibration constants, remark  
1290     angle correction constants (for the non-uniformity of sensor angle with respect to the  
1291     vertical across ES), and a MIP-GeV absolute scale factor are applied.

## 1292     Clustering

1293     After calibrated ECAL hits are formed, they must be clustered into shapes that  
1294     represent the energy deposit from a single particle. *Basic clusters* are formed around  
1295     seed hits, defined as a hit that

- 1296     • has calibrated  $E_T > 1(0.18)$  GeV in EB(EE),
- 1297     • does not originate from a dead channel or one with faulty hardware,
- 1298     • is not poorly calibrated,
- 1299     • was reconstructed with the standard algorithm (i.e. not a special recovery algo-
- 1300         rithm for channels with subpar data integrity),
- 1301     • is not saturated,
- 1302     • is not spike-like, and
- 1303     • is in time (EB).

1304   EB basic clusters are formed around the seeds via the *hybrid* algorithm, while EE basic  
 1305   clusters are formed with the `multi5x5` algorithm [78]. In addition to non-radiating  
 1306   electrons and unconverted photons, both algorithms are designed to also recover all of  
 1307   the energy associated with electron bremsstrahlung deposits and photon conversions.  
 1308   The geometry of the CMS magnetic field means that bremsstrahlung and conversions  
 1309   will tend to spread the shower out in  $\phi$ , not  $\eta$ . Both algorithms work by forming  
 1310   basic clusters around seeds, then combining the basic clusters into *superclusters* (SC)  
 1311   by searching in a window extended in the  $\phi$  direction for all basic clusters consistent  
 1312   with bremsstrahlung radiation from the primary electron, or with a photon conversion.  
 1313   Figure 6.3 illustrates the hybrid algorithm in EB. In EE, the energy deposited in ES  
 1314   must also be added into the total clustered energy sum.

1315   Figure 6.4 shows the effect of superclustering on  $Z \rightarrow ee$  reconstruction.

### 1316   **Supercluster Corrections**

1317   The total clustered ECAL energy is defined as

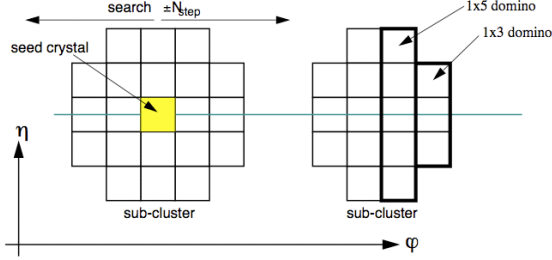


Figure 6.3: Hybrid algorithm in EB. The shower extent is essentially constant in  $\eta$ , but spreads out in  $\phi$  as the two sub-clusters (or basic clusters) are grouped into the same supercluster. Reprinted from ref. [78].

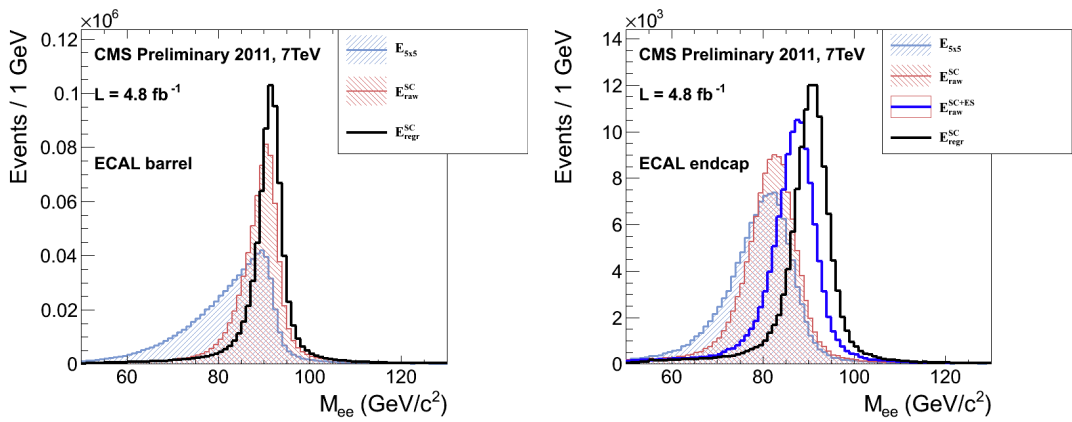


Figure 6.4:  $Z$  peak reconstructed in the dielectron channel for different kinds of clustering. The left plot is for EB and the right plot for EE. The constituent hits were calibrated with the best available intercalibrations and laser calibrations as of December 2011. The light blue histogram shows the reconstruction using a  $5 \times 5$  energy sum, the red histogram shows the reconstruction using the SC energy for crystals only (the dark blue histogram on the right-hand side adds in the energy from ES), and the black histogram shows the reconstruction after the SCs are corrected using a multivariate method [?]. Reprinted from Fig. 30 of ref. [?].

$$E = F \times \sum_{i=1}^{n_{\text{crystal}}} G \times c_i \times A_i \quad (6.1)$$

1318 where  $G$  is the ADC-GeV or MIP-GeV scale factor,  $c_i$  are the intercalibration con-  
 1319 stants,  $A_i$  is the uncalibrated hit amplitude in ADC counts, and  $F$  is a SC correction  
 1320 factor.  $G$  and  $c_i$  were explained in Sec. 6.1.1.  $F$  is a product of three factors for hybrid  
 1321 SCs (two for multi5x5 SCs) [78]:

- 1322 1.  $C_{\text{EB}}(\eta)$ , which compensates for lateral energy leakage due to the crystal off-  
 1323 pointing in EB. These corrections are taken from MC simulation [78] and were  
 1324 confirmed in test beams [73].
- 1325 2.  $f(\text{brem})$ , which corrects for biases in the clustering algorithms for showers char-  
 1326 acterized by differing amounts of bremsstrahlung. These corrections are taken  
 1327 from MC simulation [78].
- 1328 3. Residual correction  $f(E_T, \eta)$ , due to the variation in  $\eta$  of detector material  
 1329 traversed by a primary electron or photon, and to any residual  $E_T$  dependence  
 1330 of the reconstruction. These corrections are determined from MC and validated  
 1331 on  $Z \rightarrow ee$  data samples [79].

Changed

1332 As a benchmark of ECAL calibration performance, the extra energy smearing in  
 1333 MC needed to achieve data/MC agreement in the  $Z$  width was between  $\sim 0.9\%$  (in  
 1334 the central part of EB for electrons with little bremsstrahlung) and  $\sim 3.3\%$  (in the  
 1335 outer part of EE for heavily radiating electrons) [80].

### 1336 From Supercluster to Photon

1337 The CMS photon object is any SC with  $E_T > 10$  GeV and  $H/E < 0.5$ , unless the SC  
 1338  $E_T > 100$  GeV, in which case the  $H/E$  requirement is dropped.  $H/E$  is defined as the

ratio of energy in the HCAL in a 0.15 cone around the SC centroid, directly behind  
 the SC, to the SC energy. SCs with  $R9 > 0.94(0.95)$  in EB(EE), where  $R9$  is defined  
 as the ratio of the energy in the central  $3 \times 3$  cluster of crystals divided by the SC  
 energy  $E_{3 \times 3}/E_{\text{SC}}$ , are the best calibrated and most accurate type of electromagnetic  
 shower. Therefore, for these objects, the photon energy is defined as the energy sum  
 of the fully calibrated hits in the central  $5 \times 5$  cluster around the seed (with  $C_{\text{EB}}(\eta)$   
 applied for EB photons). For all other SCs, the photon energy is equal to the fully  
 corrected SC energy (cf. Sec. 6.1.1).

Reorganized

In this search, candidate photons and *fake photons* ( $f$ , “fakes”) are further selected  
 according to the criteria listed in Table 6.1. Fakes are used in the determination of  
 the QCD background, as explained in Chapter 7.

next 3

para-

graphs;

edited

Ta-

ble 6.1

caption

Table 6.1: Selection criteria for photons and fakes. “Pixel seed,”  $I_{\text{comb}}$ , and  $\sigma_{i\eta i\eta}$  are  
 defined in the text.

Variable	Cut ( $\gamma$ )	Cut ( $f$ )
SC $ \eta $	$< 1.4442$	$< 1.4442$
$H/E$	$< 0.05$	$< 0.05$
$R9$	$< 1$	$< 1$
Has pixel seed	No	No
$I_{\text{comb}}, \sigma_{i\eta i\eta}$	$< 6 \text{ GeV} \&\& < 0.011$	$(\geq 6 \&\& < 20 \text{ GeV}) \parallel \geq 0.011$

$I_{\text{comb}}$  is defined as

Updated

effective

area

$$I_{\text{comb}} = I_{\text{ECAL}} - 0.093\rho + I_{\text{HCAL}} - 0.0281\rho + I_{\text{track}} \quad (6.2)$$

where  $I_{\text{ECAL}}$ ,  $I_{\text{HCAL}}$ , and  $I_{\text{track}}$  are  $E_T$  sums in the annular regions defined in Figure 6.5  
 and  $\rho$  is the average pileup energy density in the calorimeters (per unit  $\eta \cdot \phi$ ) as  
 measured with the Fastjet algorithm [81, 82]. Note that the ECAL and track isolation  
 veto strips at constant  $\eta$  ensure that the isolation cuts are similarly efficient for  
 converted photons, radiating electrons, and unconverted photons.

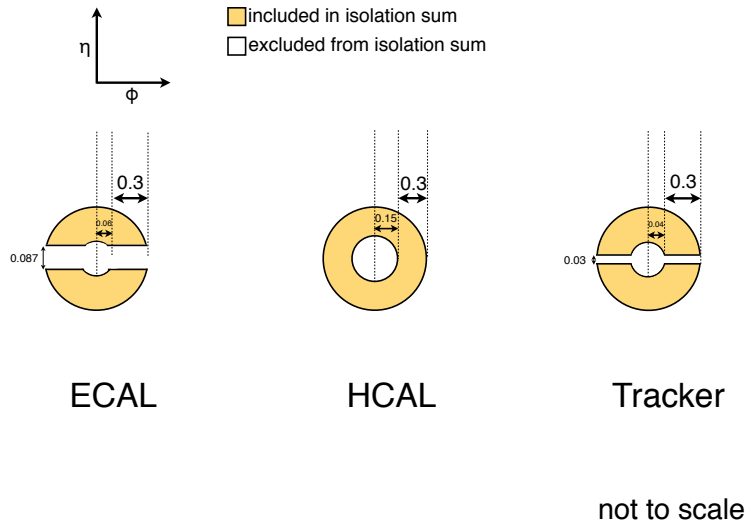


Figure 6.5: ECAL, HCAL, and track Isolation cones.

<sup>1356</sup>  $\sigma_{i\eta i\eta}$  is the log energy weighted extent of the shower in  $\eta$  and is defined as Added  $\sigma_{i\eta i\eta}$

$$\sigma_{i\eta i\eta} = \frac{\sum_{i=1}^{25} w_i (\eta_i - \bar{\eta})^2}{\sum_{i=1}^{25} w_i} \quad (6.3) \quad \text{defini-} \quad \text{tion}$$

<sup>1357</sup> where the sums run over the  $5 \times 5$  matrix of crystals surrounding the seed,  $w_i =$   
<sup>1358</sup>  $\max(0, 4.7 + \ln(E_i/E))$ ,  $E_i$  is the energy of the  $i^{\text{th}}$  crystal,  $E$  is the total energy in the  
<sup>1359</sup> 25 crystals,  $\eta_i$  is the offset in  $\eta$  of the  $i^{\text{th}}$  crystal from the seed, and  $\bar{\eta}$  is the weighted  
<sup>1360</sup> average  $\eta$  of the 25 crystals (using the  $w_i$  as weights) [83]. Changed

<sup>1361</sup> Figure 6.6 shows the  $\rho$  distribution for a sample of two-photon events, with at average  
<sup>1362</sup> least one 40 GeV and one 25 GeV photon, passing the selection requirements in  $\rho$ ; up-  
<sup>1363</sup> Table 6.1 and the trigger requirements in Table 6.3. This sample represents the full dated  
<sup>1364</sup> 2011 dataset of  $4.7 \text{ fb}^{-1}$ . Since the average  $\rho$  is  $\sim 7.5 \text{ GeV}$ , and there is a long tail fig. 6.6  
<sup>1365</sup> above this average value, it is necessary to subtract pileup energy from the ECAL  
<sup>1366</sup> and HCAL isolation cones to recover otherwise clean photons in events with large  
<sup>1367</sup> pileup. The ECAL and HCAL *effective areas* of 0.093 and 0.0281, respectively, are

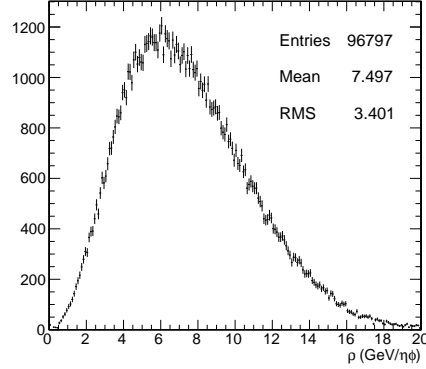


Figure 6.6:  $\rho$  distribution for a sample of two-photon events, with at least one 40 GeV and one 25 GeV photon, passing the selection requirements in Table 6.1 and the trigger requirements in Table 6.3. This sample covers the full 2011 dataset of  $4.7 \text{ fb}^{-1}$ .

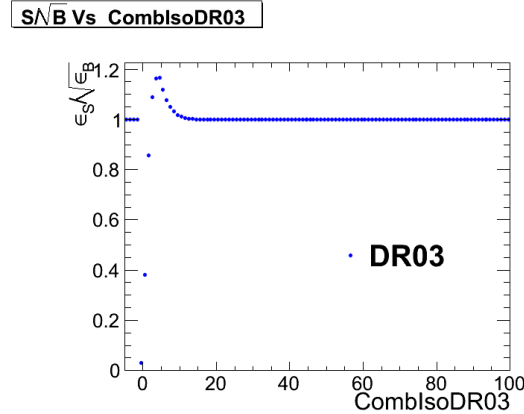


Figure 6.7:  $S/\sqrt{B}$  ( $S$  and  $B$  defined in the text) vs. combined isolation. Reprinted from Fig. 7 of ref. [84].

1368 calculated by fitting the average ECAL or HCAL isolation energy vs.  $\rho$  in a sample  
 1369 of  $Z \rightarrow ee$  events to a straight line. The slope of the line—which has the units of  $\eta \cdot \phi$ ,  
 1370 or area—is the effective area.

1371 The cut on combined isolation of 6 GeV (Table 6.1) is the result of an  $S/\sqrt{B}$   
 1372 optimization procedure [84].  $S$  is a sample of photons in simulated GGM events that  
 1373 are products of neutralino decay, while  $B$  is a sample of photons matched to generated  
 1374 hadronic jets in simulated QCD events. Figure 6.7 shows the value of  $S/\sqrt{B}$  vs.  
 1375 combined isolation, in particular the pronounced peak around 6 GeV.

New

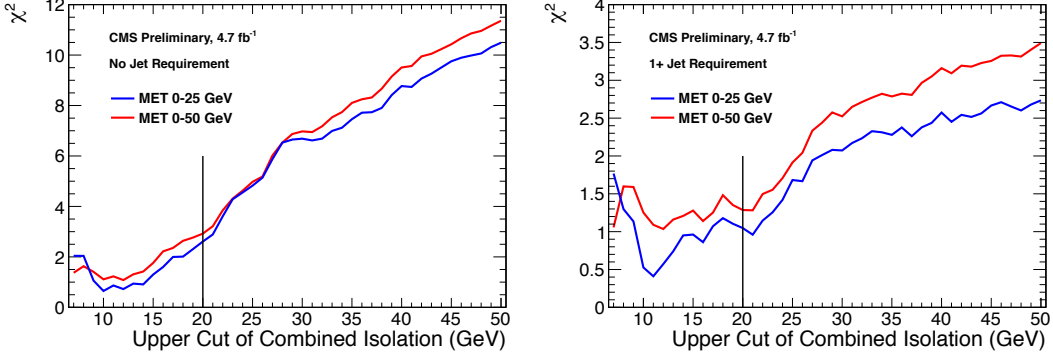


Figure 6.8: Neyman’s  $\chi^2$  between the  $ff$  and  $\gamma\gamma$   $\cancel{E}_T$  distributions, truncated at either 25 (red) or 50 (blue) GeV, vs. upper bound on fake combined isolation. The left plot includes all events; the right plot is for events with  $\geq 1$  jet defined as in Table 6.2, but with the  $\Delta R$  cleaning criteria applied to the two primary EM objects and all additional electrons, photons, and fake photons. The full reweighting and normalization procedure is employed in the  $\cancel{E}_T$  calculation (see Sec. 7.1). Error bars include statistical, reweighting, and normalization error (see Sec. 7.3). Reprinted from Fig. 9 of ref. [84].

1376        The upper bound on fake photon combined isolation guarantees that poorly iso-  
 1377        lated dijet events, with  $\cancel{E}_T$  resolution dissimilar to the candidate diphoton events,  
 1378        do not enter the  $ff$  sample. The exact value of 20 GeV (cf. Table 6.1) arises from  
 1379        a low- $\cancel{E}_T$   $ff/\gamma\gamma$   $\chi^2$  optimization procedure [84]. Figure 6.8 shows the value of the  
 1380        Neyman’s  $\chi^2$  between the  $ff$  and  $\gamma\gamma$   $\cancel{E}_T$  distributions, truncated at either 25 or 50  
 1381        GeV, vs. upper bound on fake combined isolation. As shown in the figure, 20 GeV  
 1382        very nearly minimizes the  $\chi^2$ , while also being large enough that a sufficient number  
 1383        of  $ff$  events may be collected.

1384        Finally, a “pixel seed” is defined as a hit in the pixel detector consistent with a  
 1385        track extrapolated from the position of the ECAL SC back to the primary vertex.  
 1386        Real photons, having no charge and therefore no bending in the magnetic field, should  
 1387        not have a pixel seed.

### 1388 6.1.2 Electrons

1389 Electrons are reconstructed identically to photons, except that in the electron case  
 1390 the presence of a pixel seed is enforced, rather than vetoed.<sup>2</sup> Photons and electrons  
 1391 are defined by very similar criteria so that  $Z \rightarrow ee$  events can be used to model  
 1392 the QCD background in the two-photon sample without introducing any bias in the  
 1393 electron energy measurement (cf. Sec. 7.1).

### 1394 6.1.3 Jets and Missing Transverse Energy

#### 1395 Particle Flow

1396 In this analysis, jets and  $\cancel{E}_T$  are formed from *particle flow* (PF) candidates. The parti-  
 1397 cle flow algorithm [88, 89] uses information from all CMS subdetectors to reconstruct  
 1398 as accurately as possible the positions and momenta of all visible jet constituents,  
 1399 exploiting the fine granularity of the tracker and ECAL to achieve a greatly improved  
 1400 momentum resolution over calorimeter-only jets [90]. The PF algorithm is summa-  
 1401 rized below [91].

1402 1. Reconstruct the fundamental detector objects via iterative procedures

- 1403     • Tracks in the inner silicon layers
  - 1404         – High efficiency and low fake rate for charged hadrons in jets
  - 1405         – Relaxed primary vertex constraint allows photon conversions, parti-  
 1406             cles originating from nuclear interactions in the silicon, and long-lived  
 1407             particles to be reconstructed
- 1408     • Calorimeter clusters
- 1409     • Muon tracks in the outer muon layers

---

<sup>2</sup>In many CMS analyses, electrons are reconstructed very differently from photons. In particular, a special tracking algorithm [87] is used to best follow a radiating electron. However, in this analysis, the electron tracking is not used.

1410 2. Create a “block” of linked fundamental objects

- 1411 • Link silicon tracks to calorimeter clusters via  $\Delta R_{\text{track-cluster}}$  (account for  
1412 electron bremsstrahlung)
- 1413 • Link clusters in one calorimeter layer to clusters in a separate layer via  
1414  $\Delta R_{\text{cluster-cluster}}$
- 1415 • Link silicon tracks to muon tracks via global track  $\chi^2$

1416 3. ID the particles in the block

- 1417 • If global (silicon + muon layers) muon  $p_T$  is compatible with silicon track  
1418  $p_T$ , ID as a muon and remove corresponding tracks from block
- 1419 • ID electron tracks via special algorithm and removed all corresponding  
1420 tracks and cluster from block
- 1421 • Remove fake tracks from the block Fixed
- 1422 • Remove excess track-cluster links via  $\Delta R_{\text{track-cluster}}$  minimization (but al- typo  
1423 low multiple tracks to be associated to one cluster)
- 1424 • If the cluster energy is significantly larger then the energy of the linked  
1425 track, ID as a PF photon or PF neutral hadron and remove corresponding  
1426 clusters from the block
- 1427 • If the cluster is not linked to a track, ID as a PF photon or PF neutral  
1428 hadron and remove corresponding clusters from the block
- 1429 • Remaining track-cluster links are PF charged hadrons

1430 **Jets**

1431 PF candidates are clustered into jets by means of the anti- $k_T$  algorithm with  $R = 0.5$   
1432 [92]. In this algorithm, all possible pairs of PF candidates  $i, j$  are looped over, and  
1433 the momenta of the pair that minimize the distance variable

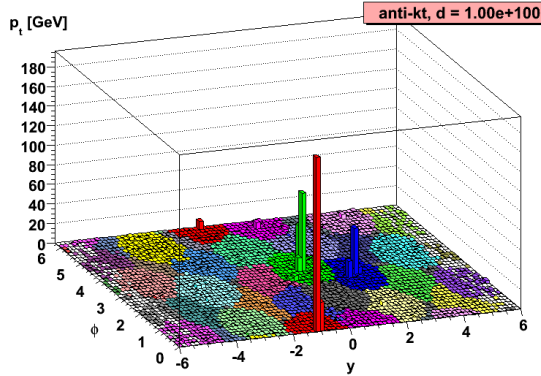


Figure 6.9: Example event display showing jets clustered via the anti- $k_T$  algorithm.  $y$  is pseudorapidity. Reprinted from slide 85 of ref. [93].

$$d_{ij} = \frac{\Delta R_{ij}^2}{R^2 \max(k_{Ti}^2, k_{Tj}^2)} \quad (6.4)$$

1434 are combined, where  $k_{Ti}$  is the transverse momentum of “combined” PF candidate  $i$ .  
 1435 The constituent PF candidates are clustered together. The process is repeated until  
 1436  $d_{ij} > 1/k_{Ti}^2$  for all pairs of clustered PF momenta [93]. An illustration is given in Fig-  
 1437 ure 6.9. The anti- $k_T$  algorithm is infrared and collinear safe, leading to well-behaved Added  
 1438 theoretical predictions and ease of comparison between data and MC simulation. It refer-  
 1439 also tends to form circular jets, making it easy for experimental effects such as ex- ence to  
 1440 pected out-of-cone energy and fiducial acceptance to be measured or simulated. For Fig. 6.9  
 1441 these reasons, the anti- $k_T$  jet clustering algorithm was chosen for this analysis.

1442 Once jets are clustered, they must be corrected for biases in the energy mea-  
 1443 surement due to non-compensation [94], invisible energy (lost to overcoming nuclear  
 1444 binding energy, in neutrinos, or in unclustered muons, for example) [94], detector  
 1445 geometry and cracks [95], zero suppression and trigger inefficiencies [96], pileup, and  
 1446 effects of the clustering algorithm [95]. Four multiplicative correction factors are ap-  
 1447 plied to the raw jet four-momentum  $p_\mu^{\text{raw}}$  [90]:

- 1448 •  $C_{\text{offset}}(p_T^{\text{raw}})$ , which accounts for extra energy due to noise, pileup, and the un-

1449 derlying event;

- 1450 •  $C_{\text{MC}}(C_{\text{offset}}p_T^{\text{raw}}, \eta)$ , which is derived from MC and accounts for most of the  $p_T$   
 1451 and  $\eta$  dependence;
- 1452 •  $C_{\text{rel}}(\eta)$ , which accounts for the remaining differences in uniformity over the  
 1453 entire calorimeter between data and MC; and
- 1454 •  $C_{\text{abs}}(C_{\text{rel}}C_{\text{MC}}C_{\text{offset}}p_T^{\text{raw}})$ , which accounts for the remaining differences in linear-  
 1455 ity over the full  $p_T$  range between data and MC.

1456 Figure 6.10 shows the total jet energy correction factor  $C_{\text{offset}}C_{\text{MC}}C_{\text{rel}}C_{\text{abs}}$  vs.  $\eta$   
 1457 for jets reconstructed with the anti- $k_T$  algorithm,  $R = 0.5$ . The PF jet corrections  
 1458 are more uniform across  $\eta$  than those of CALO jets (composed of simple calorimeter  
 1459 towers) or JPT jets (Jet Plus Tracks; composed of calorimeter energies replaced,  
 1460 where possible, with matching track  $p_T$ ) [97]. In addition, for  $p_T$  in the range 30-200  
 1461 GeV and  $|\eta|$  up to 2.0, the PF jet energy correction uncertainty is lower than that of  
 1462 the other two types of jets, and never exceeds  $\sim 3\%$  [90]. The superior performance  
 1463 of PF jets motivates their use in this search.

1464 In this analysis, candidate and QCD control events are binned by number of jets  
 1465 satisfying the criteria in Table 6.2.

## 1466 Missing Transverse Energy

1467 To be consistent with the jet reconstruction,  $\cancel{E}_T$  in this analysis is also reconstructed  
 1468 from PF candidates. Raw  $\cancel{E}_T$  is defined as

$$\cancel{E}_{T\text{raw}} = \left| - \sum_{i=1}^{n_{\text{PF}}} \vec{p}_{Ti} \right| \quad (6.5)$$

Table 6.2: Definition of HB/HE hadronic jets.

Variable	Cut
Algorithm	L1FastL2L3Residual corrected PF
$p_T$	$> 30 \text{ GeV}$
$ \eta $	$< 2.6$
Neutral hadronic energy fraction	$< 0.99$
Neutral electromagnetic energy fraction	$< 0.99$
Number of constituents	$> 1$
Charged hadronic energy	$> 0.0 \text{ GeV}$ if $ \eta  < 2.4$
Number of charged hadrons	$> 0$ if $ \eta  < 2.4$
Charged electromagnetic energy fraction	$< 0.99$ if $ \eta  < 2.4$
$\Delta R$ to nearest PF electron <sup>a</sup> , muon <sup>b</sup> , or one of the two primary EM objects	$> 0.5$

<sup>a</sup>A PF electron is defined as an electron reconstructed with the PF algorithm [85] with  $p_T > 15 \text{ GeV}$ ,  $|\eta| < 2.6$ , and  $(I_{\text{charged}} + I_{\text{photon}} + I_{\text{neutral}})/p_T < 0.2$ , where  $I_{\text{charged}}(I_{\text{photon}})(I_{\text{neutral}})$  is the sum of PF charged hadron(PF photon)(PF neutral hadron) momenta in a  $\Delta R = 0.4$  cone around the PF electron.

<sup>b</sup>Muons are reconstructed [86] from a combination of muon station and inner tracker hits. Here, a muon must have track  $\chi^2 < 10$ , at least one good muon station hit, inner track transverse impact parameter  $< 0.02 \text{ cm}$ , inner track longitudinal impact parameter  $< 0.5 \text{ cm}$ ,  $p_T > 15 \text{ GeV}$ ,  $|\eta| < 2.6$ , and  $(I_{\text{ECAL}} + I_{\text{HCAL}} + I_{\text{track}})/p_T < 0.2$ , where  $I_{\text{ECAL}}(I_{\text{HCAL}})(I_{\text{track}})$  is the sum of ECAL(HCAL)(track) momenta in a  $\Delta R = 0.3$  cone around the muon.

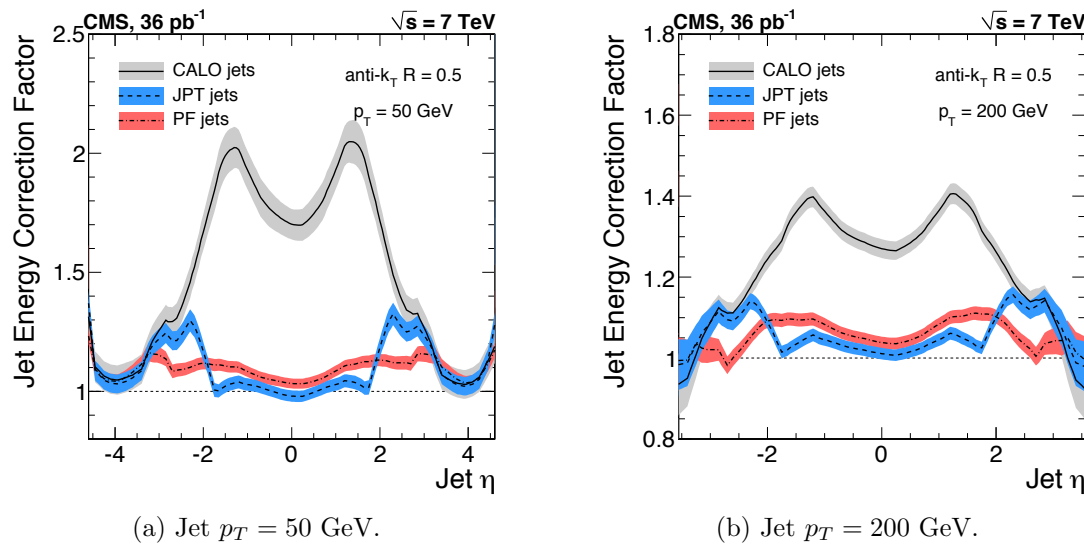


Figure 6.10: Total jet energy correction factor  $C_{\text{offset}}C_{\text{MC}}C_{\text{rel}}C_{\text{abs}}$  vs.  $\eta$ , including uncertainty band, for jets reconstructed with the anti- $k_T$  algorithm,  $R = 0.5$ . Reprinted from Fig. 26 of ref. [90].

where  $n_{\text{PF}}$  is the number of PF candidates in the event.  $\cancel{E}_{\text{raw}}$  may be corrected for the same effects that necessitate jet corrections, since  $\cancel{E}_{\text{raw}}$  is usually the result of jet mis-measurement (except, of course, in electroweak physics processes that include an energetic neutrino, or SUSY production). CMS *Type-I*  $\cancel{E}_T$  corrections simply involve replacing the PF jets with their corrected energies (cf. Sec 6.1.3) and recalculating  $\cancel{E}_T$ . Only jets with electromagnetic fraction (EMF) below 90% and  $p_T > 20 \text{ GeV}$  are replaced. This ensures that very electromagnetic jets (as well as isolated leptons, which also receive no correction), which consist chiefly of neutral pions and are measured accurately by the ECAL, do not receive a correction derived for jets with a large fraction of their energy in charged hadrons. In addition, the  $p_T$  cut guarantees that jet corrections are only applied where they are known to within a few percent. For this search, the level of agreement between the SM background estimate and the two-photon search sample in a low- $\cancel{E}_T$  control region is the same regardless of whether the  $\cancel{E}_T$  is corrected or not, so for simplicity the Type-I  $\cancel{E}_T$  corrections are not used (see Sec. ??).

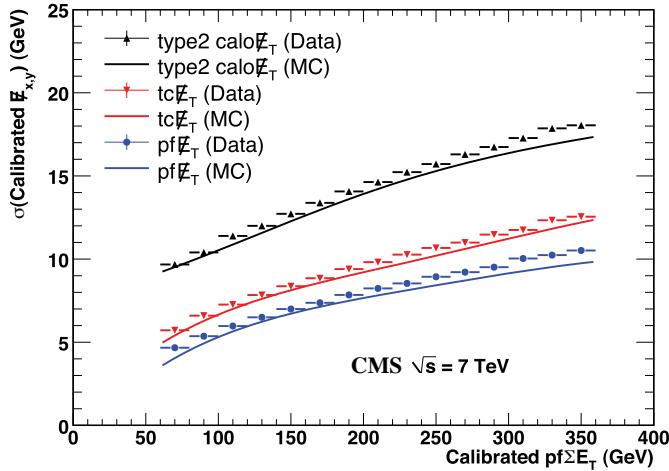


Figure 6.11:  $\sigma$  of a Gaussian fit to the x- and y-components of calibrated  $E_T$  vs. the calibrated PF  $E_T$  sum in a sample of events containing at least two jets with  $p_T > 25$  GeV.  $\sigma$  is calibrated such that the  $E_T$  scale is equal for all three algorithms. PF  $\sum E_T$  is corrected, on average, to the particle level using a Pythia v8 simulation [98]. The blue markers (data) and line (MC) refer to PF jets. Reprinted from Fig. 13 of ref. [96].

1484     Figure 6.11 shows the  $\sigma$  of a Gaussian fit to the x- and y-components of calibrated  
 1485      $E_T$  vs. the calibrated PF  $E_T$  sum in a sample of events containing at least two jets  
 1486     with  $p_T > 25$  GeV. Again, PF  $E_T$  outperforms  $E_T$  constructed of calorimeter towers  
 1487     or track-corrected calorimeter deposits.

## 1488     6.2    HLT

1489     From the objects described in Sec. 6.1, four samples of events are formed:

- 1490       •  $\gamma\gamma$  candidate sample, in which the two highest  $E_T$  objects are photons,
- 1491       •  $e\gamma$  control sample, in which the two highest  $E_T$  objects are one electron and  
           one photon,
- 1493       •  $ee$  control sample, in which the two highest  $E_T$  objects are electrons, and
- 1494       •  $ff$  control sample, in which the two highest  $E_T$  objects are fakes.

1495 In all samples, the leading EM object is required to have  $E_T > 40$  GeV, while the  
1496 trailing EM object is required to have  $E_T > 25$  GeV. The high level triggers used to  
1497 select the four samples, by run range, are listed in Table 6.3. No trigger is prescaled.

Table 6.3: HLT paths triggered by the  $\gamma\gamma$ ,  $e\gamma$ ,  $ee$ , and  $ff$  samples, by run range. No triggers are prescaled.

Run range	$\gamma\gamma$	$e\gamma$	$ee$	$ff$
160404-163261	Photon26_ IsoVL_ Photon18	Photon26_ IsoVL_ Photon18	Photon26_ IsoVL_ Photon18	Photon26_ IsoVL_ Photon18
161216-166967	Photon36_ CaloIdL_ Photon22_ CaloIdL	Photon36_ CaloIdL_ Photon22_ CaloIdL	Photon36_ CaloIdL_ Photon22_ CaloIdL	Photon36_ CaloIdL_ Photon22_ CaloIdL
166347-180252	Photon36_ CaloIdL_ IsoVL_ Photon22_ CaloIdL_ IsoVL	Photon36_ CaloIdL_ IsoVL_ Photon22_ CaloIdL_ IsoVL	Photon36_ CaloIdL_ IsoVL_ Photon22_ R9Id	Photon36_ CaloIdL_ IsoVL  Photon36_ CaloIdL_ IsoVL  Photon36_ R9Id_ Photon22_ CaloIdL_ IsoVL  Photon36_ R9Id_ Photon22_ R9Id

1498 Each piece of the HLT path name is defined as follows.

1499 • Photon: Energy deposit in the ECAL that fired an L1 trigger (cf. Sec. 5.2.1).

1500 For Photon26\_IsoVL\_Photon18, the L1 seed  $E_T$  threshold is 12 GeV, while for Switched  
 1501 all other triggers in Table 6.3 it is 20 GeV (cf. Sec. 5.2.1). HLT  
 1502 • Integer following the word **Photon**:  $E_T$  threshold in GeV for offline reconstructed path  
 1503 photon, using the full photon reconstruction of Sec. 6.1.1 minus the laser cali- names  
 1504 brations and assuming the primary vertex at (0, 0, 0). to ver-  
 1505 • **CaloIdL**: For EB photons,  $H/E < 0.15$  and  $\sigma_{inj} < 0.014$ . batim  
 1506 • **IsoVL**:  $I_{ECAL} < 0.012E_T + 6$  GeV,  $I_{HCAL} < 0.005E_T + 4$  GeV, and  $I_{track} <$  font and  
 1507  $0.002E_T + 4$  GeV. added  
 1508 • **R9Id**:  $R9 > 0.8$ . reference  
 1509 In addition, the versions of **HLT\_Photon26\_IsoVL\_Photon18** and to L1  
 1510 **Photon36\_CaloIdL\_Photon22\_CaloIdL** that were active during runs 160404-163268 section  
 1511 included a cut  $E_{max}/E_{5\times5} < 0.98$  for spike rejection.  $E_{max}$  is the energy in the Switched  
 1512 highest HLT path energy crystal of the EM cluster and  $E_{5\times5}$  is the energy in the 5×5 crystal matrix names  
 1513 around the seed crystal. For runs after 163268, Swiss cross spike rejection of individual to ver-  
 1514 crystals from HLT quantities was performed (cf. Sec. 6.1.1). All information about the batim  
 1515 evolution of the CMS HLT settings can be found in the HLT configuration browser font  
 1516 at <http://j2eeps.cern.ch/cms-project-confdb-hltdev/browser/>. Switched  
 1517 As an example of the naming convention just described, the HLT path HLT  
 1518 **Photon36\_CaloIdL\_IsoVL\_Photon22\_R9Id** is fired if one photon is found with  $E_T >$  path  
 1519 36 GeV passing the **CaloIdL** and **IsoVL** requirements, and another is found with names  
 1520  $E_T > 22$  GeV passing the **R9Id** requirement. to ver-  
 1521 For the offline  $E_T$  cuts described in this section, the triggers are > 99% efficient, batim  
 1522 as shown in Figure 6.12 [84]. The efficiencies are measured with respect to triggers font  
 1523 with lower  $E_T$  thresholds. Added  
 1524 HLT ef-  
 1525 ficiency  
 1526 discus-  
 1527 sion

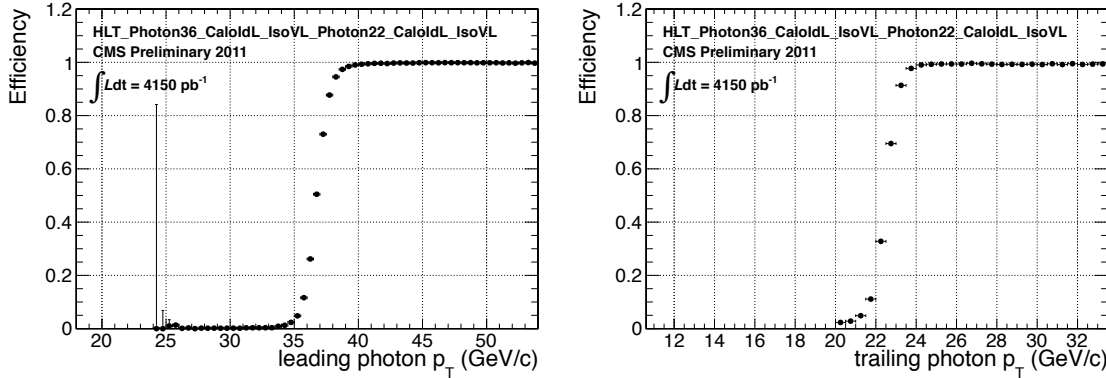


Figure 6.12: Efficiency of HLT\_Photon36\_CaloIdL\_IsoVL\_Photon22\_CaloIdL\_IsoVL for offline selected leading photon (left) and trailing photon (right) vs. photon  $p_T$ . Reprinted from Fig. 2 of ref. [84].

### 1524 6.3 Event Quality

1525 To suppress instrumental backgrounds, a set of event quality cuts are applied to the  
 1526  $\gamma\gamma$ ,  $e\gamma$ ,  $ee$ , and  $ff$  samples. First, all events are required to pass a good run selec-  
 1527 tion, as determined by the CMS Physics Validation Team (<https://twiki.cern.ch/twiki/bin/view/CMS/PVTMain>, CERN computing ID needed). The good run selec-  
 1528 tion excludes luminosity sections during which a sufficient part of the CMS detector  
 1529 was unpowered or malfunctioning. Such conditions could occur if, for example, a high  
 1530 voltage supply trips off in the middle of a run, or a DAQ error corrupts data quality  
 1531 but is not spotted until after the data have been collected. The severity of a detec-  
 1532 tor problem is judged by its effect on a wide range of analyses and reconstruction  
 1533 algorithms. Of the  $\sim 5 \text{ fb}^{-1}$  of integrated luminosity delivered by the LHC in 2011,  
 1534  $4.68 \text{ fb}^{-1}$  passed the good run selection. This analysis is performed on the entire 2011  
 1535 certified dataset.

1537 Second, all events must contain at least one good interaction vertex. The criteria  
 1538 for a good vertex are:

- 1539 •  $\chi^2 \neq 0 \parallel \text{ndof} \neq 0 \parallel N_{\text{tracks}} \neq 0$ , where  $\chi^2$  and ndof are calculated for the track  
 1540 fit to the vertex, and  $N_{\text{tracks}}$  is the number of tracks in the vertex fit

- 1541     •  $\text{ndof} > 4$
- 1542     •  $|z| < 24 \text{ cm}$ , where  $z$  is the  $z$ -coordinate of the vertex position
- 1543     •  $|\rho| < 2 \text{ cm}$ , where  $\rho$  is the transverse displacement of the vertex position from
- 1544       the beam line

1545   The good vertex requirement eliminates non-collision backgrounds such as beam  
 1546   scraping, beam halo, cosmic muon interactions, and instrumental effects.

1547   Third, the two electromagnetic objects in the  $\gamma\gamma$ ,  $e\gamma$ ,  $ee$ , and  $ff$  events must  
 1548   be separated in  $\phi$  by at least 0.05. This requirement protects against beam halo  
 1549   bremsstrahlung, in which a halo muon traveling parallel to the beam line radiates an  
 1550   energetic photon while itself depositing a large amount of energy in the ECAL. In  
 1551   this case, the two ECAL hits would likely be at the same  $\phi$  (and  $\rho$ ).

1552   Fourth, the two EM objects must be separated in  $R$  by at least 0.6. Since the  
 1553   isolation cone size used is 0.3, this ensures that the isolation energy of one EM object  
 1554   cannot be in the veto strip (Fig. 6.5) of the other.

1555   Finally, the  $\gamma\gamma$ ,  $e\gamma$ ,  $ee$ , and  $ff$  events must pass an HCAL noise filter and ECAL  
 1556   dead channel filter. The HCAL noise filter guarantees that all HCAL reconstructed  
 1557   hits are inconsistent with any noise source. Noise sources [99] include:

- 1558     • Ion feedback in the HPDs absent any true incident photons, in which a thermal  
 1559       electron ionizes a molecule in the HPD acceleration gap, faking a real signal
- 1560     • HPD discharge affecting nearly all channels in the same HPD [100], partially  
 1561       explained by the effect of the 4 T CMS magnetic field on the flashover voltage  
 1562       of the dielectric [102]
- 1563     • Concurrent signals in nearly all 72 channels of a single RBX, as yet unexplained
- 1564     • HF PMT window hits (as opposed to the usual quartz fiber hits)

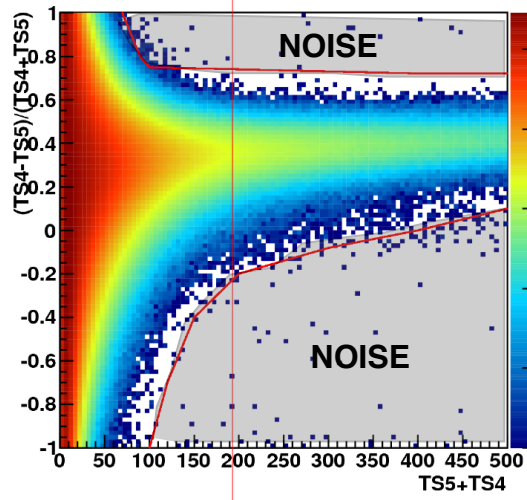


Figure 6.13:  $(TS4 - TS5)/(TS4 + TS5)$  vs.  $TS4 + TS5$  for a minimum bias sample. HB/HE hits are considered noisy if they lie in the sparsely populated gray region labeled "NOISE" defined by the curved red lines. Adapted from ref. [101].

- 1565        • ADC saturation

1566     Since HCAL noise may induce fake jets or  $E_T$ , events are rejected if any of the  
1567     following criteria are true:

- 1568        • Any HPD has  $> 17$  hits

- 1569        • A single HPD has  $> 10$  hits, but every other HPD has zero hits

- 1570        • An RBX has  $> 10$  zero-ADC-count hits

1571        • Any HB/HE reconstructed hit corresponding to an RBX with  $> 50$  GeV of  
1572        energy fails a two-dimensional cut defined by the variables  $(TS4 - TS5)/(TS4 +$   
1573         $TS5)$  vs.  $TS4 + TS5$ , where  $TS4(TS5)$  is the hit amplitude in the fourth(fifth)  
1574        time sample read out for that hit. The cut is defined in Fig. 6.13.

1575     The ECAL dead channel filter is designed to flag events in which significant EM  
1576     energy was deposited in a masked region of the ECAL by using the trigger primitive  
1577     information for the corresponding trigger tower. Energy deposited in a masked region

1578 of ECAL can cause fake  $E_T$ . Events are rejected if the trigger primitive  $E_T$  exceeds  
 1579 the maximum value of 63.75 GeV in any trigger tower that is masked in the readout.

## 1580 6.4 Photon Identification Efficiency

1581 In order to determine the cross section (or cross section upper limit) for a GGM  
 1582 signal, the photon identification efficiency is needed. Since no suitably large sample  
 1583 of  $Z \rightarrow \mu\mu\gamma$  events in CMS exists yet, the efficiency calculation relies on the similarity  
 1584 between detector response to electrons and photons. A scale factor to correct the MC  
 1585 photon ID efficiency to the real photon efficiency for the data is obtained from the  
 1586 ratio of the electron efficiency from the data to the electron efficiency from MC.  
 1587 The different types of photon ID variables—calorimeter and track isolation, ratio of ~~Removed~~  
 1588 hadronic to electromagnetic energy of the shower, and transverse shower shape—are ~~refer-~~  
 1589 chosen so that their distributions for isolated electrons and photons are similar.<sup>3</sup> ~~ence to~~  
 1590 The photon selection efficiency is ~~plots~~

$$\epsilon_\gamma = \epsilon_\gamma^{\text{MC}} \times \frac{\epsilon_e^{\text{data}}}{\epsilon_e^{\text{MC}}} \quad (6.6)$$

1591 where

- 1592 •  $\epsilon_\gamma$  is the photon ID efficiency in data,
- 1593 •  $\epsilon_\gamma^{\text{MC}}$  is the photon ID efficiency in MC,
- 1594 •  $\epsilon_e^{\text{data}}$  is the electron ID efficiency obtained using  $Z \rightarrow ee$  electrons in the data  
 1595 that satisfy the photon ID cuts, and

---

<sup>3</sup> $R9$  differs between photons and radiating electrons, but the requirement  $R9 < 1$  is loose enough not to introduce problems with the use of electrons to measure the photon ID efficiency.

- 1596     •  $\epsilon_e^{\text{data}}$  is the electron ID efficiency obtained using  $Z \rightarrow ee$  electrons in MC that  
 1597        satisfy the photon ID cuts.

1598     The ratio  $\epsilon_e^{\text{data}}/\epsilon_e^{\text{MC}}$  is defined as the scale factor by which the GGM signal MC  
 1599    photon ID efficiency must be multiplied to give an estimate of the photon ID efficiency  
 1600    in data. The photon ID requirements of Table 6.1 plus the IsoVL HLT requirement  
 1601    described in Sec. 6.2 and Table 6.3 are repeated in Table 6.4.

Table 6.4: Candidate photon ID requirements.

Variable	Cut
$I_{\text{ECAL}}$	$< 0.012E_T + 6 \text{ GeV}$
$I_{\text{HCAL}}$	$< 0.005E_T + 4 \text{ GeV}$
$I_{\text{track}}$	$< 0.002E_T + 4 \text{ GeV}$
$H/E$	$< 0.05$
$\sigma_{i\eta i\eta}$	$< 0.011$
$I_{\text{ECAL}} - 0.0792\rho + I_{\text{HCAL}} - 0.0252\rho + I_{\text{track}}$	$< 6 \text{ GeV}$
$R9$	$< 1$

#### 1602 6.4.1 Tag and Probe Method

1603   A *Z tag and probe* method is utilized to measure the efficiency of the photon ID  
 1604   cuts in Table 6.1. The tag is a well-identified electron. The probe, by contrast, is as  
 1605   loosely identified as possible, and all tags must pass the probe criteria in addition to  
 1606   the stringent tag criteria. The tag and probe criteria used in this study are shown in  
 1607   Table 6.5.

1608     The invariant mass of the tag and probe are required to be within a narrow window  
 1609    around  $Z$  mass. Assuming that the probabilities of the tag and probe legs of the  $Z$   
 1610    decay to pass the photon ID cuts are uncorrelated, the efficiency can be estimated as

$$\epsilon = \frac{N_{\text{tag-pass}}}{N_{\text{tag-pass}} + N_{\text{tag-fail}}} \quad (6.7)$$

Table 6.5: Tag and probe criteria. The superscript 0.4 indicates that the isolation variable was calculated in a cone of  $\Delta R = 0.4$  around the photon candidate. The isolations without superscripts use the standard  $\Delta R = 0.3$  cones.

Variable	Cut	
	Tag	Probe
RECO object	photon	photon
HLT	HLT_Ele17_CaloIdVT_CaloIsoVT_TrkIdT_TrkIsoVT_SC8_Mass30_v* (must have fired the 17 GeV leg)	—
$H/E$	$< 0.05$	$< 0.15$
$I_{\text{ECAL}}^{0.4}$	$< 0.006E_T + 4.2 \text{ GeV}$	—
$I_{\text{HCAL}}^{0.4}$	$< 0.0025E_T + 2.2 \text{ GeV}$	—
$I_{\text{track}}^{0.4}$	$< 0.001E_T + 2.0 \text{ GeV}$	—
$E_T$	$> 25 \text{ GeV}$	—
SC $E_T$	—	$> 15 \text{ GeV}$
SC $ \eta $	$< 1.4442$	$< 1.4442$
$\sigma_{i\eta i\eta}$	$< 0.009$	—
Has pixel seed	Yes	—
Track match type	General track <sup>a</sup>	—
Track match $\Delta R$	$< 0.04$	—
Track match $p_T$	$> 15 \text{ GeV}$	—
Track match $ \eta $	$< 1.479$	—

<sup>a</sup>A general track is reconstructed with the CMS standard combinatorial track finder [103].

1611 where  $N_{\text{tag-pass}}$  is the number of tag-probe pairs in which the probe leg passes the  
 1612 photon ID cuts under study and  $N_{\text{tag-fail}}$  is the number of tag-probe pairs in which  
 1613 the probe leg fails the cuts. Implicit in these definitions is a double counting of pairs  
 1614 in which both electrons pass the tag and probe criteria [104]. In addition, in the rare  
 1615 circumstance (less than 1% in MC [104]) that two or more probes may be matched  
 1616 to one tag, the pair with invariant mass closest to the  $Z$  mass is chosen.

1617 In practice,  $N_{\text{tag-pass}}$  and  $N_{\text{tag-fail}}$  are returned by a simultaneous unbinned maxi-  
 1618 mum likelihood fit to the invariant mass distributions of tag-pass and tag-fail events,  
 1619 with appropriate signal and background PDF assumptions. The fit form used is

$$\begin{aligned} f_{\text{tag-pass}}(m_{\text{tag-pass}}) &= \epsilon N_S f_S^{\text{pass}}(m_{\text{tag-pass}}) + N_B^{\text{pass}} f_B^{\text{pass}}(m_{\text{tag-pass}}) \\ f_{\text{tag-fail}}(m_{\text{tag-fail}}) &= (1 - \epsilon) N_S f_S^{\text{fail}}(m_{\text{tag-fail}}) + N_B^{\text{fail}} f_B^{\text{fail}}(m_{\text{tag-fail}}) \end{aligned} \quad (6.8)$$

1620 where  $f_{\text{tag-pass}}(m_{\text{tag-pass}})$  and  $f_{\text{tag-fail}}(m_{\text{tag-fail}})$  are the tag-pass and tag-fail PDFs,  
 1621 respectively;  $\epsilon$  is the efficiency;  $N_S$  is the total number of  $Z$  signal events summed over  
 1622 both samples;  $f_S^{\text{pass}}(m_{\text{tag-pass}})$  and  $f_S^{\text{fail}}(m_{\text{tag-fail}})$  are the tag-pass and tag-fail signal  
 1623 PDFs, respectively;  $N_B^{\text{pass}}$  and  $N_B^{\text{fail}}$  are the numbers of background events in the tag-  
 1624 pass and tag-fail samples, respectively; and  $f_B^{\text{pass}}(m_{\text{tag-pass}})$  and  $f_B^{\text{fail}}(m_{\text{tag-fail}})$  are the  
 1625 tag-pass and tag-fail background PDFs, respectively. This particular implementation  
 1626 of the tag and probe methodology is based on tag `CMSSW_4_2_5` of the CMSSW  
 1627 package `PhysicsTools/TagAndProbe`, and uses the MINUIT2 [105] library, as coded  
 1628 in RooFit [106], for the likelihood maximization. For this study, CMSSWv4.2.8 was  
 1629 used.

1630 For both samples, the signal shape is assumed to be a Crystal Ball function [107]  
 1631 convoluted with the  $Z$  generated lineshape, while the background shape is a PDF  
 1632 that describes the falling background as well as the kinematic turn-on at low invariant

1633 mass. The background PDF, called `RooCMSShape` [104], is given by

$$f_{\text{RooCMSShape}}(x) = \begin{cases} 1e20 & \text{for } (x - \mu)\gamma < -70 \\ 0 & \text{for } (x - \mu)\gamma > 70 \\ \text{erfc}((\alpha - x)\beta) \exp(-(x - \mu)\gamma) & \text{otherwise} \end{cases} \quad (6.9)$$

1634 where  $\alpha$ ,  $\beta$ ,  $\gamma$ , and  $\mu$  are parameters of the fit, most of which are held fixed. In the  
 1635 three lowest  $E_T$  bins, all parameters of the tag-pass and tag-fail background PDFs  
 1636 are left floating, because the effect of the relaxed  $E_T$  cuts has a significant effect on  
 1637 the background shape. More details of the signal and background PDFs are given  
 1638 in Table 6.6. The fixed signal and background parameter values were determined by  
 1639 fitting a small sample ( $0.0 \leq \eta < 0.25$ ) of `Fall11 MC signal (DYJetsToLL)` and back-  
 1640 ground (`QCD_Pt-20to30_BCToE`, `QCD_Pt-30to80_BCToE`, `QCD_Pt-80to170_BCToE`,  
 1641 `GJet_Pt-20_doubleEMEnriched`, `WJetsToLNu`, `TTJets`) with parameters left float-  
 1642 ing.<sup>4</sup>

Added

1643 Some fit examples are shown in Figures 6.14 and 6.15. In Fig. 6.14, which shows fits  
 1644 fits to data and MC for  $15 \text{ GeV} \leq \text{probe } E_T < 20 \text{ GeV}$ , the kinematic turn-on is below  
 1645 the invariant mass range covered by the plot. The exponentially falling background  
 1646 is easily seen underneath the signal, and is especially pronounced in the background-  
 1647 dominated tag-fail sample.

#### 1648 6.4.2 Photon Efficiency Scale Factor $\epsilon_e^{\text{data}}/\epsilon_e^{\text{MC}}$

1649 Figure 6.16 shows the dependence of the photon ID efficiency scale factor  $\epsilon_e^{\text{data}}/\epsilon_e^{\text{MC}}$   
 1650 on  $E_T$ ,  $\eta$ , and  $N_{\text{jet}}$ , where jets are defined as in Table 6.2, but with only the two  
 1651  $Z$  electrons considered as candidates for overlap removal. Errors are statistical only.

---

<sup>4</sup>See Appendix A for a discussion of the MC samples.

Table 6.6: Parameter values (parameter definitions are in the text) for the signal and background PDFs for the different samples. The background PDF applies to all efficiency bins except the four lowest  $E_T$  bins, which use a floating `RooCMSShape` background. When a bracketed range is given, the parameter is allowed to float within that range. When a constant is given, the parameter is fixed to that constant.

PDF	Crystal Ball fit parameters				RooCMSShape fit parameters			
	$\mu$	$\sigma$	$\alpha$	n	$\mu$	$\alpha$	$\beta$	$\gamma$
Tag-pass signal	[-1.0, 1.0]	[1.0, 3.0]	0.87	97.0	N/A	N/A	N/A	N/A
Tag-fail signal	[-1.0, 1.0]	[1.0, 3.0]	0.73	134.9	N/A	N/A	N/A	N/A
Tag-pass background	N/A	N/A	N/A	N/A	65.0	61.949	0.04750	0.01908
Tag-fail background	N/A	N/A	N/A	N/A	$\alpha$	[50.0, 100.0]	0.065	0.048

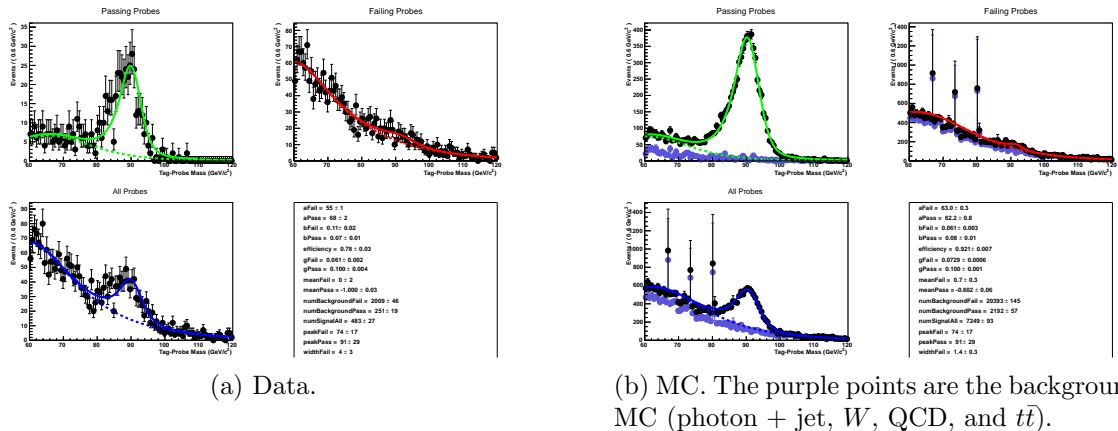


Figure 6.14: Tag and probe invariant mass fits for  $15 \text{ GeV} \leq \text{probe } E_T < 20 \text{ GeV}$ . Errors are statistical only. The tag-pass fit is shown in green, the tag-fail fit in red, and a fit to both samples in blue. Dotted lines are the background components of the fits; solid lines are signal plus background.

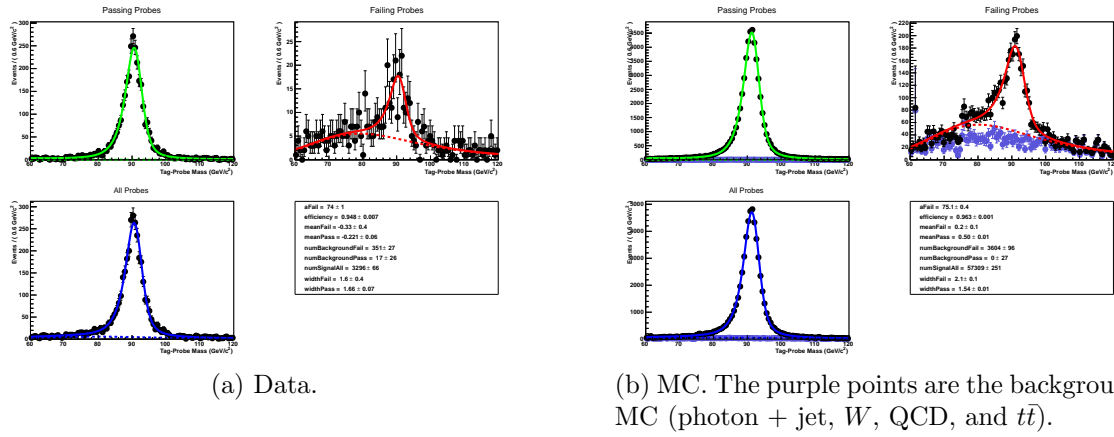


Figure 6.15: Tag and probe invariant mass fits for  $-0.25 \leq \text{probe } \eta < -0.5$ . Errors are statistical only. The tag-pass fit is shown in green, the tag-fail fit in red, and a fit to both samples in blue. Dotted lines are the background components of the fits; solid lines are signal plus background.

1652 There no significant dependence of the scale factor on these variables, so only one  
1653 scale factor is computed from the entire dataset.

1654 The effect of pileup is studied by comparing the efficiencies  $\epsilon_e^{\text{data}}$  and  $\epsilon_e^{\text{MC}}$  vs. the  
1655 number of primary vertices ( $N_{\text{PV}}$ ) in the event. The efficiency only drops a few percent  
1656 for events with large  $N_{\text{PV}}$  after using pileup-corrected isolation cuts, as can be seen in  
1657 Figure 6.17a. The MC tracks the data, and the scale factor is flat vs.  $N_{\text{PV}}$ , as shown  
1658 in Fig. 6.17b.

1659 The scale factor is measured to be  $\epsilon_e^{\text{data}}/\epsilon_e^{\text{MC}} = 0.994 \pm 0.002(\text{stat.}) \pm 0.035(\text{syst.})$ .  
1660 Four main sources of systematic error, in addition to the statistical error of 0.2%, were  
1661 studied.

1662 **Different behavior of electrons and photons in MC** Even though the photon  
1663 ID cuts are designed to be similarly efficient for both electrons and photons,  
1664 there might be a small difference in the performance between the two kinds  
1665 of particles, e.g. because of electron bremsstrahlung. To check this effect, the  
1666 MC electron ID efficiency was calculated using a  $Z \rightarrow ee$  sample and the MC  
1667 photon ID efficiency was calculated using a  $\gamma + \text{jets}$  sample. Both samples were

Official  
result  
uses this  
syst.  
error, so  
I am not  
recheck-  
ing  
it

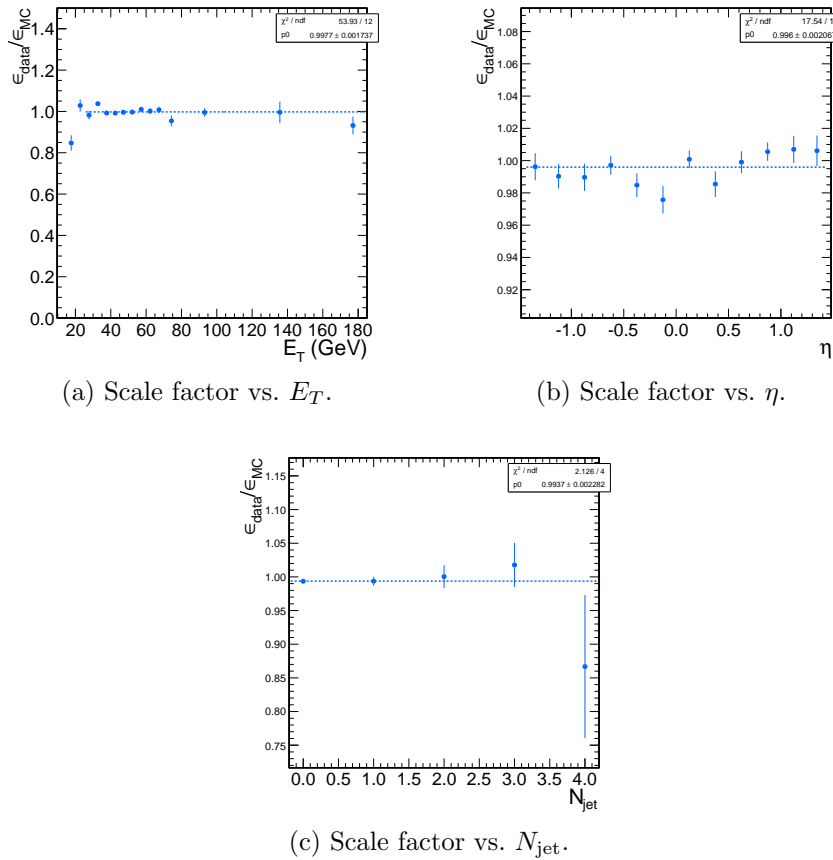


Figure 6.16: Dependence of the photon ID efficiency scale factor on some kinematic variables. Errors are statistical only.

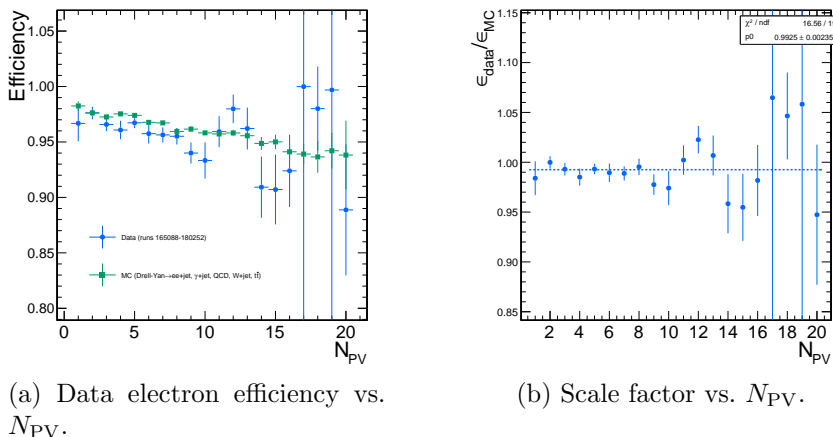


Figure 6.17: Dependence of the photon ID efficiency scale factor on the number of primary vertices per event. Errors are statistical only.

1668 reconstructed in CMSSWv3.6. Half the difference between these two results,  
 1669 0.5%, was taken as an error on the scale factor.

Corrected

1670 **Pileup** To account for the possibility that the MC simulation may not adequately some of  
 1671 reproduce the data in a high pileup environment, the data/MC scale factor these  
 1672 for events with 1-4 good reconstructed primary vertices was calculated, along bullets  
 1673 with the same for events with  $\geq 5$  good reconstructed primary vertices. The  
 1674 difference between the scale factors from both samples, 2.4%, was taken as an  
 1675 error on the scale factor from pileup.

1676 **Signal fit over/underestimation** It was found that the signal fit slightly under-  
 1677 estimates the data in the tag-pass sample, and slightly overestimates it in the  
 1678 tag-fail sample. To cover this effect with a systematic error, the efficiencies in  
 1679 data and MC, and then the scale factor, were recalculated using the background  
 1680 (from fit) subtracted integrals of the tag-pass and tag-fail distributions, rather  
 1681 than the fitted signal yields in those distributions. The difference between the  
 1682 scale factor found in this way and the nominal scale factor, 1.9%, was taken as  
 1683 an error on the scale factor.

1684 **Signal and background shape assumption** To assess the magnitude of the error  
 1685 from the signal and background shape assumptions, the tag-pass and tag-fail  
 1686 tail parameters (Crystal Ball  $\alpha$  and  $n$ ) were varied by  $\pm 1\sigma$ , and the background  
 1687 shape was varied between `RooCMSShape`, exponential, power law, and quadratic.  
 1688 All possible combinations of varied parameters were generated, and the data and  
 1689 MC were refit and new scale factors generated according to those combinations.  
 1690 The error was taken as the largest deviation of the scale factor from nominal,  
 1691 1.8%.

1692 Finally, the pixel veto efficiency was estimated from MC to be  $0.96 \pm 0.005$ (syst.),  
 1693 with error due to varying assumptions of the tracker material distribution [108].

1694

# Chapter 7

1695

## Data Analysis

1696 The signature of GGM SUSY particle production in this search is an excess of two-  
1697 photon events with high  $\cancel{E}_T$ .  $\cancel{E}_T$  is reconstructed using the particle flow algorithm  
1698 as described in Sec. 6.1.3. Candidate two-photon events, as well as control events,  
1699 are selected according to the offline object criteria presented in Secs. 6.1.1, 6.1.2,  
1700 and 6.1.3; the event quality criteria in Sec. 6.3; and the trigger requirements in Sec. 6.2.  
1701 These are summarized in Table 7.1.

Table 7.1: Selection criteria for  $\gamma\gamma$ ,  $e\gamma$ ,  $ee$ , and  $ff$  events.

Variable	Cut			
	$\gamma\gamma$	$e\gamma$	$ee$	$ff$
HLT match	IsoVL	IsoVL	IsoVL	IsoVL    R9Id
$E_T$	$> 40/ > 25 \text{ GeV}$			
$\text{SC }  \eta $	$< 1.4442$	$< 1.4442$	$< 1.4442$	$< 1.4442$
$H/E$	$< 0.05$	$< 0.05$	$< 0.05$	$< 0.05$
$R9$	$< 1$	$< 1$	$< 1$	$< 1$
Pixel seed	No/No	Yes/No	Yes/Yes	No/No
$I_{\text{comb}}, \sigma_{inj\eta}$	$< 6 \text{ GeV} \&& < 0.011$	$< 6 \text{ GeV} \&& < 0.011$	$< 6 \text{ GeV} \&& < 0.011$	$< 20 \text{ GeV} \&& (\geq 6 \text{ GeV} \parallel \geq 0.011)$
JSON	Yes	Yes	Yes	Yes
No. good PVs	$\geq 1$	$\geq 1$	$\geq 1$	$\geq 1$
$\Delta R_{\text{EM}}$	$> 0.6$	$> 0.6$	$> 0.6$	$> 0.6$
$\Delta\phi_{\text{EM}}$	$\geq 0.05$	$\geq 0.05$	$\geq 0.05$	$\geq 0.05$

1702 This search utilizes  $4.7 \text{ fb}^{-1}$  of CMS data collected during the period April  
 1703 December 2011, corresponding to the following datasets [109]:

- 1704 • /Photon/Run2011A-05Jul2011ReReco-ECAL-v1/AOD
- 1705 • /Photon/Run2011A-05Aug2011-v1/AOD
- 1706 • /Photon/Run2011A-03Oct2011-v1/AOD
- 1707 • /Photon/Run2011B-PromptReco-v1/AOD

1708 The search strategy is to model the backgrounds to the GGM SUSY signal using  
 1709  $\cancel{E}_T$  shape templates derived from the control samples, and then to look for a high- $\cancel{E}_T$   
 1710 excess above the estimated background in the  $\gamma\gamma$  sample. There are two categories  
 1711 of backgrounds: QCD processes with no real  $\cancel{E}_T$  and electroweak processes with real  
 1712  $\cancel{E}_T$  from neutrinos. The relevant QCD background processes are multijet production  
 1713 with at least two jets faking photons, photon + jet production with at least one jet  
 1714 faking a photon, and diphoton production, and  $Z$  production with a radiated photon  
 1715 where at least one of the  $Z$  decay products (typically a jet) fakes a photon. The  
 1716 relevant electroweak background processes, which are small compared to the QCD  
 1717 background, involve  $W \rightarrow e\nu$  decay with a recoiling jet that fakes a photon or a  
 1718 real radiated photon (the  $W$  may come from the decay of a top quark in  $t\bar{t}$  events).  
 1719 In both cases, the electron is misidentified as a photon due to a small inefficiency  
 1720 in reconstructing the electron pixel seed. The main diagrams contributing to the  
 1721 QCD(electroweak) backgrounds are shown in Figure 7.1(7.2).

1722 Data control samples are used to model all of the backgrounds. The primary  
 1723 control sample used to model the QCD background is the  $ff$  sample, which is similar  
 1724 to the candidate  $\gamma\gamma$  sample but with combined isolation or  $\sigma_{inj\eta}$  cuts inverted. The cuts  
 1725 on these variables are used to distinguish between photons and jets, so by inverting  
 1726 those cuts, the resulting  $ff$  sample becomes enriched with QCD dijets. Because the

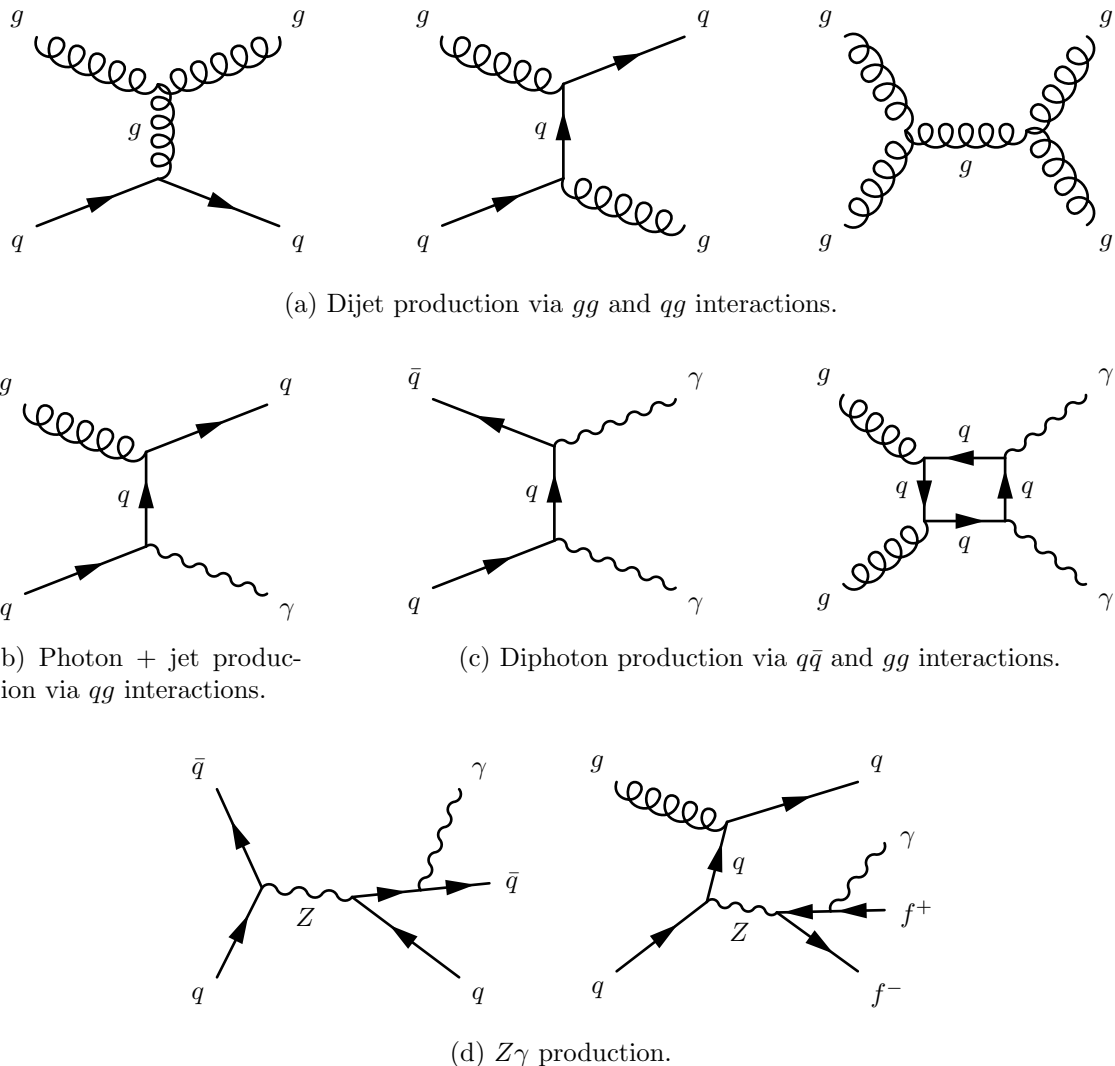


Figure 7.1: Representative Feynman diagrams of some QCD backgrounds to the GGM SUSY search.

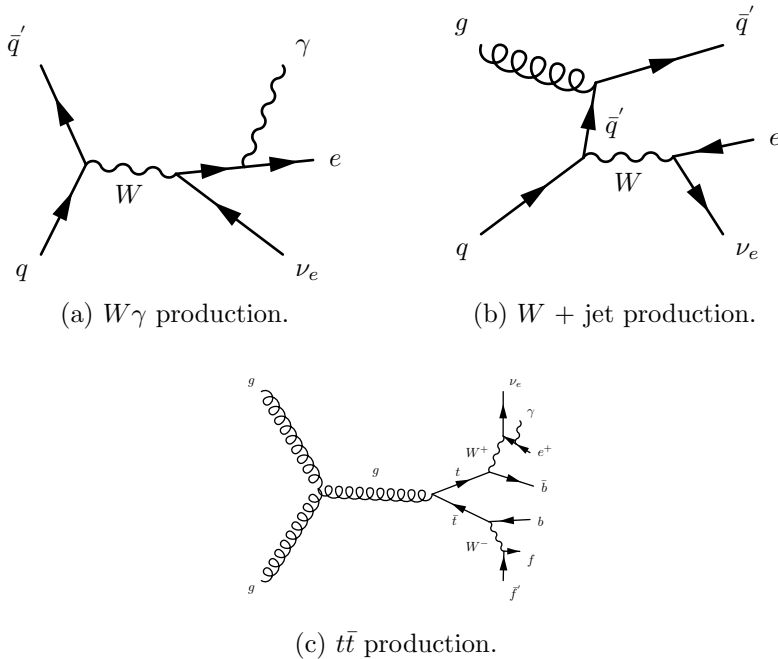


Figure 7.2: Representative Feynman diagrams of some electroweak backgrounds to the GGM SUSY search.

fake photons are still required to pass a tight cut on  $H/E$ , they are guaranteed to be very electromagnetic jets, with an EM energy scale and resolution similar to that of the candidate photons. This insures that the resulting estimate of the  $\cancel{E}_T$  shape does not have too long of a tail from severe HCAL mis-measurements that are actually rare in the  $\gamma\gamma$  sample.

As a cross-check, the  $ee$  sample is also used to model the QCD background. This sample of  $Z$  decays should have no true  $\cancel{E}_T$ , just like the  $ff$  sample, and the electron definition (differing from the photon definition only in the presence of a pixel seed) insures that the electron energy scale and resolution is similar to that of the photon.

Finally, the  $e\gamma$  sample is used to model the electroweak background from  $W \rightarrow e\nu$  decays. The  $e\gamma$   $\cancel{E}_T$  distribution is scaled by the electron $\rightarrow$ photon misidentification rate to predict the number of  $W\gamma$ ,  $W + \text{jet}$ , and  $t\bar{t}$  events in the  $\gamma\gamma$  sample.

The remainder of this chapter describes the data analysis procedures and the final results of the search. Sec. 7.1 addresses the QCD background estimation. Sec. 7.2

1741 addresses the electroweak background estimation. The chapter concludes with a dis-  
1742 cussion of systematic errors in Sec. 7.3 and a presentation of the final results in  
1743 Sec. 7.4.

## 1744 7.1 Modeling the QCD Background

### 1745 7.1.1 Outline of the Procedure

1746 Due to the fact that the CMS ECAL energy resolution is much better than the  
1747 HCAL energy resolution, the energies of the two candidate photons in the events of  
1748 the  $\gamma\gamma$  sample are typically measured to far greater accuracy and precision than the  
1749 energy of the hadronic recoil in those events. Therefore, fake  $E_T$  in the  $\gamma\gamma$  sample  
1750 is almost entirely the result of hadronic mis-measurement in QCD dijet, photon +  
1751 jet, and diphoton events. The strategy employed to model this background is to find  
1752 a control sample in data consisting of two well-measured EM objects, just like the  
1753 candidate  $\gamma\gamma$  sample, and assign each event a weight to account for the underlying  
1754 kinematic differences between the control and candidate samples. Once the reweighted  
1755  $E_T$  spectrum of the control sample is created, it is then normalized in the low- $E_T$   
1756 region, the assumption being that GGM SUSY does not predict a significant amount  
1757 of events at low  $E_T$ . There are three aspects of this QCD background estimation  
1758 procedure that bear highlighting:

1759 **Choice of control sample** Since the underlying cause of  $E_T$  in the candidate sam-  
1760 ple is mis-measured hadronic activity, a control sample with similar hadronic  
1761 activity to the candidate sample should be chosen. Hadronic activity refers to  
1762 number of jets, jet  $E_T$ , pileup, etc.

1763 **Reweighting** The control sample is reweighted so that its  $E_T$  spectrum appears as it  
1764 would if the control sample had the same kinematic properties as the candidate

sample (i.e. particle  $p_T$  and  $\eta$  distributions, etc.). By choosing an appropriate control sample and reweighting it, the control  $\cancel{E}_T$  distribution should now match both the hadronic activity and the kinematics of the candidate sample.

**Normalization** Finally, the control  $E_T$  distribution is normalized in a region of low  $\cancel{E}_T$ , where contamination from the expected GGM SUSY signal is small. This implies an extrapolation of the low- $\cancel{E}_T$  QCD background prediction to the high- $\cancel{E}_T$  signal region.

As explained in the beginning of this chapter, the  $ff$  sample is used as the primary QCD control sample, while the  $ee$  sample is used as a cross-check. Both samples have two well-measured EM objects per event, no real  $\cancel{E}_T$ , and similar hadronic activity to the  $\gamma\gamma$  sample. Figure 7.3 shows a comparison of the shapes of some distributions relevant to hadronic activity between the  $\gamma\gamma$ ,  $ee$ , and  $ff$  samples. In general, the  $ee$  sample has less hadronic activity than the  $\gamma\gamma$  and  $ff$  samples, as shown by the more steeply falling  $ee$  distributions in Figs. 7.3a, 7.3b, 7.3c, and 7.3d. In addition to the kinematic reweighting, there is also a reweighting by number of jets per event, which attempts to correct for this difference (see Sec. 7.1.2).

### 7.1.2 Reweighting

To reweight the control sample events to match the kinematics of the candidate sample events, a weight based on the  $p_T$  of the di-EM-object system and the number of jets in the event is used. As explained in Sec. 7.1.1,  $E_T$  in the  $\gamma\gamma$ ,  $ff$ , and  $ee$  samples is due to the poorly measured hadronic recoil off the well-measured di-EM system. Therefore, the  $p_T$  of the di-EM system is a good handle on the true magnitude of the hadronic recoil, which affects the measured  $\cancel{E}_T$ . The di-EM system is depicted in Figure 7.4. As shown in Figure 7.5,  $\cancel{E}_T$  is largely uncorrelated with di-EM  $p_T$ , so there is little danger of reweighting away a true signal excess.

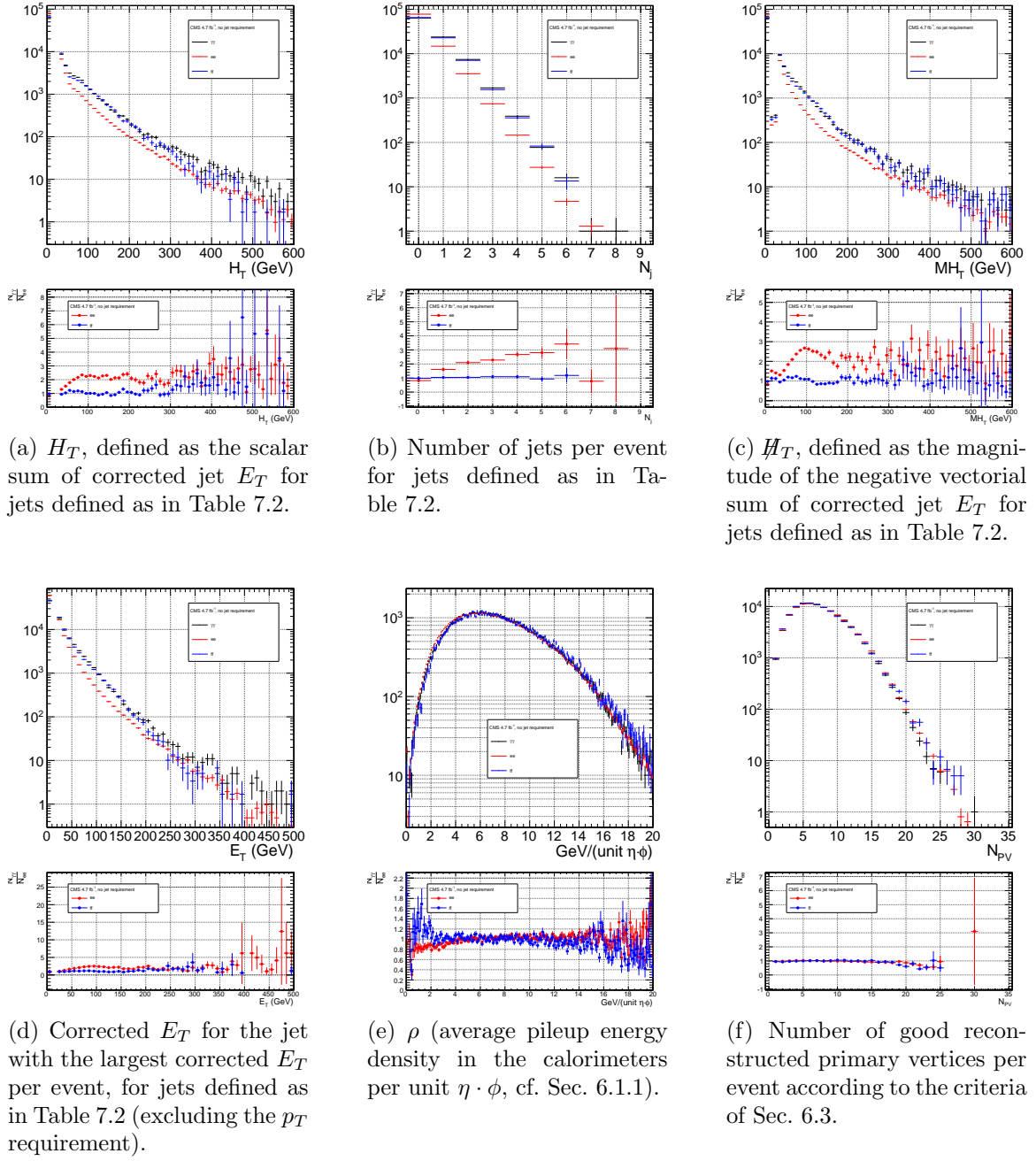


Figure 7.3: Comparison of the shapes of some distributions relevant to hadronic activity between the  $\gamma\gamma$ ,  $ee$  ( $81 \text{ GeV} \leq m_{ee} < 101 \text{ GeV}$ ), and  $ff$  samples. The  $ee$  and  $ff$  distributions are normalized to the number of events in the  $\gamma\gamma$  distribution. Errors are statistical only.

Table 7.2: Definition of HB/HE/HF hadronic jets.

Variable	Cut
Algorithm	L1FastL2L3Residual corrected PF (cf. Sec. 6.1.3)
$p_T$	$> 30 \text{ GeV}$
$ \eta $	$< 5.0$
Neutral hadronic energy fraction	$< 0.99$
Neutral electromagnetic energy fraction	$< 0.99$
Number of constituents	$> 1$
Charged hadronic energy	$> 0.0 \text{ GeV}$ if $ \eta  < 2.4$
Number of charged hadrons	$> 0$ if $ \eta  < 2.4$
Charged electromagnetic energy fraction	$< 0.99$ if $ \eta  < 2.4$
$\Delta R$ to nearest PF electron <sup>a</sup> , muon <sup>b</sup> , or one of the two primary EM objects	$> 0.5$

<sup>a</sup>A PF electron is defined as an electron reconstructed with the PF algorithm [85] with  $p_T > 15 \text{ GeV}$ ,  $|\eta| < 2.6$ , and  $(I_{\text{charged}} + I_{\text{photon}} + I_{\text{neutral}})/p_T < 0.2$ , where  $I_{\text{charged}}(I_{\text{photon}})(I_{\text{neutral}})$  is the sum of PF charged hadron(PF photon)(PF neutral hadron) momenta in a  $\Delta R = 0.4$  cone around the PF electron.

<sup>b</sup>Muons are reconstructed [86] from a combination of muon station and inner tracker hits. Here, a muon must have track  $\chi^2 < 10$ , at least one good muon station hit, inner track transverse impact parameter  $< 0.02 \text{ cm}$ , inner track longitudinal impact parameter  $< 0.5 \text{ cm}$ ,  $p_T > 15 \text{ GeV}$ ,  $|\eta| < 2.6$ , and  $(I_{\text{ECAL}} + I_{\text{HCAL}} + I_{\text{track}})/p_T < 0.2$ , where  $I_{\text{ECAL}}(I_{\text{HCAL}})(I_{\text{track}})$  is the sum of ECAL(HCAL)(track) momenta in a  $\Delta R = 0.3$  cone around the muon.

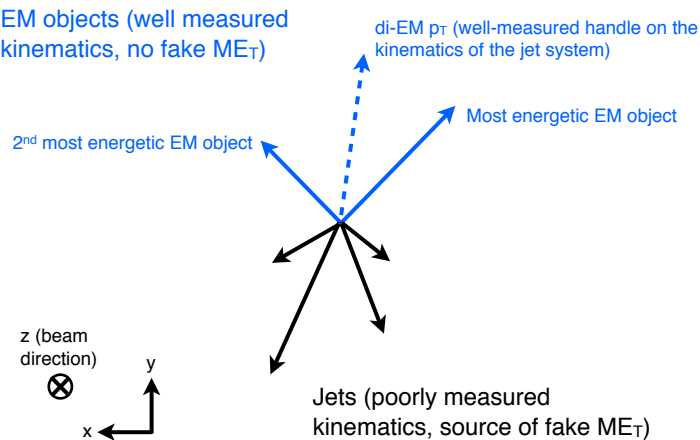
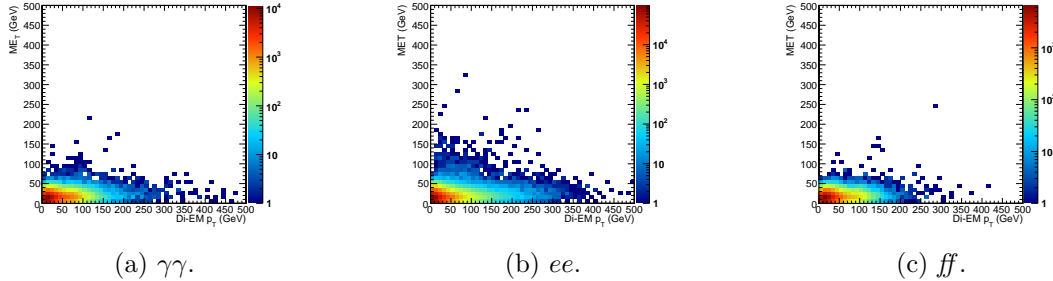


Figure 7.4: Cartoon showing the di-EM system in blue and the hadronic recoil in black. The di-EM  $p_T$  (dashed blue line) is used to reweight the control sample kinematic properties to match those of the candidate  $\gamma\gamma$  sample.

Figure 7.5:  $E_T$  vs. di-EM  $p_T$ .

Whereas the di-EM  $p_T$  reweighting accounts for differences in production kinematics between the control and  $\gamma\gamma$  samples, a simultaneous reweighting based on the number of jets in the event accounts for differences in hadronic activity between the samples, especially between  $ee$  and  $\gamma\gamma$  (cf. Fig. 7.3). Jets are defined as in Table 6.2. Figure 7.6 shows the effect of reweighting by number of jets per event, which is to increase(decrease) the tail of the  $ee$ ( $ff$ )  $E_T$  spectrum.

Although the electron and photon energies are well measured by the ECAL, the ECAL-only measurement of the fake photon energy (cf. Sec 6.1.1) is biased slightly low due to the fact that fakes (which are really jets) tend to deposit some energy in the HCAL. This can be seen in Figs. 7.7 and 7.8, which show the relative difference between the ECAL-only  $E_T$  measurement and the PF  $E_T$  measurement vs. EMF for electrons, photons, and fakes. PF  $E_T$  is defined as the L1Fast-corrected  $E_T$  of the nearest PF jet with  $p_T \geq 20$  GeV (i.e., the  $E_T$  of the PF jet object reconstructed from the same ECAL shower as the fake photon). On average, the fakes tend to deposit a few percent more energy in the HCAL than the electrons or photons, which is recovered by the PF algorithm. For this reason, the PF  $p_T$  is used in the calculation of di-EM  $p_T$  rather than the ECAL-only  $p_T$ .<sup>1</sup> This leads to a modest improvement in the agreement between the  $ee$  and  $ff$   $E_T$  spectra, as shown in Figure 7.9.

The control sample event weights are defined as

<sup>1</sup>In the few events ( $\mathcal{O}(10^{-3})$ ) in which two PF jet objects, corresponding to the two electrons or fakes, are not found, the ECAL-only  $p_T$  is used.

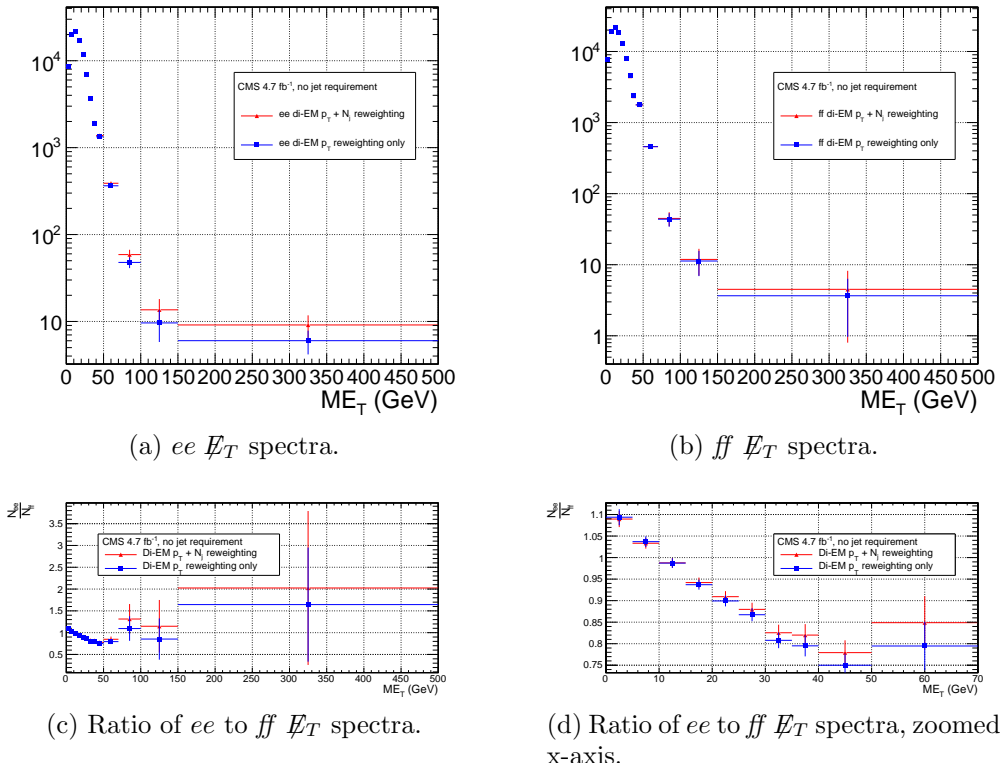


Figure 7.6:  $\cancel{E}_T$  spectra of the reweighted ee ( $81 \text{ GeV} \leq m_{ee} < 101 \text{ GeV}$ ) and ff control samples. Blue squares indicate di-EM  $p_T$  reweighting only; red triangles indicate di-EM  $p_T + \text{number of jets}$  reweighting. PF  $p_T$  (cf. p. 129) is used to calculate the di-EM  $p_T$ . The full normalization procedure is employed, along with ee sideband subtraction (discussed at the end of this section). Error bars are statistical only.

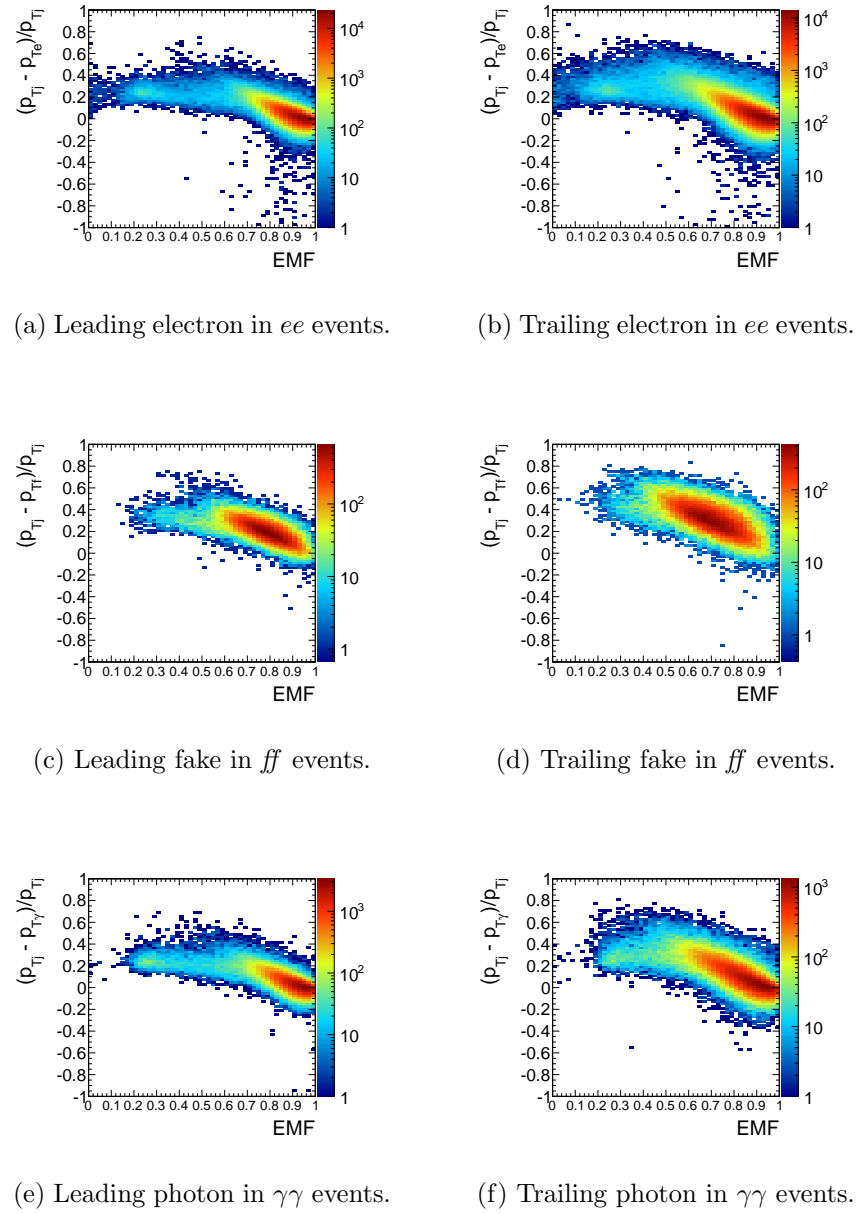


Figure 7.7: Relative difference between the ECAL-only  $E_T$  measurement and the PF  $E_T$  measurement vs. EMF. PF  $E_T$  is defined in the text.

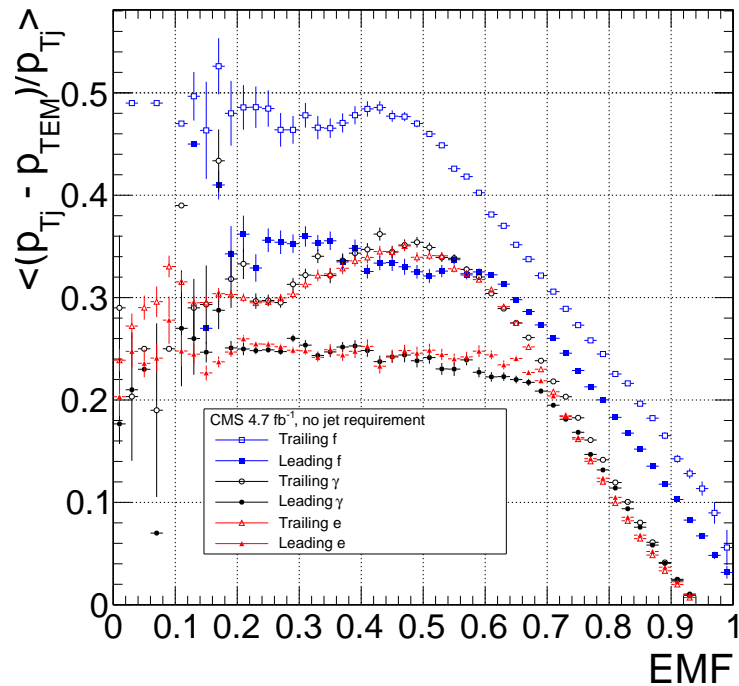


Figure 7.8: Average relative difference between the ECAL-only  $E_T$  measurement and the PF  $E_T$  measurement vs. EMF for the leading (filled marker) and trailing (open marker) electrons in  $ee$  events (red triangles), fakes in  $ff$  events (blue squares), and photons in  $\gamma\gamma$  events (black circles). These are nothing more than profile histograms of Fig. 7.7. PF  $E_T$  is defined in the text. Error bars are statistical only.

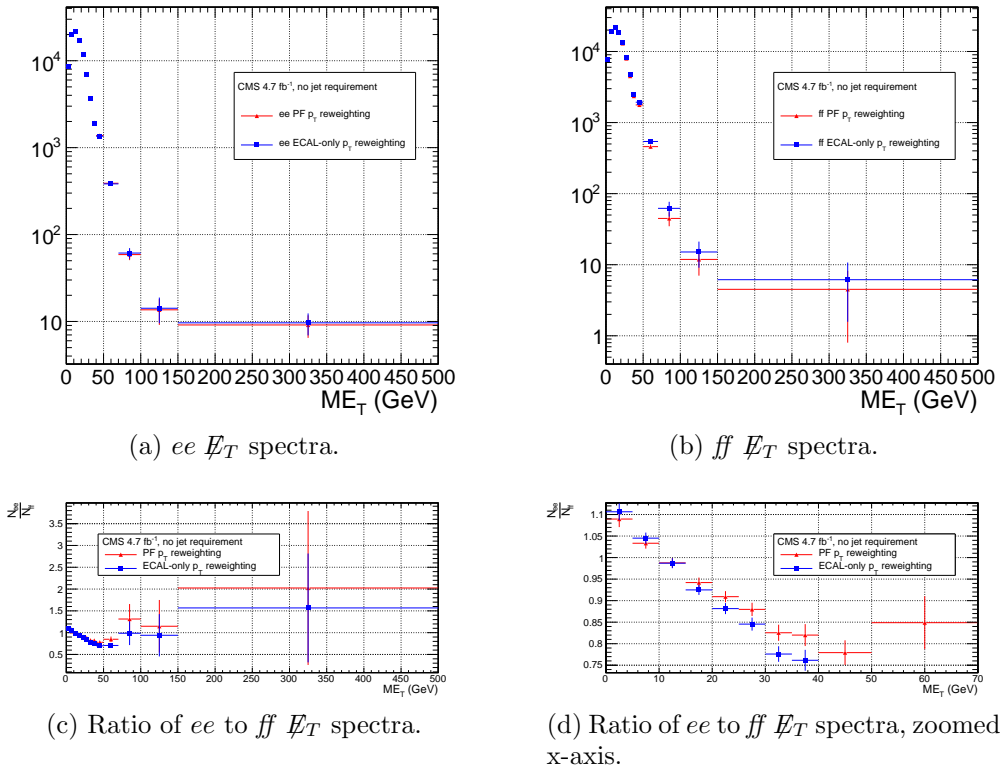


Figure 7.9:  $E_T$  spectra of the reweighted  $ee$  ( $81 \text{ GeV} \leq m_{ee} < 101 \text{ GeV}$ ) and  $ff$  control samples. Blue squares indicate reweighting using the ECAL-only  $p_T$  estimate; red triangles indicate reweighting using the PF  $p_T$  estimate. The full reweighting and normalization procedure is employed, along with  $ee$  sideband subtraction (discussed at the end of this section). Error bars are statistical only.

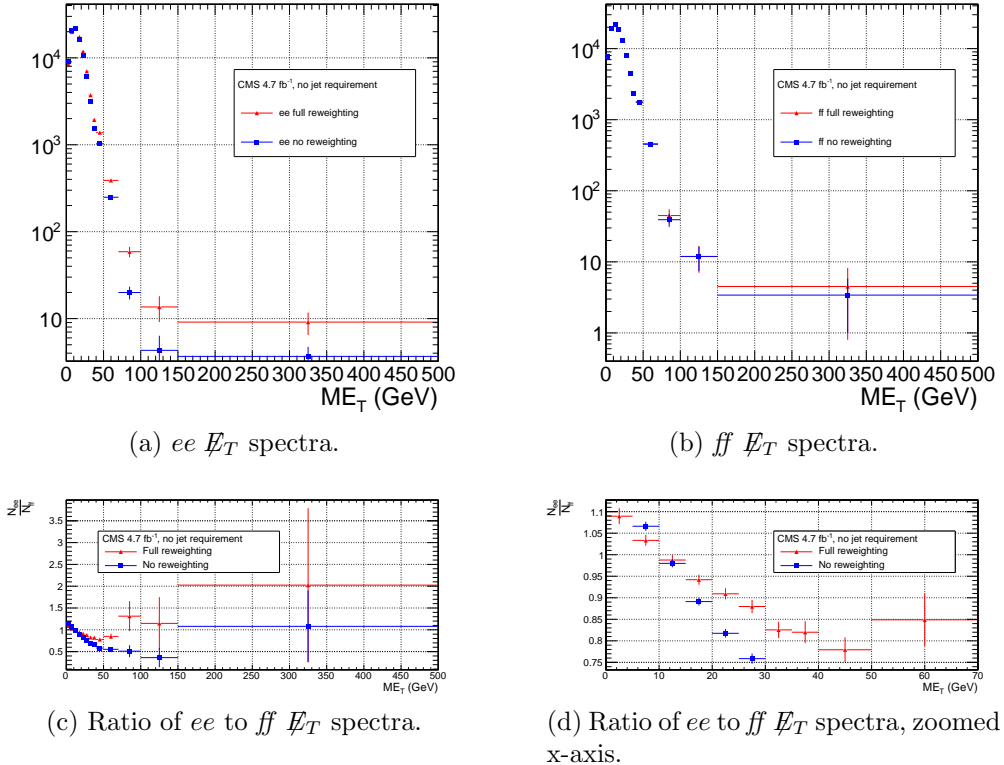


Figure 7.10:  $E_T$  spectra of the ee ( $81 \text{ GeV} \leq m_{ee} < 101 \text{ GeV}$ ) and ff control samples. Red triangles indicate full di-EM  $p_T$  + number of jets reweighting; blue squares indicate no reweighting. PF  $p_T$  (cf. p. 131) is used to calculate the di-EM  $p_T$ . The full normalization procedure is employed, along with ee sideband subtraction (discussed at the end of this section). Error bars are statistical only.

$$w_{ij} = \frac{N_{\text{control}}}{N_{\gamma\gamma}} \frac{N_{\gamma\gamma}^{ij}}{N_{\text{control}}^{ij}} \quad (7.1)$$

where  $i$  runs over the number of di-EM  $p_T$  bins,  $j$  runs over the number of jet bins,  $N_{\text{control}}$  is the total number of events in the control sample,  $N_{\gamma\gamma}$  is the total number of events in the  $\gamma\gamma$  sample,  $N_{\gamma\gamma}^{ij}$  is the number of  $\gamma\gamma$  events in the  $i^{\text{th}}$  di-EM  $p_T$  bin and  $j^{\text{th}}$  jet bin, and  $N_{\text{control}}^{ij}$  is the number of control sample events in the  $i^{\text{th}}$  di-EM  $p_T$  bin and  $j^{\text{th}}$  jet bin. The effect of the reweighting is more significant for the ee sample than for the ff sample, as shown in Figure 7.10.

1815     The  $ee$  sample contains a non-negligible background of  $t\bar{t}$  events in which both  
 1816      $W$  bosons decay to electrons. These events have significant real  $\cancel{E}_T$  from the two  
 1817     neutrinos (unlike the  $\gamma\gamma$  events), and therefore inflate the background estimate at  
 1818     high  $\cancel{E}_T$ . In order to remove the  $t\bar{t}$  contribution from the  $ee$  sample, a sideband  
 1819     subtraction method is employed.

1820     Only events in the  $ee$  sample with  $81 \text{ GeV} \leq m_{ee} < 101 \text{ GeV}$ , where  $m_{ee}$  is the  
 1821     di-electron invariant mass, are used in the QCD background estimate. This choice  
 1822     maximizes the ratio of  $Z$  signal to background. The sidebands used to estimate the  
 1823     background contribution within the  $Z$  window are defined such that  $71 \text{ GeV} \leq m_{ee} <$   
 1824      $81 \text{ GeV}$  and  $101 \text{ GeV} \leq m_{ee} < 111 \text{ GeV}$ .

1825     The full reweighting procedure is applied to the  $Z$  signal region and the two  
 1826     sideband regions independently. Only  $Z$  signal events are used in the calculation of  
 1827     the di-EM  $p_T$  weights for the  $Z$  signal region, and likewise only the events within  
 1828     a given sideband region are used in the calculation of the weights for that region.  
 1829     Assuming a constant  $t\bar{t}$  background shape, the resulting reweighted sideband  $\cancel{E}_T$   
 1830     distributions are added together and subtracted from the reweighted  $Z$  signal  $\cancel{E}_T$   
 1831     distribution. The sideband subtracted  $Z$  signal  $\cancel{E}_T$  distribution is then normalized  
 1832     as discussed in Secs. 7.1.1 and 7.1.3. The statistical and reweighting error from the  
 1833     sideband regions is propagated to the error on the final  $ee$  QCD  $\cancel{E}_T$  estimate.

1834     The di-EM  $p_T$  weights for the two  $ee$  sideband regions are shown in Figure 7.11.  
 1835     The overall scale of the weights, as well as the trend with di-EM  $p_T$ , is similar for  
 1836     the two regions (except at high di-EM  $p_T$ , where the statistics are poor anyway).  
 1837     Figure 7.12 shows the  $\cancel{E}_T$  spectra for the two sideband regions and the  $Z$  signal  
 1838     region after subtraction. The shapes of the spectra indicate that the high- $\cancel{E}_T$   $t\bar{t}$  tail,  
 1839     present in the sideband distributions, was successfully subtracted from the  $Z$  signal  
 1840     distribution.

1841     The  $ee$  ( $81 \text{ GeV} \leq m_{ee} < 101 \text{ GeV}$ ),  $ff$ , and  $\gamma\gamma$  di-EM  $p_T$  spectra for events with

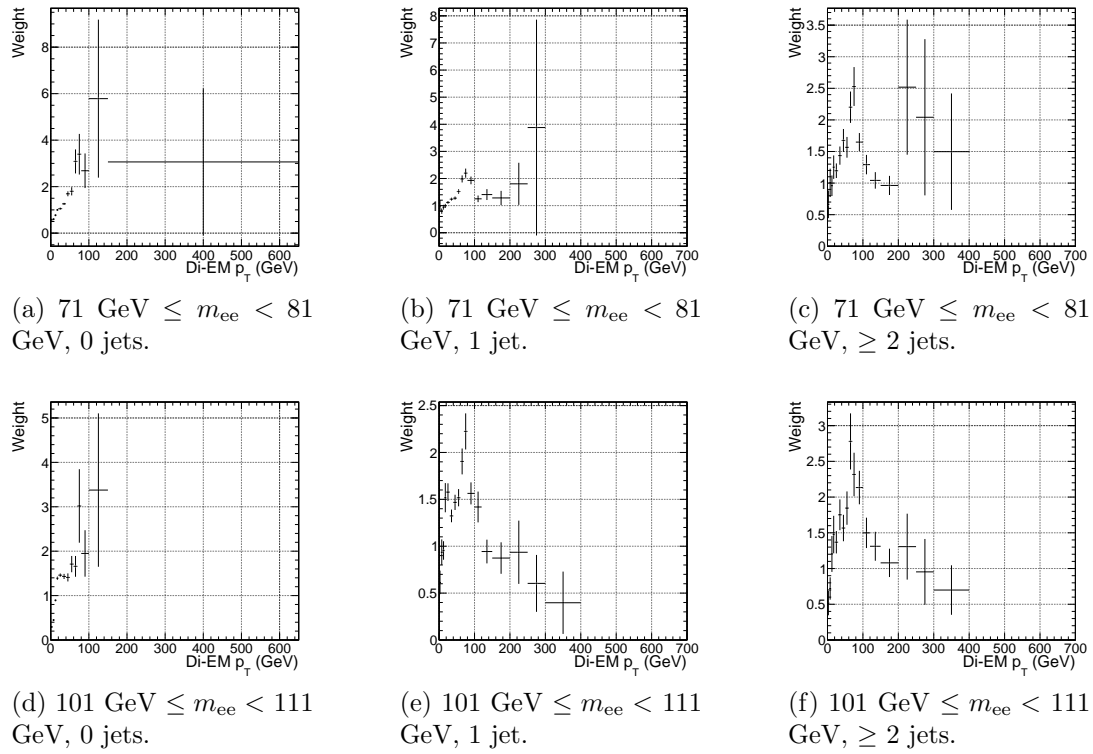


Figure 7.11:  $ee$  sideband di-EM  $p_T$  weights for events with 0, 1, or  $\geq 2$  jets (as in Table 6.2). Errors are statistical only.

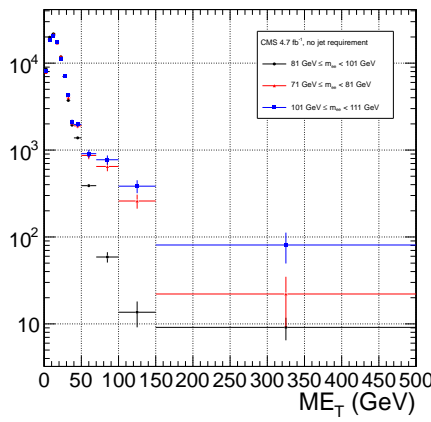


Figure 7.12:  $E_T$  spectra of the  $ee$  sample for  $71 \text{ GeV} \leq m_{ee} < 81 \text{ GeV}$  (red triangles),  $81 \text{ GeV} \leq m_{ee} < 101 \text{ GeV}$  (black circles), and  $101 \text{ GeV} \leq m_{ee} < 111 \text{ GeV}$  (blue squares). The two sideband distributions (red and blue) and the  $Z$  signal distribution (black) are normalized to the total number of  $\gamma\gamma$  events. Errors are statistical only.

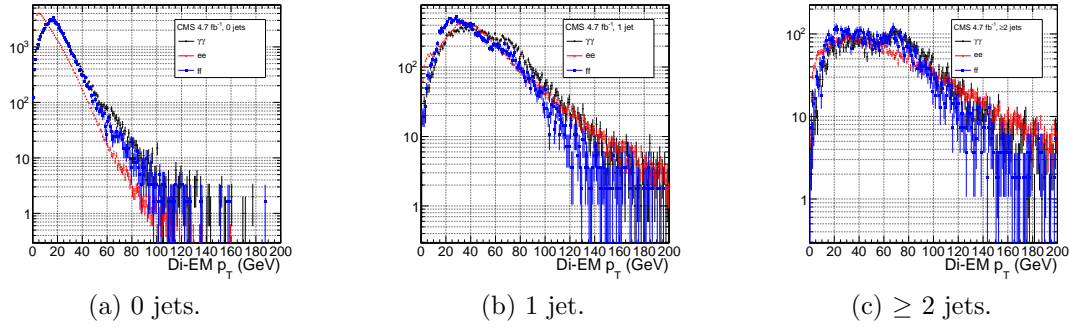


Figure 7.13:  $ee$  ( $81 \text{ GeV} \leq m_{ee} < 101 \text{ GeV}$ ) (red triangles),  $ff$  (blue squares), and  $\gamma\gamma$  (black circles) di-EM  $p_T$  spectra for events with 0, 1, or  $\geq 2$  jets (as in Table 6.2). Errors are statistical only.

0, 1, or  $\geq 2$  jets (as in Table 6.2) are shown in Figure 7.13. Broad humps in the  $ff$  and  $\gamma\gamma$  spectra are due to kinematic  $\Delta R$  and  $p_T$  turn-ons that are suppressed in the  $ee$  sample due to the invariant mass cut. Figure 7.14 shows the weights applied to the  $ee$  ( $81 \text{ GeV} \leq m_{ee} < 101 \text{ GeV}$ ) and  $ff$   $E_T$  spectra as a function of di-EM  $p_T$  and number of jets per event.

### 1847 7.1.3 Normalization

After reweighting, the  $\cancel{E}_T$  distributions of the QCD control samples are normalized to the  $\cancel{E}_T < 20$  GeV region of the candidate  $\gamma\gamma \cancel{E}_T$  spectrum, where signal contamination is low. The normalization factor is  $(N_{\gamma\gamma}^{\cancel{E}_T < 20\text{GeV}} - N_{e\gamma}^{\cancel{E}_T < 20\text{GeV}})/N_{\text{control}}^{\cancel{E}_T < 20\text{GeV}}$ , where  $N_{e\gamma}^{\cancel{E}_T < 20\text{GeV}}$  is the expected number of electroweak background events with  $\cancel{E}_T < 20$  GeV (discussed in Section 7.2).

## <sup>1853</sup> 7.2 Modeling the Electroweak Background

<sup>1854</sup>  $W\gamma$ ,  $W + \text{jet}$ , and  $t\bar{t}$  processes in which the  $W$  decay electron is misidentified as a  
<sup>1855</sup> photon (due to a failure to properly associate a pixel seed to the electron candidate)  
<sup>1856</sup> can contribute significantly to the high- $\cancel{E}_T$  tail of the  $\gamma\gamma$   $\cancel{E}_T$  spectrum. To estimate

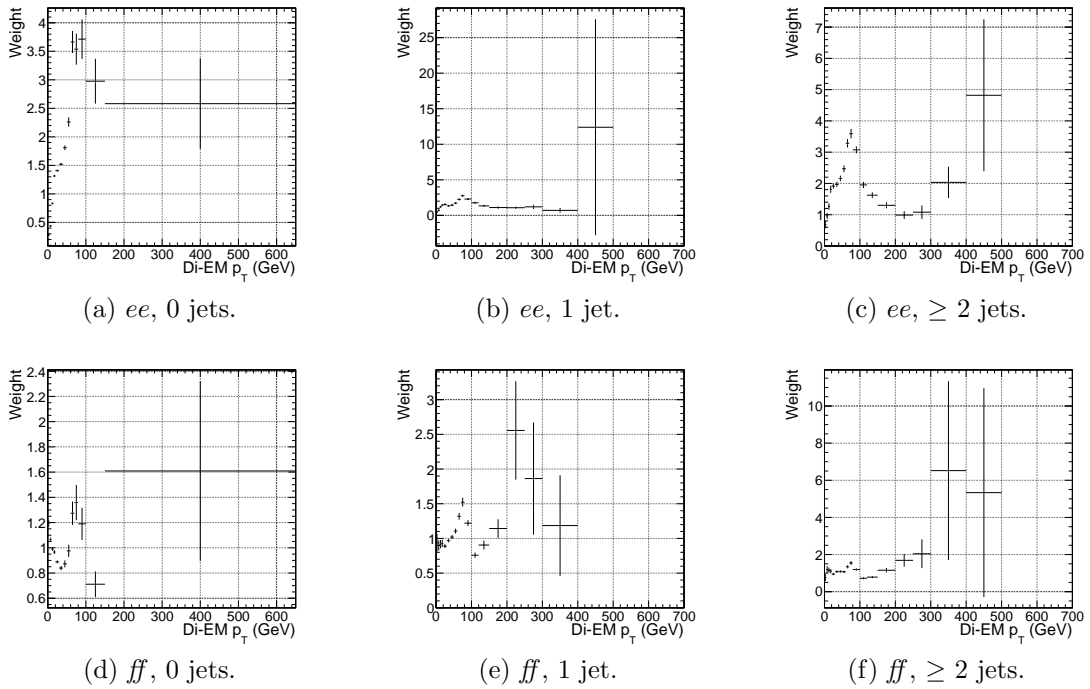


Figure 7.14:  $ee$  ( $81 \text{ GeV} \leq m_{ee} < 101 \text{ GeV}$ ) and  $ff$  di-EM  $p_T$  weights for events with 0, 1, or  $\geq 2$  jets (as in Table 6.2). Errors are statistical only.

1857 this background, the  $e\gamma$  sample, which is enriched in  $W \rightarrow e\nu$  decays, is scaled by  
 1858  $f_{e \rightarrow \gamma}/(1 - f_{e \rightarrow \gamma})$ , where  $f_{e \rightarrow \gamma}$  is the rate at which electrons are misidentified as photons.  
 1859 The derivation of this scaling factor comes from the two equations

$$N_{e\gamma}^W = f_{e \rightarrow e} N_W \quad (7.2)$$

$$N_{\gamma\gamma}^W = (1 - f_{e \rightarrow e}) N_W \quad (7.3)$$

1860 where  $N_{e\gamma}^W$  is the number of  $W$  events in the  $e\gamma$  sample in which the electron was  
 1861 correctly identified,  $f_{e \rightarrow e}$  is the probability to correctly identify an electron,  $N_W$  is  
 1862 the true number of triggered  $W \rightarrow e\nu$  events, and  $N_{\gamma\gamma}^W$  is the number of  $W$  events in  
 1863 the  $\gamma\gamma$  sample in which the electron was misidentified as a photon. The contribution  
 1864 from  $Z \rightarrow ee$  can be neglected (i.e.  $f_{e \rightarrow \gamma}$  is small and the  $Z$  contribution involves  
 1865  $f_{e \rightarrow \gamma}^2$ , since both electrons have to be misidentified). Since  $f_{e \rightarrow e} = 1 - f_{e \rightarrow \gamma}$ , solving

<sup>1866</sup> for  $N_{\gamma\gamma}^W$  gives

$$N_{\gamma\gamma}^W = \frac{f_{e\rightarrow\gamma}}{1 - f_{e\rightarrow\gamma}} N_{e\gamma}^W \quad (7.4)$$

<sup>1867</sup>  $f_{e\rightarrow\gamma}$  is measured by fitting the  $Z$  peaks in the  $ee$  and  $e\gamma$  samples. The number of  
<sup>1868</sup>  $Z$  events fitted in the  $ee$  and  $e\gamma$  samples, respectively, is given by

$$N_{ee}^Z = (1 - f_{e\rightarrow\gamma})^2 N_Z \quad (7.5)$$

$$N_{e\gamma}^Z = 2f_{e\rightarrow\gamma}(1 - f_{e\rightarrow\gamma}) N_Z \quad (7.6)$$

<sup>1869</sup> where  $N_Z$  is the true number of triggered  $Z \rightarrow ee$  events. Solving for  $f_{e\rightarrow\gamma}$  gives

$$f_{e\rightarrow\gamma} = \frac{N_{e\gamma}^Z}{2N_{ee}^Z + N_{e\gamma}^Z} \quad (7.7)$$

<sup>1870</sup> A Crystal Ball function is used to model the  $Z$  signal shape in both the  $ee$  and  
<sup>1871</sup>  $e\gamma$  samples, while an exponential convoluted with an error function (`RooCMSShape`,  
<sup>1872</sup> see Sec. 6.4.1) is used to model the background shape. The fixed fit parameters are  
<sup>1873</sup> identical for the two samples, but the other parameters are allowed to float indepen-  
<sup>1874</sup> dently. Table 7.3 shows the values and ranges of the fixed and floating fit parameters,  
<sup>1875</sup> respectively.

<sup>1876</sup> Fits to the  $ee$  and  $e\gamma$  invariant mass spectra are shown in Figure 7.15. Figure 7.16  
<sup>1877</sup> indicates that the dependence of  $f_{e\rightarrow\gamma}$  on the electron  $p_T$  and  $\eta$  is small. (Note that all  
<sup>1878</sup> fit parameters are floating in the  $p_T$ -dependent fits.) Therefore, a constant misidenti-  
<sup>1879</sup> fication rate (derived from all  $ee$  and  $e\gamma$  events), rather than a  $p_T$ - and  $\eta$ -dependent  
<sup>1880</sup> misidentification rate, is used in the final electroweak background estimate, with the

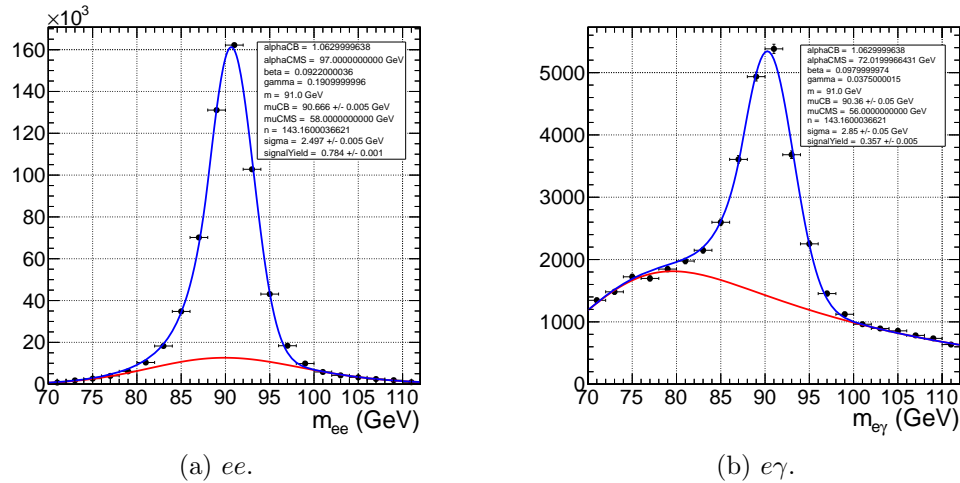


Figure 7.15: Fits to the  $ee$  and  $e\gamma$  invariant mass spectra using the Crystal Ball RooCMSShape function described in the text and in Table 7.3. The total fit is shown in blue, while the background component is shown in red.

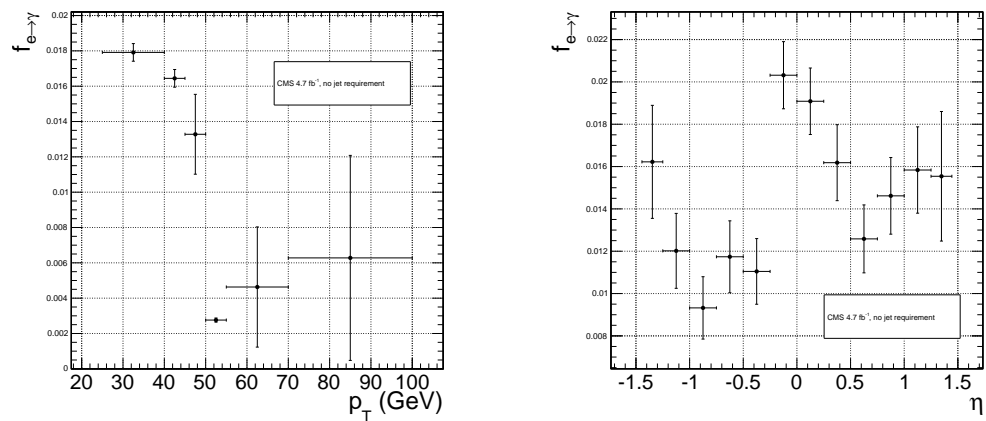
difference between the constant rate and the rate for electrons with  $p_T$  between 25 and 40 GeV (the range in which the bulk of the trailing photons in the  $\gamma\gamma$  sample lie) taken as a systematic error.

Using the integrals of the  $Z$  fits shown in Fig. 7.15, Eq. 7.7, and the  $p_T$  systematic discussed above,  $f_{e \rightarrow \gamma}$  is calculated to be  $0.014 \pm 0.000(\text{stat.}) \pm 0.004(\text{syst.})$ . The scaled  $e\gamma$  MET distribution is shown in Figure 7.17.

In the  $36 \text{ pb}^{-1}$  version of this analysis [110], it was shown that the  $ee$  sample could accurately predict the QCD and real  $Z$  contribution to the  $e\gamma$  sample at low  $\cancel{E}_T$ , and that the expectation from  $W \rightarrow e\nu$  MC accounted for the remaining  $W$  contribution at high  $\cancel{E}_T$ . A plot of the  $\cancel{E}_T$  distributions of the 2010  $e\gamma$  sample and the predicted components is shown in Figure 7.18. This exercise helps to validate both the QCD and electroweak background prediction methods.

Table 7.3: Parameter values for the signal and background PDFs for the  $ee$  and  $e\gamma$  samples. When a bracketed range is given, the parameter is allowed to float within that range. When a constant is given, the parameter is fixed to that constant.

PDF	Crystal Ball fit parameters				RooCMSShape fit parameters			
	$\mu$	$\sigma$	$\alpha$	n	$\mu$	$\alpha$	$\beta$	$\gamma$
$ee$ signal	[86.2, 96.2]	[1.0, 5.0]	1.063	143.16	N/A	N/A	N/A	N/A
$e\gamma$ signal	[86.2, 96.2]	[1.0, 5.0]	1.063	143.16	N/A	N/A	N/A	N/A
$ee$ background	N/A	N/A	N/A	N/A	58	97.0	0.0922	0.191
$e\gamma$ background	N/A	N/A	N/A	N/A	56	72.02	0.098	0.0375



(a)  $f_{e \rightarrow \gamma}$  vs. electron  $p_T$ . For the lowest  $p_T$  bin, the fit to the  $e\gamma$  spectrum does not converge well, so the  $Z$  signal fraction is fixed to the value in Fig. 7.15b.

(b)  $f_{e \rightarrow \gamma}$  vs. electron  $\eta$ .

Figure 7.16:  $f_{e \rightarrow \gamma}$  vs. electron  $p_T$  and  $\eta$ .

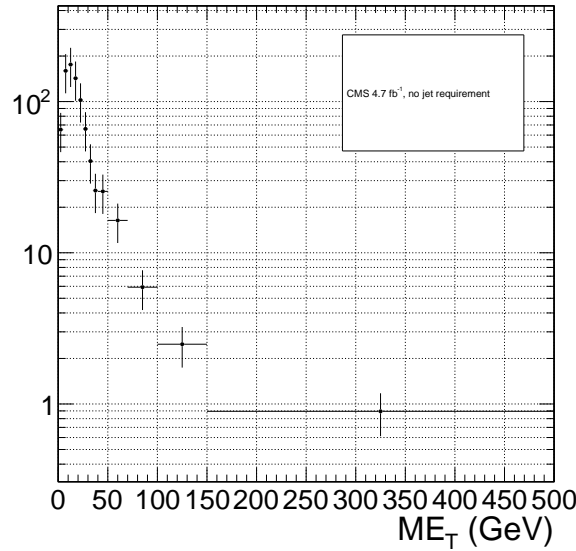


Figure 7.17:  $\cancel{E}_T$  spectrum of the  $e\gamma$  sample after scaling by  $f_{e \rightarrow \gamma}$ . The total error on  $f_{e \rightarrow \gamma}$  is propagated to the total error on the electroweak background estimate.

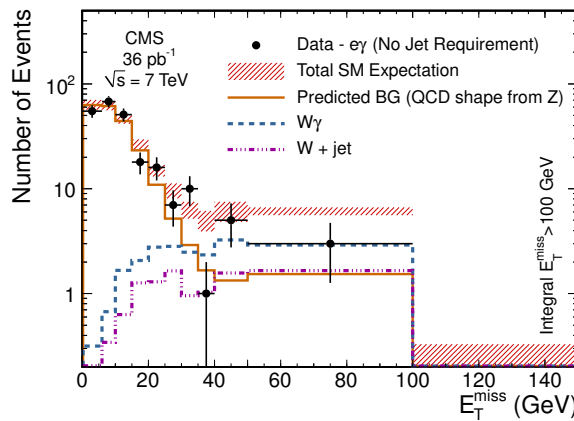


Figure 7.18:  $\cancel{E}_T$  spectrum of the  $e\gamma$  sample in  $36 \text{ pb}^{-1}$  of 2010 LHC data scaled by the 2010 measured  $f_{e \rightarrow \gamma}$  (black dots), QCD and real  $Z$  predicted background from the 2010  $ee$  sample (solid orange line), MC  $W + \text{jet}$  estimate (dash-dotted purple line), and MC  $W\gamma$  estimate (dashed blue line). The total  $e\gamma$  prediction (red band) is the sum of the  $ee$ ,  $W + \text{jet}$ , and  $W\gamma$  predictions. Reprinted from Fig. 2 of ref. [110].

### 1893 7.3 Errors on the Background Prediction

1894 The statistical error on the final background estimate in a particular  $\cancel{E}_T$  bin comes  
 1895 from three sources: the number of control sample events collected in that bin, the  
 1896 statistical error on the weights applied to events in that bin, and the statistics of the  
 1897 normalization region. In the case of the  $ee$  control sample, there are contributions  
 1898 from the statistics of the  $m_{ee}$  sidebands as well.

1899 In order to estimate the statistical error due to the reweighting procedure, 1000  
 1900 toy sets of weights are generated. Each set includes a weight for each (di-EM  $p_T$ ,  $N_j$ )  
 1901 bin, with the values picked from a Gaussian distribution with mean and standard  
 1902 deviation equal to the observed weight for that bin and its statistical error. The effect  
 1903 of reweighting error is not correlated between  $\cancel{E}_T$  bins. For each of the 1000 exper-  
 1904 iments, the control sample data are reweighted according to the generated weights,  
 1905 and the background estimates are calculated for each  $\cancel{E}_T$  bin. Since the distribution  
 1906 of the toy background estimates follows a Gaussian distribution in each  $\cancel{E}_T$  bin, the  
 1907 RMS spread of the estimates is taken as the statistical error due to reweighting. This  
 1908 procedure is carried out for the  $ff$ ,  $ee$ , low sideband  $ee$ , and high sideband  $ee$  samples.

1909 The total statistical error on the background estimate per  $\cancel{E}_T$  bin is given by

$$\sigma_{\text{stat}}^2 = \sigma_{\text{stat,QCD}}^2 + \sigma_{\text{stat,EW}}^2 \quad (7.8)$$

1910 where  $\sigma_{\text{stat,QCD}}^2$  is the square of the total statistical error on the QCD prediction in  
 1911 the  $\cancel{E}_T$  bin

$$\sigma_{\text{stat,QCD}}^2 = \sigma_{\text{stat},s}^2 + \sigma_{\text{Poisson,QCD}}^2 + \sigma_{\text{reweight},s}^2 + \sigma_{\text{reweight,QCD}}^2 \quad (7.9)$$

1912 and  $\sigma_{\text{stat,EW}}$  is the Poisson error on the number of  $e\gamma$  events in the  $\cancel{E}_T$  bin ( $= \sqrt{N_{e\gamma}}$ ,  
 1913 where  $N_{e\gamma}$  is the prediction in the  $\cancel{E}_T$  bin after scaling by  $f_{e\rightarrow\gamma}$ ). The contributions  
 1914 to  $\sigma_{\text{stat,QCD}}^2$  are discussed below.

- 1915 •  $\sigma_{\text{stat},s}^2$  is the statistical error contributed by the normalization factor  $s$  (i.e. from  
 1916 Poisson error in the normalization region  $\cancel{E}_T < 20$  GeV):

$$\begin{aligned}\sigma_{\text{stat},s}^2 = & \frac{N_{\text{control}}^2}{(N_{\gamma\gamma}^{\text{norm}} - N_{e\gamma}^{\text{norm}})^2} (\sigma_{\text{Poisson},\gamma\gamma}^{\text{norm}})^2 + (\sigma_{\text{Poisson},e\gamma}^{\text{norm}})^2 + \\ & \frac{N_{\text{control}}^2}{(N_{\text{control}}^{\text{norm}})^2} (\sigma_{\text{Poisson,control}}^{\text{norm}})^2\end{aligned}\quad (7.10)$$

1917 where  $N_{\text{control}}$  is the number of reweighted, normalized events in the  $\cancel{E}_T$  bin,  
 1918  $N_{\gamma\gamma}^{\text{norm}}$  is the number of  $\gamma\gamma$  events in the normalization region,  $N_{e\gamma}^{\text{norm}}$  is the num-  
 1919 ber of  $e\gamma$  events in the normalization region (after scaling by  $f_{e\rightarrow\gamma}$ ),  $\sigma_{\text{Poisson},\gamma\gamma}^{\text{norm}}$   
 1920 is the Poisson error on the number of  $\gamma\gamma$  events in the normalization region  
 1921 ( $= \sqrt{N_{\gamma\gamma}^{\text{norm}}}$ ),  $\sigma_{\text{Poisson},e\gamma}^{\text{norm}}$  is the Poisson error on the number of  $e\gamma$  events in the  
 1922 normalization region ( $= \sqrt{N_{e\gamma}^{\text{norm}}}$ ),  $N_{\text{control}}^{\text{norm}}$  is the number of QCD control ( $ee$   
 1923 or  $ff$ ) events in the normalization region, and  $\sigma_{\text{Poisson,control}}^{\text{norm}}$  is the Poisson error  
 1924 on the number of QCD control ( $ee$  or  $ff$ ) events in the normalization region  
 1925 ( $= \sqrt{\sum_{i=1}^{N_{\text{control}}^{\text{norm}}} w_i^2}$ , where  $w_i$  is the di-EM  $p_T$  weight applied to event  $i$ ). For  
 1926 the  $ee$  control region,  $N_{\text{control}}$  and  $N_{\text{control},\text{norm}}$  are sideband subtracted, and  
 1927  $\sigma_{\text{Poisson,control}}^{\text{norm}}$  includes the Poisson error on the number of sideband events.

- 1928 •  $\sigma_{\text{Poisson,QCD}}$  is the Poisson error due to the number of QCD control ( $ee$  or  $ff$ )  
 1929 events in the  $\cancel{E}_T$  bin, equal to  $\sqrt{\sum_{i=1}^{N_{\text{control}}^{\text{norm}}} w_i^2}$ , where  $w_i$  is the di-EM  $p_T$  weight  
 1930 applied to event  $i$ . For the  $ee$  control region,  $\sigma_{\text{Poisson,QCD}}$  includes the Poisson  
 1931 error on the number of subtracted sideband events.  
 1932 •  $\sigma_{\text{reweight},s}$  is the error contributed by the control sample reweighting in the nor-

1933        malization region ( $= \frac{N_{\text{control}}^2}{(N_{\text{control}}^{\text{norm}})^2} \sigma_{\text{reweight,control}}^{\text{norm}}$ ).  $\sigma_{\text{reweight,control}}^{\text{norm}}$  is the quadrature  
 1934        sum of the RMS of the 1000 toy reweighting experiments for each  $\cancel{E}_T$  bin in the  
 1935        normalization region. For the  $ee$  control sample, it also includes (in quadrature)  
 1936        the RMS of the toys in the sideband samples.

- 1937        •  $\sigma_{\text{reweight,QCD}}$  is the error contributed by the control sample reweighting in the  $\cancel{E}_T$   
 1938        bin ( $= s\sigma_{\text{reweight,control}}$ ).  $\sigma_{\text{reweight,control}}$  is the RMS of the 1000 toy reweighting  
 1939        experiments for the  $E_T$  bin. For the  $ee$  control sample, it also includes (in  
 1940        quadrature) the RMS of the toys in the sideband samples.

1941        The dominant source of systematic error on the background estimate is the slight  
 1942        difference in hadronic activity between the  $ee$ ,  $ff$ , and  $\gamma\gamma$  samples. This results in a  
 1943        small bias ( $\sim 1$  GeV) of the  $ee$   $\cancel{E}_T$  distribution towards lower values with respect to  
 1944        the  $ff$  and  $\gamma\gamma$  samples, as shown in Figure 7.19. Therefore, the  $ff$  sample is used as  
 1945        the primary QCD background estimator, and the difference between the  $ee$  and  $ff$   
 1946        predictions is assigned as an error on the knowledge of the hadronic activity. For  $\cancel{E}_T$   
 1947         $> 100$  GeV, this error amounts to 43% of the total QCD + electroweak background  
 1948        estimate.

1949        The second largest source of systematic error comes from the  $p_T$  dependence of the  
 1950         $e \rightarrow \gamma$  misidentification rate (see 7.2). For  $\cancel{E}_T > 100$  GeV, the expected electroweak  
 1951        background is  $3.4 \pm 1.0$  events, so this error amounts to 4.8% of the total QCD +  
 1952        electroweak background estimate.

1953        The assumption of a constant  $t\bar{t}$  and  $W + \text{jets}$  background shape under the  $Z$   
 1954        peak in the  $ee$  sample induces a systematic error on the  $ee$  sideband-subtracted back-  
 1955        ground prediction. To assess the magnitude of this error, the sideband subtraction  
 1956        (see Sec. 7.1.2) is performed once using only the prediction from the high sideband,  
 1957        and once using only the prediction from the low sideband. In each of these cases, the  
 1958        prediction is weighted by a factor of two, to account for the fact that the sideband  
 1959        regions are only half as wide (10 GeV) as the signal region (20 GeV). The maximum

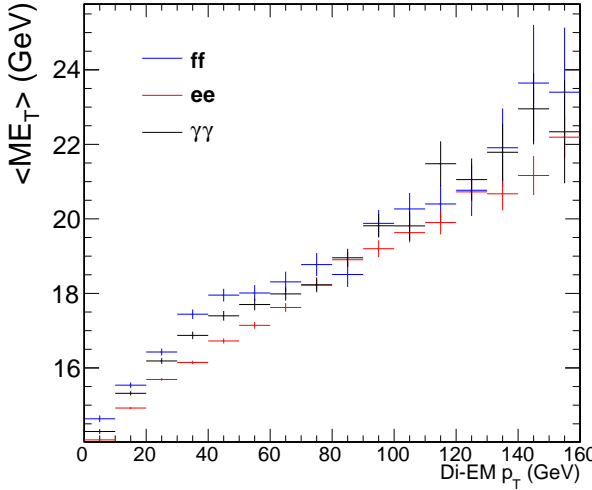


Figure 7.19: Average  $\mathcal{E}_T$  vs. di-EM  $p_T$  for the  $ff$  (blue),  $ee$  (red), and  $\gamma\gamma$  (black) samples.

1960 variation from the nominal  $ee$  estimate is taken as the error, which amounts to 11%  
 1961 for  $\mathcal{E}_T > 100$  GeV.  $\mathcal{E}_T$  distributions using the nominal  $ee$  sideband subtraction, the  
 1962 low-sideband-only subtraction, and the high-sideband-only subtraction are shown in  
 1963 Figure 7.20.

Added

1964 Finally, the few percent error on the jet energy correction factors introduces an this  
 1965 error on the final background estimate through (a) the use of the PF  $p_T$  to measure para-  
 1966 the di-EM  $p_T$ , (b) the counting of jets passing a 30 GeV  $p_T$  threshold for placement of graph  
 1967 the event in an  $N_j$  bin for reweighting, and (c) the counting of jets above threshold for  
 1968 the  $\geq 1$ -jet version of the selection. To estimate this error, 100 pseudo-experiments  
 1969 are generated with identical properties as the true data sample, except with corrected  
 1970 jet energies (in all events) all shifted by an amount  $r\sigma(p_T, \eta)$ .  $r$  is a random number  
 1971 drawn from a Gaussian distribution with mean 0 and width 1, and  $\sigma(p_T, \eta)$  is the  
 1972 uncertainty on the jet energy correction factor (which, like the correction factor itself,  
 1973 is a function of  $p_T$  and  $\eta$ ). The same factor  $r$  is applied to all jets in all events in the  
 1974 pseudo-experiment because the jet energy correction errors are correlated from jet to  
 1975 jet (they result from e.g. uncertainties in MC simulation or uncertainties in ECAL

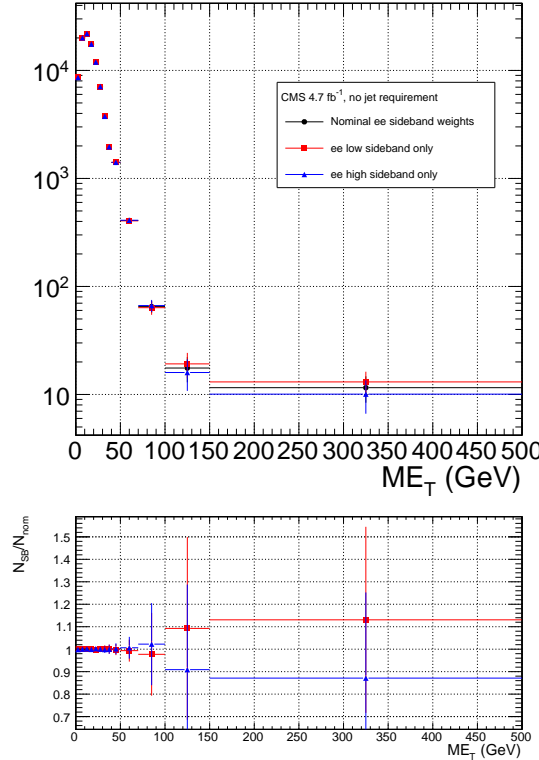


Figure 7.20:  $ee$   $E_T$  distributions using the nominal sideband subtraction (black circles), low sideband only (red squares), and high sideband only (blue triangles). The bottom plot shows the ratio of the low sideband distribution to the nominal (red squares) and the ratio of the high sideband distribution to the nominal (blue triangles).

1976 energy scale [90]). The standard error of the mean of the 100 resulting background  
 1977 estimates in each relevant  $E_T$  bin is taken as the error. The error in each  $E_T$  bin is  
 1978 assumed to be uncorrelated. This process is repeated for both the inclusive and  $\geq 1$ -  
 1979 jet selections. For  $E_T \geq 100$  GeV, the jet energy correction uncertainty is 1.5% (2.2%)  
 1980 of the total background for the inclusive ( $\geq 1$ -jet) selection.

1981 The uncertainty in how to define the (di-EM  $p_T$ ,  $N_j$ ) bins, especially at high di-  
 1982 EM  $p_T$  where the statistics are low, is covered by the 1000-toys procedure as long as  
 1983 the bins are not too coarse. This is shown in Figure 7.21. If the bins are too coarse,  
 1984 the details of the shape of the di-EM  $p_T$  spectra are lost, and the reweighting has a  
 1985 smaller effect.

1986 The use of uncorrected instead of corrected PF  $E_T$  (see Sec. 6.1.3) makes no

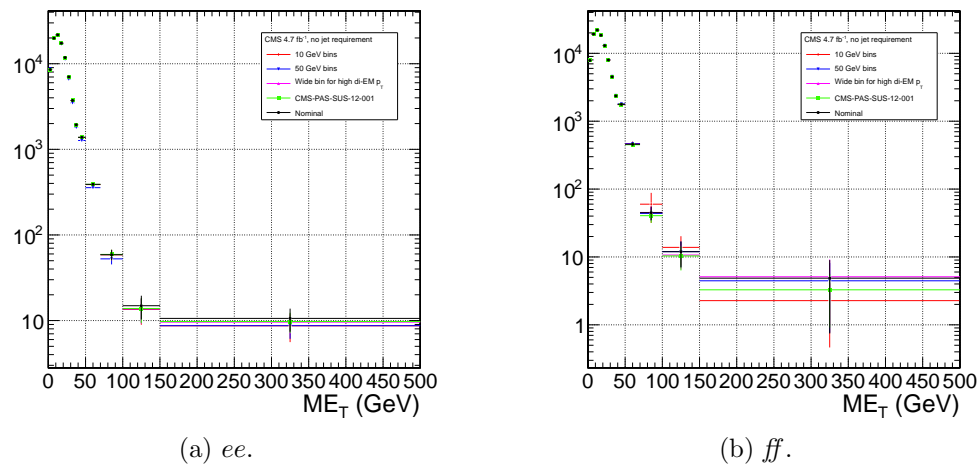


Figure 7.21: Comparison of  $\cancel{E}_T$  distributions for five different di-EM  $p_T$  bin definitions: uniform bins of width 10 GeV (red diamonds); uniform bins of width 50 GeV (blue downward-pointing triangles); bins with lower edges  $\{0.0, 5.0, 10.0, 15.0, 20.0, 30.0, 40.0, 50.0, 60.0, 70.0, 80.0, 100.0, 750.0\}$  GeV for 0-jet events and  $\{0.0, 5.0, 10.0, 15.0, 20.0, 30.0, 40.0, 50.0, 60.0, 70.0, 80.0, 100.0, 150.0\}$  GeV for  $\geq 1$ -jet events (magenta upward-pointing triangles), i.e. a single wide bin at high di-EM  $p_T$ ; bins with lower edges  $\{0.0, 5.0, 10.0, 15.0, 20.0, 30.0, 40.0, 50.0, 60.0, 70.0, 80.0, 100.0, 150.0\}$  GeV for 0-jet events and  $\{0.0, 5.0, 10.0, 15.0, 20.0, 30.0, 40.0, 50.0, 60.0, 70.0, 80.0, 100.0, 120.0, 150.0, 200.0\}$  GeV for  $\geq 1$ -jet events (green squares), i.e. the bins used in ref. [29]; and the nominal bin definitions shown in Fig. 7.14 (black circles).

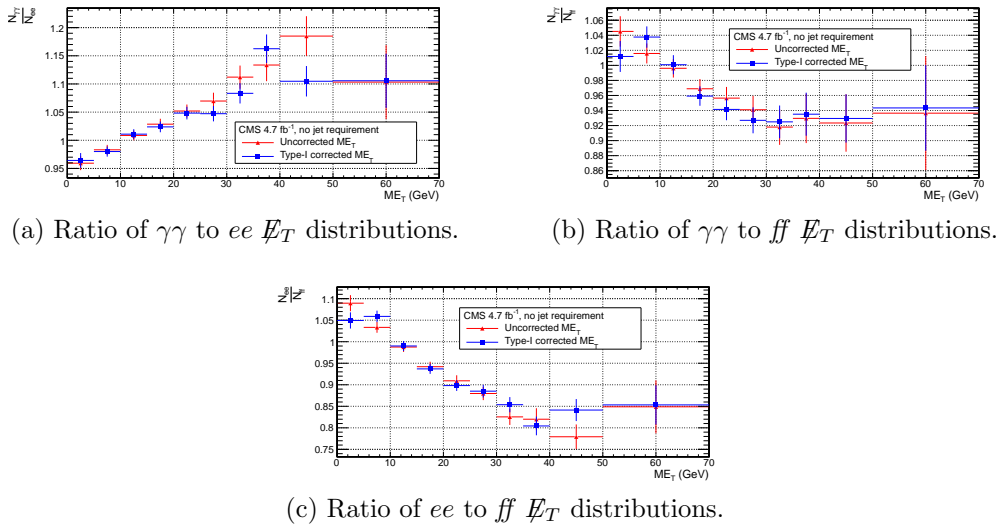


Figure 7.22: Agreement between  $\gamma\gamma$ ,  $ee$ , and  $ff$  samples for uncorrected (red triangles) and corrected (blue squares)  $\not{E}_T$ .

difference in the agreement of the background predictions and the search sample in a control region at low  $\not{E}_T$ , as shown in Figure 7.22. Since the control samples are derived from the same data as the search sample, any biases in the  $\not{E}_T$  reconstruction due to jet energy scale are present equally in both samples.

Tables 7.4 and 7.5 list all the errors on the  $ee$  and  $ff$  QCD background predictions, respectively, for the  $\not{E}_T$  bins used in the search. Table 7.6 lists the errors on the electroweak background prediction. Finally, Table 7.7 shows the errors on the total QCD + electroweak background prediction, broken down by origin (statistical or systematic) and QCD background estimation sample ( $ee$  or  $ff$ ). In the final result, only the  $ff$  QCD estimate is used.

## 7.4 Results

Figure 7.23( 7.24) shows the  $\not{E}_T$  distribution of the inclusive( $\geq 1$ -jet)  $\gamma\gamma$  search sample along with the predicted  $\not{E}_T$  distributions of the QCD and electroweak backgrounds. The observed number of two-photon events, background estimates and their errors,

Table 7.4: Errors on the  $ee$  QCD background prediction as a fraction of the  $ee$  prediction.

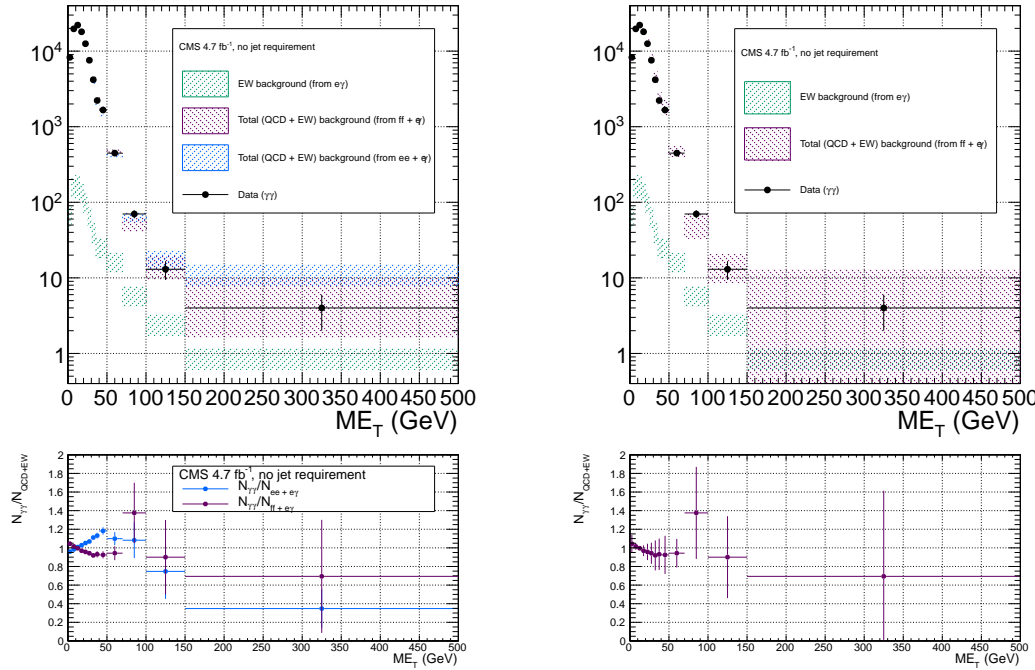
Source of error	Fractional uncertainty (%)				
	[50, 60)	[60, 70)	[70, 80)	[80, 100)	$\geq 100$
Total	3.9	8.1	16	25	25
Statistics	3.6	7.8	16	24	22
No. events	3.6	7.7	15	24	20
In norm. region	0.43	0.44	0.46	0.55	0.51
In this $E_T$ bin	3.5	7.7	15	24	20
Reweighting	0.73	1.2	3.5	4.3	7.7
In norm. region	0.19	0.19	0.2	0.24	0.23
In this $E_T$ bin	0.71	1.2	3.5	4.3	7.7
Systematics	2.6	4.4	1.2	7.5	14
$f_{e \rightarrow \gamma}$ (in norm. region)	0.0012	0.0012	0.0013	0.0015	0.0014
$m_{ee}$ background shape	1.4	2	0.72	5.5	12
Jet energy scale	2.2	3.9	0.96	5.1	6.9

Table 7.5: Errors on the  $ff$  QCD background prediction as a fraction of the  $ff$  prediction.

Source of error	Fractional uncertainty (%)				
	[50, 60)	[60, 70)	[70, 80)	[80, 100)	$\geq 100$
Total	15	25	61	34	64
Statistics	7.2	14	30	33	38
No. events	7.1	14	29	33	36
In norm. region	0.64	0.64	0.64	0.64	0.64
In this $E_T$ bin	7.1	14	29	33	36
Reweighting	0.85	2.7	5.1	6.9	13
In norm. region	0.27	0.27	0.27	0.27	0.27
In this $E_T$ bin	0.81	2.6	5.1	6.9	13
Systematics	13	21	53	6.6	52
$ee/ff$ difference	13	21	53	5.5	52
$f_{e \rightarrow \gamma}$ (in norm. region)	0.0012	0.0012	0.0012	0.0012	0.0012
Jet energy scale	0.099	1.7	1.8	3.5	1.8

Table 7.6: Errors on the  $e\gamma$  electroweak background prediction as a fraction of the  $e\gamma$  prediction.

Source of error	Fractional uncertainty (%)				
	[50, 60)	[60, 70)	[70, 80)	[80, 100)	$\geq 100$
Total	29	29	30	30	30
Statistics	3.6	5.2	6.7	7.2	6.5
Systematics ( $f_{e \rightarrow \gamma}$ )	29	29	29	29	29



(a)  $ee + e\gamma$  and  $ff + e\gamma$ . The widths of the bands correspond to the errors given in Table 7.7, excluding the error associated with the difference between the  $ee$  and  $ff$  QCD estimates for the  $ff + e\gamma$   $E_T$  distribution.

(b)  $ff + e\gamma$ . The widths of the bands correspond to the errors given in Table 7.7, including the error associated with the difference between the  $ee$  and  $ff$  QCD estimates.

Figure 7.23:  $E_T$  distribution of the  $\gamma\gamma$  search sample (black circles) along with the predicted  $E_T$  distributions of the QCD and electroweak backgrounds (blue band for  $ee$  QCD prediction + electroweak prediction, purple band for  $ff$  QCD prediction + electroweak prediction). The electroweak background prediction is shown in green. The bottom plots show the ratio of the  $\gamma\gamma E_T$  distribution to the  $ee + e\gamma$  background distribution (blue) and  $ff + e\gamma$  background distribution (purple).

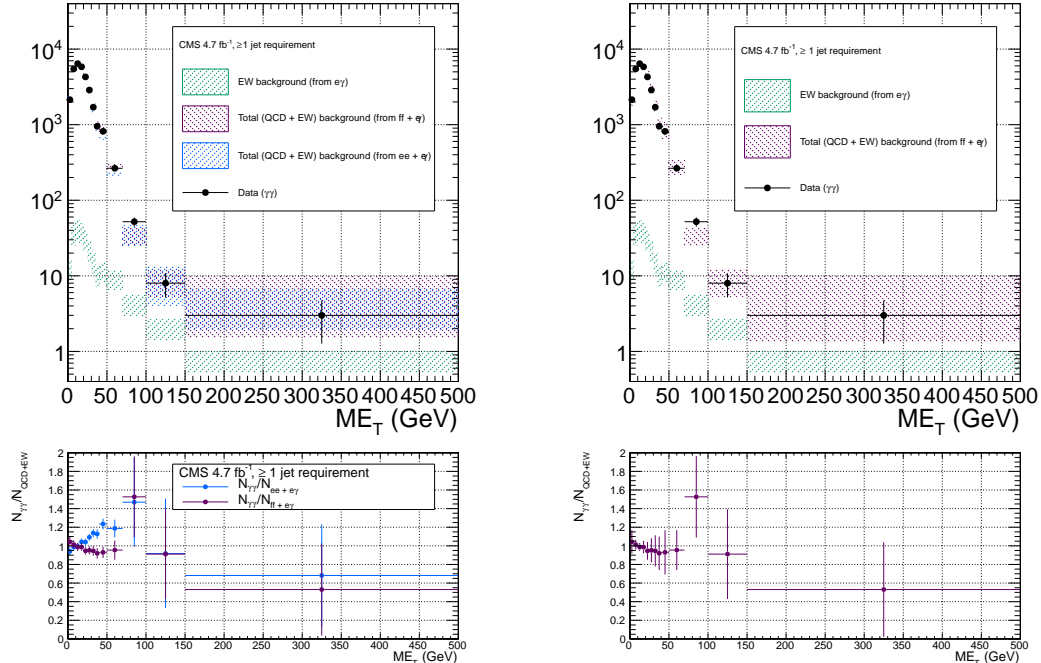
and expected number of inclusive( $\geq 1$ -jet) two-photon events from two representative GGM SUSY models are listed in Table 7.8( 7.9). (Details of the SUSY MC production are given in Chapter 8 and App. A.) No deviation from the Standard Model prediction is observed in the  $\gamma\gamma$  search sample.

Table 7.7: Errors on the total QCD + electroweak background prediction as a fraction of the total prediction.

Source of error	Fractional uncertainty (%)				
	[50, 60)	[60, 70)	[70, 80)	[80, 100)	$\geq 100$
Total ( $ee + e\gamma$ )	3.9	7.8	15	22	22
Statistics	3.4	7.3	14	21	18
QCD	3.4	7.3	14	21	18
Electroweak	0.13	0.3	0.53	0.79	0.76
Systematics	2.7	4.5	2.6	7.4	13
QCD	2.5	4.1	1.1	6.7	12
Electroweak	1	1.7	2.3	3.2	3.4
Total ( $ff + e\gamma$ )	14	24	54	30	54
Statistics	6.9	13	26	29	30
QCD	6.9	13	26	29	30
Electroweak	0.11	0.24	0.79	0.83	1.1
Systematics	12	20	47	6.7	43
QCD	12	20	47	5.8	43
Electroweak	0.9	1.3	3.4	3.4	4.8

Table 7.8: Observed numbers of two-photon events, background estimates and their errors, and expected numbers of two-photon events from two representative GGM SUSY models (details of MC simulation given in Chapter 8 and App. A) for the  $E_T$  bins used in the search. Errors on the background estimates are detailed in Tables 7.4, 7.5, 7.6, and 7.7. Errors on the expected numbers of GGM events are purely statistical.

Source	No. events				
	[50, 60)	[60, 70)	[70, 80)	[80, 100)	$\geq 100$
Observation ( $\gamma\gamma$ )	354	93	37	33	17
Predicted background ( $ff + e\gamma$ )	$361 \pm 51.5$	$113 \pm 27.1$	$26.9 \pm 14.5$	$23.9 \pm 7.23$	$20.2 \pm 10.9$
$m_{\tilde{q}} = 720$ GeV $M_3 = 720$ GeV $M_1 = 375$ GeV	$13.3 \pm 2.13$	$17.7 \pm 2.46$	$15.3 \pm 2.33$	$42.9 \pm 3.82$	$966 \pm 18.3$
$m_{\tilde{q}} = 1440$ GeV $M_3 = 1440$ GeV $M_1 = 375$ GeV	$0.008 \pm 0.003$	$0.009 \pm 0.003$	$0.012 \pm 0.003$	$0.030 \pm 0.005$	$1.92 \pm 0.04$



(a)  $ee + e\gamma$  and  $ff + e\gamma$ . The widths of the bands correspond to the errors given in Table 7.7, excluding the error associated with the difference between the  $ee$  and  $ff$  QCD estimates for the  $ff + e\gamma$   $E_T$  distribution.

(b)  $ff + e\gamma$ . The widths of the bands correspond to the errors given in Table 7.7, including the error associated with the difference between the  $ee$  and  $ff$  QCD estimates.

Figure 7.24:  $E_T$  distribution of the  $\gamma\gamma + \geq 1$  jet search sample (black circles) along with the predicted  $E_T$  distributions of the QCD and electroweak backgrounds (blue band for  $ee$  QCD prediction + electroweak prediction, purple band for  $ff$  QCD prediction + electroweak prediction). The electroweak background prediction is shown in green. The bottom plots show the ratio of the  $\gamma\gamma E_T$  distribution to the  $ee + e\gamma$  background distribution (blue) and  $ff + e\gamma$  background distribution (purple).

Table 7.9: Observed numbers of two-photon +  $\geq 1$ -jet events, background estimates and their errors, and expected numbers of two-photon +  $\geq 1$ -jet events from two representative GGM SUSY models (details of MC simulation given in Chapter 8 and App. A) for the  $\cancel{E}_T$  bins used in the search. Errors on the background estimates are detailed in Tables 7.4, 7.5, 7.6, and 7.7. Errors on the expected numbers of GGM events are purely statistical.

Source	No. events				
	[50, 60)	[60, 70)	[70, 80)	[80, 100)	$\geq 100$
Observation ( $\gamma\gamma + \geq 1$ jet)	202	63	27	25	11
Predicted background ( $ff + e\gamma$ )	$200 \pm 35.4$	$77.7 \pm 28.1$	$19.4 \pm 8.55$	$14.7 \pm 7.04$	$14.4 \pm 5.59$
$m_{\tilde{q}} = 720$ GeV $M_3 = 720$ GeV $M_1 = 375$ GeV	$13.3 \pm 2.13$	$17.7 \pm 2.46$	$15.3 \pm 2.33$	$42.9 \pm 3.82$	$965 \pm 18.3$
$m_{\tilde{q}} = 1440$ GeV $M_3 = 1440$ GeV $M_1 = 375$ GeV	$0.008 \pm 0.003$	$0.009 \pm 0.003$	$0.012 \pm 0.003$	$0.031 \pm 0.004$	$1.92 \pm 0.04$

# <sup>2005</sup> Chapter 8

## <sup>2006</sup> <sup>2007</sup> Interpretation of Results in Terms of GMSB Models

<sup>2008</sup> As shown in Figs. 7.23 and 7.24 and Tables 7.8 and 7.9, no excess of events above  
<sup>2009</sup> the Standard Model expectation is found in either the  $\geq 0$ - or  $\geq 1$ -jet analyses for the  
<sup>2010</sup> GMSB-sensitive region  $\cancel{E}_T \geq 50$  GeV. Therefore, upper limits on the production cross  
<sup>2011</sup> sections of various GMSB models are calculated and then translated into statements of  
<sup>2012</sup> exclusion. Section 8.1 describes the GMSB models that were generated with MC and  
<sup>2013</sup> tested for exclusion. The upper limit calculation and translation to model exclusions  
<sup>2014</sup> is laid out in Section 8.2. The upper limits themselves are presented in Section 8.3,  
<sup>2015</sup> and, finally, the exclusions are presented in Section 8.4.

### <sup>2016</sup> 8.1 Simplified Models

<sup>2017</sup> The exclusion reach of the two-photon search is presented for three different two-  
<sup>2018</sup> dimensional scans in GMSB parameter space. The first scan covers the bino NLSP  
<sup>2019</sup> scenario of Sec. 3.5. In this scan,  $M_2$ , which controls the amount of wino mixing, is  
<sup>2020</sup> set to 3.5 TeV.  $M_1$ , which controls the amount of bino mixing, is set to 375 GeV.  
<sup>2021</sup> This insures that all gauginos except the lightest neutralino are too heavy to be

2022 produced in significant numbers at the LHC. All other mass parameters except for  
 2023  $M_3$  ( $\sim$ gluino mass) and  $m_{\tilde{q}}$  ( $\sim$ first- and second-generation squark mass) are set to  
 2024 3.5 TeV, which insures that squark/gluino decay to intermediate states such as third-  
 2025 generation squarks or any flavor of lepton is strongly suppressed.  $M_3$  and  $m_{\tilde{q}}$  are  
 2026 scanned over from  $M_3 = m_{\tilde{q}} = 400$  GeV to  $M_3 = m_{\tilde{q}} = 2$  TeV in 80-GeV steps.  
 2027 The resulting simplified model consists only of a gluino, first- and second-generation  
 2028 squarks, and the lightest neutralino and its decay products (the gravitino is forced to  
 2029 be the LSP). The scan in  $M_3$ - $m_{\tilde{q}}$  space illuminates the sensitivity of the two-photon  
 2030 search to different levels of signal hadronic activity.

2031 The second scan is identical to the first except that the values of  $M_1$  and  $M_2$   
 2032 are inverted ( $M_1 = 3.5$  TeV and  $M_2 = 375$  GeV). This corresponds to the wino  
 2033 NLSP scenario of Sec. 3.5. Now, both the lightest neutralino and the lightest chargino  
 2034 have masses of order 375 GeV, and are therefore produced with approximately equal  
 2035 frequency in the gluino and squark decays. The chargino decays to  $W + \tilde{G}$ , so final  
 2036 states in this scan often include leptons or large jet multiplicity. Since there is no  
 2037 guarantee that two neutralinos will be produced and will decay to two photons, this  
 2038 search is not well optimized for the wino NLSP scenario. However, a related CMS  
 2039 search with one photon and  $\geq 3$  jets has an exclusion reach of  $\sim 1$  TeV in  $M_3$  and  
 2040  $m_{\tilde{q}}$  for this scenario [29].

2041 The third scan is  $M_3$  vs.  $M_1$  for  $m_{\tilde{q}}$ ,  $M_2$ , and all other mass parameters equal to  
 2042 2.5 TeV.  $M_3$  is scanned from 160 GeV to 2 TeV in 80-GeV steps, while  $M_1$  is scanned  
 2043 from 150 GeV to 1050 GeV in 100-GeV steps.  $M_3 < M_1$  is not allowed, as this would  
 2044 imply that the gluino, not the lightest neutralino, is the NLSP. This scan highlights  
 2045 the performance of the two-photon search as a function of  $M_1$  (i.e. as a function of  
 2046 decays open to the neutralino), whereas the previous two scans keep  $M_1$  fixed.

2047 For each scan, the sparticle mass spectrum is generated with SuSpect 2.41 [121]  
 2048 and the decay widths with SDECAY 1.3 [122]. The event data (including produc-

2049 tion, unstable particle decay, parton showering, and hadronization) is generated with  
 2050 Pythia 6.422 [128], using the sparticle mass spectra and decay widths as inputs. The  
 2051 gravitino is always forced to be the LSP. The simulated data are reconstructed with  
 2052 CMSSWv4.2.2, which uses a detector simulation based on GEANT 4 [123]. Next to  
 2053 leading order cross sections are calculated with PROSPINO 2.1 [124], and shown in  
 2054 Figure 8.1 for the three signal MC scenarios.

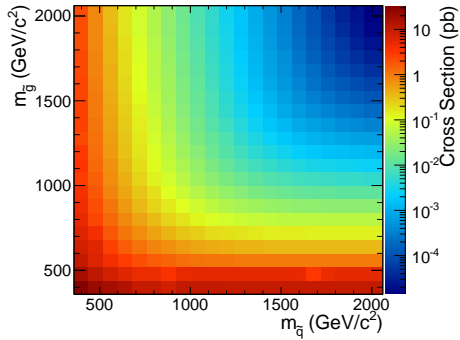
## 2055 8.2 Upper Limit Calculation and Model Exclusion

2056 The upper limits are calculated according to the prescription followed for the 2011  
 2057 ATLAS + CMS Higgs limit combination [111]. This prescription utilizes the frequen-  
 2058 tist  $\text{CL}_s$  method [112] with profile likelihood test statistic [113]. The  $\text{CL}_s$  method and  
 2059 the profile likelihood are explained in Section 8.2.2, using specific signal MC points to  
 2060 illustrate the procedure. First, however, the signal MC acceptance  $\times$  efficiency, which  
 2061 is an input to the limit setting procedure, is presented in Section 8.2.1.

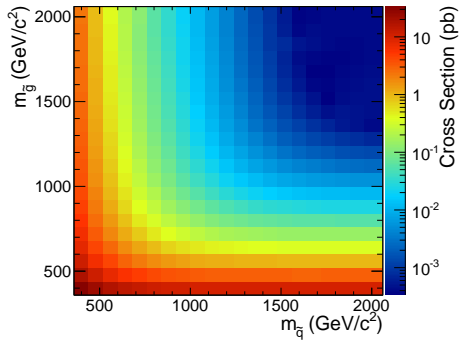
### 2062 8.2.1 Signal Acceptance $\times$ Efficiency

2063 The signal acceptance  $\times$  efficiency (denoted  $\mathcal{A} \times \epsilon$ ), defined for each signal point as  
 2064 the number of  $\gamma\gamma$  events selected with  $\cancel{E}_T \geq 50$  GeV divided by the total number of  
 2065 events generated, is shown in Figure 8.2 for the three different scenarios described in  
 2066 Sec. 8.1.

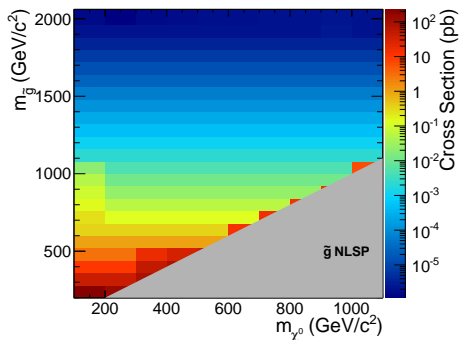
2067 In Figs. 8.2a and 8.2b, the large drop in  $\mathcal{A} \times \epsilon$  for  $m_{\tilde{q}} > M_3$  is due to an increase  
 2068 in the number of jets produced per event and a consequent reduction in the number  
 2069 of photons that pass the  $I_{\text{comb}} < 6$  GeV cut. For  $m_{\tilde{q}} > M_3$ , there is more phase space  
 2070 available to produce gluinos in the hard scatter than squarks. However, since gluinos  
 2071 must decay via squarks, and in these models all squarks are heavier than the gluino,  
 2072 only the two-jet decay  $\tilde{g} \rightarrow qq\tilde{\chi}^0$  is available. Conversely, when  $m_{\tilde{q}} < M_3$ , there is



(a)  $M_2$  decoupled ( $M_2 = 3.5$  TeV),  $M_1 = 375$  GeV,  $M_3$  vs.  $m_{\tilde{q}}$ .



(b)  $M_1$  decoupled ( $M_1 = 3.5$  TeV),  $M_2 = 375$  GeV,  $M_3$  vs.  $m_{\tilde{q}}$ .



(c)  $m_{\tilde{q}}$  decoupled ( $m_{\tilde{q}} = 2.5$  TeV),  $M_3$  vs.  $M_1$ .

Figure 8.1: Next to leading order cross sections for the three different MC scenarios described in the text.

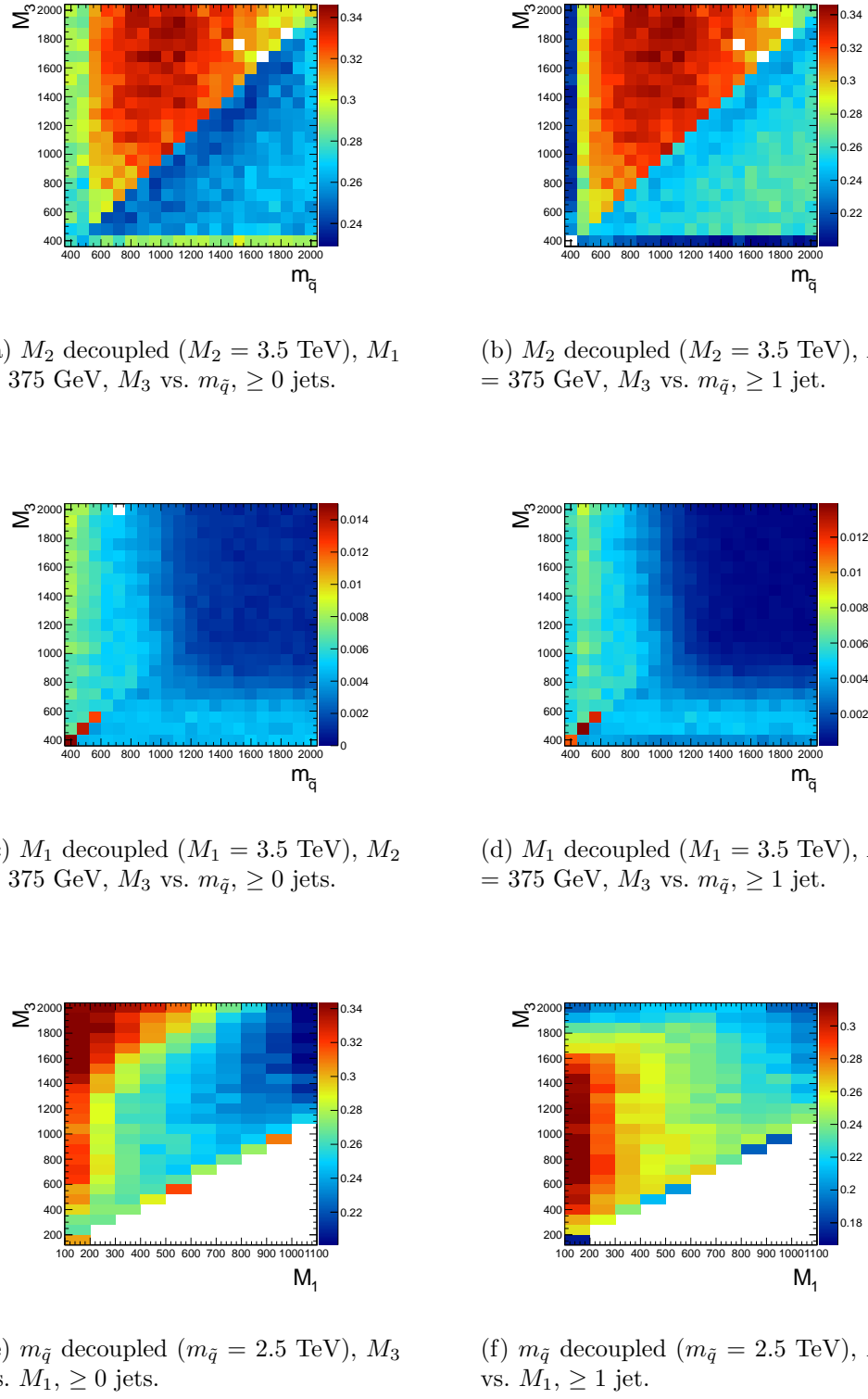


Figure 8.2: Signal acceptance  $\times$  efficiency (defined in the text) for the three different scenarios described in Sec. 8.1.

more phase space available to produce squarks, which may then decay via one jet as  $\tilde{q} \rightarrow q\tilde{\chi}^0$ . Jets in SUSY events may be very close to the neutralino decay photons, and as a result the photons may fail the strict isolation requirements, leading to lower  $\mathcal{A} \times \epsilon$  for jet-rich events. The worsened acceptance along  $M_3 = 400$  GeV and  $m_{\tilde{q}} = 400$  GeV in Fig. 8.2b is due to efficiency of the jet cut, which decreases drastically as  $M_3$  and  $m_{\tilde{q}}$  approach  $M_1$  because of shrinking phase space to produce hard jets in the squark and gluino decays to neutralinos.

The broad peak in  $\mathcal{A} \times \epsilon$  shown in Fig. 8.2a for  $m_{\tilde{q}} < M_3$  and  $\sim 600$  GeV  $< m_{\tilde{q}} < \sim 1600$  GeV is due to the  $\cancel{E}_T > 50$  GeV cut. The efficiency of the cut decreases as  $m_{\tilde{q}}$  decreases because of the fixed  $M_1$  of 375 GeV. If the squark-neutralino mass splitting gets too small, the likelihood of producing an energetic enough gravitino to pass the  $\cancel{E}_T$  cut decreases.

$\mathcal{A} \times \epsilon$  is generally much lower for the  $M_2 = 375$  GeV grid (Figs. 8.2c and 8.2d) due to the larger contribution from chargino decays to  $W + \tilde{G}$ , which do not give rise to photons in the final state. The increased acceptance for  $M_3 > m_{\tilde{q}}$  is due to the same jet multiplicity issue affecting the  $M_1 = 375$  GeV grid. As  $M_3$  and  $m_{\tilde{q}}$  increase relative to the fixed  $M_2$ , the jets from squark and gluino decay get more energetic, increasing the chance that they will overlap with the neutralino decay photon and cause it to fail the isolation cut. For  $m_{\tilde{q}} \gtrsim 1$  TeV and  $M_3 \gtrsim 800$  GeV, the acceptance is so low that not enough events were simulated to see the acceptance decrease over the statistical error.

In Fig. 8.2e, the neutralino is always heavy enough to guarantee decay to a photon that can pass the 40 GeV  $p_T$  cut.  $\mathcal{A} \times \epsilon$  increases as  $M_3$  increases because the larger gluino-neutralino mass splitting gives the neutralino a larger kinetic energy, increasing the chance that it will decay to a photon with 40 GeV  $p_T$  or higher. After the bino mass increases beyond the threshold needed to produce high  $p_T$  photons,  $\mathcal{A} \times \epsilon$  decreases with increasing  $M_1$ , independent of gluino mass, because higher  $M_1$  means more phase

2100 space is open to decays of the form  $\tilde{\chi}_1^0 \rightarrow Z\tilde{G}$  and  $\tilde{\chi}_1^0 \rightarrow H\tilde{G}$ . The two-photon search  
 2101 is naturally not as efficient for these decays.

Added

2102 There is a small chance that some real GMSB signal events could be reconstructed signal  
 2103 as  $ff$  events in the data. To correct the signal acceptance for this effect, the number contamination  
 2104 of signal events reconstructed as  $ff$  events is subtracted from the number of signal  $\gamma\gamma$  ination  
 2105 events, effectively reducing the signal acceptance. This is generally a small correction par.  
 2106 ( $\sim 5\%$ ).

## 2107 8.2.2 $CL_s$ and the Profile Likelihood Test Statistic

2108 The process of setting a cross section upper limit entails (1) defining a test statistic,  
 2109 (2) generating a distribution for that test statistic under the signal + background  
 2110 and background-only hypotheses, and (3) deciding whether or not the observed value  
 2111 of the test statistic is more compatible with the signal + background (i.e. weaker  
 2112 upper limit) or background-only (i.e. stronger upper limit) hypotheses by considering  
 2113 where it falls within the test statistic distributions. An important requirement on the  
 2114 choice of test statistic is that it be able to effectively discriminate between the signal  
 2115 + background and background-only hypotheses, i.e. the shape of its distribution for  
 2116 these two hypotheses should be different. The procedure for determining the exclud-  
 2117 ability of a particular model given the value of the test statistic observed should not  
 2118 give rise to pathological behavior in the presence of small signals, low statistics, or  
 2119 weak sensitivity to models, as is commonly the case in high energy physics. These  
 2120 demands on the test statistic and the limit setting procedure itself dictate the choice  
 2121 of the profile likelihood test statistic and  $CL_s$  procedure.

2122 In the remainder of this section, the notation is taken from ref. [111].

2123 **Profile Likelihood**

2124 For a specific model of GMSB, the limit setting procedure concerns the question of  
 2125 whether to reject the signal + background hypothesis  $\mu s + b$  in favor of the background-  
 2126 only (Standard Model) hypothesis of  $b$  ( $\mu = 0$ ).  $\mu$  is a dimensionless signal strength  
 2127 parameter.  $s$  is the expected number of signal events, calculated from MC simulated  
 2128 signal events as in Secs. 8.1 and 8.2.1.  $b$  is the expected number of background events,  
 2129 estimated in Chap. 7. By the Neyman-Pearson lemma [114], the ratio of the likelihood  
 2130 of  $\mu s + b$  to the likelihood of  $b$  is the test statistic with the highest power to reject  $\mu s + b$   
 2131 at whatever confidence level is desired. In practice, this means that the likelihood ratio  
 2132 is the best discriminator between the GMSB and Standard Model hypotheses.

2133 The likelihood of the signal + background hypothesis as a function of the data  
 2134 (either real or generated) is defined as

$$\mathcal{L}(\text{data}|\mu, \theta) = \prod_{i=1}^N \frac{(\mu s_i(\theta) + b_i(\theta))^{n_i}}{n_i!} e^{-\mu s_i(\theta) - b_i(\theta)} p(\tilde{\theta}|\theta) \quad (8.1)$$

2135 where  $N = 5$  is the number of  $E_T$  bins used in the analysis ([50, 60) GeV, [60,  
 2136 70) GeV, [70, 80) GeV, [80, 100) GeV, and [100,  $\infty$ ) GeV);  $s_i(\theta)$  and  $b_i(\theta)$  are the  
 2137 expected number of signal and background events in  $E_T$  bin  $i$ , respectively;  $n_i$  is the  
 2138 number of events observed in  $E_T$  bin  $i$ ; and  $\theta$  represents all the nuisance parameters  
 2139 (uncertainties).  $p(\tilde{\theta}|\theta)$  represents the product of probability distribution functions  
 2140 (PDFs) for the nuisance parameters, where  $\tilde{\theta}$  is the default value of the nuisance  
 2141 parameter. In this analysis, there are eight experimental nuisance parameters per  $E_T$   
 2142 bin, given here as relative errors on the expected number of signal events:

- 2143 • Uncertainty on the measured integrated luminosity (4.5% in all bins) [115]
- 2144 • Uncertainty on the signal acceptance due to  $\epsilon_e^{\text{data}}/\epsilon_e^{\text{MC}}$  and the pixel veto effi-  
 2145 ciency error (cf. Sec. 6.4.2) (8% in all bins)

- 2146     ● Uncertainty on the signal acceptance due to imperfect pileup simulation (2.6%  
 2147               in all bins)
  
- 2148     ● Systematic uncertainty on QCD background prediction due to difference be-  
 2149               tween  $ff$  and  $ee$  estimates (5.5%-53% of the QCD background depending on  
 2150               bin)
  
- 2151     ● Systematic uncertainty on electroweak background prediction due to  $p_T$  depen-  
 2152               dence of  $f_{e \rightarrow \gamma}$  (29%-30% of the electroweak background depending on bin)
  
- 2153     ● Statistical uncertainty on the signal acceptance (1.8%-100% depending on model  
 2154               and bin)
  
- 2155     ● Statistical uncertainty on the QCD background prediction (7.2%-38% of the  
 2156               QCD background depending on bin)
  
- 2157     ● Statistical uncertainty on the electroweak background prediction (3.6%-7.2% of  
 2158               the electroweak background depending on bin)
  
 2159     and one very small theoretical nuisance parameter: the uncertainty on the signal  
 2160     acceptance due to underlying parton distribution function (PDF) uncertainties. In  
 2161     the limit-setting code, the uncertainties on signal acceptance due to photon efficiency  
 2162     and PDF errors are added in quadrature and treated as one. The uncertainty on the  
 2163     signal acceptance due to jet energy correction uncertainties is negligible, due to the  
 2164     presence of many hard jets in GMSB signal events. The uncertainties on integrated  
 2165     luminosity and pileup are 100% correlated between  $\cancel{E}_T$  bins, and the uncertainty on  
 2166     signal acceptance can usually be treated similarly because the error on  $\epsilon_e^{\text{data}}/\epsilon_e^{\text{MC}}$  often  
 2167     dominates the PDF error on acceptance (although these three uncertainties are 0%  
 2168     correlated with each other).

2169     To estimate the uncertainty due to imperfect simulation of LHC pileup, the square  
 2170     of the average data efficiency for photons over the range 1-15 reconstructed primary

vertices (see Fig. 6.17a), weighted by the number of  $\gamma\gamma$  events per primary vertex bin, is calculated. The efficiency per primary vertex bin is estimated from a linear fit to Fig. 6.17a. The process is repeated for MC using the entire range of primary vertices in Fig. 6.17a (all MC signal points have the same pileup simulation). The error is taken as  $2 \times |\text{avg. data efficiency squared} - \text{avg. MC efficiency squared}| / (\text{avg. data efficiency squared} + \text{avg. MC efficiency squared})$ .

Each nuisance parameter PDF is modeled by a log-normal distribution:

$$p(\tilde{\theta}|\theta) = \frac{1}{\sqrt{2\pi} \ln \kappa} \exp\left(-\frac{(\ln \tilde{\theta}/\theta)^2}{2(\ln \kappa)^2}\right) \frac{1}{\tilde{\theta}} \quad (8.2)$$

where  $\tilde{\theta} = 1$  and  $\kappa = 1 +$  the one-standard-deviation relative error on the nuisance parameter (e.g. for the 4.5% error due to integrated luminosity,  $\kappa = 1.045$ ).

Similarly, the likelihood of the background-only hypothesis as a function of the data (either real or generated) is defined as

$$\mathcal{L}(\text{data}|0, \theta) = \prod_{i=1}^N \frac{b_i(\theta)^{n_i}}{n_i!} e^{-b_i(\theta)} p(\tilde{\theta}|\theta) \quad (8.3)$$

The profile likelihood test statistic is defined as

$$\tilde{q}_\mu = -2 \ln \frac{\mathcal{L}(\text{data}|\mu, \hat{\theta}_\mu)}{\mathcal{L}(\text{data}|\hat{\mu}, \hat{\theta})}, 0 \leq \hat{\mu} \leq \mu \quad (8.4)$$

where the  $\hat{\theta}_\mu$  maximize  $\mathcal{L}(\text{data}|\mu, \hat{\theta}_\mu)$  when it is evaluated at a particular  $\mu$ , and  $\hat{\mu}$  and  $\hat{\theta}$  are the global maximum likelihood estimators of  $\mu$  and  $\theta$ . The condition  $\hat{\mu} \leq \mu$  insures that the obtained cross section upper limit is one-sided, i.e. there is no possibility to find a lower limit on the cross section. The profile likelihood test

2187 statistic has the nice property that in the asymptotic (large statistics) limit its PDF  
 2188 can be approximated by analytic formulae, eliminating the need to generate multiple  
 2189 toy experiments to get the PDF. However, the approximation breaks down for small  
 2190 numbers of observed events, so in practice the asymptotic limit is only used as a first  
 2191 guess at the location of the true limit.

2192 The PDFs  $f(\tilde{q}_\mu | \mu, \hat{\theta}_\mu^{\text{obs}})$  and  $f(\tilde{q}_\mu | 0, \hat{\theta}_0^{\text{obs}})$  for the profile likelihood test statistic  
 2193 under the signal + background and background-only hypotheses, respectively, are  
 2194 obtained by generating toy MC pseudo-experiments.  $\hat{\theta}_\mu^{\text{obs}}$  and  $\hat{\theta}_0^{\text{obs}}$  maximize Eqs. 8.1  
 2195 and 8.3, respectively, when they are evaluated for the observed data. For each  $\mu$  (and  
 2196 the background-only hypothesis  $\mu = 0$ ), the pseudo-experiments are generated by  
 2197 picking random values of  $s$  and  $b$  from a Poisson distribution with the  $\theta$  fixed as just  
 2198 described.

2199 **CL<sub>s</sub>**

2200 In the classical frequentist approach, a signal model may be excluded at the 95%  
 2201 confidence level (CL) if the probability of any measurement of the test statistic to be  
 2202 greater than or equal to the observed value given the signal + background hypothesis  
 2203 is 5%. This means that the observed value of the test statistic is so incompatible  
 2204 with what one would expect to observe if the signal model were true that, under the  
 2205 assumption that the signal model *is* true, the chance of observing a test statistic even  
 2206 further afield from the signal expectation is only 5%. Mathematically,

$$\begin{aligned} p_\mu &\equiv P(\tilde{q}_\mu \geq \tilde{q}_\mu^{\text{obs}} | \mu s + b) = \int_{\tilde{q}_\mu^{\text{obs}}}^{\infty} f(\tilde{q}_\mu | \mu, \hat{\theta}_\mu^{\text{obs}}) d\tilde{q}_\mu \\ p_\mu &\leq 0.05 \Rightarrow \text{exclude } \mu \end{aligned} \quad (8.5)$$

2207 where  $\tilde{q}_\mu^{\text{obs}}$  is the observed value of the test statistic and  $p_\mu$  is the p-value. As indicated  
 2208 in Eq. 8.5, the p-value is simply the integral of the PDF of  $\tilde{q}_\mu$  from  $\tilde{q}_\mu^{\text{obs}}$  to infinity.

2209 By construction, the classical 95% CL frequentist approach described above will  
 2210 reject a true signal + background hypothesis 5% of the time. This can happen if the  
 2211 experiment gets “unlucky” and the observation fluctuates low, causing  $\tilde{q}_\mu^{\text{obs}}$  to fall in  
 2212 the tail of the  $\tilde{q}_\mu$  distribution. This poses a problem for the case of very weak signals  
 2213 ( $\mu \sim 0$ ), because it will lead to spurious exclusions of models to which the experiment  
 2214 has little sensitivity. To avoid this pitfall, the  $\text{CL}_s$  limit setting method is used.

2215 In the  $\text{CL}_s$  method, the classical frequentist p-value of Eq. 8.5 is simply divided by  
 2216 one minus the p-value of the background-only hypothesis, and it is this ratio, rather  
 2217 than the p-value of the signal + background hypothesis alone, that is required to be  
 2218  $\leq 0.05$ . Mathematically,

$$1 - p_0 \equiv P(\tilde{q}_\mu \geq \tilde{q}_\mu^{\text{obs}} | b) = \int_{\tilde{q}_\mu^{\text{obs}}}^{\infty} f(\tilde{q}_\mu | 0, \hat{\theta}_0^{\text{obs}}) d\tilde{q}_\mu \quad (8.6)$$

$$\text{CL}_s(\mu) \equiv \frac{p_\mu}{1 - p_0} \quad (8.7)$$

$$\text{CL}_s(\mu) \leq 0.05 \Rightarrow \text{exclude } \mu$$

2219 where  $p_0$  is the p-value for the background-only hypothesis ( $\mu = 0$ ). In the case of  
 2220 low sensitivity to  $\mu$ ,  $p_\mu \lesssim 1 - p_0$ , so  $\text{CL}_s(\mu) \lesssim 1$  and  $\mu$  will not be excluded. On the  
 2221 contrary, for high sensitivity to  $\mu$  ( $\mu s \gg \sigma_b$ ),  $p_\mu \ll 1 - p_0$ , so models that can be  
 2222 excluded by the criterion  $p_\mu \leq 0.05$  will also be excluded by the criterion  $\text{CL}_s \leq 0.05$ .  
 2223 Compared to the classical frequentist method,  $\text{CL}_s$  limits can be a little stronger in  
 2224 the case of low signal sensitivity [111].

2225 To determine the upper limit on the cross section of a particular model, the lowest  
 2226 value of  $\mu$  for which  $\text{CL}_s(\mu) \leq 0.05$ , denoted  $\mu^{95\% \text{CL}}$ , is found. The cross section upper  
 2227 limit of that model is then simply  $\mu^{95\% \text{CL}}$  multiplied by the expected cross section of

2228 the model (cf. Fig. 8.1).

2229 In contrast to the observed upper limit, the expected upper limit is calculated from  
 2230 an ensemble of background-only MC pseudo-experiments. The distribution  $f(\mu_{\text{pseudo}}^{\text{95%CL}})$   
 2231 is plotted (one entry per pseudo-experiment). The median expected upper limits and  
 2232  $\pm 1\sigma$  and  $\pm 2\sigma$  bands are defined as

$$0.5 = \int_0^{\mu_{\text{exp}}^{\text{95%CL}}} f(\mu_{\text{pseudo}}^{\text{95%CL}}) d\mu_{\text{pseudo}}^{\text{95%CL}} \quad (8.8)$$

$$0.16 = \int_0^{\mu_{-1\sigma,\text{exp}}^{\text{95%CL}}} f(\mu_{\text{pseudo}}^{\text{95%CL}}) d\mu_{\text{pseudo}}^{\text{95%CL}} \quad (8.9)$$

$$0.84 = \int_0^{\mu_{+1\sigma,\text{exp}}^{\text{95%CL}}} f(\mu_{\text{pseudo}}^{\text{95%CL}}) d\mu_{\text{pseudo}}^{\text{95%CL}} \quad (8.10)$$

$$0.025 = \int_0^{\mu_{-2\sigma,\text{exp}}^{\text{95%CL}}} f(\mu_{\text{pseudo}}^{\text{95%CL}}) d\mu_{\text{pseudo}}^{\text{95%CL}} \quad (8.11)$$

$$0.975 = \int_0^{\mu_{+2\sigma,\text{exp}}^{\text{95%CL}}} f(\mu_{\text{pseudo}}^{\text{95%CL}}) d\mu_{\text{pseudo}}^{\text{95%CL}} \quad (8.12)$$

2233 The technical procedure followed to calculate the 95% CL cross section upper  
 2234 limits for each GMSB model tested is given below.

- 2235 1. Calculate a guess for the median expected limit and  $\pm 2\sigma$  error bands ( $\mu_{\pm 2\sigma,\text{guess}}^{\text{95%CL}}$ )  
   2236 using the asymptotic formulae for  $f(\tilde{q}_\mu | 0, \hat{\theta}_0^{\text{obs}})$ .
- 2237 2. Calculate observed ( $\mu_{\text{obs,asym}}^{\text{95%CL}}$ ), median expected ( $\mu_{\text{exp,asym}}^{\text{95%CL}}$ ), and  $\pm 1\sigma$  ( $\mu_{\pm 1\sigma,\text{asym}}^{\text{95%CL}}$ )  
   2238 and  $\pm 2\sigma$  ( $\mu_{\pm 2\sigma,\text{asym}}^{\text{95%CL}}$ ) expected CL<sub>s</sub> limits using the asymptotic formulae for  
   2239  $f(\tilde{q}_\mu | \mu, \hat{\theta}_\mu^{\text{obs}})$  and  $f(\tilde{q}_\mu | 0, \hat{\theta}_0^{\text{obs}})$ . Restrict the range of  $\mu_{\text{obs,asym}}^{\text{95%CL}}$  and  $\mu_{\text{exp,asym}}^{\text{95%CL}}$  to  
   2240  $[0, 5 \times \mu_{\pm 2\sigma,\text{guess}}^{\text{95%CL}}]$  (this avoids pathological behavior of the limit-setting code  
   2241 when the expected number of signal events is much greater than the observed  
   2242 number of events and only introduces a  $\sim 5\%$  upward bias in the observed limit,  
   2243 well within the  $\pm 1\sigma$  error bands).
- 2244 3. Calculate median expected ( $\mu_{\text{exp}}^{\text{95%CL}}$ ) and  $\pm 1\sigma$  ( $\mu_{\pm 1\sigma}^{\text{95%CL}}$ ) and  $\pm 2\sigma$  ( $\mu_{\pm 2\sigma}^{\text{95%CL}}$ ) ex-

2245 pected  $\text{CL}_s$  limits using 100 toy MC pseudo-experiments to generate  $f(\tilde{q}_\mu|\mu, \hat{\theta}_\mu^{\text{obs}})$   
 2246 and  $f(\tilde{q}_\mu|0, \hat{\theta}_0^{\text{obs}})$ . Restrict the range of  $\mu_{\text{exp}}^{95\%\text{CL}}$  to  $[0, 5 \times \mu_{\pm 2\sigma, \text{guess}}^{95\%\text{CL}}]$ .

2247 4. If  $\mu_{\pm 2\sigma}^{95\%\text{CL}}$  could not be calculated, set  $\mu_{\pm 2\sigma}^{95\%\text{CL}} = \mu_{\pm 2\sigma, \text{asym}}^{95\%\text{CL}}$  instead.

2248 5. If  $\mu_{+2\sigma}^{95\%\text{CL}} \neq \mu_{-2\sigma}^{95\%\text{CL}}$  and  $\mu_{\text{obs}, \text{asym}}^{95\%\text{CL}} > 0.0001$ :

2249     • If  $\mu_{\text{obs}, \text{asym}}^{95\%\text{CL}} > \mu_{+2\sigma}^{95\%\text{CL}}$ , set  $\mu_{+2\sigma}^{95\%\text{CL}} = 1.3 \times \mu_{\text{obs}, \text{asym}}^{95\%\text{CL}}$ .

2250     • If  $\mu_{\text{obs}, \text{asym}}^{95\%\text{CL}} < \mu_{-2\sigma}^{95\%\text{CL}}$ , set  $\mu_{-2\sigma}^{95\%\text{CL}} = 0.7 \times \mu_{\text{obs}, \text{asym}}^{95\%\text{CL}}$ .

2251 6. If  $\mu_{+2\sigma}^{95\%\text{CL}} = \mu_{-2\sigma}^{95\%\text{CL}}$ , set  $\mu_{\pm 2\sigma}^{95\%\text{CL}} = \mu_{\pm 2\sigma, \text{asym}}^{95\%\text{CL}}$  instead.

2252 7. Scan over 100 equally spaced test values of  $\mu$  between  $\mu_{-2\sigma}^{95\%\text{CL}}$  and  $\mu_{+2\sigma}^{95\%\text{CL}}$  and,  
 2253 if  $\mu > 0.0001$ , calculate the  $\text{CL}_s$  p-value ( $p_\mu$ ) for this test value of  $\mu$  to  $10^{-6}$   
 2254 precision using a minimum of 500 toy experiments to generate  $f(\tilde{q}_\mu|\mu, \hat{\theta}_\mu^{\text{obs}})$  and  
 2255  $f(\tilde{q}_\mu|0, \hat{\theta}_0^{\text{obs}})$ .

2256 8. Determine the observed ( $\mu_{\text{obs}, \text{scan}}^{95\%\text{CL}}$ ), median expected ( $\mu_{\text{exp}, \text{scan}}^{95\%\text{CL}}$ ), and  $\pm 1\sigma$  ( $\mu_{\pm 1\sigma, \text{scan}}^{95\%\text{CL}}$ )  
 2257 and  $\pm 2\sigma$  ( $\mu_{\pm 2\sigma, \text{scan}}^{95\%\text{CL}}$ ) expected  $\text{CL}_s$  limits from the scan p-values for the signal  
 2258 + background and background-only pseudo-experiments.

2259 Finally, a particular GMSB model is excluded if the upper limit on the cross  
 2260 section for that model is less than the expected theoretical cross section.

### 2261 8.3 Cross Section Upper Limits

2262 Figure 8.3 shows the observed upper limits on the cross sections for the models de-  
 2263 scribed in Sec. 8.1. In some ( $\mathcal{O}(10^{-3})$ ) cases, the upper limit is zero due to a compu-  
 2264 tational failure. The upper limit for these points is estimated from the average of the  
 2265 upper limits of the four neighboring points, as shown in Figure 8.4. If any of the four  
 2266 points is also missing a valid upper limit, it is dropped from the average. The errors

2267 on the individual upper limits used in the estimate are propagated to the error on  
 2268 the average.

## 2269 8.4 Exclusion Contours

2270 Exclusion contours for the GMSB models discussed above are shown in Figure 8.5. The  
 2271 contours are derived from plots of predicted cross section minus cross section upper  
 2272 limit ( $\sigma \times (1 - \mu^{95\%CL})$ ), where  $\sigma$  is the nominal value of the predicted cross section  
 2273 for a given GMSB model) vs. the two model parameters of interest, so the values are  
 2274 either negative (not excluded) or positive (excluded). Sometimes, a particular point  
 2275 may have a different sign than its four same-sign neighbors (cf. Fig. 8.4) due to a  
 2276 fluctuation. In these cases,  $\sigma \times (1 - \mu^{95\%CL})$  for the anomalous point is estimated  
 2277 as the average  $\sigma \times (1 - \mu^{95\%CL})$  of the four neighboring points. The errors on the  
 2278 individual values of  $\sigma \times (1 - \mu^{95\%CL})$  used in the estimate are propagated to the error  
 2279 on the average.

2280 In the plots in Fig. 8.5, the expected limit (i.e. the contour derived from  $\sigma \times (1 -$   
 2281  $\mu_{\text{exp,scan}}^{95\%CL})$ ) is drawn in dark orange and the  $1\sigma$  experimental band around the expected  
 2282 limit (i.e. the shaded region between the contours derived from  $\sigma \times (1 - \mu_{\pm 1\sigma, \text{scan}}^{95\%CL})$ ) is  
 2283 drawn in light orange. The values of  $\mu_{\text{exp,scan}}^{95\%CL}$  and  $\mu_{\pm 1\sigma, \text{scan}}^{95\%CL}$  only reflect the experimental  
 2284 uncertainties given in Sec. 8.2.2.

2285 The observed limits (derived from  $\sigma \times (1 - \mu_{\text{obs,scan}}^{95\%CL})$ ) and  $1\sigma$  theoretical error  
 2286 bands around the observed limits in Fig. 8.5 are drawn in blue. The contours that  
 2287 define this band are derived from  $\pm(\sigma_{\pm 1\sigma} - \sigma \mu_{\text{obs,scan}}^{95\%CL})$ , where  $\sigma_{\pm 1\sigma}$  is the nominal  
 2288 value of the predicted cross section  $\pm$  the one-standard-deviation theoretical error on  
 2289 the predicted cross section. In this way, the experimental and theoretical errors, the  
 2290 latter due to imperfect knowledge of the predicted cross section, are shown separately.  
 2291 Comparing with Fig. 8.1, one can easily see that the shapes of the exclusion curves

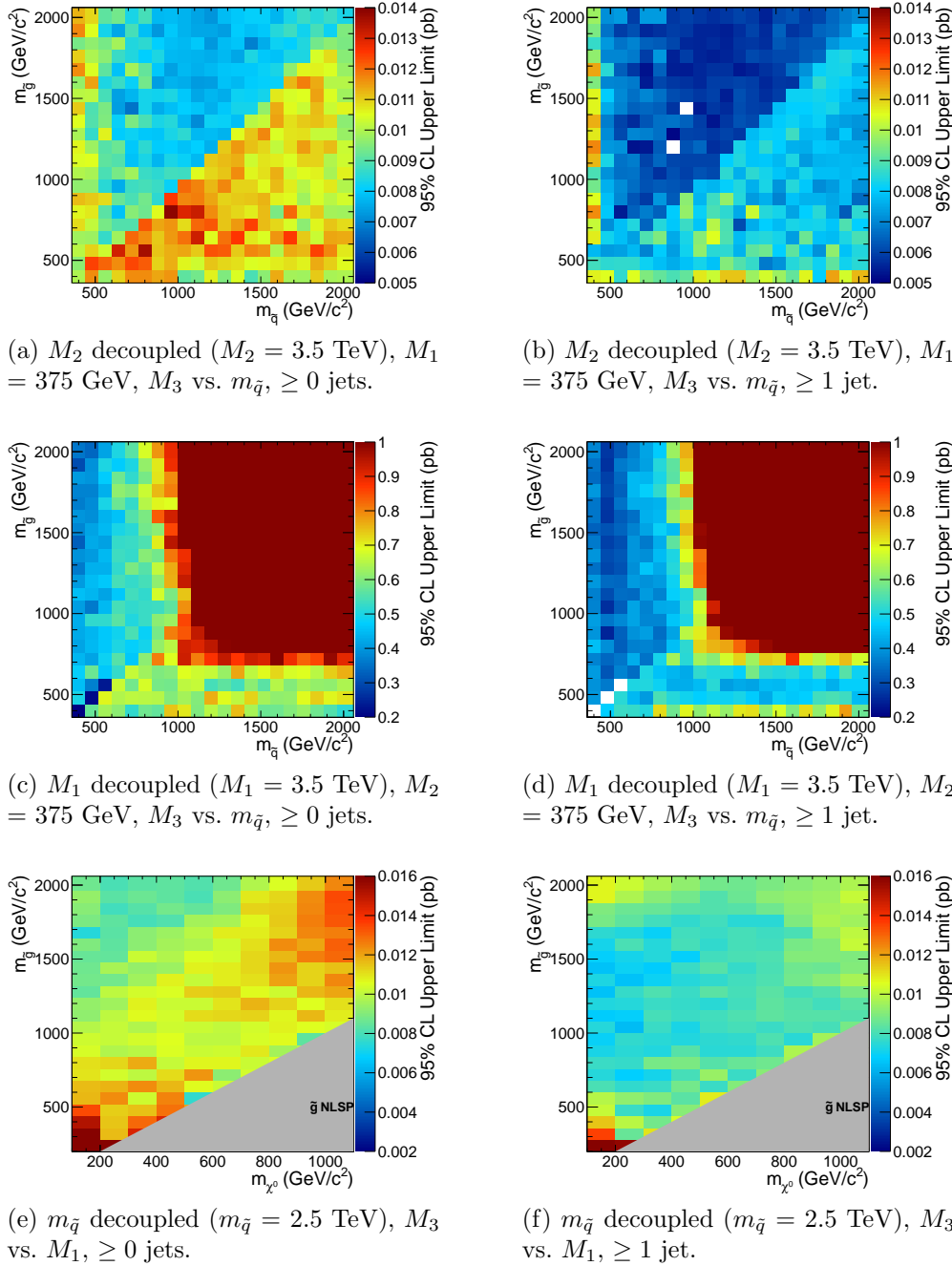


Figure 8.3: Cross section upper limits for the three different scenarios described in Sec. 8.1.

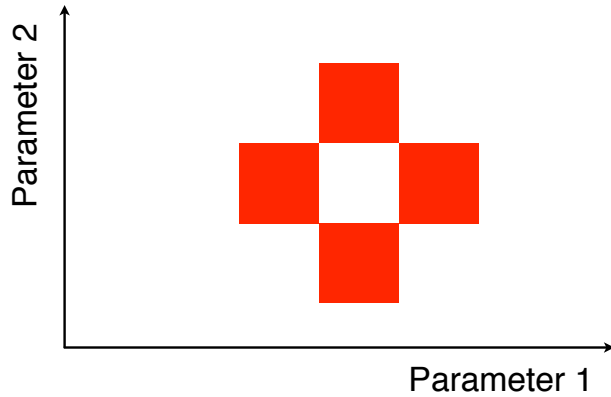


Figure 8.4: Diagram of the points (red squares) used in the estimation of an upper limit when a computational failure occurs (middle white square).

2292 are driven by the contours in the expected cross section plane.

2293 The dominant theoretical uncertainties on the GMSB cross sections are due to:

- 2294 • PDF uncertainty (4%-100% depending on model)
- 2295 • Renormalization scale uncertainty (0.036%-25% depending on model)

2296 The PDF4LHC [116] recommendations are used to calculate the effect of these un-  
 2297 certainties on the GMSB cross sections. The recommendations state that PDF sets  
 2298 from MSTW08 [117], CTEQ6.6 [118], and NNPDF2.0 [119] should be considered in  
 2299 the determination of the PDF uncertainties, because these three PDF sets include  
 2300 constraints from the Tevatron and from fixed target experiments, as well as from  
 2301 HERA [?], and are thus the most complete.

2302 Each collaboration's PDF prediction comes from a global fit to experimental data  
 2303 with a certain number of free parameters. The best fit parameters come from mini-  
 2304 mizing the  $\chi^2$ ; increasing the  $\chi^2$  by one from its minimum can be written in terms of  
 2305 the  $N$ -dimensional Hessian error matrix [?] where  $N$  is the number of free parameters.

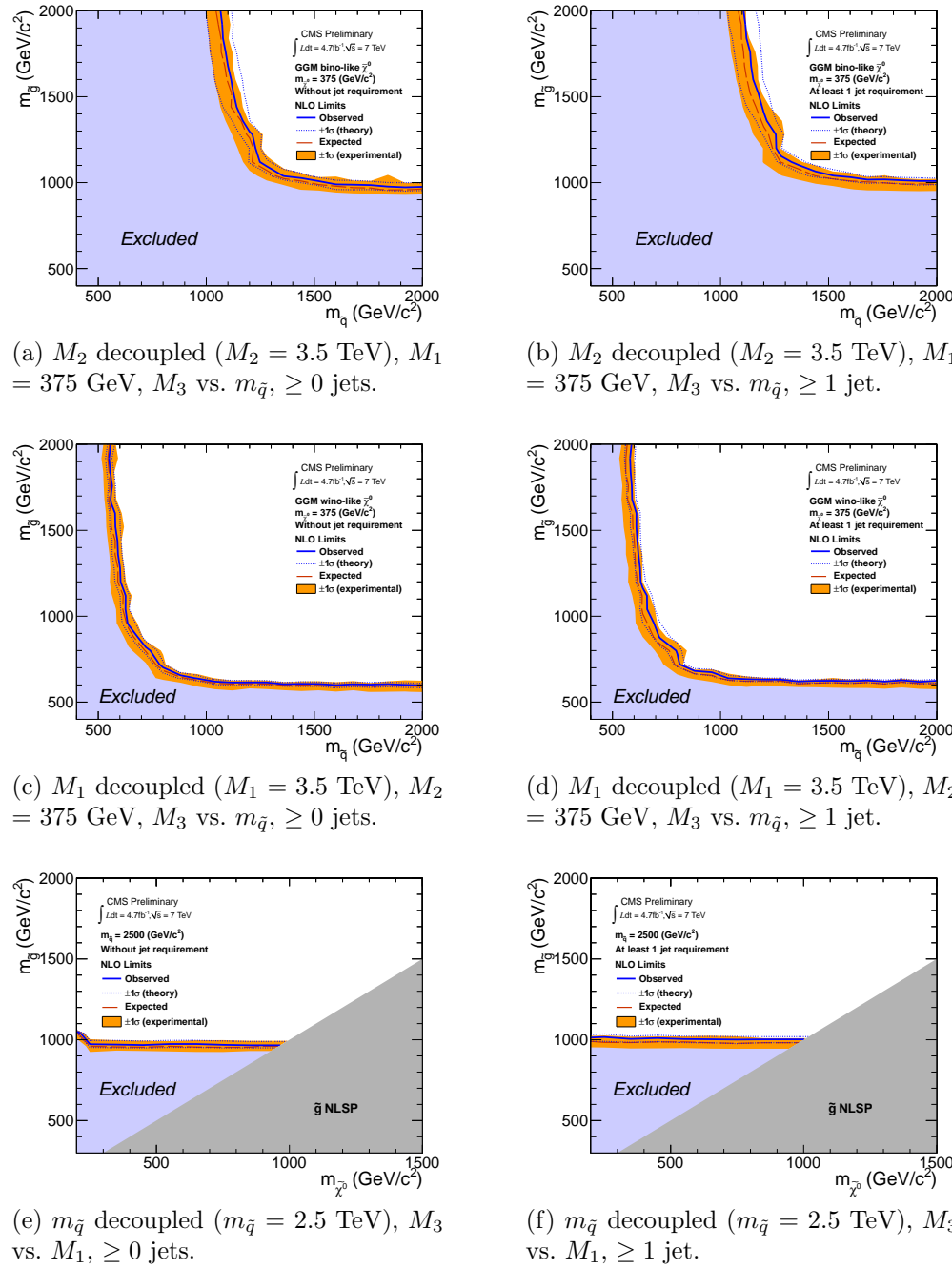


Figure 8.5: Exclusion contours for the three different scenarios described in Sec. 8.1.

2306 To form the  $i^{\text{th}}$  pair of members of the PDF set, the PDF is evaluated once at the  
 2307 parameter values given by the  $i^{\text{th}}$  eigenvector of the Hessian matrix, and then again  
 2308 at the parameter values given by the negative of the  $i^{\text{th}}$  eigenvector. Each PDF set  
 2309 therefore contains  $2N$  members, corresponding to the positive and negative values of  
 2310 the  $N$  eigenvectors [120].

2311 To calculate the PDF uncertainties for a given GMSB model, the leading order  
 2312 Pythia cross section is reweighted by a factor of the error PDF divided by the leading  
 2313 order PDF with which the model was generated. This is repeated for each error PDF  
 2314 in a given PDF set. The  $\pm 1\sigma$  deviations are proportional to the maximum difference  
 2315 between cross sections obtained this way. The actual equation for the  $\pm 1\sigma$  errors is  
 2316 Eq. (43) of ref. [120]. In the same way, the  $\pm 1\sigma$  errors are calculated for the CTEQ6.6,  
 2317 MSTW08, and NNPDF2.0 PDF sets. The total error is given by the half the difference  
 2318 between the largest  $+1\sigma$  deviation and the smallest  $-1\sigma$  deviation [116].

2319 The uncertainties on the signal cross sections due to the choice of renormaliza-  
 2320 tion/factorization scale ( $\alpha_S(M_Z)$ ) are evaluated by calculating the PROSPINO next  
 2321 to leading order cross section once with  $\alpha_S(M_Z)$  halved, then once with  $\alpha_S(M_Z)$  dou-  
 2322 bled. The lower error on the cross section is taken as the absolute difference between  
 2323 the nominal and halved-scale values of the cross section, while the upper error is taken  
 2324 as the absolute difference between the nominal and doubled-scale values. The PDF  
 2325 and  $\alpha_S$  uncertainties are added in quadrature to give the total PDF uncertainty.

2326 Note that the quoted GMSB cross sections are evaluated at next to leading order  
 2327 using PROSPINO, but it is the leading order Pythia cross sections that are reweighted  
 2328 to the next to leading order MSTW08, CTEQ6.6, and NNPDF2.0 PDFs to get the  
 2329 error bands. In addition, since to a good approximation the GMSB production cross  
 2330 sections for the  $M_3$ - $m_{\tilde{q}}$  scans only depend on  $M_3$  and  $m_{\tilde{q}}$ , the same PDF errors per  
 2331 point are used for the  $\tilde{B}$ -like and  $\tilde{W}$ -like grids.

2332 **Chapter 9**

2333 **Conclusion**

2334 The results of a search for evidence of new particle production via final states with  
2335 2 photons, large  $\cancel{E}_T$ , and  $\geq 0$  or  $\geq 1$  jet in  $pp$  collisions at  $\sqrt{s} = 7$  TeV have been  
2336 presented. No deviation in the production rate from that predicted by the Standard  
2337 Model has been found. The null results were used to constrain general models of  
2338 gauge mediated supersymmetry breaking. In these types of models, gluinos and first-  
2339 and second-generation squarks are restricted to masses above  $\sim 1$  TeV.

2340 These bounds on supersymmetry do not exclude it completely. The gluinos and  
2341 first- and second-generation squarks can be a little bit heavier (but not too much  
2342 heavier than a few TeV) and still imply an elegant supersymmetric solution to the  
2343 hierarchy problem. More importantly, the bounds on the first- and second-generation  
2344 squarks say nothing about the stop squark, which is intimately connected to the Higgs  
2345 mass. At one loop order in the supersymmetric Standard Model, the lightest Higgs  
2346 mass is given by [125]

$$m_h^2 \lesssim m_Z^2 + \frac{3g^2 m_t^4}{8\pi^2 m_W^2} \left[ \ln \frac{M_S^2}{m_t^2} + \frac{X_t^2}{M_S^2} \left( 1 - \frac{X_t^2}{12M_S^2} \right) \right] \quad (9.1)$$

2347 where  $g$  is the  $SU(2)_L$  coupling constant,  $M_S^2$  is the average of the two observable

stop squared masses, and  $X_t$  is a parameter that characterizes stop mixing. The Higgs mass is directly sensitive to the stop mass, for which the only current lower bound of 330 GeV [126] is much weaker than for the first- and second-generation squarks (and highly model dependent). The current hints of a Higgs with mass  $\sim 125$  GeV [15, 16] point to a stop mass below 2 TeV if SUSY is really a symmetry of nature, depending on model.

Future searches for GMSB could look for either direct pair production of stops decaying via top quarks to neutralinos that then decay to photons, or for stops produced in the decay of a heavier pair-produced particle like the gluino. Looking for a final state containing a top, antitop, and  $\geq 1$  photon may be advantageous because the expected SM background should be small.

Top quark reconstruction depends heavily on  $b$  jet identification. The same  $b$  tagging techniques needed to find stops could also be applied to a search for a Higgsino-like neutralino decaying primarily to  $b\bar{b}$ . If gaugino mixing were in a certain corner of parameter space, then photon +  $b\bar{b}$  events might provide a window onto GMSB.

There are a number of interesting possibilities for future GMSB searches in addition to those just outlined. SUSY searches will likely remain a fruitful avenue of investigation throughout the lifetime of the LHC.

2366 **Appendix A**

2367 **Monte Carlo Samples**

2368 A number of MC samples are utilized in this analysis and referred to throughout the  
2369 text. Below is a list of the MC samples used and an explanation of what the sample  
2370 names mean.

2371 **A.1 List of Samples**

2372 1. Drell-Yan + up to 2 hard jets:

2373     /DYJetsToLL\_TuneZ2\_M-50\_7TeV-madgraph-tauola/  
2374     Fall11-PU\_S6\_START42\_V14B-v1/AODSIM

2375 2. QCD enriched with  $B$  and  $D$  meson decays to electrons:

2376     /QCD\_Pt-20to30\_BCtoE\_TuneZ2\_7TeV-pythia6/  
2377     Fall11-PU\_S6\_START42\_V14B-v1/AODSIM,  
2378     /QCD\_Pt-30to80\_BCtoE\_TuneZ2\_7TeV-pythia6/  
2379     Fall11-PU\_S6\_START42\_V14B-v1/AODSIM,  
2380     /QCD\_Pt-80to170\_BCtoE\_TuneZ2\_7TeV-pythia6/  
2381     Fall11-PU\_S6\_START42\_V14B-v1/AODSIM

2382 3. Photon + jet doubly enriched with jets passing an EM filter:

2383       /GJet\_Pt-20\_doubleEMEnriched\_TuneZ2\_7TeV-pythia6/  
 2384       Fall11-PU\_S6\_START42\_V14B-v1/AODSIM

2385     4.  $W$  leptonic decays + up to 2 hard jets:

2386       /WJetsToLNu\_TuneZ2\_7TeV-madgraph-tauola/  
 2387       Fall11-PU\_S6\_START42\_V14B-v1/AODSIM

2388     5.  $t\bar{t}$  + up to 2 hard jets:

2389       /TTJets\_TuneZ2\_7TeV-madgraph-tauola/  
 2390       Fall11-PU\_S6\_START42\_V14B-v2/AODSIM

## 2391   A.2   Explanation of Naming Conventions

2392     • L: charged lepton

2393     • B:  $B$  hadron

2394     • C:  $D$ , or charmed, hadron

2395     • E: electron or positron

2396     • G: photon

2397     • W:  $W$  boson

2398     • Nu: neutrino

2399     • T: top quark

2400     • TuneZ2: Pythia tune incorporating 2010 LHC data with CTEQ6L1 [118] PDFs  
 2401           [127]

2402     • M-50: Generated  $l^+l^-$  invariant mass threshold of 50 GeV

2403     • 7TeV: Generated center-of-mass energy 7 TeV

- 2404     ● **pythia6**: Parton showering and hadronization simulated with Pythia v6.424
- 2405         [128]
- 2406     ● **madgraph**: Hard interaction generated with MadGraph 5 [129]
- 2407     ● **tauola**:  $\tau$  decays generated with Tauola [130]
- 2408     ● **PU\_S6**: Generated with S6 pileup scenario, which has a mean between 6 and
- 2409         7 interactions per crossing, and includes pileup from the neighboring bunch
- 2410         crossings according to a Poisson distribution with mean equal to the number of
- 2411         interactions in the in-time crossing [131]
- 2412     ● **START42\_V14B**: Reconstructed with best alignment and calibration constants
- 2413         and magnetic field conditions as of August 3, 2011
- 2414     ● **Pt\_XtoY**:  $X \leq \text{generated } \hat{p}_T < Y$
- 2415     ● **BCToE**: Only keeps events if they contain at least one electron with  $E_T > 10$
- 2416         GeV in  $|\eta| < 2.5$  that came from a  $b$  or  $c$  quark
- 2417     ● **doubleEMEnriched**: Enriched in photons, electrons, electrons from  $b/c$  decay,
- 2418         and electromagnetic jets [132]
- 2419     ● **AODSIM**: Run through full CMS reconstruction algorithm based on a GEANT 4
- 2420         [123] detector simulation; AOD data tier, including generator-level information

# <sup>2421</sup> Bibliography

- <sup>2422</sup> [1] <http://cms.web.cern.ch/news/cms-detector-design> (2011).
- <sup>2423</sup> [2] S.L. Glashow, J. Iliopoulos, and L. Maiani, *Phys. Rev. D* **2** (1970) 1285; S.L. Glashow, *Nucl. Phys.* **22(4)** (1961) 579; J. Goldstone, A. Salam, and S. Weinberg, *Phys. Rev.* **127** (1962) 965; S. Weinberg, *Phys. Rev. Lett.* **19** (1967) 1264; A. Salam and J.C. Ward, *Phys. Lett.* **13(2)** (1964) 168.
- <sup>2427</sup> [3] M. Gell-Mann, *Phys. Lett.* **8** (1964) 214; G. Zweig, *CERN 8419/TH. 412* (1964) (unpublished).
- <sup>2429</sup> [4] J. Drees, *Int. J. Mod. Phys.* **A17** (2002) 3259.
- <sup>2430</sup> [5] P.W. Higgs, *Phys. Lett.* **12(2)** (1964) 132; P.W. Higgs, *Phys. Rev. Lett.* **13** (1964) 508; P.W. Higgs, *Phys. Rev.* **145** (1966) 1156.
- <sup>2432</sup> [6] I. Aitchison, *Supersymmetry in Particle Physics: An Elementary Introduction* (Cambridge University Press, Cambridge 2007), p. 4.
- <sup>2434</sup> [7] C. Quigg, in *Flavor Physics for the Millennium: TASI 2000, Boulder, 2000*, edit by J. L. Rosner (World Scientific, Singapore, 2001), p. 3.
- <sup>2436</sup> [8] L. Álvarez-Gaumé and J. Ellis, *Nature Phys.* **7** (2011) 2.
- <sup>2437</sup> [9] G. Arnison et al. (UA1 Collaboration), *Phys. Lett.* **B122** (1983) 103.
- <sup>2438</sup> [10] G. Arnison et al. (UA1 Collaboration), *Phys. Lett.* **B126** (1983) 398.

- 2439 [11] J. Gunion, H.E. Haber, G. L. Kane, and S. Dawson, *The Higgs Hunter's Guide*,  
 2440 (Addison-Wesley, Redwood City, 1990).
- 2441 [12] S. P. Martin, *A Supersymmetry Primer* **v4** (2006) 86. [arXiv:hep-ph/9709356](#).
- 2442 [13] K. Nakamura et al. (Particle Data Group), *J. Phys.* **G37** (2010) 075021.
- 2443 [14] G. Jungman, M. Kamionkowski, and K. Griest, *SU* **4240-605** (1995).
- 2444 [15] S. Chatrchyan et al. (CMS Collaboration), *Phys. Lett.* **B710** (2012) 26.
- 2445 [16] G. Aad et al. (ATLAS Collaboration), *Phys. Lett.* **B710** (2012) 49.
- 2446 [17] M. Dine and W. Fischler, *Phys. Lett.* **B110** (1982) 227; C.R. Nappi and B.A.  
 2447 Ovrut, *Phys. Lett.* **B113** (1982) 175; L. Alvarez-Gaumé, M. Claudson, and M.B.  
 2448 Wise, *Nucl. Phys.* **B207** (1982) 96; M. Dine and A.E. Nelson, *Phys. Rev.* **D48**  
 2449 (1993) 1277; M. Dine, A.E. Nelson, and Y. Shirman, *Phys. Rev.* **D51** (1995)  
 2450 1362; M. Dine, A.E. Nelson, Y. Nir, and Y. Shirman, *Phys. Rev.* **D53** (1996)  
 2451 2658.
- 2452 [18] A.H. Chamseddine, R. Arnowitt, and P. Nath, *Phys. Rev. Lett.* **49** (1982) 970; R.  
 2453 Barbieri, S. Ferrara, and C.A. Savoy, *Phys. Lett.* **B119** (1982) 343; L.E. Ibáñez,  
 2454 *Phys. Lett.* **B118** (1982) 73; L.J. Hall, J.D. Lykken, and S. Weinberg, *Phys. Rev.*  
 2455 **D27** (1983) 2359; N. Ohta, *Prog. Theor. Phys.* **70** (1983) 542; J. Ellis, D.V.  
 2456 Nanopoulos, and K. Tamvakis, *Phys. Lett.* **B121** (1983) 123; L. Alvarez-Gaumé,  
 2457 J. Polchinski, and M. Wise, *Nucl. Phys.* **B221** (1983) 495.
- 2458 [19] P. Meade, N. Seiberg, and D. Shih, *Progr. Theor. Phys. Suppl.* **177** (2009) 143.
- 2459 [20] G. Aad et al., *CERN-PH-EP-2011-160* (2011).
- 2460 [21] T. Aaltonen et al., *Phys. Rev. Lett.* **104** (2010) 011801.
- 2461 [22] CMS Collaboration, *CMS-PAS-SUS-11-009* (2011).

- 2462 [23] <http://en.wikipedia.org/wiki/Tevatron>.
- 2463 [24] E. Fernandez et al., *Phys. Rev. Lett.* **54** (1985) 1118; E. Fernandez et al., *Phys.*  
 2464 *Rev.* **D35** (1987) 374; D. Decamp et al., *Phys. Lett.* **B237(2)** (1990) 291; F.  
 2465 Abe et al., *Phys. Rev. Lett.* **75** (1995) 613; S. Abachi et al., *Phys. Rev. Lett.* **75**  
 2466 (1995) 618; G. Alexander et al., *Phys. Lett.* **B377(4)** (1996) 273; S. Aid et al.,  
 2467 *Z. Phys.* **C71(2)** (1996) 211; S. Aid et al., *Phys. Lett.* **B380(3-4)** (1996) 461; B.  
 2468 Aubert et al., *Phys. Rev. Lett.* **95** (2005) 041802.
- 2469 [25] O. Buchmueller et al., *CERN-PH-TH/2011-220* (2011).
- 2470 [26] <https://twiki.cern.ch/twiki/bin/view/CMSPublic/PhysicsResultsSUS>.
- 2471 [27] G. Aad et al., *JINST* **3** (2008) S08003.
- 2472 [28] B.C. Allanach et al., *Eur. Phys. J.* **C25** (2002) 113.
- 2473 [29] CMS Collaboration, *CMS-PAS-SUS-12-001* (2012).
- 2474 [30] A. Boyarsky, J. Lesgourges, O. Ruchayskiy, and M. Viel, *CERN-PH-TH/2008-*  
 2475 *234* (2009).
- 2476 [31] E. Komatsu et al., *Astrophys. J. Suppl. Ser.* **180** (2009) 330.
- 2477 [32] C.-H. Chen and J.F. Gunion, *Physical Review* **D58** (1998) 075005.
- 2478 [33] F. Staub, W. Porod, J. Niemeyer, *JHEP* **1001** (2010) 058.
- 2479 [34] L. Evans and P. Bryant (eds.), *JINST* **3** (2008) S08001.
- 2480 [35] <http://cms.web.cern.ch/news/summary-2011-p-p-running> (2011).
- 2481 [36] <http://public.web.cern.ch/public/en/lhc/Facts-en.html> (2008).
- 2482 [37] CERN, <http://cdsweb.cern.ch/record/833187> (2005).

- 2483 [38] RGBStock.com, <http://www.rgbstock.com/photo/n7EsabW/Airplane> (2011).
- 2484 [39] R. Flükiger, S. Y. Hariharan, R. Küntzler, H. L. Luo, F. Weiss, T. Wolf, and J.  
2485 Q. Xu, in *Landolt-Börnstein: Numerical Data and Functional Relationships in*  
2486 *Science and Technology*, edited by R. Flükiger and W. Klose (Springer, 2012).
- 2487 [40] Y.-P. Sun, F. Zimmermann, and R. Tomás, in Proceedings of the 23<sup>rd</sup> Particle Ac-  
2488 celerator Conference, Vancouver, 2009, <http://accnet.web.cern.ch/accnet/>  
2489 Literature/2009/TH5PFP016-Sunpdf.pdf (unpublished).
- 2490 [41] O.S. Brüning et al. (eds.), *CERN-2004-003-V-1*, <http://lhc.web.cern.ch/lhc/LHC-DesignReport.html> (2004).
- 2492 [42] CERN, <http://cdsweb.cern.ch/record/841568/files/> (1993).
- 2493 [43] P. Komorowski and D. Tommasini, in *Proceedings of the 1998 International*  
2494 *Computational Accelerator Physics Conference, Monterey, 1998*, edited by K.  
2495 Ko and R. Ryne (SLAC, Stanford, 1998), p. 192, [http://www.slac.stanford.edu/econf/C980914/papers/ICAP98\\_eConf.pdf](http://www.slac.stanford.edu/econf/C980914/papers/ICAP98_eConf.pdf).
- 2497 [44] <http://lhc-machine-outreach.web.cern.ch/lhc-machine-outreach/components/magnets.htm> (2008).
- 2499 [45] S. Chatrchyan et al. (CMS Collaboration), *JINST* **3** (2008) S08004.
- 2500 [46] G.L. Bayatian et al. (CMS Collaboration), *CERN/LHCC 2006-001*, edited by  
2501 D. Acosta (2006).
- 2502 [47] M. Ivova, talk given at the Swiss Ph.D. School on Particle and Astroparticle  
2503 Physics (CHIPP), Monte Verita' (2010).
- 2504 [48] G. Bolla et al., *Nucl. Instr. Meth. Res.* **A461** (2001) 182.

- 2505 [49] [https://twiki.cern.ch/twiki/pub/CMSPublic/DPGResultsTRK/\\_imgf9e0ee48ebca770d7774454532b4b4ee.png](https://twiki.cern.ch/twiki/pub/CMSPublic/DPGResultsTRK/_imgf9e0ee48ebca770d7774454532b4b4ee.png) (2011).
- 2507 [50] [https://twiki.cern.ch/twiki/pub/CMSPublic/DPGResultsTRK/\\_img7569b7652b3f7c15030a11a4223e631c.png](https://twiki.cern.ch/twiki/pub/CMSPublic/DPGResultsTRK/_img7569b7652b3f7c15030a11a4223e631c.png) (2011).
- 2509 [51] [https://twiki.cern.ch/twiki/pub//CMSPublic/DPGResultsTRK/hv11\\_d1.png](https://twiki.cern.ch/twiki/pub//CMSPublic/DPGResultsTRK/hv11_d1.png) (2011).
- 2511 [52] [https://twiki.cern.ch/twiki/pub/CMSPublic/DPGResultsTRK/\\_imga571742cbed3a14a9e2581ae95efa54c.gif](https://twiki.cern.ch/twiki/pub/CMSPublic/DPGResultsTRK/_imga571742cbed3a14a9e2581ae95efa54c.gif) (2011).
- 2513 [53] <https://twiki.cern.ch/twiki/pub//CMSPublic/DPGResultsTRK/StripHitRes2.gif> (2011).
- 2515 [54] [https://twiki.cern.ch/twiki/pub//CMSPublic/EcalDPGResults/histories2\\_laser.png](https://twiki.cern.ch/twiki/pub//CMSPublic/EcalDPGResults/histories2_laser.png) (2012).
- 2517 [55] [https://twiki.cern.ch/twiki/pub//CMSPublic/EcalDPGResults/electronres\\_eb\\_inclusive.png](https://twiki.cern.ch/twiki/pub//CMSPublic/EcalDPGResults/electronres_eb_inclusive.png) (2012).
- 2519 [56] [https://twiki.cern.ch/twiki/pub//CMSPublic/EcalDPGResults/electronres\\_ee\\_inclusive.png](https://twiki.cern.ch/twiki/pub//CMSPublic/EcalDPGResults/electronres_ee_inclusive.png) (2012).
- 2521 [57] <https://twiki.cern.ch/twiki/pub//CMSPublic/EcalDPGResults/seed-time.EEEE.png> (2012).
- 2523 [58] N. Akchurin and R. Wigmans, *Rev. Sci. Instrum.* **74** (2003) 2955.
- 2524 [59] CMS Collaboration, *CMS-DP 2010-025* (2010).
- 2525 [60] [https://twiki.cern.ch/twiki/pub/CMSPublic/PhysicsResultsMUO/dimuMass\\_2011Run\\_1fb\\_20July2011.pdf](https://twiki.cern.ch/twiki/pub/CMSPublic/PhysicsResultsMUO/dimuMass_2011Run_1fb_20July2011.pdf) (2011).
- 2527 [61] S. Chatrchyan et al. (CMS Collaboration), *JHEP* **4** (2012) 33.

- 2528 [62] W.H. Smith, P. Chumney, S. Dasu, F. Di Lodovico, M. Jaworski, J.R. Lackey, and  
 2529 P. Robl in *Proceedings of the 7<sup>th</sup> Workshop on Electronics for LHC Experiments,*  
 2530 *Stockholm, 2001*, edited by C. Isabella (CERN, Geneva, 2001), p. 238.
- 2531 [63] R. Brun and F. Rademakers, *Nucl. Inst. Meth. Res.* **A389** (1997) 81. See also  
 2532 <http://root.cern.ch/>.
- 2533 [64] J. Guteleber and L. Orsini, *Cluster Comput.* **5** (2002) 55.
- 2534 [65] D. Box, D. Ehnebuske, G. Kakivaya, A. Layman, N. Mendelsohn, H.F.  
 2535 Nielsen, S. Thatte, and D. Winer, *W3C Note 08*, <http://www.w3.org/TR/2000/NOTE-SOAP-20000508/> (2000).
- 2537 [66] R. Arcidiacono et al., talk given at the 10<sup>th</sup> ICAL-EPCS International Conference  
 2538 on Accelerator and Large Experiment Physics Control Systems, Geneva (2005).
- 2539 [67] J. Knobloch et al., *CERN-LHCC-2005-024* (2005).
- 2540 [68] R. Brunelière, *Nucl. Instr. Meth. Res.* **A572** (2007) 33.
- 2541 [69] S. Chatrchyan et al. (CMS Collaboration), *JINST* **5** (2010) T03011.
- 2542 [70] CMS Collaboration, *CMS PAS EGM-10-002* (2010).
- 2543 [71] P. Meridiani and C. Seez, *CMS IN-2011/002* (2011).
- 2544 [72] P. Adzic et al. (CMS Electromagnetic Calorimeter Group), *Eur. Phys. J.* **C44S2**  
 2545 (2006) 1.
- 2546 [73] P. Adzic et al. (CMS Electromagnetic Calorimeter Group), *JINST* **3** (2008)  
 2547 P10007.
- 2548 [74] M. Malberti, *Nuc. Sci. Symposium Conference Record NSS/MIC IEEE* (2009)  
 2549 2264.

- 2550 [75] S. Chatrchyan et al. (CMS Collaboration), *JINST* **5** (2010) T03010.
- 2551 [76] R. Paramatti, *J. Phys. Conf. Ser.* **293** (2011) 012045.
- 2552 [77] Y. Yang, [http://www.hep.caltech.edu/cms/posters/Pi0Poster\\_CMSWeekDec2011.pdf](http://www.hep.caltech.edu/cms/posters/Pi0Poster_CMSWeekDec2011.pdf) (2011).
- 2554 [78] M. Anderson, A. Askew, A.F. Barfuss, D. Evans, F. Ferri, K. Kaadze, Y. Maravin,  
2555 P. Meridiani, and C. Seez, *CMS IN-2010/008* (2010).
- 2556 [79] <https://twiki.cern.ch/twiki/bin/view/CMS/ECALEnergyScaleCorrections>.
- 2557 [80] The H $\rightarrow \gamma\gamma$  working group, *CMS AN-2011/426* (2011).
- 2558 [81] M. Cacciari, *LPTHE-P06-04* (2006).
- 2559 [82] M. Cacciari, G.P. Salam, and G. Soyez, *CERN-PH-TH-2011-297* (2011).
- 2560 [83] S. Chatrchyan et al. (CMS Collaboration), *Phys. Rev. Lett.* **106** (2011) 082001.
- 2561 [84] A. Askew, B. Cox, D. Elvira, Y. Gershtein, M. Hildreth, D. Jang, Y.-F. Liu, D.  
2562 Mason, D. Morse, U. Nauenberg, M. Paulini, R. Stringer, R. Yohay, and S.L.  
2563 Zang, *CMS AN-2011/515* (2011).
- 2564 [85] F. Beaudette, D. Benedetti, P. Janot, and M. Pioppi, *CMS AN-2010/034* (2010).
- 2565 [86] M. Konecki, in Proceedings of the European Physical Society Europhysics Con-  
2566 ference on High Energy Physics, Krakow, 2009, Eur. Phys.Soc. Mulhouse (ed.)  
2567 (unpublished).
- 2568 [87] W. Adam, R. Früwirth, A. Strandlie, and T. Todorov, *J. Phys.* **G31** No. 9 (2005).
- 2569 [88] CMS Collaboration, *CMS PAS PFT-09-001* (2009).
- 2570 [89] CMS Collaboration, *CMS PAS PFT-10-002* (2010).

- 2571 [90] S. Chatrchyan et al., *JINST* **6** (2011) P11002.
- 2572 [91] CMS Collaboration, *CERN-PH-EP* **2011-102** (2011).
- 2573 [92] M. Cacciari, G.P. Salam, and G. Soyez, *JHEP* **0804** (2008) 063.
- 2574 [93] G. Salam, talk given at CERN Theory Institute: SM and BSM Physics at the  
2575 LHC (2009).
- 2576 [94] C.W. Fabjan and R. Wigmans, *Rep. Prog. Phys.* **52** (1989) 1519.
- 2577 [95] <http://www-cdf.fnal.gov/physics/new/top/2004/jets/cdfpublic.html>  
2578 (visited on 16 January 2011).
- 2579 [96] S. Chatrchyan et al. (CMS Collaboration), *JINST* **6** (2011) P09001.
- 2580 [97] CMS Collaboration, *CMS PAS JME-09-002* (2009).
- 2581 [98] T. Sjöstrand, S. Mrenna, and P. Z. Skands, *Comput. Phys. Commun.* **178** (2008)  
2582 852.
- 2583 [99] S. Chatrchyan et al. (CMS Collaboration), *JINST* **5** (2010) T03014.
- 2584 [100] J. P. Chou, S. Eno, S. Kunori, S. Sharma, and J. Wang, *CMS IN-2010/006*  
2585 (2010).
- 2586 [101] Y. Chen, talk given at a meeting of the CMS JetMET group (2011).
- 2587 [102] R. Korzekwa et al., *iEEE Trans. Elec. Dev.* **38** (1991) 745.
- 2588 [103] W. Adam, Th. Speer, B. Mangano, and T.Todorov, *CMS NOTE* **2006/041**  
2589 (2006).
- 2590 [104] G. Daskalakis, D. Evans, C.S. Hill, J. Jackson, P. Vanlaer, J. Berryhill, J. Haupt,  
2591 D. Futyan, C. Seez, C. Timlin, and D. Wardrope, *CMS AN-2007/019* (2007).

- 2592 [105] F. James and M. Roos, *Comput. Phys. Commun.* **10** (1975) 343.
- 2593 [106] W. Verkerke and D.P. Kirkby, *CHEP-2003-MOLT007* (2003).
- 2594 [107] J.E. Gaiser, Ph.D. thesis, Stanford University (1982).
- 2595 [108] A. Askew, S. Arora, Y. Gershtein, S. Thomas, G. Hanson, R. Stringer, W.  
2596 Flanagan, B. Heyburn, U. Nauenberg, S.L. Zang, R. Nandi, D. Elvira, D. Mason,  
2597 M. Balazs, B. Cox, B. Francis, A. Ledovskoy, and R. Yohay, *CMS AN* **2010/271**  
2598 (2010).
- 2599 [109] Information about all CMS datasets is available from the CMS Data Aggrega-  
2600 tion System (DAS), located at the URL <https://cmsweb.cern.ch/das/>.
- 2601 [110] S. Chatrchyan et al., *Phys. Rev. Lett.* **106** (2011) 211802.
- 2602 [111] G. Aad et al. (ATLAS Collaboration), S. Chatrchyan et al. (CMS Collabora-  
2603 tion), and LHC Higgs Combination Group, *CMS-NOTE-2011/005* (2011).
- 2604 [112] A.L. Read, in *Proceedings of the First Workshop on Confidence Limits, Geneva,*  
2605 *2000*, edited by L. Lyons, Y. Perrin, and F.E. James (CERN, Geneva, 2000), p.  
2606 81.
- 2607 [113] G. Cowan, K. Cranmer, E. Gross, and O. Vitells, *Eur. Phys. J.* **C71** (2011)  
2608 1554.
- 2609 [114] J. Neyman and E.S. Pearson, *Phil. Trans. R. Soc. Lond.* **A231** (1933) 289.
- 2610 [115] CMS Collaboration, *CMS PAS EWK-11-001* (2011).
- 2611 [116] S. Alekhin et al. (The PDF4LHC Working Group), [arXiv:1101.0536 \[hep-ph\]](https://arxiv.org/abs/1101.0536);  
2612 M. Botje et al. (The PDF4LHC Working Group), [arXiv:1101.0538 \[hep-ph\]](https://arxiv.org/abs/1101.0538);  
2613 <http://www.hep.ucl.ac.uk/pdf4lhc/index.html>.

- 2614 [117] A.D. Martin, W.J. Stirling, R.S. Thorne, and G. Watt, *Eur. Phys. J.* **C63**  
2615 (2009) 189.
- 2616 [118] P. M. Nadolsky, H.-L. Lai, Q.-H. Cao, J. Huston, J. Pumplin, D. Stump, W.-K.  
2617 Tung, and C.-P. Yuan, *Phys. Rev.* **D78** (2008) 013004.
- 2618 [119] R.D. Ball, L. Del Debbio, S. Forte, A. Guffanti, J.I. Latorre, J. Rojo, and M.  
2619 Ubiali, *Nucl. Phys.* **B838** (2010) 136.
- 2620 [120] J.M. Campbell, J.W. Huston, and W.J. Stirling, *Rep. Prog. Phys.* **70** (2007) 89.
- 2621 [121] A. Djouadi, J.-L. Kneur, G. Moultaka, [arXiv:hep-ph/0211331](#) (2005).
- 2622 [122] M. Muhlleitner, A. Djouadi, Y. Mambrini, *Comput. Phys. Commun.* **168** (2005)  
2623 46.
- 2624 [123] J. Allison et al., *IEEE Trans. Nucl. Sci.* **53(1)** (2006) 270.
- 2625 [124] W. Beenakker, R. Hoepker, M. Spira, [arXiv:hep-ph/9611232](#) (1996).
- 2626 [125] M. Carena, J.S. Conway, H.E. Haber, and J.D. Hobbs, *FERMILAB-Conf-00*  
2627 **279-T** (2000). [arXiv:hep-ph/0010338](#)
- 2628 [126] ATLAS Collaboration, *ATLAS-CONF 2012-036* (2012).
- 2629 [127] R. Field, talk given at LHC Physics Centre at CERN Minimum Bias and Un-  
2630 derlying Event Working Group Meeting (2011).
- 2631 [128] T. Sjöstrand, S. Mrenna, and P. Z. Skands, *JHEP* **0605** (2006) 026.
- 2632 [129] J. Alwall, M. Herquet, F. Maltoni, O. Mattelaer, and T. Stelzer, *JHEP* **1106**  
2633 (2011) 128.
- 2634 [130] Z. Was, *Nucl. Phys. Proc. Suppl.* **98** (2001) 96.

2635 [131] <http://cmslxr.fnal.gov/lxr/source/SimGeneral/MixingModule/python/>  
2636 mix\_E7TeV\_Fall2011\_Reprocess\_50ns\_PoissonOOTPU\_cfi.py (2011).  
  
2637 [132] <http://cmslxr.fnal.gov/lxr/source/GeneratorInterface/GenFilters/>  
2638 src/doubleEMEnrichingFilterAlgo.cc (2011).